Investigations of high pressure phase diagrams of MgO-SiO2 systems with laser shock compression

Riccardo Maria Bolis

NNT : 2017SACLX056

Thèse de doctorat

Laser shock compression studies of MgO-SiO_2 systems at high pressures

Thèse de doctorat de l'Université Paris-Saclay
préparée à l'École Polytechnique

École doctorale n°572 Onde et Matière
EDOM
Spécialité de doctorat: physique

Thèse présentée à Palaiseau, le 12/10/2017, par

Riccardo Bolis

Composition du Jury :

Patrick Renaudin Directeur de recherche, CEA-DAM	Président
Thomas Boehly Senior Scientist, University of Rochester (LLE)	Rapporteur
Laurent Berthe Directeur de recherche, ENSAEM (PIMM)	Rapporteur
Patrick Audebert Directeur de recherche, Ecole Polytechnique (LULI)	Examinateur
Guillaume Fiquet Directeur de recherche, Université Pierre et Marie Curie (IMPMC)	Examinateur
Thibaut de Resseguier, Directeur de recherche, Université de Poitiers (Pprime)	Examinateur
Alessandra Benuzzi-Mounaix Directeur de recherche, Ecole Polytechnique (LULI)	Directeur de thèse
Alessandra Ravasio chargé de recherche, Ecole Polytechnique (LULI)	Co-Directeur de thèse
Tommaso Vinci Ingénieur, Ecole Polytechnique (LULI)	Invité

Contents

Introduction

In the last decade a huge number of exoplanets has been discovered (3498 confirmed planet, 26/06/2017), placing planetology among research topics of broad and current interest. Planets of various sizes and masses have been found, and those discoveries provide the insights for a better understanding of planetary formation, evolution and dynamics. In this context the quest of habitable planets started to get fascinating results, as for example 7 Earth-like planets have been recently observed orbiting around the dwarf star TRAPPIST-1 [Gillon et al., 2017].

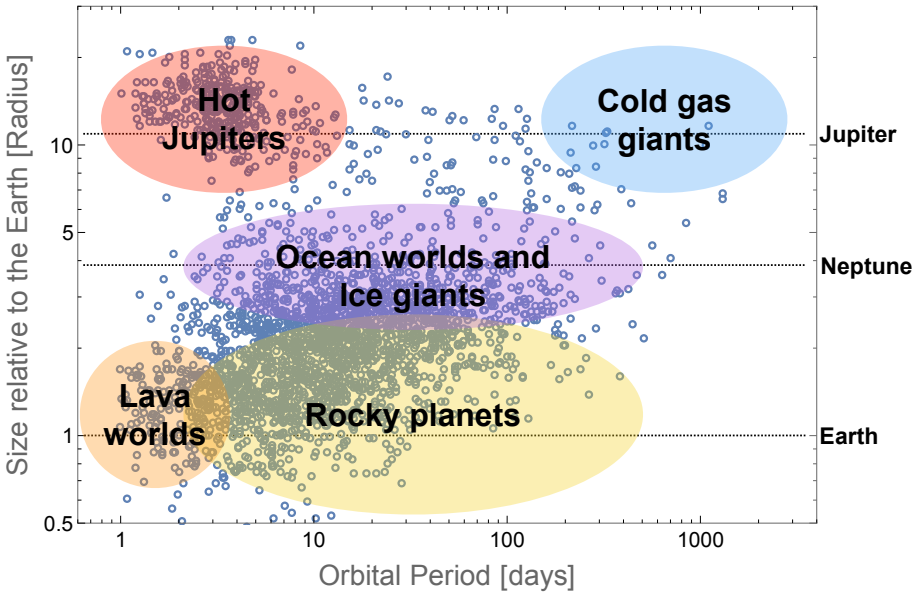

Figure 1: The population of exoplanets detected up to June 2017 and represented on radius (relative to the Earth) and orbital period diagram. Coloured areas classify exoplanets according to the planet type.

Most exoplanets have been detected with two methods: Transit Photometry (1) and

Doppler Spectroscopy (2). Transit Photometry detects drops of the visual brightness of star induced by the transit of a planet. Doppler Spectroscopy can detect redshifts or blueshifts of the star spectrum that are induced by the star response to the planet's gravity. Method 2) provides the mass of the planet, while method 1) can provide the radius as well as the atmosphere composition and the surface temperature of the detected planet. Both techniques access the planetary orbiting period.
These quantities provide valuable constraints for the modelling of the planetary structure, dynamics and evolution.
However to this aim, it is also necessary to know equations of state (EoS) and physical properties of the planetary components. Indeed, models of planetary internal structures are based on the system of hydrostatic equations closed by the equation of state of the assumed interior components. Similarly, for modelling other large-scale planetary phenomena other information about the planetary constituents are needed. For example the generation of the magnetic field is strictly correlated to the electrical conductivity and the rheological properties of the planetary components.
Therefore the knowledge of the planetary interior components, of their EoS and of their physical properties is a key element for advancing in the study of planets. Unfortunately the composition of an exoplanet is not an easy-accessible information. There are only two observable constraints that limit the range of possible composition of a given exoplanet. The first is the planetary mean density. The second is the composition of the host star and the host star-planet distance. However the relation between stellar abundances and planetary compositions is not straightforward, depending for example on the planetary forming-process within the accretion disk.
In this puzzling context planets of the Solar System are taken as a reference. Indeed, thanks to their proximity to the Earth more observables are available (like gravitational moments or planetary magnetic fields). This allowed developments of models that describe at a first stage the bodies of the Solar System, though with some questions left open (e.g. we will see in the following that our knowledge of the cores of Jupiter, Saturn, Uranus and Neptune is limited).
In the following we briefly report the most current and widely accepted models of the internal structures of Solar System planets. This will allow to have an overview of the most abundant planetary constituents and of their thermodynamic conditions.

The Earth In this context, obviously the Earth is a privileged case. The availability of precise seismological data facilitated to build a model that explains a wide number of large scale phenomena.
It is widely accepted that the Earth can be divided in three layers. The innermost layer is a metallic core of radius 3500 km, surrounded by a rocky shell (mantle) of radius 2900 km which is in turn surrounded by a thin solid rocky crust with a different

composition that the mantle.
The Earth's core can be divided in inner and outer cores that are respectively solid and liquid. Both cores are mainly composed of iron and nickel alloys.
The Earth's mantle can be divided in upper mantle, mainly composed by olivine $(Mg, Fe)_2SiO_4$ and pyroxene minerals, and a lower mantle dominated by bridgmanite $(Fe,Mg)SiO_3$ and ferropericlase (Fe, Mg)O. At the base of the mantle, close to core-mantle boundary (CMB), bridgmanite transforms into a polymorph with post-perovskite structure. The Earth's core most abundant composant is Fe, but also Ni and lighter elements (S, O, Si, C, and H) are present as 10% of the core mass.
Rocky exoplanets are expected to present similar internal structures, with differences for planets with larger sizes or with different Mg/Si ratio in comparison to the Earth.

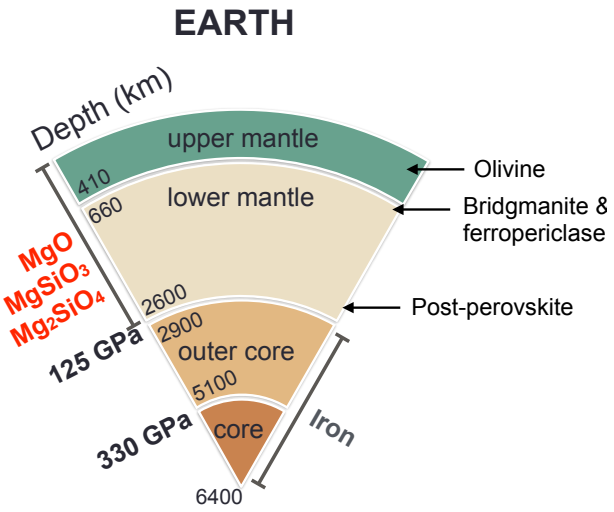

Figure 2: Earth's internal structures and compositions.

Gas giants: Jupiter and Saturn Jupiter and Saturn interior models satisfying observational constraints predict the occurrence of three layers (see fig. 3) [Guillot, 2005]. A central dense core is surrounded by a hydrogen-helium layer with a mixing ratio of ~ 0.27 for Jupiter and ~ 0.3 for Saturn, which is in turn surrounded by an outer hydrogen-helium envelope with a lower mixing ratio (~ 0.23 for Jupiter and 0.2 for Saturn). The global composition of this outer layer is expected to be the same as the one of the deep atmosphere. Thermodynamic conditions at the boundaries between the different layers are reported in fig. 3.
The nature of the giant planet core is not yet well understood. Recently models that match observational constraints obtained cores $<$ 10 Earth's Masses. However the

composition of the core is still unknown. A composition of Ice and Rocks (silicates and magnesium oxides) is the most likely.
The internal structures of cold gas giant exoplanets is expected to reflect those of Saturn and Jupiter.

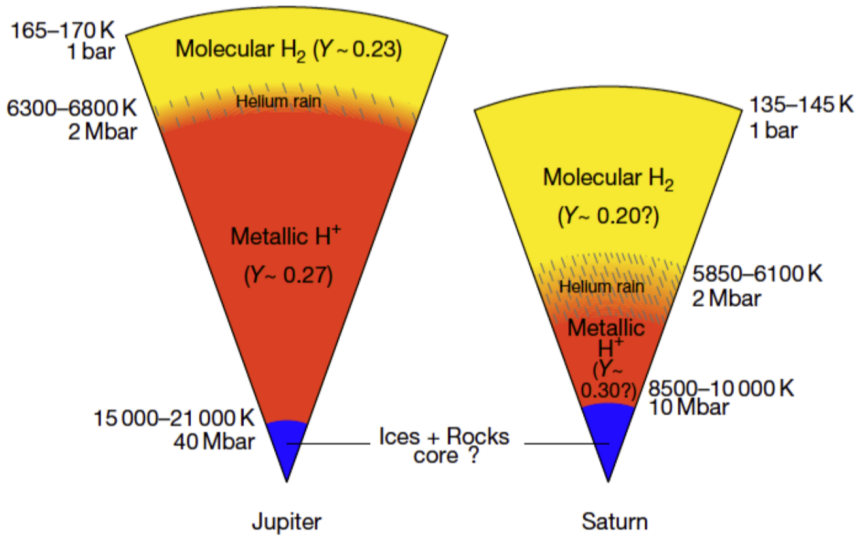

Figure 3: Jupiter's and Saturn's internal structures and compositions, from [Guillot, 2005]. Y is the mixing ratio.

Icy giants: Uranus and Neptune Observed gravitational moments allow to infer the density profiles of Uranus and Neptune. These profiles match the densities of Hydrogen and Helium in the outermost part of the planet. For inner layers density profiles match with densities typical of ices (mixtures of H_2O, CH_4, and NH_3) that are expected to transform into ionic liquids at deeper layers.
Uranus and Neptune are then modelled to be composed of three layers (see fig. 4) [Guillot, 2005]. The inner layers is a central rocky core composed of iron and magnesium silicates. This core is surrounded by an ice layer and by an outer gaseous envelope of hydrogen and helium. Thermodynamic conditions at the boundaries between the different layers are reported in fig. 4.
Ocean worlds and icy giant internal structures are expected to reflect those of Uranus and Neptune.

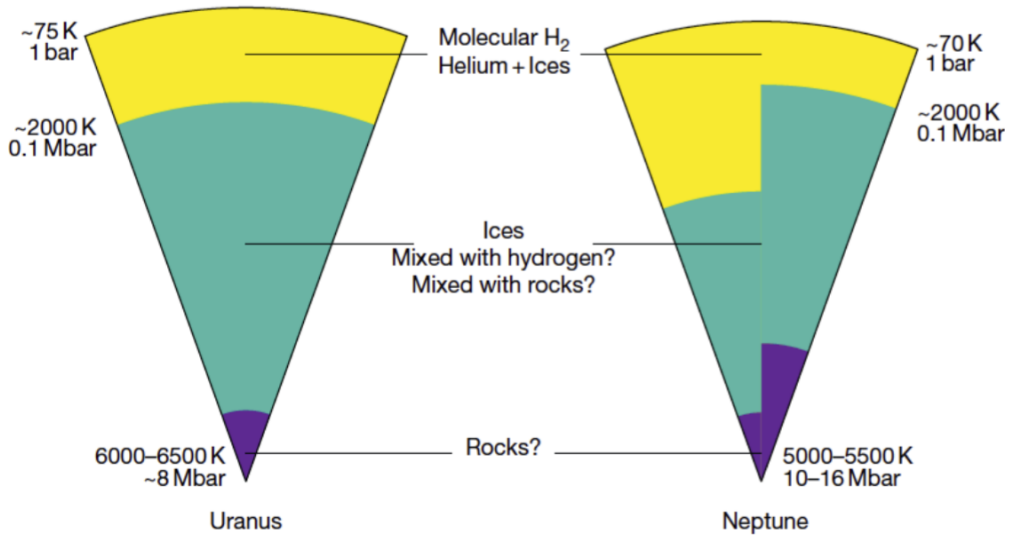

Figure 4: Uranus' and Neptune's internal structures and compositions, from [Guillot, 2005].

According to its mean density and its distance from the host star, an exoplanet can be associated to a planet of the Solar System. For example, internal compositions of Earth-like planets and Super-Earths (also called rocky planets) are reasonably assumed to be similar to the one of the Earth [Duffy et al., 2015], at least as a starting point. Differences will consist in the thermodynamic conditions at which the components are subjected. For example pressure and temperature at the core-mantle boundary of a Super-Earth of 10 Earth Masses are expected to be $\sim$ 1 TPa and $\sim$ 5000 K [Valencia et al., 2006; Stixrude, 2014]. Similarly the highest pressure and temperature in the core are 15000K [Stixrude, 2014] and 3.5 TPa [Valencia et al., 2006].
In a similar way, among the cold gas giants there are planets even bigger than Jupiter. Therefore planetary components of these planets, also called Super-Jupiters, are subjected to thermodynamic conditions more extreme even than those found in Jupiter.

Determining equation of state, phase diagram and physical properties of matter at the extreme conditions that we reviewed is a challenging problem. Planetary interiors lie in a regime at the intersection between condensed matter and plasma physics. This regime, called Warm Dense Matter (WDM), spans densities typical of solids and temperatures between few 0.1 eV to few tens of eV (see fig. 5). In such regime neither the approximation typical of condensed matter nor those typical of classical plasma physics are valid. Temperatures and densities are respectively too high to allow to describe WDM as a solid or as an ideal plasma. At WDM temperature

and pressure conditions, plasmas are slightly ionised, strongly coupled and partially degenerate.

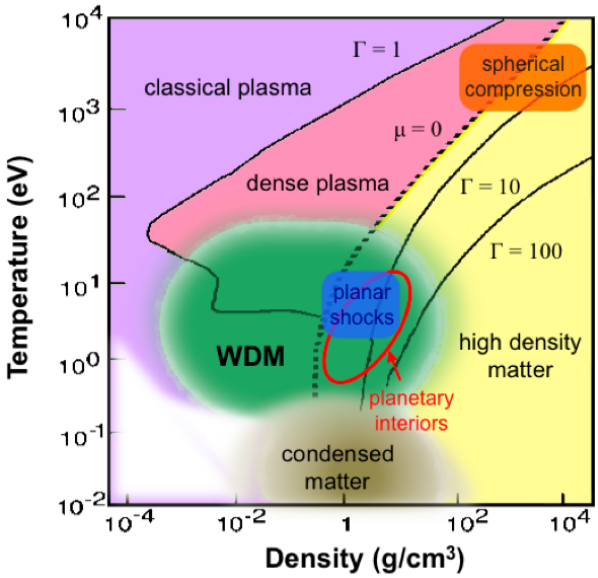

Figure 5: Temperature-Density phase diagram contextualising the WDM regime. WDM lies between the plasma and condensed matter regimes. Planetary interiors (pointed by the red arrow) are located in the high density region of the WDM regime.

From the theoretical point of view, quantum mechanical theory provides methods for studying matter in WDM regime. Such methods consists in density functional theory (DFT) calculations combined with molecular dynamics (MD). DFT provides the electronic structures of the sample under investigations, which allows calculation of the potentials for simulating the ions dynamics with MD. This combination of DFT + MD calculations is also called ab initio molecular dynamics (AIMD) or quantum molecular dynamics (QMD). The development of this tool constitutes a great step forward in the study of WDM. However such calculations need to be tested, confirmed by and compared with experiments.

Therefore experiments have a key role to advance the understanding of matter at planetary interior conditions. Experimentally, the first challenge consists in reaching such extreme conditions. Last decades saw important progresses in the field. Essentially the techniques for reaching high pressure conditions can be divided into static and dynamic compression methods. For static compression, Diamond Anvil Cell (DAC) is the most widely used and efficient instrument. As shown in fig. 6 it allows to study high pressure temperature conditions up to 350 GPa and 6000 K. Technical difficulties prevent the study of high temperature conditions for higher pressures. At the

time of the writing, the highest pressure reached with DAC is 1 TPa [Dubrovinskaia et al., 2016] but at ambient temperature.

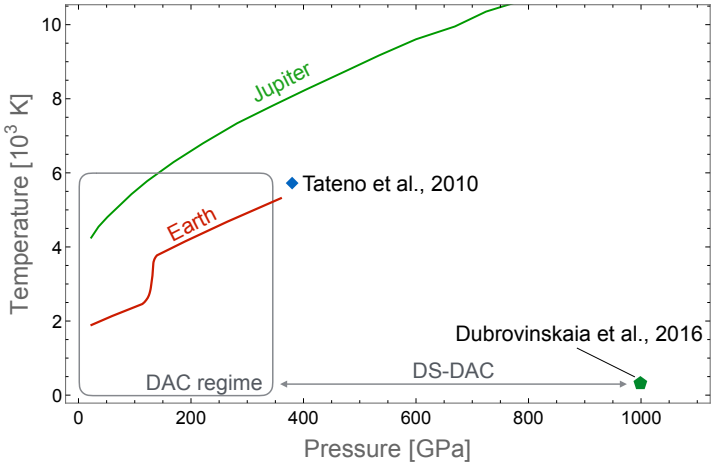

Figure 6: Conditions achievable using different methods of static pressure generation.

Concerning dynamic compression methods, the advent of of high power laser (NIF, LMJ, Omega, LULI2000, GEKKOXII) and Z-pinch facilities (SANDIA) extended significantly the available range of pressure. Previously, gas gun were the most widely used instrument to dynamically compress materials. Gas gun and Z-pinch typically achieve pressure < 500 GPa. This limit can be overcome with high power laser where P$>$ 1TPa can be achieved.
There are two dynamic compression methods: shock compression and ramp compression. A shock wave is the fastest mechanical loading that can be applied to a material and it is a highly irreversible process. Therefore the shock technique allows to reach high pressures, but also very high temperature due to strong entropy increase. It follows that shock compression is a valid instrument for studying melting at high pressure. Shocks typically melts materials of planetary interest at pressures between 100 and 450 GPa and temperatures between 2500 and 5000K. These and even higher pressure-temperature can be reached with laser driven shocks.
For investigating high pressure and lower temperature states more representative of planetary conditions, ramp compression needs to be used. With this latter loading technique material is compressed at a slower rate with respect to the shock. Typically laser ramp compression are characterised by rise times of $\sim$ 10 ns. Such loading rates produce quasi-isentropic compression, with a low amount of heating. The development of this technique is ongoing and further advances have been made in recent

years [Smith et al., 2014; Coppari et al., 2013].

The application of high power laser to study planetary components saw an outstanding development in the last decades. First high pressures were achieved in the 1980s with a study on Al [Trainor et al., 1979; Cauble et al., 1993]. First laser shocks with the high quality to measure equation of state were obtained in the 90's [Koenig et al., 1994, 1995]. To reach this result optical lasers can be directly irradiated on the sample [Koenig et al., 1995] or converted in X-rays that then irradiated the samples [Löwer et al., 1994]. Both methods, developed in the 90's, can provide reliable equation of states. These advances paved the way for the determination of equation of state and physical properties of planetary relevant materials. Deuterium EoS has been widely studied in late 1990s and early 2000s on different facilities: [Collins et al., 1998b,a; Da Silva et al., 1997] at Nova laser, [Knudson et al., 2003] at Sandia Z-pinch, [Boehly et al., 2004] at Omega laser. Water at conditions relevant for Neptune has been studied by [Celliers et al., 2004b; Koenig et al., 2004] in various facilities (Phebus laser and the LULI facility in France, the Omega laser in Rochester and the Vulcan laser in the UK). At the same time additional studies addressed the EoS and melt of Fe at Earth core pressure-temperature conditions [Benuzzi-Mounaix et al., 2002; Nguyen and Holmes, 2004]. Other works investigated diamond melting [Eggert et al., 2010] and high pressure properties (up to 5 TPa) [Smith et al., 2014] at conditions relevant for Uranus and Neptunes and for carbon-enriched Super-Earths respectivley.

More recently, in order to directly access to the microscopic properties of matter at planetary conditions, new techniques and experimental platforms that allow to couple X-Ray diagnostic (e.g. XAFS spectroscopy or X-ray diffraction) have been developed. Thank to such advances, the electronic and structural properties of materials compressed at planetary relevant conditions can now be measured.
For example EXAFS measurements on shock or ramp compressed Fe have been successfully performed at Omega [Yakobi et al., 2005, 2008; Ping et al., 2013b]. Diagnostics for XANES spectroscopy have been developed at LULI2000 and successfully applied on shocked Al [Benuzzi-Mounaix et al., 2011; Festa, 2013; Dorchies et al., 2015] and shocked SiO_2 [Denoeud et al., 2014]. XANES measurements on laser compressed Fe have been performed also at SLAC using the bright X-ray source of LCLS [Harmand et al., 2015].
At LCLS, also X-ray diffraction (XRD) on shocked materials can be successfully performed [Gleason et al., 2015, 2017]. However in such case the range of achievable pressure is limited at few Mbar by the power of the drive laser. For this reason XRD diagnostics have been also developed at high power laser facilities, where higher pressures can be reached. At OMEGA a method for obtaining XRD on compressed solids has been implemented and successfully tested [Rygg et al., 2012] providing interesting

results on MgO [Coppari et al., 2013]. At GEKKOXII, XRD on shocked Fe [Denoeud et al., 2016b] provided results relevant for geophysics. XRD studies on laser shocked samples have been performed also at NIF and will be soon reported [Rygg, in prep.]. Quite recently, other efforts have been made for approaching to the more complex compounds that occur in planetary interiors, for example (Fe,Mg)SiO_3 or (Fe, Mg)$_2SiO_4$. To this aim, experimental campaigns on the building blocks (MgO, SiO_2, $MgSiO_3$, etc.) of such compounds have been already performed. SiO_2 has been widely investigated and with diverse techinques. SiO_2 melting line has been constrained in a large region of the phase diagram by optical measures of shock velocities and temperatures [Hicks et al., 2006; Millot et al., 2015]. At the same time, XANES spectroscopy measured SiO_2 band gap closure mechanism [Denoeud et al., 2014], liquid structural properties [Denoeud et al., 2016a] and validated DFT models predicting melting line and conductivity [Mazevet et al., 2015].
Fewer studies existed on MgO at the time of this thesis. Phase boundaries and EoS have been studied with optical measurements coupled to shock compression [McWilliams et al., 2012; Root et al., 2015; Miyanishi et al., 2015] and with X-ray diffraction coupled to ramp compression [Coppari et al., 2013]. However the picture provided by these studies presents controversies about phase boundaries in the phase diagram.
Information about the high pressure region of $MgSiO_3$ and Mg_2SiO_4 phase diagrams are even scarcer. At the beginning of this Phd. project, only one study on laser shock compressed $MgSiO_3$ to high pressure (200 GPa<P<500 GPa) was reported [Spaulding et al., 2012] and there were no experimental studies about Mg_2SiO_4 at P>200 GPa.

Figure 7: LULI laser hall.

The purpose of this thesis is to advance in the knowledge of MgO, $MgSiO_3$ and Mg_2SiO_4 properties at planetary relevant conditions. To this aim we performed three experimental campaigns, using laser-driven shock compression to study phase diagrams of of MgO, $MgSiO_3$ and Mg_2SiO_4. For each campaign, properties of the com-

pressed materials have been characterised with diagnostics specific to the campaign purpose:

1. In the first campaign, performed at LULI2000 and GEKKOXII, we studied the occurrence of phase transitions in high pressure-temperature MgO, $MgSiO_3$ and Mg_2SiO_4 (at conditions with P>200 GPa along the Hugoniot). To this aim we used rear side optical diagnostics to measure shock properties as velocity, reflectivity and temperature. Our results mainly concern the liquid phases of the studied materials. They imply a reinterpretation of the phase diagram of MgO, $MgSiO_3$ and Mg_2SiO_4 with important geophysical implications, albeit at higher temperatures than those occurring in planetary interiors. Examples of implications are the determination of planetary temperature profiles and modelling of geochemical differentiation.

2. In the second campaign, performed at LULI2000, we used XANES spectroscopy to investigate the electronic and structural properties in a large region of the MgO phase diagram. In this experiment indeed we probed MgO on shock compression and in release, thus accessing to a wider range of conditions. With the help of DFT + MD calculations we interpreted our results on the basis of the microscopic behaviours. This shed new light on the metallisation mechanism of MgO and on the structural properties of liquid MgO.

3. In the third campaign, performed at MEC, we obtained the first characterisation of the structural changes occurring on shocked $MgSiO_3$ glass and Mg_2SiO_4 crystal for conditions between 0-120 GPa along the Hugoniot. This has been possible thanks to the high intense X-Rays of the LCLS free electron laser that allows to obtain XRD spectra also for amorphous and liquid phases. Our results provide new insights for the comprehension of meteorite impact phenomena.

PLAN OF THE THESIS

CHAPTER 1 provides a description of the technique of laser shock compression and of the methods for diagnosing shock compressed materials. We will describe in detail the diagnostic used in this thesis: VISAR, SOP, XANES and X-ray diffraction.

CHAPTER 2 is dedicated to the first experimental campaigns on the occurrence of phase transitions in the high pressure-temperature regions of MgO, $MgSiO_3$ and Mg_2SiO_4 phase diagrams. The chapter starts with a description of the motivations of the experiment followed by a review of the theoretical and experimental literature on the high pressure temperature regions of the studied phase diagrams. After this introduction, the experimental set up is reported with a consistent part dedicated to the target design, that has been done with the help of hydrodynamic simulations and experimentally tested. Then data and results obtained for each materials are described in details, always in comparison with the existing literature.

CHAPTER 3 describes the experimental investigation of electronic and structural properties of high pressure-temperature MgO performed with XANES spectroscopy. Obtaining exploitable XANES spectra of the Mg K-edge of laser shocked MgO was not trivial because of the low X-ray transmission in the Mg K edge spectral region. For this reason, a section is dedicated to the experimental set up that has been carefully designed to maximise the signal. After that, the method for determining probed hydrodynamic conditions is reported. Then XANES data for selected thermodynamic conditions will be shown in order to evidence separately the effects of temperature and density. The last and consistent section presents the interpretation that we performed with the help of ab initio calculations.

CHAPTER 4 is dedicated to the investigation of the structural changes induced by shocks in $MgSiO_3$ glass and Mg_2SiO_4 crystal performed with X-ray diffraction at LCLS. The chapter starts with the motivations of this experiment and with a detailed review on the existing shock compression studies on $MgSiO_3$ glass and Mg_2SiO_4 crystal for pressures up to $\sim$200 GPa. The experimental set up is briefly described and the most of the chapter is dedicated to present the obtained X-ray diffraction patterns and to discuss the interpretation on the basis of pressure estimations and comparison with the existing literature.

Chapter 1

Generation and characterisation of laser-shock compressed matter.

In this chapter we present the laser driven shock compression technique and the experimental methods used in this thesis to characterise shock compressed matter.
First we describe the laser-solid interaction to understand how a laser couples with the solid and generates a compression wave. Then we will discuss the behaviour of shock waves propagating into a solid, also describing what happens at solid interfaces and when a shock induces a phase transition.
Finally we will describe the optical and X-ray diagnostics techniques that we used to diagnose shocked compressed matter: velocity interferometry (VISAR), streaked optical pyrometry (SOP), X-ray diffraction (XRD) and X-ray absorption (XANES).

1.0.1 Laser-matter interaction and shock compression

In this section we discuss the interaction between a solid and a high power laser beam. Solids are characterised by a certain skin depth, that corresponds to the penetration length of the electromagnetic wave in the material. In the volume defined by the skin depth and the focal spot, the atoms of the solid are ionized by the laser via different ionisation mechanisms according to the laser intensity. Subsequently, electrons and ionised atoms are heated by the laser and an expanding plasma is thus generated (see fig. 1.1). Here, we will see the main physical processes associated to the plasma generation, the laser-plasma interaction and the shock generation.

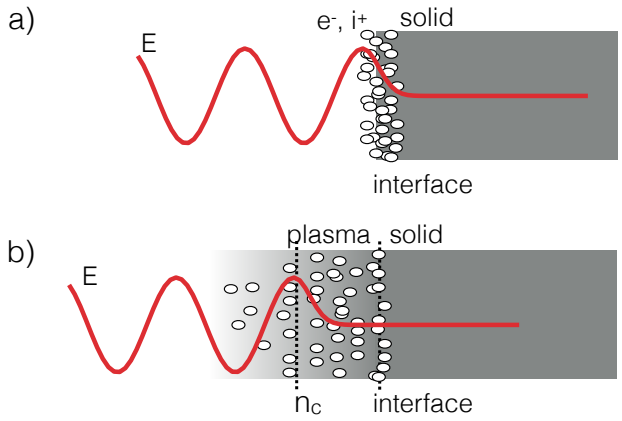

Figure 1.1: Laser-matter interaction at the first stages. a) In the first femto-picoseconds the laser ionises the atoms of the solid in a region near to the surface. The spatial range of interaction between the laser and the atoms inside the solid is given by the laser penetration depth (skin depth). b) Later in time the ionised atoms forms a plasma that expands as it is heated by the laser. However the laser can transfer its energy to the plasma just in the low density region, i.e. before plasma critical density n_c.

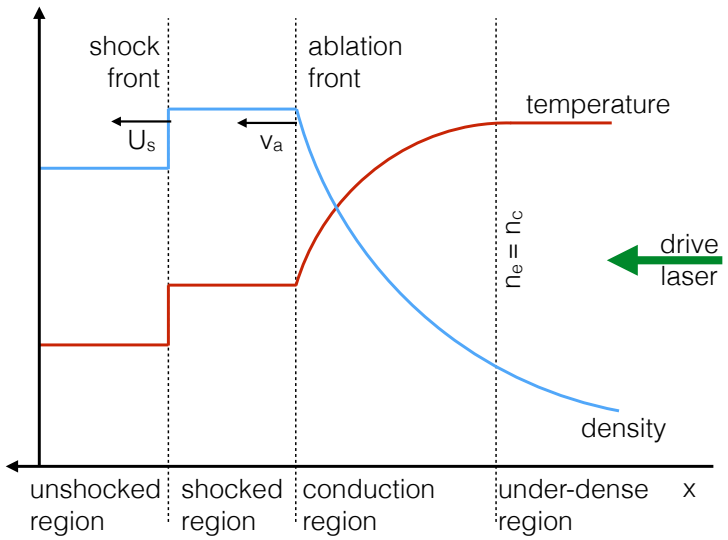

Figure 1.2: Density and temperature profiles of a target irradiated by an intense nanosecond laser pulse. Here the laser has already generated the plasma and can penetrate inside the plasma up to the critical density.

1.0.1.1 Ionisation mechanisms and heating in the skin depth

Lasers can ionise matter with various mechanisms according to the laser intensity. For high laser intensities $I > 10^{10} W cm^{-2}$ a phenomenon called *multiphoton ionisation* takes place. In this process many photons take part to the excitation and emission of a single electron. Indeed, because of the high light intensity, the rate which the photons reach the electron with is larger than the electron de-excitation rate. Thus an electron is subjected to a sequence of excitations until it has an energy larger than the ionisation energy.
At intensities around $10^{14} W cm^{-2}$ the number of photons is sufficient not only to ionise the atom but also to promote the electron into the continuum with residual kinetic energy.
At intensities $> 10^{14} W cm^{-2}$ (i.e. at conditions higher than those reached in this thesis) the so called *tunnel ionisation*, takes place. The laser electric potential strongly interacts with the Coulomb potential well that becomes lower and narrower, allowing the supra thermal electrons to escape by tunnel effect.
These processes ionise atoms and generate a free electron plasma.

1.0.1.2 Laser plasma interaction

The laser field couples with free electrons forcing them to oscillate and inducing collision with ions. In this way, this plasma is strongly heated and expands. Here we focus on the case of a nanosecond laser.
At the nanosecond time scale the plasma, with thermal velocities of 10^3 km/s, has the time to significantly expand. It follows that after ionisation processes the laser interacts and propagates with an inhomogeneous expanding plasma. Typical temperature and density profile are represented in fig. 1.2
Using Maxwell equations without taking into account magnetic terms we can derive the dispersion relation for the propagation of an electrostatic wave through a plasma:

$$\omega_L{}^2 = k^2 c^2 + \omega_p{}^2 \tag{1.1}$$

where k is the wave number and $\omega_p{}^2$ is the non-relativistic electron plasma frequency $\omega_p{}^2 = (n_e e^2)/(\epsilon_0 m_e)$. If ω_L is equal to ω_p it follows that $k = 0$. This means that for $\omega_L < \omega_p$ the laser cannot propagate anymore in the plasma.
An inhomogeneous plasma can be divided in two regions above and below the critical density $n_{crit} = \epsilon_0 m_e \omega^2 / e^2$. For $n < n_{crit}$ the plasma is said to be under-dense (or otherwise plasma corona) and the laser propagates and heats the plasma. For $n > n_{crit}$ this plasma region is said over-dense or conducting region. Here the laser cannot propagate (it is reflected at the critical density). Hence here the energy transfer is not due to a direct laser-plasma coupling. Transports in the under-dense and over-

dense regions are described respectively in the next two paragraphs and in paragraph 1.0.1.5.

1.0.1.3 Energy transfer in the under-dense region: collisional absorption

In sub-critical densities up to intensities of around $10^{15} W cm^{-2}$ the dominant plasma absorption mechanism is the electron damping mechanism. The motion of an electron that oscillates in the laser field can be damped because of the interaction of the electron with a massive ion. In this way the energy is transferred from the laser light to the plasma thermal energy. This process is known as collisional absorption or inverse bremsstrahlung absorption. The damping coefficient of the laser wave energy due to this mechanism is dependent on the electronic density, electronic temperature and on the atomic number [Wilks and Kruer, 1997]:

$$k_{ibr} \propto \frac{Z {n_e}^2}{{T_e}^{3/2}} \left(1 - \frac{n_e}{n_{crit}}\right)^{-1/2} \tag{1.2}$$

Hence, the inverse bremsstrahlung absorption is proportional to the atomic number and the electron density and inversely proportional to the temperature. In particular the absorption will reach a maximum value for density approaching the critical density.

1.0.1.4 Collisionless absorption

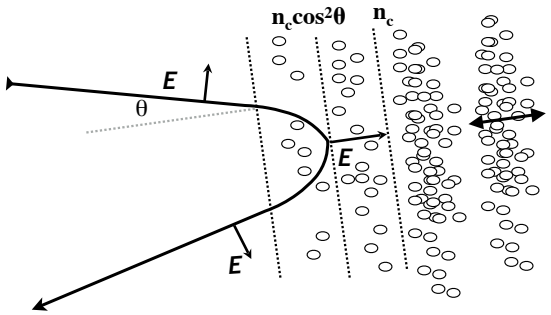

Figure 1.3: A p polarized wave is continuously deflected in the medium because of the density gradient and it is reflected at $n_c \cos\theta$. An evanescent wave penetrates beyond the reflecting surface and since the electric field and the density gradient have the same direction it excites plasmonic waves.

The collisionless absorption mechanism takes place when a laser electric field component excites plasmons in a region around the critical density. Indeed from the plasma dispersion relation it follows that electromagnetic waves can penetrate beyond the critical density surface only as evanescent wave (k imaginary). If the electric field $\vec{E}$ and the density gradient $\vec{\nabla} n$ have the same direction (p polarization), such damped waves can drive a resonant absorption, exciting plasmons. For this mechanism to be efficient the incidence angle θ between the target surface and the laser beam must be nonzero, i.e. oblique incident. In this case the laser electric field can accelerate some electrons to a high energy. This population of fast electrons can perturbate the system penetrating deeply into the sample and heating it up before the shock. However this phenomenon is negligible if: $I_{las}[\mathrm{W/cm^2}] \leq 10^{14}/\lambda^2[\mu\mathrm{m}]$ [Garban-Labaune et al., 1982]. This condition is respected for the drive laser pulses used to generate the shock in our experiments. In our experiments the drive laser intensities varied in the range of $1 - 9 \cdot 10^{13}$ W/cm^2 for $\lambda = 0.526$ μm and collisionless absorption did not play a role. To generate X-rays for XANES instead we used laser pulses with a much higher intensity, i.e. $\sim 3.4 \cdot 10^{17}$ W/cm^2. In this latter case the collisionless absorption has an impact on the energy transport.

1.0.1.5 Transport in the conducting (over-dense) region

The energy absorbed in the underdense region is transported to the cold and dense region of the target via different mechanisms: electronic thermal conductivity for low Z material ($Z < 10$); fast electron and UV-X rays for high Z materials ($Z \gg 10$).
Here we focused on thermal conductivity because in laser driven shock compression experiment it is a common practice to use plastic (very low Z) as ablator. This is done to avoid the preheating due to X-Rays or fast electrons emitted by the hot ($\sim$ KeV) plasma corona. Indeed it has been shown that the lower the Z number of the ablator the lower the X-Ray emission [Mochizuki et al., 1986]. For low Z material it has been shown that the heat flux is [Spitzer and Härm, 1953]:

$$Q_{SH} = -k_0 {T_0}^{5/2} \frac{dT_e}{dx} \tag{1.3}$$

where k_0 is the electronic thermal conductivity. However this equation has been obtained with a first order perturbative theory of the distribution function valid only if $\lambda_e/L \ll 1$ where λ_e is the electron mean free path and $L = |T_e/\nabla T_{e|}$. It has been shown that for $\lambda_e/L > 0.02$ second order terms are not negligible [Gray et al., 1977]. Moreover for steeper gradient experimental measurements found heat fluxes 10-100 times bigger than the theoretical prediction by Spitzer-Harm [Gray and Kilkenny, 1980]. It has been demonstrated that a good description of heat fluxes reached with the laser intensities typical of our experiments is given by empirical equations

$$Q = \epsilon min(|Q_{SH}, f, N_e, kT_e|) \tag{1.4}$$

$$Q^{-1} = {Q_{SH}}^{-1} + (\epsilon f N_e k T_e)^{-1} \tag{1.5}$$

where $f < 1$ is the flux limiter value and ϵ is the sign of dT_e/dx. In particular, the hydrodynamic simulations, that we performed as a support of experiments in this thesis, used formula 1.5 with $f = 0.06$, as was found with sophisticated theoretical results proposed by Luciani et al. [1983].

1.0.1.6 Ablation process and shock compression

The reaction to the plasma expansion produces high pressure that can generate a shock that propagates into the sample. It has been demonstrated that the ablation pressure can be written as a function of the laser parameter (intensity I, wavelength λ, time length τ) [Mora, 1982]:

$$P_a[Mbar] \simeq 11.6\ I^{3/4}\,[10^{14} W cm^{-2}]\ \lambda^{-1/4}\,[\mu m]\ \Big(\frac{A}{2Z}\Big)^{7/16}\Big(\frac{Z^*\tau[ns]}{3.5}\Big)^{-1/8} \tag{1.6}$$

where Z is the atomic number and Z^* is the average ionisation degree. This equation is valid only for high collisional absorptions and if $I < I_c$ where I_c is given by:

$$I_c[W cm^{-2}] \simeq 2.\ 10^{13}\ \lambda^{-5}\ [\mu m]\Big(\frac{Z^*}{3.5}\Big)^{3/2}\Big(\frac{A}{2Z}\Big)^{5/4}\tau^{3/2}\ [ns] \tag{1.7}$$

During this thesis, we used pulse lengths of 1.2-1.5 ns, 0.3 ns and 10 ns to drive shocks in the decaying shock, the XANES and the XRD experiments respectively. This means that considering $Z^* = 3.5$ for an ablator of CH we find $I_{c,ds}$ =0.56-1.7·10^{15} W/cm^2, $I_{c,XN}$=7·10^{13} W/cm^2 and $I_{c,XRD}$=1.3·10^{16} W/cm^2 for the decaying shock, the XANES and the XRD experiments respectively. In all our experiment the laser intensities on target have always been $< I_c$.

To sum up, the laser generates a plasma ionising, with various mechanisms, the external layers of the sample. Then the energy is transferred from the laser to the plasma via collisional absorption and thus the plasma expands in the vacuum. As a reaction, the sample experience a compression due to a shock wave that propagates into the sample.

1.0.2 Shock physics

In this section, we will describe the shock wave physics that is necessary for our study. First of all we define a shock wave and describe how it emerges from a perturbation of a fluid. Then we describe its behaviour at interfaces and at phase transitions.

1.0.2.1 Sound waves and shocks

A shock wave is a propagating discontinuity of the thermodynamic quantities (P, T, ρ) of a medium. Formally it emerges as a non linear solution of the equation of conservation of the mass, momentum and energy of a fluid. In the case of a perfect fluid these equation are:

$$\frac{\partial \rho}{\partial t} + \frac{\partial \rho u}{\partial x} = 0 \tag{1.8}$$

$$\frac{\partial \rho u}{\partial t} + \frac{\partial}{\partial x}\big(P + \rho u^2\big) = 0 \tag{1.9}$$

$$\frac{\partial}{\partial t}\Big[\rho\big(\epsilon + \frac{1}{2}u^2\big)\Big] = -\frac{\partial}{\partial x}\Big[\rho u\big(\epsilon + \frac{1}{2}u^2\big) + Pu\Big] \tag{1.10}$$

where u is the fluid velocity.

Linear acoustic: sound waves If we apply a small planar perturbation of pressure ΔP, density $\Delta\rho$ and velocity Δu to a perfect fluid initially at rest (starting conditions: $P_0, \rho_0, u_0 = 0$), i.e. perturbations such that $\frac{\Delta P}{P_0} \ll 1$, $\frac{\Delta\rho}{\rho_0} \ll 1$ and $\frac{\Delta u}{c} \ll 1$ where c is the sound velocity, we can solve equations 1.8, 1.9 and 1.10 in a linear approximation. These small oscillations around the equilibrium are so called sound waves. Thus substituting $P = P_0 + \Delta P$, $\rho = \rho_0 + \Delta_0\rho$ and $u = \Delta u$ in equations 1.8 and 1.9 and neglecting the second order terms (linear approximation) we obtain:

$$\frac{\partial \Delta\rho}{\partial t} + \rho_0 \frac{\partial \Delta u}{\partial x} = 0 \tag{1.11}$$

$$\frac{\partial \Delta u}{\partial t} + \frac{1}{\rho}\frac{\partial \Delta P}{\partial x} = 0 \tag{1.12}$$

Defining the sound speed as $c^2 = (\partial P/\partial\rho)$ and considering that the particle motion in sound wave for a perfect fluid is adiabatic, a small change in pressure is proportional to a small change in the density that has as a constant of proportionality the square of the sound speed:

$$\Delta P = \Big(\frac{\partial P}{\partial \rho}\Big)\Delta\rho = c^2\Delta\rho \tag{1.13}$$

Solving the system of equations 1.11, 1.12, 1.13 we find a wave equation for the perturbation:

$$\frac{\partial^2\Delta\phi}{\partial t^2} = c^2\frac{\partial^2\Delta\phi}{\partial x^2} \tag{1.14}$$

where ϕ represents each of the variables P, ρ, u. There are two kinds of solutions for equation 1.14: $\Delta\phi = \Delta\phi(x-t)$ and $\Delta\phi = \Delta\phi(x+t)$, representing for $c > 0$ waves propagating in the positive and in the negative direction respectively.

Non linear solutions If the small perturbation conditions do not hold true, the equations of conservation cannot be linearly approximated. As a solution, it follows a wave that propagates with a velocity that depends on the amplitude of the wave itself. In other words the wave distortes while propagating. Combining eq. 1.8 and the definition of sound speed, still considering the isentropic hypothesis, we obtain:

$$\frac{1}{\rho c}\frac{\partial P}{\partial t} + \frac{u}{\rho c}\frac{\partial P}{\partial x} + c\frac{\partial u}{\partial x} = 0 \tag{1.15}$$

Adding and subtracting this equation to eq 1.9 we obtain the two following equations:

$$\Big[\frac{\partial u}{\partial t} + \big(u+c\big)\frac{\partial u}{\partial x}\Big] + \frac{1}{\rho c}\Big[\frac{\partial P}{\partial t} + \big(u+c\big)\frac{\partial P}{\partial x}\Big] = 0 \tag{1.16}$$

$$\Big[\frac{\partial u}{\partial t} + \big(u-c\big)\frac{\partial u}{\partial x}\Big] + \frac{1}{\rho c}\Big[\frac{\partial P}{\partial t} + \big(u-c\big)\frac{\partial P}{\partial x}\Big] = 0 \tag{1.17}$$

The solutions are waves that propagate in the positive or negative x direction with a velocity $u \pm c(u)$:

$$u = f\big[x - [u \pm c(u)]t\big] \tag{1.18}$$

$$c = g[x - [u \pm c(u)]t] \tag{1.19}$$

In this case, different from the case of small perturbations, the fluid and wave velocities

depend on the amplitude of the wave itself. Hence the propagation speed is dependent on the wave amplitude too. In particular the bigger the amplitude the faster the wave. This means that the wave distorts during its propagation, as shown in the figure 1.4. Some of the solutions represented in fig. 1.4 are physically meaningless. Indeed for the profiles at time $t = 1.5$ and $t = 2$ (red lines) there are points (all the points after the black line) that corresponds to more than one velocity value. This is clearly unphysical. Indeed, in reality, viscosity prevents the overshooting to take place controlling the steepening of the shock wave. Thus the crest approaches the front or the rear of the wave until it forms a steep step, with a thickness of around a few mean free paths in a gas or lattice spacings in a crystal.

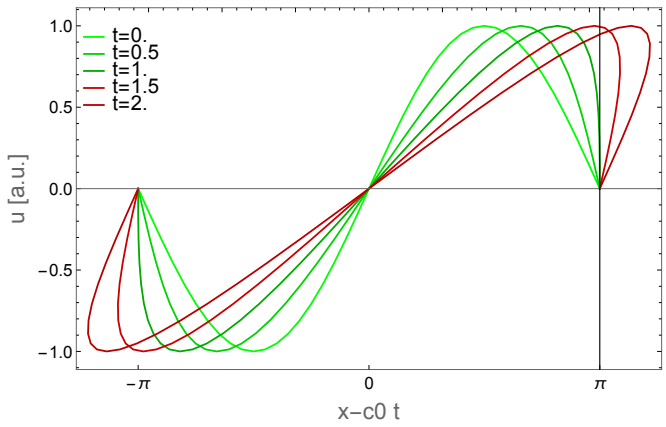

Figure 1.4: Wave deformation due to the non linearity of the fluid dynamics.

1.0.2.2 Conservation Law

From the fluid equations 1.8, 1.9 and 1.10 which holds for a planar shock it is possible to obtain the conservations laws or jump conditions of a planar shock wave:

$$\rho_1 u_1 = \rho_2 u_2 \tag{1.20}$$

$$\rho_1 u_1^2 + p_1 = \rho_2 u_2^2 + p_2 \tag{1.21}$$

$$\left[\rho_1 u_1 \left(\epsilon_1 + \frac{u_1^2}{2}\right) + p_1 u_1\right] = \left[\rho_2 u_2 \left(\epsilon_2 + \frac{u_2^2}{2}\right) + p_2 u_2\right] \tag{1.22}$$

where labels 1 and 2 denote respectively upstream and downstream fluids with respect to the shock ($u_1 = -U_S$ is the velocity, in the shock frame of reference, of the upstream flux that moves toward the shock; while u_2 is the velocity of the downstream flux, that moves from the shock). If now we write these equations in the frame reference

of the laboratory, i.e. in the frame where the upstream fluid is at rest, we have just to substitute the velocities u_1 and u_2 with the velocities of the shock U_s and of the downstream fluid $u_p = U_s + u_2$.

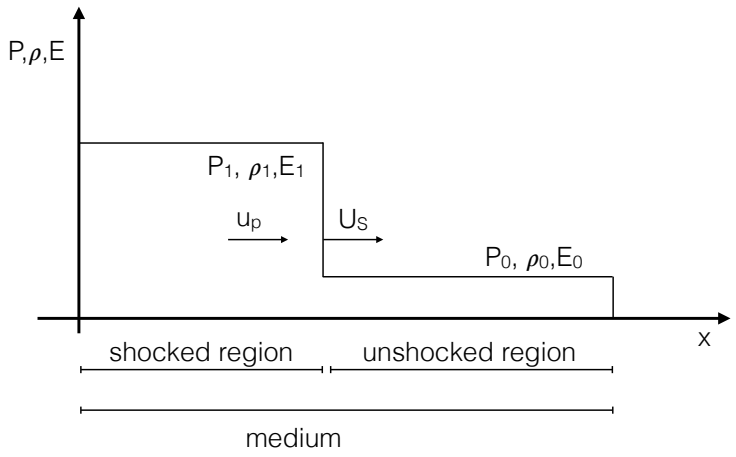

Figure 1.5: Pressure, density and energy profile of a medium compressed by a shock wave.

Thus equations 1.20, 1.21 and 1.22 become

$$\rho_1 U_s = \rho_2 \big(U_s - u_p\big) \tag{1.23}$$

$$\rho_1 U_s u_p = P_2 - P_1 \tag{1.24}$$

$$E_2 - E_1 = \frac{1}{2}(P_2 - P_1)(V_1 - V_2) \tag{1.25}$$

These are the Rankine-Hugoniot equations and describe the conservation of the mass, momentum and energy across a planar shock, i.e. between the shocked and unshocked fluid. The Rankine-Hugoniot equations constitute a system of three equations with 5 unknown variables P, ρ, E, U_s, u_p. However the thermodynamic quantities P, ρ and E are related by the equation of state of the medium $f = f(P, \rho, V) = 0$. Hence to determine the equation of state of a material in a shock wave experiment it is necessary to measure at least two of the parameters P, ρ, E, U_s, u_p (absolute EoS measurement). Usually in this case the measured quantities are U_s and u_p, though u_p is not always straightforward to characterise.
Instead, if the equation of state is known it is sufficient to measure just one parameter to get all the others. Indeed in such case it is possible to express each of unknown

variables (P, ρ, E, U_s, u_p) as a function of a single one among them. In particular, from eq 1.25, it is possible to relate P to V obtaining a function

$$P = P_H(V, P_0, V_0) \tag{1.26}$$

that represents the so called Hugoniot curve, i.e. the states that can be reached by a shock for starting conditions P_0 and V_0 .

Shock entropy For weak shocks, i.e. $P_2 \approx P_1$ eq 1.25 becomes $\Delta E \approx -P_0 \Delta V$ meaning that in this case the shock wave tends to behave as an isentrope. However, if the condition $P_2 \approx P_1$ does not hold shock compression is strongly dissipative and thus irreversible. In particular the stronger the shock the more the entropy increases. As an example we can consider the entropy of a perfect gas

$$S = c_V \ln(PV^\gamma) + S_0 \tag{1.27}$$

where $c_V = PV/(T(\gamma - 1))$ and γ is the Gruneisen parameter. The entropy increase due to a shock wave compression is given by the following relation

$$\Delta S = \frac{P_0 V_0}{T_0(\gamma - 1)} \ln \left(\frac{P_1}{P_0} \left[\frac{\frac{(\gamma-1)P_1}{P_0} + (\gamma + 1)}{\frac{(\gamma+1)P_1}{P_0} + (\gamma - 1)} \right]^\gamma \right) \tag{1.28}$$

showing that ΔS increases with P_1/P_0 and goes to zero for $P_1/P_0 \to 0$. It's worth noting that the entropy increase ΔS has been derived just using the conservation laws although it is generated by mechanisms relying on viscosity and thermal conductivity. This increment in entropy is what distinguish Hugoniots from isentropics.

1.0.2.3 Shock temperature

As we have already seen the Rankine-Hugoniot equations link the pressure, volume and the energy to the shock velocity and the fluid velocity of a shock compressed material. Thus in the case of well known equations of state given one of these variables, it is possible to obtain the others. However Rankine-Hugoniot equations do not provide the means to get the shock temperature. From the following equations[1]

[1]The thermodynamic potentials respect the Scwharz theorem for analytic functions. In other words. there is a symmetry in the order of differentiation of the thermodynamic potentials. In symbols this is written in the following way:

$$\frac{\partial_i}{\partial x_i} \frac{\partial_j \Phi}{\partial x_j} = \frac{\partial_j}{\partial x_j} \frac{\partial_j \Phi}{\partial x_j} \tag{1.29}$$

$$P - \rho^2\Big(\frac{\partial E}{\partial \rho}\Big)_T = T\Big(\frac{\partial P}{\partial \rho}\Big) \tag{1.31}$$

$$\Big(\frac{\partial E}{\partial \rho}\Big)_T = \Big(\frac{\partial E}{\partial \rho}\Big)_P + \Big(\frac{\partial E}{\partial P}\Big)_\rho \Big(\frac{\partial P}{\partial \rho}\Big)_T \tag{1.32}$$

$$\Big(\frac{\partial P}{\partial \rho}\Big)_T = -\Big(\frac{\partial T}{\partial \rho}\Big)_P \Big(\frac{\partial P}{\partial T}\Big)_\rho \tag{1.33}$$

we find a differential equation for T

$$T(P,\rho) = \left[\rho^2\Big(\frac{\partial E}{\partial P}\Big)_\rho\right]\Big(\frac{\partial T}{\partial \rho}\Big)_P - \left[\rho^2\Big(\frac{\partial E}{\partial \rho}\Big)_P - P\right]\Big(\frac{\partial T}{\partial P}\Big)_\rho \tag{1.34}$$

that states that the temperature cannot be calculated directly from the variables P, ρ and E. Indeed it depends on the derivative of the energy with respect to the pressure and the density. This means that the temperature does not depend only on P, ρ and E along the Hugoniot but even on a part of the phase space around the curve. Therefore the temperature must be determined independently from the other thermodynamic variables.

1.0.2.4 Rarefaction waves

We now consider the case where the piston decelerates or moves away from the fluid. The solution to this problem [Zeldovich and Raizer, 1965] is a rarefaction wave, i.e. in a density perturbation of the medium that propagates at the speed of sound lowering the density of the medium. In particular for a piston that starts to move at zero velocity and accelerates to reach a constant velocity v_p the solution consists in a perturbation with a velocity profile that varies from c_0 (the sound speed of the unperturbed medium) to $c_1 - v_p$, where c_1 is the sound speed of the perturbed fluid. Treating the propagation of a rarefaction wave as a self similar motion one can prove that a rarefaction wave is isentropic [Zeldovich and Raizer, 1965].

where Φ is a thermodynamic potential and x_i and x_j its variables. If we consider the Helmholtz free energy $F(T,V)$ it follows:

$$P - \rho^2\Big(\frac{\partial E}{\partial \rho}\Big)_T = T\Big(\frac{\partial P}{\partial \rho}\Big) \tag{1.30}$$

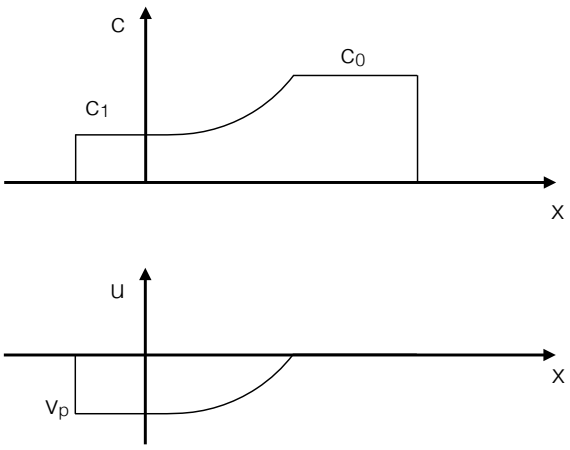

Figure 1.6: Sound speed and fluid velocity spatial profiles for a rarefaction wave generated by a piston that accelerates away from the fluid starting at zero velocity and reaching a velocity v_p.

1.0.2.5 Propagation at an interface and impedance matching

The targets used in high power laser experiments are typically made of multiple layers. Thus the behaviour of the shock at an interface is crucial in laser shock experiments. An interface is a surface at equilibrium, i.e. the fluid velocity u_p and the pressure P are conserved across the interface. However the other thermodynamic quantities as the density and the temperature can have different values since they are defined by the equation of state. Indeed for a given pressure the density of a material is given by the equation of state and does not depend on the properties of the material beyond the interface.

For a material compressed from a starting density ρ_0 to a state A_0, it is possible to define the shock impedance as $Z = \rho_0 U_s$. The momentum equation $P = \rho_0 U_s u_p$ forms a line in $P - u_p$ plane called the Rayleigh line. The shock impedance coincides with the slope of the straight line that links A_0 to the starting conditions O in the plane $P - u_p$ (see fig. 1.7). A_0 belong the curve, called *Hugoniot*, that describe the final states (P, u_p) accessible with shock compression for given starting conditions. The behaviour of a shock at an interface between materials A and B depends on the relative values of shock impedances Z_A and Z_B of the two materials. There are two possibilities: the impedance of the material A is bigger then the impedance of the material B ($Z_B > Z_A$) or the opposite ($Z_A > Z_B$).

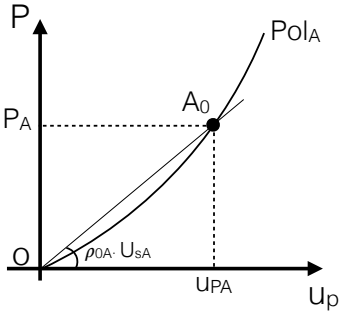

Figure 1.7: Pol_A represents the Hugoniot of a material A, i.e. the states that a shock can explore in the $P - u_p$ phase diagram for given starting conditions. A_0 represents the compressed state produced by a shock with velocity U_{SA} for a starting density ρ_0. A_0 is given by the intersection of the Hugoniot and the Rayleigh line with slope $U_{SA} \cdot \rho_0$, that is the shock impedance. Hence for known Hugoniot to get the compressed state (P_A) it is sufficient to know the initial density and to measure the shock velocity U_{SA}.

Let's consider the first case. At the beginning the shock propagates in the medium A, which is thus compressed by the shock to the state A_0, as shown in figure 1.8. The transmitted shock is represented by the point B_0 on the Hugoniot of the material B Pol_B. Since the pressure is equal on both sides separated by the interface, the reflected shock is represented by the same B_0 pressure but this time on the Hugoniot (Pol_{AC}) of the material A with starting conditions A_0. Thus the point B_0 is given by the intersection between Pol_B and Pol'_{AC}. The reflecting shock with pressure B_0 propagates in the medium perturbed by the incident shock.
Let's consider the second case now. Of course, as before, the states created by the incident and the transmitted shock lay on the Hugoniot Pol_A and Pol_B respectively. However this time the Hugoniot of material B is lower than the one of material A. Hence the state B_0 created by the transmitted is given by the intersection by the rarefaction isentrope of the medium A and the Hugoniot Pol_B, as shown in figure.

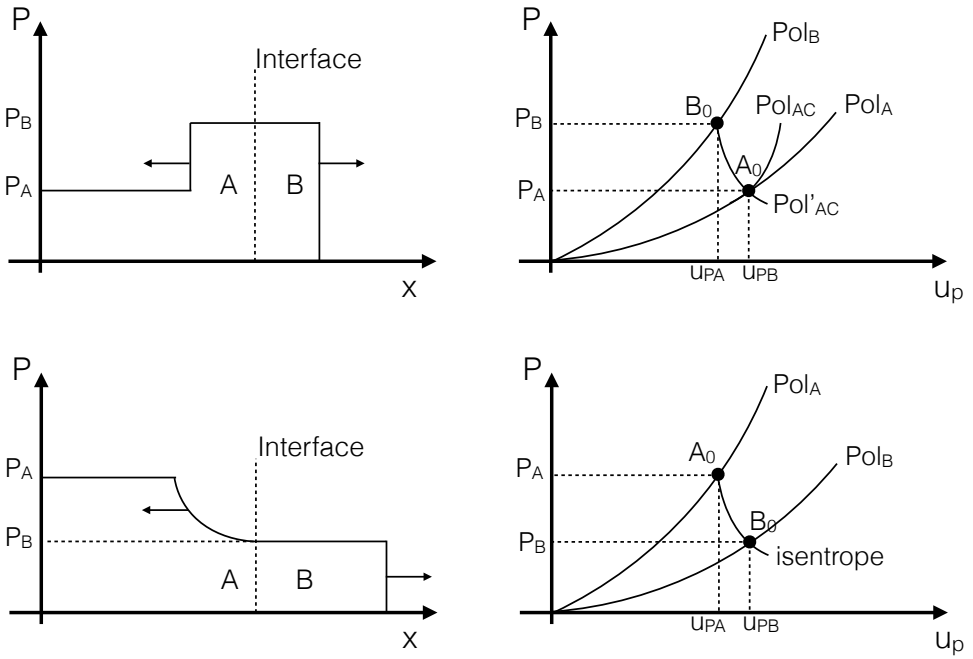

Figure 1.8: At the top left, shock propagation at an interface that separates materials A and B with $Z_B > Z_A$. A shock is transmitted in material B and another shock is reflected in material A. The pressure is equal on both sides separated by the interface, i.e. the transmitted and reflected shocks compress material A and B to the same pressure. On the right the compressed states created by the shock in material A and B are represented by the black points (A_0 and B_0) on the Hugoniots Pol_A and Pol_B respectively. The compressed state B_0 created in material B lies at the intersection between the Hugoniot Pol_B and the Hugoniot of the reflected shock Pol'_AC. Hugoniots Pol_A, Pol_B and Pol'_AC represent the states that a shock can explore in material A at starting conditions, in material B at starting conditions and in material A compressed to the state A_0 respectively.
At the bottom left, shock propagation at an interface that separates materials A and B with $Z_B < Z_A$. In this case instead of a reflected shock we have a rarefaction wave and thus instead of the reflected Hugoniot Pol'_{AC} we have the isentrope is_A.

A technique ("impedance matching") allows to measure the equation of state of a sample relies on these phenomena. This technique consists in monitoring the shock propagation through an interface, measuring the shock velocities both in the material before (A) and in material beyond the interface (B). If the equation of state of one of the two materials (reference material) is known, all the ingredients necessary to express all the quantities (P, ρ, u_p, U_s, E) as a function of one single quantity among them are available. Indeed the equation of state of the material gives the isentrope or Hugoniot curves shown in the figures 1.9, while from the shock velocities it is

possible to calculate the impedance in the two materials. The intersection among the straight lines and Hugoniots or isentropes gives the final states in material A and B. In conclusion this technique gives an indirect measurement of the equation of state.

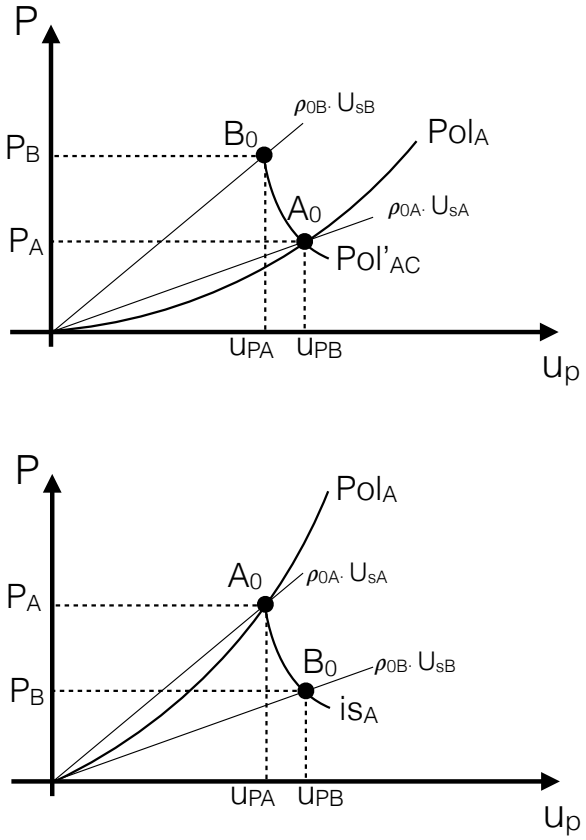

Figure 1.9: At the top impedance match technique applied in the case $Z_B > Z_A$. The measurement of U_{SA} allows to determine A_0 at the intersection between the Hugoniot Pol_A (that is known) and the straight line $P = \rho_{0A} U_{SA} u_p$. The measurement of U_{SB} allows to find the final state B_0 at the intersection between the Hugoniot Pol'_{AC} (that is known) and the straight line $P = \rho_{0B} U_{SB} u_p$.
At the bottom impedance match technique applied in the case $Z_A > Z_B$. The technique is the same than for the case $Z_B > Z_A$ except that here the final state is given by the intercection with the isentrope.

1.0.2.6 Decaying shock

In laser driven shock compression experiments, once the laser pulse ends a rarefaction wave is generated and propagates from the ablation front toward the shock. The

rarefaction wave travelling in a compressed medium is faster than the shock wave and will overtake the shock front.

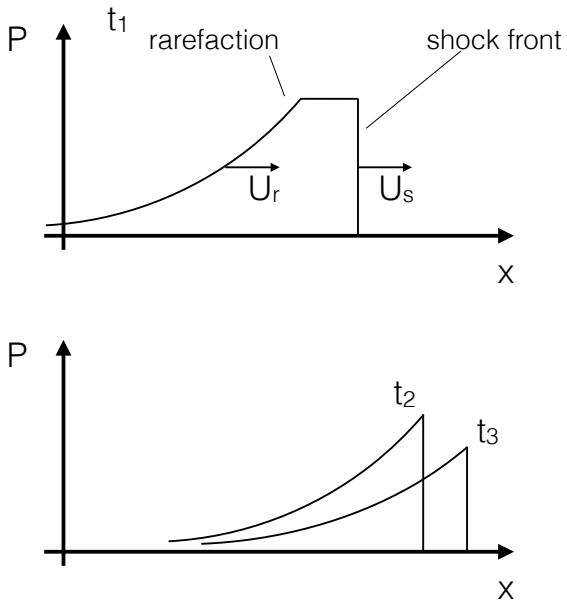

Figure 1.10: Schematic of the pressure profile generated by an implosive loading for different times. At the top (time t_1) the shock propagates with a velocity U_s followed by a rarefaction wave that travels at a velocity U_r bigger than U_s as explained in the text. At the bottom the rarefaction wave reaches the shock wave at time t_2 and the pressure (as the other thermodynamic quantities) starts to decrease (as shown for time t_3)

To have a clearer picture of the phenomenon we can consider the case of an ideal gas with adiabatic index γ. In the case of strong shock the shock velocity and the velocity of the compressed fluid can be expressed as

$$U_s = \sqrt{\frac{(\gamma+1)^2 P_1}{2(\gamma-1)\rho_1}} \tag{1.35}$$

$$u_{p1} = \sqrt{\frac{2P_1}{(\gamma-1)\rho_1}} \tag{1.36}$$

The front of the rarefaction wave propagates at the sound speed $c_1 = \sqrt{\gamma P_1/\rho_1}$ inside the shocked material which is moving also at the fluid velocity U_p. Thus the

velocity of the rarefaction front in the laboratory frame of reference is

$$U_r = c_1 + u_{p1} = \frac{2}{\gamma + 1}\Big[1 + \sqrt{\frac{\gamma(\gamma - 1)}{2}}\Big]U_s \tag{1.37}$$

Therefore it is evident that $U_r > U_s$, i.e. that the rarefaction wave overtakes the shock. Indeed a strong shock ($P \gg P_0$) is always supersonic if compared to the uncompressed ($U_s > c_0$) medium and subsonic if compared to the compressed medium $U_s < u + c$. When the rarefaction wave reaches the shock, the pressure starts to decrease as well as the other thermodynamic quantities as the density, the temperature and the entropy. A solution to the problem of the rate of decrease is proposed by [Zeldovich and Raizer, 1965] in the case of planar adiabatic flows of a perfect gas with initial pressure and sound velocity of the medium equal to zero, i.e. $P_0 = 0$ and $c_{s0} = 0$. The shock behaviour is dependent on the pressure pulse shape only for timescale comparable to the pulse duration τ. For $t \gg \tau$, the initial scale of the problem no longer affect the process and analytical solutions can be found in the self-similar form [Zeldovich and Raizer, 1965].
The self-similar solution gives for the shock velocity $U_s = \dot{X} \sim t^{(\alpha-1)}$ where α is a constant. For adiabatic flows of gases it can be shown that $1/2 < \alpha < 2/3$ meaning that U_s is always a function that decreases in time [Zeldovich and Raizer, 1965]. An analytical solution has been proposed also for finite initial sound speed c_0 and pressureP_0 [Sharma et al., 1987].
What we have seen up to now is valid for a perfect gas, but the problem has been solved too for the impulsive loading of a material described by a Mie-Gruneisen equation of state [Anisimov and Kravchenko, 1985]. The only difference relies on the equation of state. As in the case of an ideal gas the motion of the shock front is described by the relation $X(t) = At^{\alpha}$ with $1/2 < \alpha < 2/3$, as α is not dependent on the thermodynamic properties of the medium.

Due to experimental constraints, in our experiments with decaying shocks we were obliged to detect the shock decay at time close to the laser loading. In general, we characterised the shock wave for ~ 7 ns after that entered in the (transparent) sample under investigation, which usually happens 1-2 ns after the laser loading. Thus since the pulse lengths that we used were $\sim$ 1-2 ns, the condition $t \gg \tau$ is not respected. Therefore, to describe the time evolutions of pressure and temperature profiles in our experiment self-similar solutions cannot be used. Decaying shock velocity time profiles determined experimentally always showed exponential decays. In particular shock velocity profiles obtained with impulsive loading on SiO_2 [Hicks et al., 2006], Diamond [Eggert et al., 2010], MgO [McWilliams et al., 2012] and stishovite [Millot et al., 2015] have been well interpolated with single exponential or double exponential

decaying functions.
Moreover for designing and interpreting our experiments we used hydrodynamical simulations, in particular the code MULTI [Ramis et al., 1988], obviating the need for precise analytic solutions.

1.0.2.7 Phase transitions

When compressing a sample, a shock can induce a phase transition. Phase transitions are classified by the behaviour of the derivative of a thermodynamic potential to an intensive parameter. A first order phase transition occurs when such a derivative presents a discontinuity. This kind of transition involves a latent heat absorption or release. Examples of first order phase transitions are melting, polymorphic phase transition and liquid-gas phase transition.
On the contrary a second order or continuous phase transition does not present a discontinuity in the first order derivative of the thermodynamic potential to the intensive parameter. But these transitions do exhibit a divergency in the susceptibility. An example of this kind of transition is the liquid He - superfluid He transition (at the transition boundary the specific heat diverges).

The phase transitions relevant to the physics of planetary interiors are typically polymorphic transitions (first or second order), melting (first order), crystallisation, liquid-liquid transitions, amorphisation and dissociation. In this study we will investigate some of them.
Polymorphic transitions are defined as the transformation of a solid crystal into another phase with the same chemical composition but different crystal structure. Polymorphic transitions can have reconstructive character or displacive (martensitic) character. In the first case the chemical bonds are broken and reconstructed to form a new crystal structure (first order class). Martensitic transition instead are driven by material shear strains. Set of atoms are displaced to form a new crystal structure. These transitions usually belong to the second-order class, but they can also have a weak first order thermodynamic character (very low latent heat). Usually under shock compression polymorphic transition implies an increment of the density.
Melting is the phase transition from a solid to a liquid and for many planetary relevant materials it has been investigated both with static and dynamic compression. A melting process usually implies a significant latent heat absorption and usually the liquid phase is less dense than the solid one.

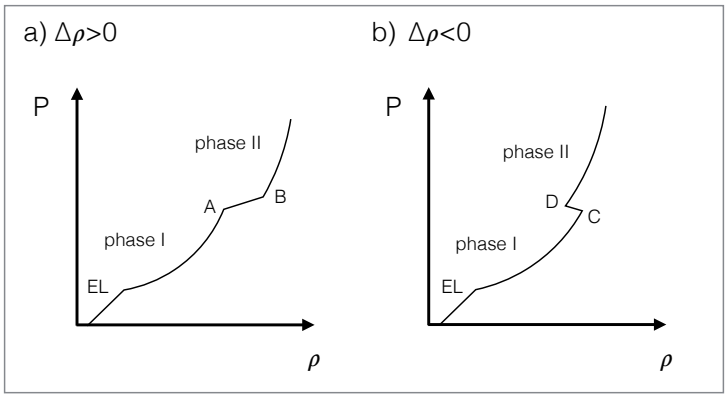

Figure 1.11: The figure represent shock $P - \rho$ curves crossing phase boundaries for two types of transition. EL is the elastic limit, and from EL to A or to EL to C the material is in its phase I. In the segments AB and DC the material at the shock front is in a two-phase state, and after points B and D the material at the shock front is in the single phase II.

The volume change at a phase transition has as effect to reshape the Hugoniot curve explored by the shock. Figure 1.11 shows the Hugoniot curves in the cases of transitions with $\Delta\rho > 0$ and a $\Delta\rho < 0$. Before the points A and C the material at the shock front is in the single phase I, while in the segments AB and DC the material at the shock front is in a two-phase state. Then after points B and D the material is completely transformed in the single phase II. The extension of the coexistence regions AB and CD is given by the density difference between the two phases. The curvatures of the Hugoniot in the two phases are different since the bulk modulus (or the compressibility which is its inverse) changes at the transition.
If the volume change at the phase boundary is large enough, the transition can be detected characterising U_s-u_p curves with steady shocks or (in some cases) U_s time profiles with decaying shocks. Indeed abrupt slope changes in P- ρ curves translate into slope changes in U_s-u_p detectable with steady shocks (we recall that P, ρ, U_s, u_p are related by the Rankine-Hugoniot equations), while significant volume changes can produce imprints in shock velocity time profiles of decaying shocks (as shock decay rates would be different in the two phases).
However, with U_s-u_p measurements, the detection of phase transitions with a small volume change like melting is delicate [McQueen et al., 1970; Brown and McQueen, 1986; Root et al., 2015]. This is true also for decaying shocks: small volume changes would not produce significant changes in the decay rate of shock velocity, as already observed in different experiments [Eggert et al., 2010; Hicks et al., 2006]. In such cases other observables than the shock velocity need to be used to the detect the transition. One of them is the thermal emission or the temperature.

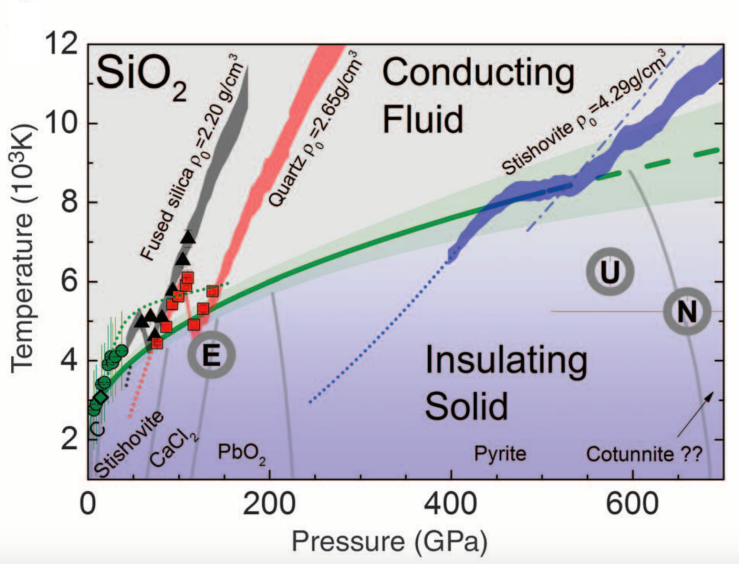

Figure 1.12: Phase diagram of SiO_2 from [Millot et al., 2015]. The black, red and blue coloured areas represent respectively the P-T curves of shocked fused silica, quartz and stishovite. The shock compression brings fused silica and alpha quartz to metastable states before melting (superheating), while the P-T curve of shocked stishovite exhibits the coexistence region which follows the phase boundary.

The latent heat involved in the transition reshapes the pressure temperature curve explored by a shock. At the phase boundary for increasing shock pressures the temperature does not increase before that the shock has provided enough energy to melt completely the material. Hence the P-T curve of the shock exhibits a region of coexistence of the solid and liquid phases which is superimposed to the melting phase boundary. The P-T curve of shocked stishovite (represented in fig. 1.12) manifests this behaviour.
In other cases, as the heating rate at the melting phase boundary during a shock compression is extremely high (10^{13}-10^{15} K/s), the material does not have the time to melt and it is kept in a metastable solid state at temperatures above the melting line. This is because the temperature rises faster than the rate of rearrangement of atoms required to melt. Then, at a certain temperature[2], the material relaxes to the

[2]A theory for predicting the maximum superheating achievable for a given heating rate has been developed by [Luo and Ahrens, 2003; Luo et al., 2003; Luo and Ahrens, 2004] in the framework of homogeneous nucleation. They proposed a relation between the maximum amount of superheating, the heating rate and the nucleation energy barrier given by:

$$\beta = (A_0 - b\, log Q)\, \theta_c\, (\theta_c - 1)^2 \tag{1.38}$$

where β is the nucleation energy barrier, Q is the heating rate, θ_c=T_c/T_m where T_c is the highest

equilibrium state i.e. to the liquid phase. This phenomenon is called super-heating or superheated melting. Superheated melting under shock compression has been observed for various materials (alkali halides, silicates, transition metals)[3]. In particular the superheated melting of alpha quartz and fused silica has been observed also with decaying shocks [Hicks et al., 2006; Millot et al., 2015] as reported fig. 1.12.

The occurrence of superheating or of large latent heat absorption at melting allows to detect the transition with the technique of the decaying shock. In the case of a superheated melting the decaying shock thermal emission time profile exhibits a bump. Instead in the case of a "normal" melting it exhibits a plateau which corresponds to the region of the P-T curves superimposed to the phase boundary.

1.0.2.8 Splitting shock waves at phase transition

The behaviour of a shock wave that crosses a phase boundary depends on the transition type. As we have seen, polymorphic transitions under shock compression usually implies an increment of the density, while with melting the material undergo to a phase with a lower density.

In the case of a transition with $\Delta\rho > 0$ (usually true for polymorphic transitions), the emergence of a convexity along the $P-\rho$ or $P-V$ shock curves is responsible for a rather interesting shock behaviour. Let us consider a Hugoniot of the type shown in figure 1.13. In the region O-A the material is in the phase I, while in the region B-end is in the phase II. In the region AB the two phases coexist. Slopes of the curves O-A and B-end are different because of different compressibility in the two phases. Let us now consider a steady shock compressing the material at a pressure P_F. It travels at a velocity U_S given by the slope of the straight line that links point O and F in the P-V diagram, i.e.:

$$U_S = V_0\Big(\frac{P_F - P_0}{V_0 - V_F}\Big)^{1/2} \tag{1.40}$$

temperature reached by the metastable solid and T_m is the melting temperature. A_0 and b are constant and are equal to 59.39 and 2.33 respectively. The nucleation energy barrier is defined as

$$\beta = \frac{16\pi\gamma_{sl}^3}{3\Delta H_m^2 k T_m} \tag{1.39}$$

where ΔH_m is the heat of fusion per unit volume and $\gamma_s l$ is the solid-liquid interfacial energy. However applying such theory in order to calculate the maximum temperature reached by the metastable solid in superheating is quite complicated as material properties as the solid-liquid interfacial energy or the heat of fusion per unit volume have to be known.

[3]examples: alkali halides: NaCl, CsBr, KBr; silicates: $MgSiO_3$, Mg_2SiO_4, SiO_2; transition metals: Fe, V, Mo, Ta. For more details see [Luo and Ahrens, 2004]

In the case we are describing the point F is at the phase II, which means the shock is compressing the material to a phase different from the starting one. In other word the material undergoes a phase transition driven by the shock. This, according to the kinetics of the transition, could result in a thickening of the shock front, as shown in the image 1.14. This behaviour is typical of compressing shock with pressure $P > P_E$ (Rayleigh line linking E and O is tangent to the Hugoniot at point A). For pressure P_N: $P_B < P_N < P_E$ Rayleigh line ON intersects the Hugoniot three times. This is unphysical and what really happens is that the shock wave splits in two waves. The first shock compresses the sample to the state A, then a second wave compresses the sample from the state A to the state N. The velocity of the first shock is given by the slope of the straight line OA. The second shock instead travels with a velocity that is given by the sum of the particle velocity u_a of the sample compressed by the first wave and the slope of the line AN.

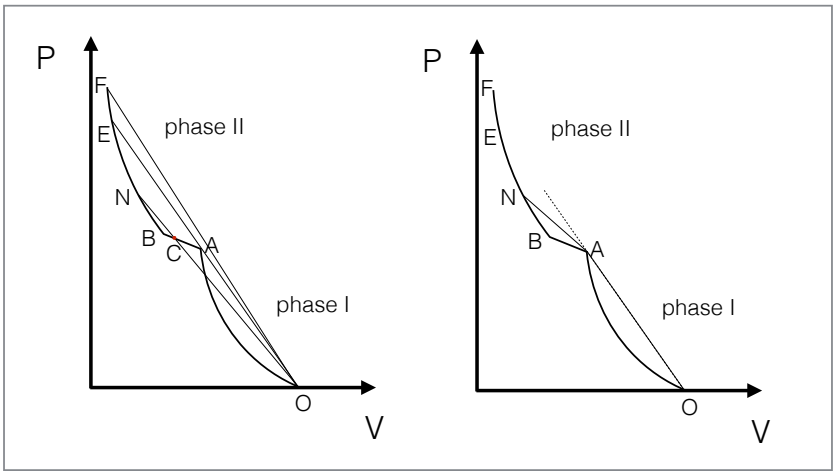

Figure 1.13: The figure represent shock $P-V$ curve crossing phase boundaries for a typical polymorphic transition. From O to A the material is in its phase I. In the segment AB material at the shock front is in a two-phase state, and after points B the material at the shock front is in the single phase II. The slopes of line OF gives the velocity for a shock with pressure P_F. Line OE is the limiting case since it is tangent to point A and line ON unphysically crosses the P-V curve three times.

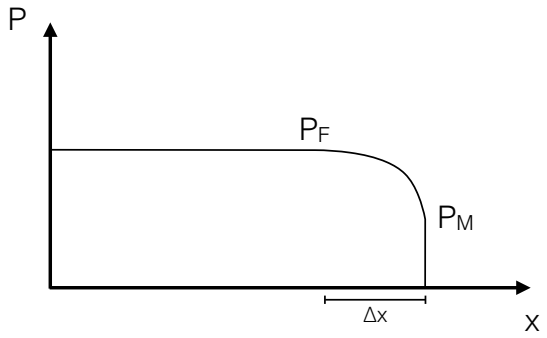

Figure 1.14: Thickening of the shock front due to a transition kinetics slower than the time necessary to reach the thermodynamic equilibrium in the single phase material. The shock compresses the material to the metastable state M and the thickness Δx of the shock front depends on the relaxation time of the transition necessary to reach the final state F. Tipically this phenomenon takes place for polymorphic phase transitions.

It can be demonstrated that the second shock wave is slower than the first one. Indeed the velocity of the first wave in the frame of the moving material behind U_1' it is equal to the difference of the velocity U_1 and of the particle velocity u_a:

$$U_1' = U_1 + u_A \tag{1.41}$$

Then from equation 1.23 and 1.24 it is possible to express the particle velocity u_a as it follows:

$$u_A = (P_A - P_0)^{1/2}(V_0 - V_A)^{1/2} \tag{1.42}$$

Substituting this last expression in the sum 1.41 we obtain the following expression for the velocity of shock 1relative to the material moving with velocity u_a:

$$U_1' = V_A\Big(\frac{P_A - P_0}{V_0 - V_A}\Big)^{1/2} \tag{1.43}$$

and since the slope of OA is bigger than the slope of AN, i.e. $(P_A - P_0)/(V_0 - V_A) > (P_N - P_A)/(V_A - V_N)$ it follows that $U_1' > U_2'$. Thus the second shock is too slow to overtake the first one.
Physically, the first shock compresses the sample to a pressure P_A, where the material is still in its first phase while the second shock force the material to undergo the transition. For $P_A < P_N < P_B$ the transformation is not complete and the second shock brings the material to a two phase state.

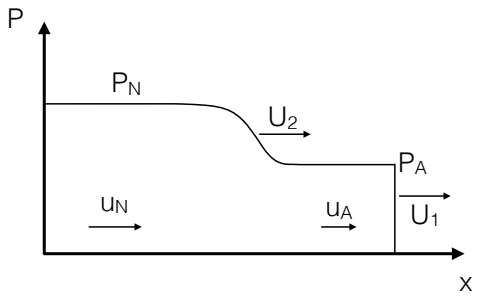

Figure 1.15: Shock wave splitting at a phase transition described by a convex region in the shock P-V curve.

This split of the shock waves usually occurs for polymorphic phase transitions. Despite their particular interest for the study of phase transitions, the states in the region between P_A and P_E are inaccessible by instantaneous shock velocity measurements. Therefore the characterisation of the shock velocity time profile during the propagation of a decaying shock is not a reliable technique for the detection of such transitions. The only possible signature of the transition on the U_S should be a change in the decaying rate at the shock splitting. However the magnitude of this effect is generally small, leading to difficulties in the interpretation of the velocity profiles.
Instead, the states P_A and P_C, and thus the discontinuity along the Hugoniot, can be determined with absolute EoS measurements (measurements of average U_S and u_p) or with the impedance matching technique.

Differently from polymorphic transitions, when the Hugoniot crosses a melting line the hydrodynamic stability is conserved and the material melts at the shock front. Hence in this case the metastable region along the Hugoniot can be characterised with the decaying shock technique too as it has been done in many recent works [Millot et al., 2015; McWilliams et al., 2012; Eggert et al., 2010].

1.0.3 Diagnosing warm dense matter using visible diagnostics.

Once the shock is generated it is necessary to characterise it in order to infer the thermodynamic conditions of the compressed material. The two most common diagnostic used in laser driven shock experiments are the Velocity Interferometer System for Any Reflector (VISAR) and the Streaked Optical Pyrometry (SOP). Both these optical

diagnostics get information from the rear surface of the target (front side corresponds to the laser side).

1.0.3.1 VISAR

The Velocity Interferometer System for Any Reflector (VISAR) is considered now the standard high-precision velocity diagnostic for shock compression phenomena. Indeed it allows to measure the velocity of any reflecting moving surface taking advantage from the Doppler effect. For example, in the case of a transparent sample and a reflecting shock it is possible to directly measure the shock velocity. Otherwise if the medium is not transparent but it is reflecting, VISAR can measure the free surface velocity (which is ~ 2 times the fluid velocity, in the case of a weak shock) when the shock breaks out.
VISAR principally consists of a probe laser beam, a modified Mach Zehnder interferometer, a streak camera, and two optical systems. One optical system transfers a magnified image of the sample from the chamber to the image plane mirror of the interferometer, while the other transfers such image from the interferometer to the camera. The heart of the VISAR diagnostic is the interferometer (represented in fig. 1.16) that is specially designed to generate a precise and known delay in one of its arm. To correct the optical path lenght an etalon is introduced in front of mirror 2 of the interferometer (see fig. 1.16).

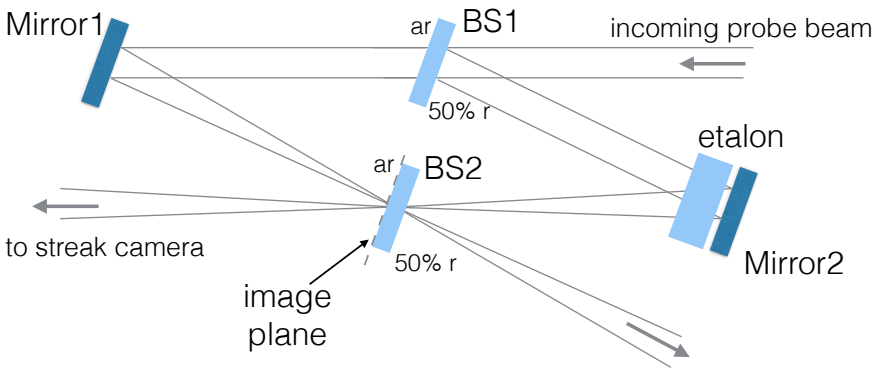

Figure 1.16: Schematic of the VISAR interferometer. BS1 and BS2 are the two 50% beam splitter. Both the beam splitter have an anti-reflecting coating on the surface opposite to the incoming beam. In front of mirror 2 it is placed an etalon with a well known thickness and refraction index.

The etalon introduces a delay given by:

$$\tau \simeq \frac{2h}{c}(n - 1/n) \tag{1.44}$$

where h is the thickness of the etalon, n is the etalon index of refraction and c is the speed of light.

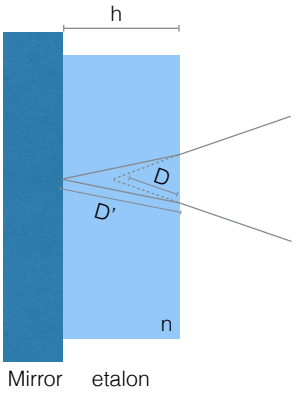

Figure 1.17: Optical path in the etalon. The etalon deflects the probe beam modifying the traveled distance (D' in the etalon in place of D in the air). This difference introduces a time delay between the two arms..

If the probe beam is reflected by a stationary surface the interference pattern is constant in time. In particular for a interferometer configuration with the beam splitter BS2 tilted with an angle α the interfringe distance is equal to $\lambda/\sin(\alpha)$. On the contrary, for a moving surface the interference pattern changes in time. Indeed a propagating surface as a shock or a free surface reflects a light beam with a modified wavelength according to the surface velocity (Doppler effect):

$$\lambda(t) = \lambda_0 + \frac{1 + v(t)/c}{1 - v(t)/c} \tag{1.45}$$

where λ_0 is the wavelength of the incident beam, $\lambda(t)$ is the wavelength of the reflected beam and $v(t)$ is the surface velocity. Since in our experiments the velocity of the reflecting surfaces are around few tens of km/s (< 30 km/s), the wavelength changes due to the Doppler effect are relatively small. Hence, we can consider that the etalon refraction index varies linearly with the wavelength:

$$n(\lambda) = n_0 + \left(\frac{dn}{d\lambda}\right)_{\lambda_0} (\lambda(t) - \lambda_0) \tag{1.46}$$

For the same reason we can consider $v(t) << c$ which allows to simplify eq. 1.45 in

$$\Delta\lambda \simeq -2\lambda_0 \frac{v(t)}{c} \tag{1.47}$$

Solving the system of equations 1.44, 1.46 and 1.47 τ becomes

$$\tau \simeq \tau_0 + 2\tau_0 \frac{v(t)}{c}\delta \tag{1.48}$$

where:

$$\delta = -\frac{\lambda_0 n_0}{{n_0}^2 - 1}\Big(\frac{dn}{d\lambda}\Big)_{\lambda_0} \tag{1.49}$$

and:

$$\tau_0 = \frac{2h}{c}(n_0 - 1/n_0) \tag{1.50}$$

For time $t > \tau$ both the arms of the interferometer have a frequency modified by the Doppler effect:

$$\frac{\omega_0}{(1 - 2v(t)/c)} \tag{1.51}$$

In addition the second arm is delayed by a time τ. Thus the electric fields associated to the two arms and the intensity resulting from the interference are given by the following equations:

$$E_1 = E_0 \exp\Big[i\Big(\frac{\omega_0 t}{1 - 2v(t)/c} - \vec{k_1}\cdot\vec{x}\Big)\Big] \tag{1.52}$$

$$E_2 = E_0 \exp\Big[i\Big(\frac{\omega_0}{1 - 2v(t)/c}(t - \tau(t)) - \vec{k_2}\cdot\vec{x}\Big)\Big] \tag{1.53}$$

$$I(y) = 2{E_0}^2\Big(1 + \cos\Big(\frac{\omega_0\tau(t)}{1 - 2v(t)/c} + ky\sin\alpha\Big)\Big) \tag{1.54}$$

Combining eq. 1.55 and eq. 1.48 and simplifying for small $v(t)/c$, we obtain:

$$I(y) = 2{E_0}^2\Big(1 + \cos\Big(ky\sin\alpha + \omega_0\tau_0 + 2\omega_0\tau_0\frac{v(t)}{c}(1+\delta)\Big)\Big) \tag{1.55}$$

where the argument inside the cosine represent the phase difference between the two arms of the interferometer. The first and the second term occur also for stationary reflecting surfaces and are introduced respectively by the tilt of the beam splitter and delay of the second arm due to the etalon. Instead, the third term represents the phase component introduced by the moving surface:

$$\phi_v = 2\omega_0\tau_0\frac{v(t)}{c}(1+\delta) \tag{1.56}$$

Hence we can define the displacement per unit fringe by the ratio between ϕ_v and 2π:

$$F(t) = \frac{\phi_v}{2\pi} = \frac{2\tau_0(1+\delta)v(t)}{\lambda_0} \tag{1.57}$$

Thus the velocity sensitivity or velocity per fringe (VPF), is given by

$$VPF = \frac{\lambda_0}{2\tau_0(1+\delta)} \tag{1.58}$$

The velocity sensitivity for a surface propagating into a medium with a refractive index n_m is $VPF_m = VPF \cdot n_m^{-1}$. Thus the velocity of a surface propagating into a medium or in vacuum is simply given by the product of the velocity sensitivity and the measured displacement. However analysing the interference pattern it is possible to infer just the displacement that corresponds to a fraction of fringe. To solve the ambiguity on the number N of entire fringes displaced it is necessary to use at least two VISARs with two different sensitivities.
At the same time the intensity time profile of the registered fringes is a measure of the moving surface reflectivity (see chapter 2 for more details).

1.0.3.2 SOP

The SOP (Streaked Optical Pyrometer) is a diagnostic designed to measure the thermal emission time evolution of the shock front. It consists simply of a streak camera, of an optical system that produces a magnified image of the target rear side on the slit of the streak camera and of a gaussian filter to select a narrow band of the emitted light.
Assuming the grey body hypothesis, the recorded signal intensity (i.e. the number of counts N_c) is proportional to the spectral radiance:

$$L(\lambda_0, T) = (1 - R(\lambda_0))\frac{2hc^2}{\lambda_0^5}\frac{1}{\exp\left(\frac{hc}{k_b\lambda_0 T}\right) - 1} \tag{1.59}$$

where R is the reflectivity obtained with VISAR diagnostics and λ_0 is the selected wavelength using an interferometric filter.
In particular the camera output recorded onto one single pixel of the camera is:

$$N_c = \int_{A_{pixel}} dA \int_{\Omega} d\Omega \int_{\Delta t} dt \int_{-\infty}^{\infty} d\lambda \; C_o(\lambda) \; C_{sc}(\lambda) \quad L_s(\lambda) \tag{1.60}$$

where $C_o(\lambda)$ is the product of the transmission/reflectance of all the components of the optical system, $C_{sc}(\lambda)$ is the response of the streak camera, A_{pixel} is the area of the pixel, Ω is the subtended solid angle and Δt is the exposure time [Miller et al., 2007]. The pixel area A_{pixel} is equal to $(B\Delta x/M)^2$, where B is the binning, Δx is the pixel dimension and M is the magnification of the optical system. The time integral gives simply Δt, which is equal to $W_s/\eta B\Delta x$, where W_s is the width of the camera slit and η is the sweep rate. Thus the integral 1.61 becomes:

$$N_c = \frac{B\Delta x W_s \Omega_{lens}}{\eta M^2} \int_{-\infty}^{\infty} d\lambda \; C_o(\lambda) \; C_{sc}(\lambda) \quad L_s(\lambda) \tag{1.61}$$

Where Ω_{lens} is the solid angle subtended by the camera. Considering that the measured light has a narrow spectrum around a wavelength λ_0 in comparison to the Planckian spectrum emitted by a source with a temperature of few 1000 K the and by defining the intensity $I = N_c/(1-R)$ the solution of this integral gives a temperature-intensity relation of the following form:

$$T = \frac{T_0}{\ln(1 + A/I)} \tag{1.62}$$

where $T_0 = hc/\lambda_0$ and A is a constant value that depends on the response of streak camera, on the transmittance of the optical system and on the geometry of the system [Miller et al., 2007]:

$$A = \frac{2B\Delta x W_s \Omega_{lens} \langle C_0 C_{sc} \rangle hc^2 G}{\eta M^2 \lambda_0^5} \tag{1.63}$$

where G is a constant factor depending on the gain of the streak camera, h is simply the Planck constant, c is the speed of light, and $\langle C_0 C_{sc} \rangle$ is the average of the product of C_0 and C_{sc}. Thus to get A from 1.63 it is necessary to determine all the parameters present in the formula, which is not convenient in most of the cases. A more convenient strategy is to determine A using equation 1.62. To this aim it is sufficient to use a reference, emitting at a well known temperature. As a reference it is possible to use a standard material (e.g SiO_2) for which the relations temperature/shock velocity and reflectivity/shock velocity had been precisely measured. With these relations and several reference shots on SiO_2 measuring simultaneously the shock velocity and SOP signal, it is possible to determine A from 1.62. Another approach is to use a calibrated lamp as a reference. In this case the temperature of the lamp is known, the intensity I is measured and thus it is possible to solve eq. 1.62. For the experiments performed during this thesis we used both the approaches as we will see more in details in the experiment chapters. X-ray

1.0.4 Diagnosing warm dense matter with X-ray diagnostics

As we discussed, rear side optical diagnostics as VISAR and SOP gives a fundamental contribution in the study of high pressure phase diagram. Measures of U_s-u_p gives reliable results for what concerns the determination of equation of state (P-ρ relations) and in detecting phase transitions (corresponding to discontinuity or slope change of U_s-u_p). Similarly decaying shock study can be used to detect the occurrence of phase transitions and melting in particular, looking for velocity or thermal emission jumps. However such studies do not furnish direct information on the structural properties of the phase reached with the compression. Therefore the interpretation of the nature of the phase is not straightforward and can lead to controversy [Spaulding et al., 2012; Militzer, 2013]. In some cases, P-ρ or P-T curves can be interpolated with Mie-Gruneisen models thus interpreting the nature of the phases occurring along such curves. However such indirect guesses of the nature of the phases can lead to misinterpretation as in the case of SiO_2. In such case an indirect study [Panero et al., 2003] concluded that a dense amorphous phase occurs along the Hugoniot of fused silica, but this interpretation has been disproved by direct measurement performed with Xray diffraction on shocked compressed fused silica [Gleason et al., 2015] that got first observations of the crystallisation of fused silica in stishovite.

Indeed intense X-ray beams can be used to directly access to structural and electronic properties of shock compressed materials and therefore to the nature of the phase under investigation.
In this thesis we used two X-ray techniques: X-ray diffraction (XRD) and X-ray absorption near edge spectroscopy (XANES). X-ray diffraction is principally used to access to the structural information of a sample. If the sample is a plasma (in such case we speak about X-ray scattering), quasi-transparent to the X-ray probe beam, and the photon-plasma interactions are quasi-elastic, then the angle resolved spectrum generated by scattered X-rays is a measurement of the atomic structure and of short range correlations. For a given angle from the energy spectrum of scattered X-rays it is possible to obtain density, ionic and electronic temperature and the structure of the sample, although a theoretical model is necessary in this case. In the case of crystals, the X-ray scattering is coherent and it is called diffraction. X-ray diffraction gives access to the structural properties of the crystal, allowing to infer the crystal structure and to determine the spacings between the lattice planes. Similarly X-ray scattering can be used on amorphous materials or liquid to determine the structure factor or more in general to get information about correlations in the investigated sample.

X-ray absorption spectroscopy is typically used to measure the light absorption linked to the excitation of core electrons. It gives access to the electronic properties of the investigated materials. XANES spectroscopy in particular is a highly resolved measurement of the absorption spectra in a region around an absorption edge. Absorption edges are defined according to initial core level of the excited electron. For example, K, L and M edges refers to quantum numbers n=1, n=2 and n=3 respectively. XANES spectroscopy measures the electronic excitation from a core state to an unoccupied state allowed by the quantum selection rules. E.g. for the K edge the most intense absorption feature will correspond to 1s to p-like level electronic transitions. We will describe XANES spectroscopy more in details in the following.

Certainly, to characterise materials with these techniques, intense X-ray sources are needed. Therefore, before describing X-ray diffraction and XANES spectroscopy (techniques used in this thesis), we will see how to generate intense enough X-ray sources. Then we will give a brief description of XANES spectroscopy and X-ray diffraction.

1.0.4.1 X-ray generation

Laser shock compression experiments impose to use an X-ray probe beam shorter than the time scale of pressure and temperature variations inside the shocked material. Otherwise the signal will be an integral over different hydrodynamic conditions and it won't be significant. A synchronisation with the nanosecond drive beam used to compress the sample guarantees the possibility to choose the time delay between the two laser pulses in order to probe different states.
Another constraint is the intensity. The intensity has to be high enough to produce an exploitable signal. Typically for XANES spectroscopy X-ray source producing 10^{10} photons/ev/sr are needed.
Here we review the techniques that we used in this thesis to generate short and intense X-rays to couple to laser shock compression. In particular we used the X-ray beam of the LCLS free electron laser and X-rays produces by a short high power laser[4] .

Free electron laser Free electron lasers (FEL) can provide X-ray beams with extremely high intensity (e.g. $\sim 2 \cdot 10^{33}$ photons/s/mm^2/mrad^2/0.1%bandwidth at LCLS) and extremely short wavelenghts (e.g. at LCLS the minimum wavelength is 0.15 nm). Such X-ray beams are produced by accelerated electron bunchs that travel through an undulator, which is a periodic arrangement of magnetic dipoles

[4]Other methods are available to couple short and intense X-rays to laser shock compression. Recently the X-ray beam of the synchrotron ESRF has been used to probe laser-shock compressed matter with EXAFS [Torchio et al., 2016].

that produces a periodically alternating static magnetic field. The electrons thus are forced to follow a sinusoidal path, emitting a collimated radiation along the axis of motion. Actually to this aim there are two conditions to satisfy: first electrons have to be relativistic and second the angle θ (see fig. 1.0.4.1) has to be smaller than the radiation angle. If the FEL works at high energies (extreme UV or X-ray) the emitted radiation cannot be amplified in a cavity since no mirrors can reflect X-rays. There is another process that allows to amplify the intensity of the radiation and it is called Self-Amplified Spontaneous Emission (SASE). The SASE process takes place when electrons have velocities close to the speed of light and the density of the injected electron bunch is uniform. For such initial conditions, the radiation emitted by the electrons interact with the electrons themselves, modulating the electron density. This interaction take place for each period of the undulator and it has as a result a transfer of energy from electrons to photons at certain selected energies. This amplification of radiation at some selected wavelength saturates in $10 - 20$ gain length L_g that is defined as the ratio between the undulator wavelength and $4\pi\rho$ (where ρ is the electron bunch density). Hence, considering both the length of the linear accelerator that brings electrons to relativistic energies before the injection in the undulator and the length of the undulator itself, such systems needs a total length of the order of the km. Hence X-ray Fel are expensive facilities and this is why at the moment only three of them have been built: LCLS at Stanford, California, SACLA in Japan, and X-Fel in Hamburg.
In the context of this thesis we performed an XRD experiment at LCLS at the MEC end-station which is provided with a high-power laser beam. Indeed the X-ray beam of LCLS is well adapted for X-ray diffraction because of its small spectral width (ΔE/E is $\sim 1{\cdot}10^{-3}$ at ~ 8 keV)

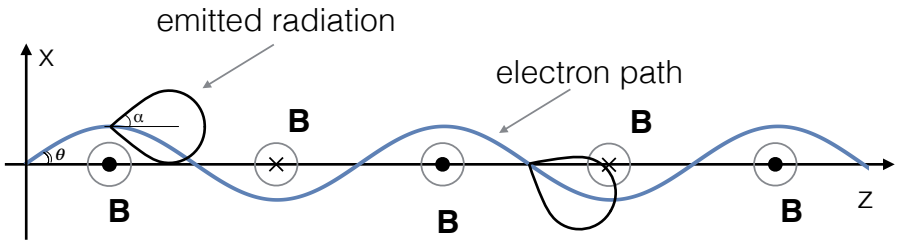

Figure 1.18: Schematic of the electron bunch path in a Fel undulator.

X-ray source produced by a short high power laser pulse. As we have already seen in section 1.0.1, the interaction between an intense laser pulse and a solid target

produces, at the very early stages, an expanding plasma. In the case of very short pulses (around few ps) a steep density gradient characterises the expanding plasma. The temperature of this plasma corona can be very high, reaching its maximum close to the skin depth, before the laser intensity is completely damped.

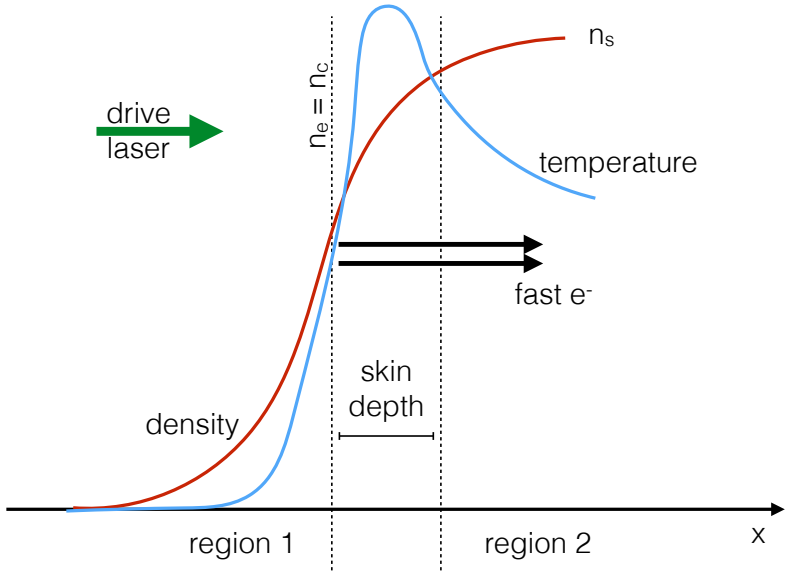

Figure 1.19: Density and temperature profiles of a plasma generated by the interaction between a ps long laser beam and a solid target.

In this regime (i.e. for intensities I $\sim 3.4{\cdot}10^{17}$ W/cm^2) a significant part of the laser energy ($\propto I^{3/4}\lambda^{3/2}$) is transferred to the electrons by a non collisional mechanisms (e.g. resonant absorption). As shown in section 1.0.1.4 and figure 1.3 these fast electrons are excited and start to propagates inside the material at a depth equal to the skin depth of the sample. Thus the skin depth divides the system expanding plasma/solid in two regions. Beyond the skin depth, where the sample is mostly still cold and solid, the sample atoms are excited by the fast electrons and emits photons at X-ray energies. Before the skin depth, where the plasma is very hot and dense, a variety of emission processes thermally excited can take place.

Thermal Emission. The dominant emission from the region before the skin depth is due to ion excitations and de-excitations. In a high temperature plasma ions excited to instable states and electronic transition produces an emission that is of course correlated to the electronic temperature and to the ionisation of the plasma. X-ray emission is induced by de-excitation from continuum state to N, M and L and K bands for examples, as shown in figure 1.20 on the left. Moreover a Bremsstralhung emission is present too. This means that the emission due to the plasma corona

produced during the interaction of a short high-power laser and a solid corresponds to emission lines superimposed to a continuum spectrum. An example of that is the thermal emission of Al represented in fig. 1.20 on the right. Emission lines from band L, M and K are superimposed to a continuous lower emission.

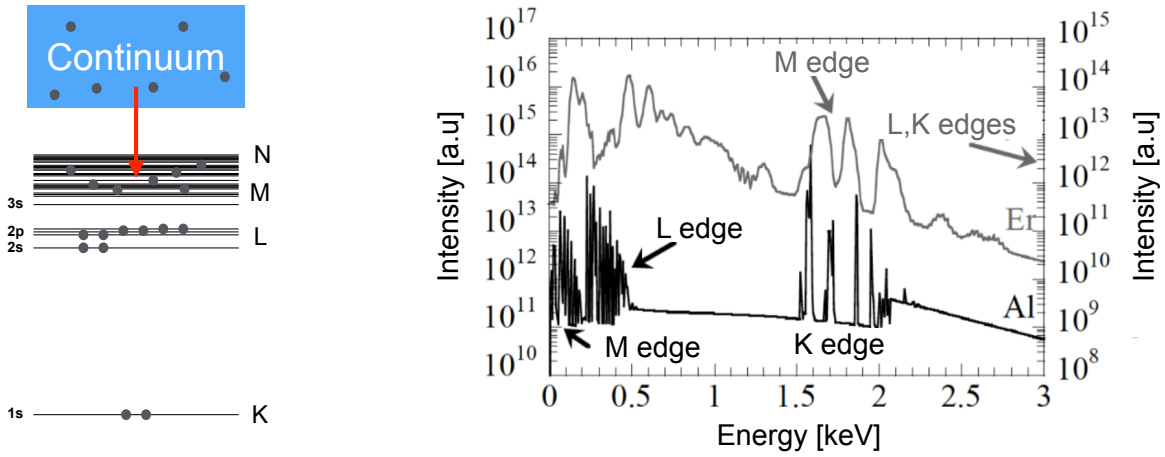

Figure 1.20: Left: Band M thermal emission principle. Right: comparison of the emission spectra of Al (Z=13) (black line) and Erbium (Z=68) obtained with the code Averroes-Transpec for T_e=400eV and $N_e = N_c$ =1.7 $\cdot 10^{21}$ e^-/cc [Harmand, 2009].

The emission spectrum shown here well represents the fact that the L or M band are linked to very dense and intense emission lines (much more than the K band). For this reason M and L band emission can be used to produce a relatively broad band intense X-ray emission suitable for performing X-ray absorption spectroscopy for example. Al M and L band are at relatively low energy. For generating a broad band emission from M and L lines at higher energy it is sufficient to choose a material with a higher Z. For example for X-ray absorption measurements of the Si K edge of shocked SiO_2 at ∼1.85 KeV have been successfully performed at LULI with backlighter of Erbium (Z=68) et Ytterbium (Z=70) irradiated by a 5 ps, 50μm and 20J laser pulse. Other laser generated (laser beams of 2.5 ps and 25-30J) M-L band X-ray emission uniform over a range of ∼ 150 eV between 1.5 and 1.65 keV have been characterised by F. Dorchies and A. Levy for Dysprosium (Z=66), Erbium (Z=68) and Ho (Z=67) and reported in [Festa, 2013] (see fig. 1.21).

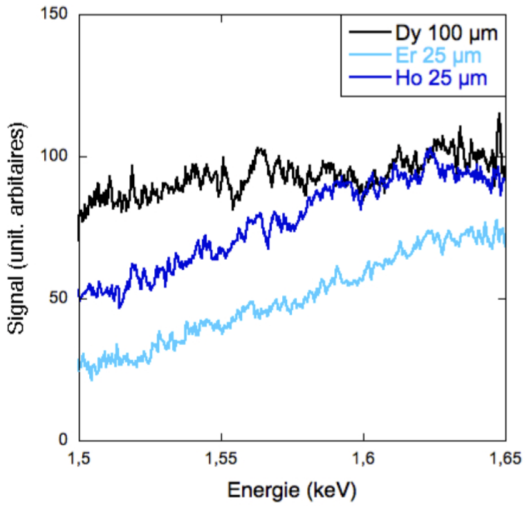

Figure 1.21: Experimental M-L band emission spectra obtained irradiating a Dysprosium (Z=66), Erbium (Z=68) and Ho (Z=67) target with a laser pulse of 2.5 ps and 25-30 J [Festa, 2013].

Emission induced by fast electrons. Fast electrons, because of their high kinetic energy, can knock out the core shells electrons of target atoms. In particular, if the energy of fast electrons is higher than the ionisation threshold of the shell K, an electron of the shell K is promoted to the continuum. As a consequence the atom that hosts the ejected electron has hole in the K shell, which is an energetically unstable configuration. Then the ground state of such an ion is soon reached thanks to the transition of an outer shell electron to the shell K. Such electronic transition produces a K emission. The most intense emission will be the one due to the most likely transition, that is the Kα, i.e. the 2p-1s transition.
The main feature of these X-ray sources is to be monochromatic. For this reason, it is used for diagnostics that necessitate a monochromatic source as for X-ray diffraction. However, it is worth noting that also Bremsstrahlung emission can be produced by free electrons deflected by ions. Such emission will produce a background noise.

1.0.5 X ray diffraction

We already mention that X-ray diffraction gives access to the structural properties of a sample.
Let's consider an X-ray beam interacting with an atom. The electric field of the electromagnetic interacts with the electronic clouds of the atom forcing them to oscillate coherently with the filed oscillation. As the effect of the field on the ion is

negligible, as they are more massive and stay at rest, the system oscillating electrons - ions can be considered as an oscillating dipole. Such a dipole isotropically emits electromagnetic waves with the same frequency of the interacting X-rays.

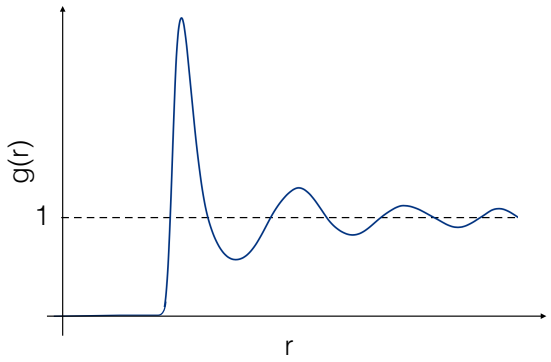

Figure 1.22: Typical pair correlation function of a liquid or a glass.

In liquid, glasses or crystals these diffused radiations interfere and at a given time generate intensity pattern that are related to the the static structure factor:

$$S(\boldsymbol{k}) = \frac{\rho_0}{2\pi} \int_V e^{-i\boldsymbol{k}\cdot(\boldsymbol{r}-\boldsymbol{r}')} < \rho(\boldsymbol{r}), \rho(\boldsymbol{r}') > d^3(\boldsymbol{r}-\boldsymbol{r}') \tag{1.64}$$

where $\boldsymbol{k}$ is the probe beam wavenumber, $\boldsymbol{r}$ is the position of an atom/particle of the system and $\boldsymbol{r}'$ is the position of another atom/particle of the system. The average $< \rho(\boldsymbol{r}), \rho(\boldsymbol{r}') >$ gives is the density of probability that an atom/particle have coordinates described by $\boldsymbol{r}$ and another particle is in $\boldsymbol{r}'$ at a given time. The structure factor is linked to the pair correlation function $g(\boldsymbol{r})$ (that gives the probability of finding a particle at a distance r from another particle):

$$g(\boldsymbol{k}) = \int_V e^{-i\boldsymbol{k}\cdot\boldsymbol{r}} g(\boldsymbol{r}) = S(\boldsymbol{k}) - \rho(2\pi)^3\delta(\boldsymbol{k}) \tag{1.65}$$

where $g(\boldsymbol{r}) = < \rho(0)\rho(\boldsymbol{r}) >$.
Fig. 1.22 shows a typical pair correlation function of a liquid or a glass: structure disappeared for high r as in liquid or glasses there is no long range order.

In crystals, on the contrary the pair correlation function and therefore the structure factor (more directly linked to the measured signal) would exhibit a long range order reflecting the lattice structure. In particular the diffused wavelengths interfere constructively and the signal exhibits peaks if the Bragg law is respected:

$$n\lambda = 2d\sin\theta \tag{1.66}$$

where d is the lattice plane spacing, λ is the X-ray wavelength, n is an integer, and 2θ is the deviation angle. This law can be easily explained with a geometrical view of the phenomenon. As represented in figure 1.23, we can conside two rays of the X-ray beam: rays $r_2$and r_1. r_1 is reflected by an atom of the lattice and r_2 by an atom of another lattice plane. Thus r_1 travels for a longer distance than r_2. If this distance, that is equal to $2c$ where c is the segment represented in the curve, is equal to an integer multiple of the wavelenght n λ (with n integer) then the to rays will interfere constructively. This distance $2c$ is equal to $2d\sin\theta$ and hence the condition to have a constructive interference is given by the Bragg law.

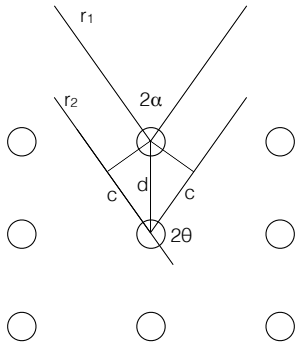

Figure 1.23: Schematic of the diffraction in crystal

1.0.6 X-ray Absorption Spectroscopy

As we already mentioned for this Phd. project we performed a XANES (X-ray Absorption Near Edge Structure Spectroscopy) experiment in order to study the electronic and structural properties of shocked MgO. In this section, before going through the details of XANES spectroscopy, we introduce more in general the absorption spectroscopy discussing the light - solid target interaction.

To explain the interaction between light and a solid target we can approximate the solid target as a discrete particle system. In general the probability for an interaction event to occur when a beam irradiates a discrete particle system is defined by the cross section, which expresses such probability in term of the effective area of interaction between the beam and the particle. This of course is valid for absorption but also for light scattering. Then the total number of absorption or scattering events will

be given by the product between the beam intensity I_0 (i.e. the number of photon) and the cross section σ.
Here we are interested in describing the attenuation of an electromagnetic wave that propagates through the particle system. Obviously such attenuation depends on target thickness and density. If we consider a target of infinitesime thickness δx and volume density ρ, then the probability of interaction between the beam and a particle of the target is $\rho\sigma\delta x = \mu\delta x$, where μ is defined as the linear attenuation coefficient or absorption coefficient. A thick target can be seen as a superimposition of various layers of thickness δx. For n layers the target thickness will be $n\delta x$. Thus the probability for a photon to be transmitted in such a target is equal to $(1-\mu\delta x)^n$ that for $n \to \infty$ tends to $\exp(-\mu x)$.
Another equivalent way to see the phenomenon is to consider that the intensity decrease dI in a thickness dx is given by the product of the intensity value just before dx and μdx: $dI = I\mu dx$. Hence it follows that $I = I_0 \exp(-\mu x)$. Thus at x equal to $l_a = 1/\mu$, which is the so called absorption length, the light beam decreased to $1/e$.

The absorption coefficient μ depends on the beam energy and on the atomic properties as it follows:

$$\mu \approx \frac{\rho Z^4}{AE^3} \tag{1.67}$$

so it's linear with the density, proportional to the fourth power of Z and inversely proportional to the third power of the energy E. In addition to what reported here, an absorption spectrum presents some edge absorption due to photoelectric effect.

1.0.6.1 X-ray absorption near the edge.

A photon with energy $h\nu$ can transfer its energy to an atom or a solid exciting an electron from a starting atomic level or solid band with energy E_i to another energy level E_f, where E_f-E_i=$h\nu$. If the photon energy is bigger than the difference E_{bind} - E_i, where E_{bind} represents the binding energy, the excited electron is promoted to the continuum. Thus for X-ray energies equal to the binding energies of core-level electrons the absorption spectrum does not decay as E^{-3} but exhibits sharp rises called spectrum edges. XANES in particular measures and analyses the spectrum region close to a selected edge.
The probability of photoelectric effect, i.e. a transition to a bound state $|\phi_i\rangle$ to a free state $|\phi_f\rangle$ in a perturbed atom is given by the Fermi's Golden Rule that states

$$\sigma_{i,f}(\nu) = a\, h\nu \mid \langle \phi_f | \, \mathbf{R} \, | \phi_i \rangle \mid^2 \tag{1.68}$$

where $\phi_{i,f}$ are the initial and final wave-function. We remark that $|\phi_i\rangle = |\phi_{bound}\rangle$ and $|\phi_f\rangle = |\phi_{free}\rangle$. $\mathbf{R}$ is the electric dipole operator of the atom, while a is just a constant.
If the ion is surrounded by free electrons and if these free electrons are degenerate (high density and low temperature) then the photoionisation cross section is given by

$$\sigma_{i,f}(\nu) = a\, h\nu \mid \langle \phi_f | \, \mathbf{R} \, | \phi_i \rangle \mid^2 (1 - f(E)) \tag{1.69}$$

where $f(E)$ is the Fermi-Dirac distribution function. The term $\langle \phi_f | \, \mathbf{R} \, | \phi_i \rangle \mid^2$ contains the electronic band structure, while the term $(1 - f(E))$ describes the occupation of the electronic states close to the continuum.

$$f(E) = \frac{1}{1 + \exp\{(E - E_F(\rho, T_e))/k_B T_e\}} \tag{1.70}$$

where $E_F(\rho, T_e)$ is the chemical potential[5] such that at zero kelvin is equal to the Fermi energy and T_e is the electronic temperature. In the expression $(1 - f(E))$ there is the dependency of the transition cross section on the temperature and the energy. In particular case of an ideal metal [Dorchies et al., 2015] this expression defines the slope of the absorption spectrum edge, which gets smoother the higher the temperature.

However the free electron wave-function does not correspond to the final wave-function. Indeed it is necessary to consider also the interactions of the ejected electron with the nearest atoms. It follows that the final wave-function will be the superimposition of the free electron wave-function $|\phi_{free}\rangle$ and the wave-function of the photo-electron scattered by the nearest atoms $|\phi_{diff}\rangle$:

$$|\phi_f\rangle = |\phi_{free}\rangle + |\phi_{diff}\rangle \tag{1.71}$$

Thus the final wave-function contains precious information. Indeed the diffuse wave-function depends on the local order close to the absorbing atom. Therefore the oscillations present in an absorption spectrum are related to the multiple or single scattering of the photo-electron emitted by the absorbing atom.

We can define two regimes according to the energy of the emitted photo-electron. For high energies, i.e. in the region of the spectrum farther from the edge, the largest contribution to the absorption is from the back-scattered or single-scattered photo-electrons. The spectroscopy that explores this region of the spectrum is called EXAFS (Extended X-ray Absorption Fine Structures). At lower energies, closer to the edge,

[5] In some cases it is called Fermi energy or Fermi level also for temperature T > 0

oscillations are mostly due to multiple scattering of the photo-electron. These latter oscillations are studied by XANES spectroscopy. The dependance of these behaviours on the energy can be explained as it follows. The X-ray energy $h\nu$ is related to the electron kinetic energy $E_{e^- kin}$ and thus to the wavelength λ of the photo-electron wave-function by the following relation:

$$h\nu - E_{bound} = E_{e^- kin} = \hbar^2 k^2/(2m) = 4\pi^2\hbar^2/(2m\lambda^2) \tag{1.72}$$

where E_{bound} is the binding energy. Hence the X-ray energy is inversely proportional to the photo-electron wavelength that can be longer or shorter than the interatomic distances. In the first case we talk about XANES regime since the photoelectron wave-function is diffused many times, while in the latter case we talk about EXAFS regime or single scattering regime.

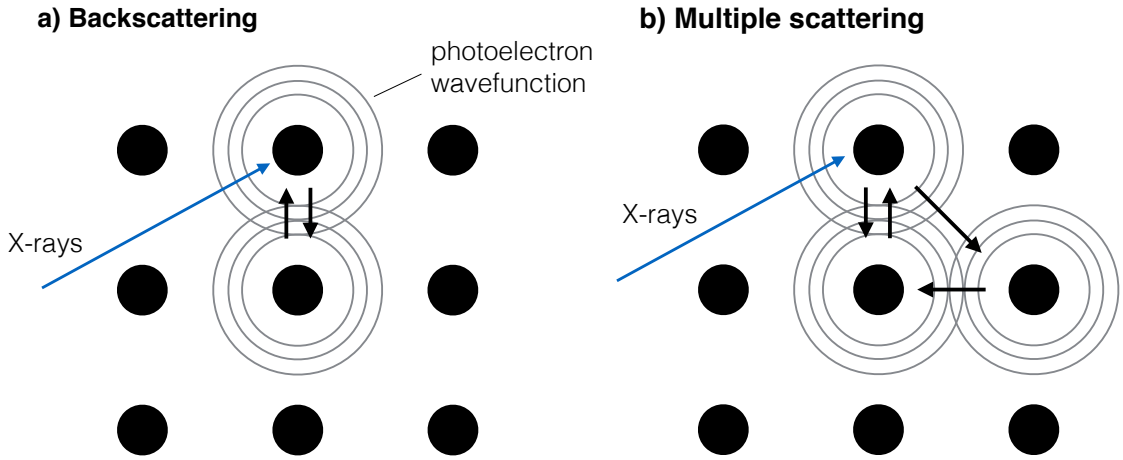

Figure 1.24: Schematic of the XANES and EXAFS regime: the first (on the right) is characterised by multiple scattering, while the second (on the left) is characterised by backscattering.

In the EXAFS case equation 1.69 can be simplified in an analytical expression that can be Fourier transformed to get the interatomic distances of the medium. However since the amplitude of EXAFS oscillations is low, there are strong constraints on the X-ray source specifications. Indeed, in addition to a broad spectral band (more than 200 eV) the X-ray beam is required to be very intense. Such conditions can be reached at synchrotron or at extremely high power laser facilities as Omega[6] where

[6]Omega laser system is provided of 60 beams and delivers up to 40 kJ of energy at 351 nm.

tens of kJ can be deposited on CH sphere inducing an implosion emitting broadband and intense (10^{11}-10^{12} photons/eV/sr) X-rays [Yakobi et al., 2005, 2008; Ping et al., 2013a; Ping and Coppari, 2016].
In the case of XANES, The amplitude of oscillations is larger and thus easier to measure than EXAFS oscillations. Moreover the interested spectral region is narrower. This further simplify the experimental conditions required to perform XANES. However, although experimentally easier, XANES has its drawback. The interpretation is much more complicated than for EXAFS. This is because in this case equation 1.69 can neither be simplified nor Fourier transformed. So to interpretation of XANES data are usually supported by theoretical models.
There are two features of a XANES spectrum that are particularly significant. The first is the position the spectrum edge. The edge energy position is related to the energy difference between core states (E1s usually, depending on the considered edge) and the lowest unoccupied states. It is therefore linked to the gap properties of the material under investigation. In the case of a metal, lowest unoccupied states corresponds to the Fermi energy, while for a dielectric the lowest unoccupied state are at the edge of the conduction band. In some cases, changes in the position of the XANES edge induce by temperature or pressure are linked to transition from a dielectric to a metal [Denoeud et al., 2014].
The second feature are the XANES spectral structures. These derive from two contributions: the shape of the unoccupied electronic bands and the multiple scattering. As we said, pattern produced by the multiple scattering are correlated to the local order of the investigated sample. Therefore XANES spectroscopy can be used to investigate both electronic and structural properties of a given sample.

Determination of the Absorption coefficient A practical way to measure the absorbed spectrum is to measure the transmission $T(E)$ of the beam through the sample that is given by the ratio between the intensity of the transmitted beam I_t and the intensity of the incident beam I_i. More in details in this way it is possible to get the absorption coefficient μ (that depends linearly on the density $\mu \propto \rho$) that is related to the transmission by the Beer-Lambert formula $T(E) = \exp[-\mu d]$, where d is the thickness of the sample. As we said $T(E) = I_t(E)/I_i(E)$, so the absorption coefficient is given by $\mu(E) = -(1/d) \cdot \ln(I_t(E)/I_i(E))$. In particular to facilitate XANES and EXAFS analysis we can isolate the typical oscillations $\chi(E)$ subtracting the absorption coefficient with the absorption coefficient for the single atom μ_0 and normalizing with the edge amplitude $\Delta\mu_0$:

$$\chi(E) = \frac{\mu(E) - \mu_0(E)}{\Delta\mu_0(E)} \tag{1.73}$$

Chapter 2

Decaying shock studies of phase transitions in MgO, $MgSiO_3$ and Mg_2SiO_4

2.1 Introduction

In this chapter we present a decaying shock study of the phase diagram of MgO, $MgSiO_3$ and Mg_2SiO_4 between 0.2-1.2 TPa, 0.12- 0.5 TPa and 0.2-0.85 TPa respectively.

A detailed knowledge of the high pressure regions of these phase diagrams is essential to properly model interior structures and dynamics of terrestrial planets. As Mg, Si and O dominate by far the chemical composition of their mantles, the study, in a first step, of the magnesian end members allows to model the interior structures avoiding the experimental and theoretical complexities induced by more minor elements such as Ca, Al or Fe. Such models have so far given good results in the best known terrestrial case. While Diamond Anvil Cell (DAC) measurements have substantially contributed to the knowledge of the upper regions of the mantles our comprehension of the processes governing the deeper mantles is limited mainly due to the inadequate characterisation of silicates properties at high pressures. Different topics regarding planetary differentiation, internal dynamic and magnetic field generation require a more precise thermodynamic model of their phase diagram above 200 GPa. The thermal profiles of super-Earth's interiors are controlled by the phase transitions of these compounds in this high pressure regime [Stixrude, 2014]. For example, the core mantle boundary (CMB) in GJ876d, a super Earth with 7.5 Earth masses, is expected to be seated at 1000 GPa [Valencia et al., 2006] and the tem-

perature at the CMB is assumed to be controlled by the melting curve of mantle components [Stixrude, 2014; Gaidos et al., 2010]. Experimental data between 100 and 1000 GPa are thus needed to well constrain melting lines of mantle components and thus Earth-like and super-Earth's CMB conditions [Du and Lee, 2014]. A relevant geophysical problem is to understand whether equimolar proportion of MgO and SiO_2 are the most abundant constituent of the planetary interiors or if on the contrary, the planet is dominated by the ternary combination $MgSiO_3$. To this aim it is necessary to know the free energy of the dissociation of $MgSiO_3$ into MgO + SiO_2 at the conditions that can be found in planetary interiors, i.e. ranging between 0 to 2 TPa and 10000 to 30000 K. In this context the dissociation of Mg_2SiO_4 into $MgSiO_3$ + MgO has its importance. Although the boundaries are not well constrained, above a certain pressure the Mg_2SiO_4 and the $MgSiO_3$ are certainly dissociated into MgO + SiO_2. To models such situations it is crucial to have a detailed knowledge of MgO and SiO_2 relative densities and viscosities. This would allow to describe planetary stratifications due to the differentiation between MgO and SiO_2 that could have visible effect on the mass-radius relation for example.
In addition to that, there are cases in which planetary mantles present an Mg/Si ratio > 1. This could be due to planetary differentiation processes or to stellar nebular Mg/Si fractionations. One example of that is the model proposed by Fiquet et al. [2008] for the Earth's lower mantle, which is proposed to be composed by an assemblage of (Mg, Fe)SiO_3 bridgmanite (or post-perovskite depending on the pressure) + ferropericlase (Mg,Fe)O respectively for the 70% and the 20% of the mixture. Hence liquid or solid (depends on the size of the planet and on the internal region considered) MgO can cohabit the planetary interior with liquid or solid $MgSiO_3$. Therefore the knowledge of melting lines of MgO and $MgSiO_3$, of their densities and viscosities is of great importance for modelling planetary differentiation in such situations.
Another key point for its geophysical implications concerns the metallisation of the planetary constituents. This is fundamental to comprehend a macroscopic characteristic as the planetary magnetic field. For example, indeed the metallisation of liquid silicates under extreme conditions has been proposed to promote part of the mantle to a potential magnetic field generator [Ziegler and Stegman, 2013; McWilliams et al., 2012; Millot et al., 2015].

It is therefore a strong requirement to study these mineral phase diagrams over a wider pressure and temperature range. In this context dynamic compression is the only available technique to study such high pressure-temperature (P-T) conditions. Various theoretical and few experimental studies have lately been carried on dynamically compressed MgO, MgSiO3, and Mg_2SiO_4 phases, but some controversies are not solved yet.

Calculations [Oganov et al., 2003; Wu et al., 2008; Cebulla and Redmer, 2014; Boates and Bonev, 2013; Miyanishi et al., 2015; Musella, 2016] and experiments [Zerr et al., 1998; Coppari et al., 2013] agree that MgO phase diagram is composed by two solid crystalline phases (with B1 and B2 structures) and a liquid phase. However phase boundary positions in the P-T diagram remain uncertain. Recent decaying [McWilliams et al., 2012] and steady [Miyanishi et al., 2015; Root et al., 2015] shock experiments claim to have observed signatures of melting and of the B1-B2 transitions, but at discordant P-T conditions. Furthermore, McWilliams et al. [2012] observed that along the Hugoniot, MgO melts directly into a metallic liquid, suggesting that MgO melt could play an important role in magnetic field generation in terrestrial planets. Moreover, the B1-B2 phase transition strongly affects super-Earth mantle rheological properties [Karato, 2011] with implications for orbital and thermal evolutions.

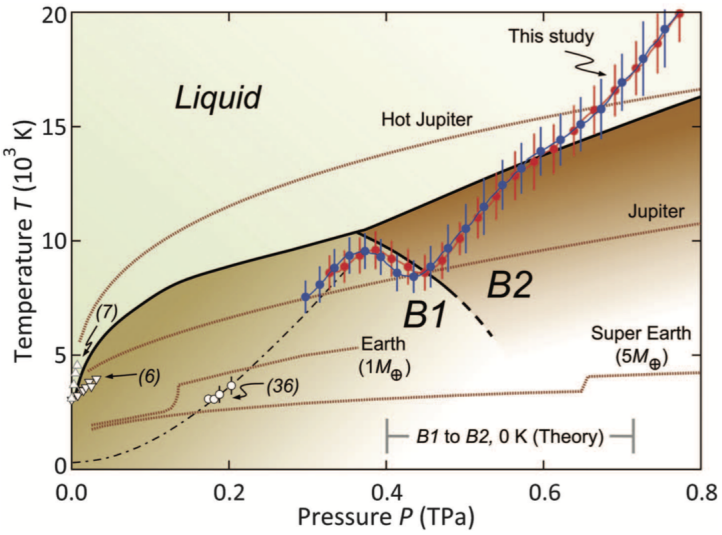

Figure 2.1: MgO phase diagram as reported in [McWilliams et al., 2012]. Blue and red dots represent decaying shock measurements.

Concerning the $MgSiO_3$ phase diagram, below the melting line calculations predict two solid phases with bridgmanite and postperovskite structures. In the $MgSiO_3$ melt region, a peculiar liquid-liquid phase transition has been observed in decaying shocks experiments, from both glass and single-crystal starting materials [Spaulding et al., 2012]. However, either this transition is not predicted [Militzer, 2013] or its nature is contested [Boates and Bonev, 2013]. This controversy together with the strong implications that a liquid-liquid transition would have for planetary interiors (through geochemical differentiation [Spaulding et al., 2012]) encourages deeper in-

vestigations.

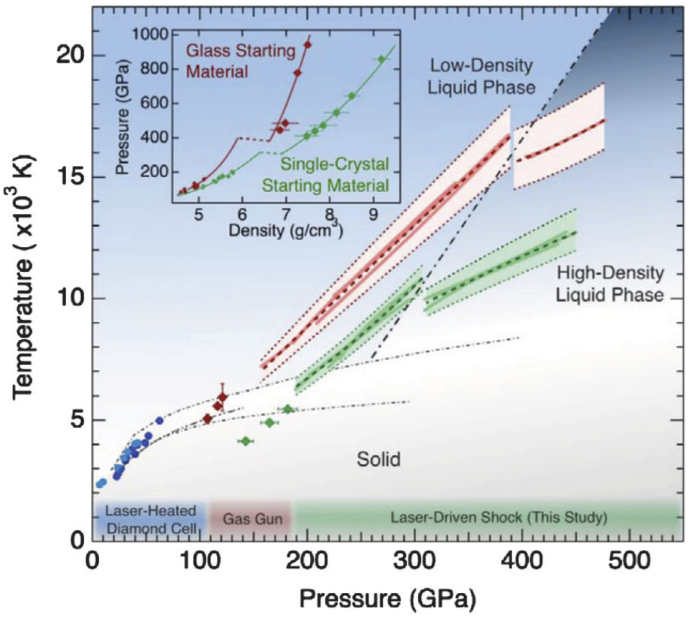

Figure 2.2: $MgSiO_3$ phase diagram as reported in [Spaulding et al., 2012]. Red and green lines represent decaying shock measurements for single crystal and glass starting materials respectively. The black dot-dashed line represent the liquid-liquid phase boundary.

A few data exist on the Mg_2SiO_4 phase diagram. Indeed, it has been explored with shock compression up to 200 GPa by Mosenfelder et al. [2007], Lyzenga et al. [1983], and Luo and Ahrens [2004], and at higher pressures by Sekine et al. [2016] very recently. Sekine et al. [2016] claimed that forsterite melt displays a partial phase separation of MgO crystallites, phase transition of the high pressure MgO, and remelting. It is based on the Hugoniot measurements (referred on the quartz Hugoniot data) and thermodynamic analysis of temperature measurements.

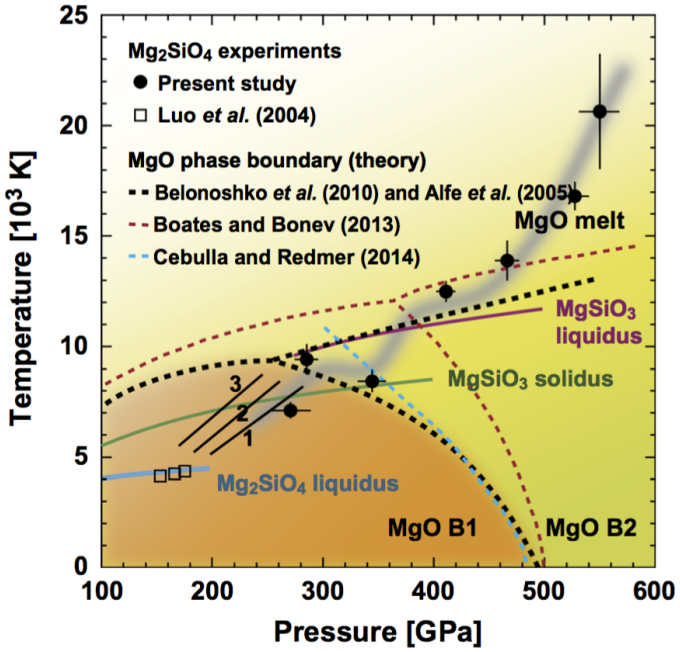

Figure 2.3: Mg_2SiO_4 phase diagram as reported in[Sekine et al., 2016]. Black dots represent steady shock measurements. Dashed lines represent MgO phase boundaries.

Decaying shocks are an efficient method to study phase transitions in transparent materials. A reflecting and not sustained shock is launched into an initially transparent material. Its propagation is monitored measuring time evolutions of thermal emission, shock velocity, and optical reflectivity at the shock front. As the shock is not sustained, the pressure, temperature, and shock velocity gradually decrease in time, following the Hugoniot curve. Phase transition may exhibit strong variations in temperature and/or in shock speed due to release of latent heat or to strong volume change. To detect these variations with optical diagnostics, the release of latent heat or the volume change must be large enough to produce observable imprints on the measured histories and need precise measurements. Moreover, the transition kinetics must be fast enough to occur before the shock front has propagated over distances exceeding the optical depth. Our results imply a reinterpretation of the behaviour of these compounds along the Hugoniot.

2.2 Experimental Setup

We performed decaying shock measurements on two different facilities: at LULI in Francs (Ecole Polytechnique) and at GEKKO in Japan (Osaka University). The experimental setups were similar. On both facilities, shocks have been generated with high power lasers and characterised with rear side optical diagnostics (two VISARs and SOP).
The design of the experimental setup used at LULI is represented in figure 2.4 and in figure 2.5. Figure 2.4 shows a conceptual layout of the key elements present in the chamber, while figure 2.5 gives the details of the optical system that images the target on the streaks.

2.2.1 Drive lasers

As shown in fig. 2.4 at LULI we focused up to two frequency-doubled laser beams (wavelength = 0.532 μm) with a 1.2-1.5 ns pulse duration. The maximal energy delivered at λ=0.532 nm at LULI was $\sim$ 750 J. Focal spots were smoothed with Hybrid Phase Plates, thus obtaining a flat intensity profile of 600 μm.
At GEKKO we irradiated targets with six to nine beams of 2.5 ns at 0.351 μm. Focal spots have been smoothed with Kinophorm Phase Plates to a 600 μm focal spot diameter. The total energy was $\leq$ 900 J.
Because of the use of phase plates only a fraction of the delivered laser energy irradiates the target. As the laser energy is measured before the phase plate, the amount of energy irradiated on target is not known. To this aim, we performed hydrodynamic simulations tuning the laser intensity in order to reproduce measurements of the shock velocity in SiO_2, which is a reference material. This allowed us to determine the numerical laser intensities irradiated on target, that varied between 0.1 and 1 $\times$ 10^{14} W/cm^2.

2.2.2 Optical system

The design of the optical path from the target to the streaks is represented in figure 2.4 and in figure 2.5. The light coming from the rear side of the target is collected with an achromatic triplet lens with focal length = 16 cm placed at a distance of $\sim$ 19 cm from the rear surface of the target. The light beam is then collimated by lens L1 and separated in two beams by the dichroic mirror M1. This mirror allows the separation between the two diagnostics: VISAR (that uses ω ant 2 ω probe beams) and SOP, which measure the shocked target self emission. More precisely, the self emission beam is imaged onto the streak camera slit by lens L2 with a magnification M $\sim$ 6 and spectrally filtered at 450 nm with a gaussian filter (FWHM = 40 nm). The

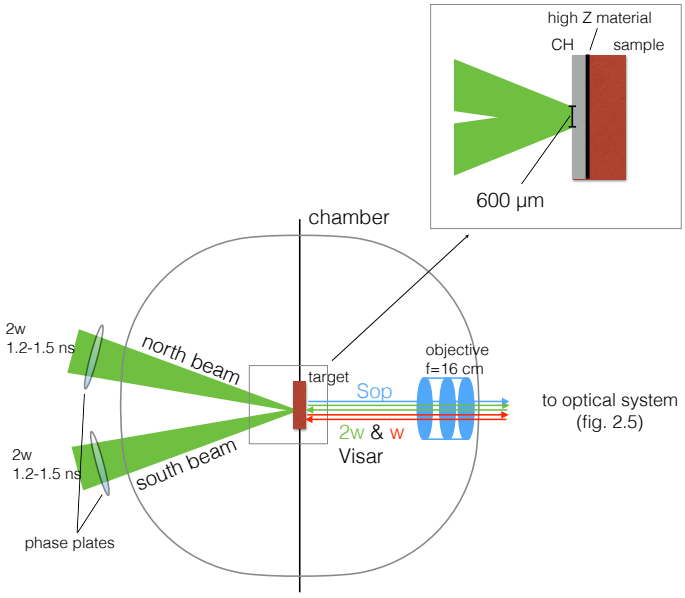

Figure 2.4: Conceptual layout of the key experimental elements in the vacuum chamber used at LULI, with a zoom on the target on top.

visar probe beams instead are separated by beam splitter M4. Then lenses L3 and L5 focused the beams on beam splitters BS2 respectively for the ω and 2ω VISAR interferometer systems (see fig 1.16). In such a way the rear side of the target is imaged onto interferometer beam splitters BS2 . Finally these images are transferred to the ω and 2ω streak cameras by lenses L4 and L6 respectively. The optical path was designed as represented for two reason: 1) in order to minimise the number of light transits through beam splitters, i.e. to minimise the vignetting issues and the loss of light; 2) in order to image the rear surface of the target with a magnification of around 5-8 at the streaks. The distances reported in fig. 2.5 correspond to a magnification of 5. Playing with the positions of lenses L4 and L6 it was possible to decrease or increase such a magnification for VISAR streaks.

To evaluate the size of the probed area for each optical diagnostics we placed in the chamber a target with concentric circumferences of known diameter imprinted on the rear surface. The images produced on streak photocatods with this target are shown in figure 2.6. From these images we obtained the size magnified onto a single pixel: VISAR 2ω: 1.17 μm; VISAR ω: 1.45 μm; SOP: 1.51 μm. This information will be used to measure shock front sizes.

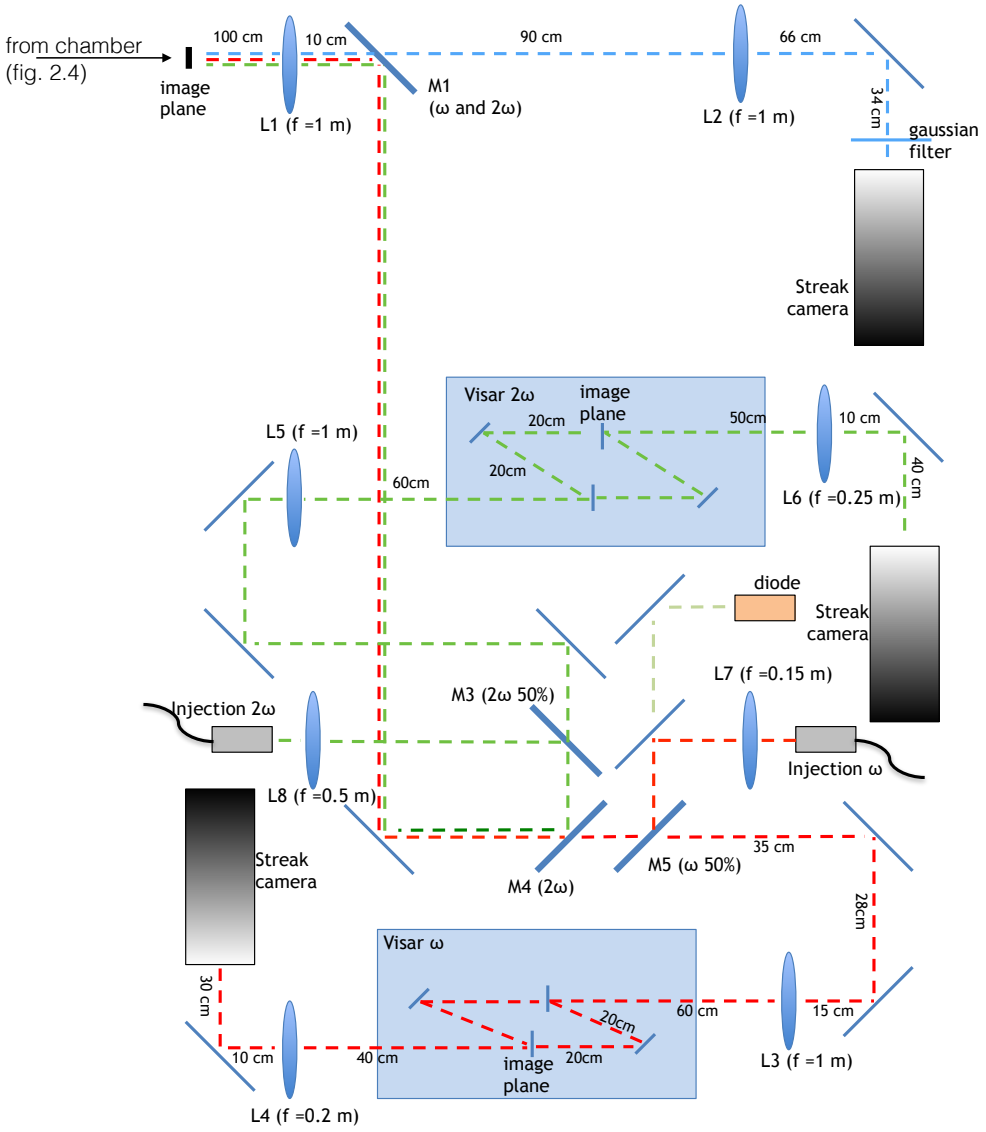

Figure 2.5: Design of the VISAR and SOP optical system used at LULI.

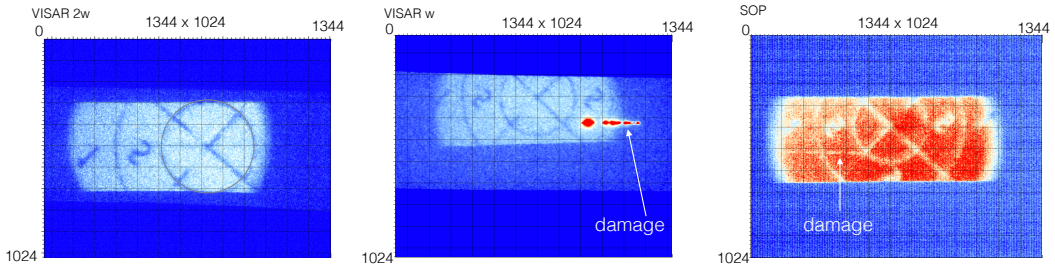

Figure 2.6: VISAR and SOP images used for the evaluation of the sizes of the probed area for each optical diagnostic at LULI. When slit are closed the defects on VISAR ω and SOP do not affect the measured signals.

2.2.3 Diagnostics

VISAR Two independent VISAR systems with different sensitivities were used both at LULI and GEKKO. Indeed, as explained in sec. 1.0.3.1, two VISARs are needed to determine the velocity of a moving reflector without any ambiguity.
At LULI the VISAR probe beams were provided by a Q-switched YAG laser with a pulse duration of ~ 10 ns at the fundamental wavelength $\lambda = 1064$ nm and at the second harmonic $\lambda = 532$ nm.
The interferometers are represented in fig. 1.16. For greater clarity we report in fig. 2.7 the picture of the ω VISAR interferometer. As shown in the picture the etalon is mounted on a motorised stage that can be translated with sub-micrometric precision. This allowed to play with the length of the BS1 - mirror2 - BS2 arm precisely enough to produce the interference pattern.
We chose 15.2 mm and 5.11 mm thick etalons for the ω and 2ω systems respectively. In such a way ω and 2ω VISAR sensitivities VPF_V were 6.8 km/(s·fringe) and 9.75 km/(s·fringe) respectively. The smallest fringe shift that it is possible to distinguish is $\sim 1/20$ of fringe [Celliers et al., 2004a]. Therefore the smallest detectable velocity change is ~ 0.34 km/s in vacuum and $0.34/n$ km/s in a material with index of refraction n. As streak cameras we used two Hamamatsu C 7700 with photocathode S20 and S1 for the VISAR system at 2ω and ω respectively.
At GEKKO, both VISARs operated at $\lambda = 532$ nm with sensitivities of 7.432 km/(s·fringe) and 4.476 km/(s·fringe), allowing to detect velocity changes down to 0.22 km/s in vacuum. Measured velocities were in the range of 10-28 km/s.

LULI

	VISAR 1 (ω)	VISAR 2 (2ω)
sensitivity (vacuum)	6.8 km/s/fringe	9.75 km/s/fringe

GEKKO

	VISAR 1 (ω)	VISAR 2 (ω)
sensitivity (vacuum)	7.432 km/s/fringe	4.476 km/s/fringe

Table 2.1: Table of VISAR sensitivities used at LULI and at GEKKO

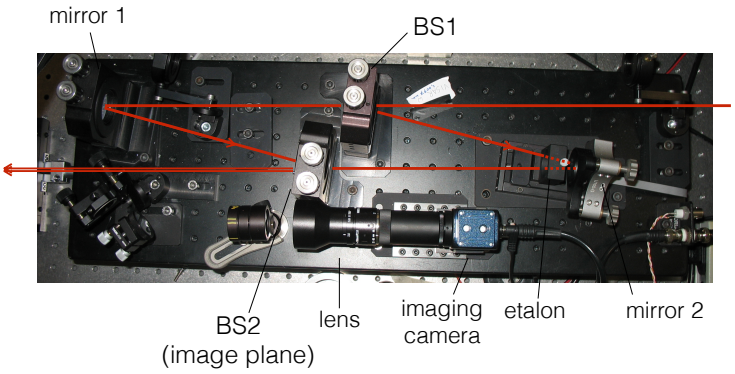

Figure 2.7: Picture of the ω VISAR interferometer used at LULI.

SOP The Streak Optical Pyrometry system set up at LULI consists in an optical system comprehensive of a gaussian filter centered at $\lambda = 450$ nm (FWHM= 40 nm), and a streak camera. The streak camera we used was an Hamamatsu C 7700 with photocathode S20.
As explained in section 1.0.3.2 the SOP needs to be calibrated in order to get the relation 1.62 between the measured intensity and the temperature. We recall that there are two calibration methods. A possibility is to calibrate the SOP to a reference material (e.g SiO_2). In this case, since the relations temperature/shock velocity and reflectivity/shock velocity of the reference material are known, it is possible to get the intensity-temperature relation (eq. 1.62) from the measured intensity, shock velocity and reflectivity. Otherwise an absolute calibration can be performed, using for example a calibrated lamp as a reference. Detection limits of the SOP used in this campaign were $\sim$ 6000 K.

2.2.4 SOP calibration

In this section we report the SOP calibrations performed at LULI and at GEKKO.

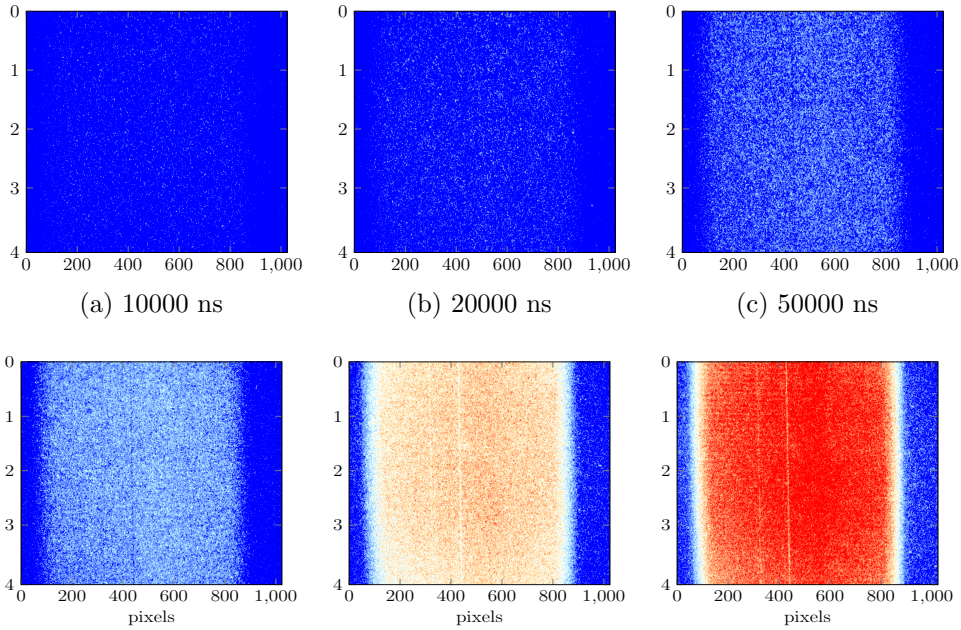

(a) 10000 ns (b) 20000 ns (c) 50000 ns

(d) 100000 ns (e) 500000 ns (f) 1000000 ns

Figure 2.8: One SOP signal of the radiation thermally emitted by the calibrated lamp is reported for some selected sweep rate (or time window) of the camera.

LULI calibration At LULI, we performed an absolute calibration using a tungsten ribbon lamp (Osram WI 17/G) with a known spectral radiance [Ruprechter, 2000]. The ribbon shape of the filament is crucial in this calibration. Indeed the spectral power of a planar surface and mapped to another surface (in our case the pixel area) can be calculated with Planck's law. We powered the lamp with a steady current of 15 A producing a radiance that corresponds to a 2588 $\pm$ 15 K gray-body emission, as reported in the work just cited. Indeed, as the reflectivity of the ribbon filament at 2588 K was not zero at 450 nm (we recall that our SOP system has a gaussian filter at 450 nm with a FWHM = 40 nm, see fig. 2.5), we used the Planck's law for a gray body (see eq. 1.59). This simply means that we corrected the emissivity ϵ of the ribbon filament using the Kirchhoff's Law $\epsilon(\omega) = 1 - R(\omega)$, being the reflectivity $R(\omega)$ of the filament reported in [Ruprechter, 2000].

The lamp filament was imaged to the streak by the same optical system of the experiment (see fig. 2.5).
With such a configuration we collected a set of SOP data for each sweep rate available in the streak camera. Indeed for a body emitting at a given temperature the intensity measured by the camera is inversely proportional to the sweep rate. This is equivalent

to say that, as pointed by eq. 1.63, the constant A is inversely proportional to the sweep rate η (or, equivalently, directly proportional to the time window.) For each sweep rate we performed 100 measurements. This has been done in order to have a good photon count statistic at high sweep rate too. Examples of a single acquisition for some sweep rates are shown in figure 2.8. As shown, the output measurements of a streak camera consists in an image of 1024 x 1344 pixels. To obtain the radiance emitted by the lamp it is necessary to subtract the background noise from the measured intensity. We evaluated the background performing 100 acquisitions with the camera shutter closed. The background resulted from the average of these 100 measurements. The background was not homogeneous meaning that we had to subtract it from the measured intensity pixel by pixel. Only after that we averaged the matrices resulting from the subtraction over all the pixels. These average values versus the respective time windows were interpolated with the function

$$I = \alpha \cdot \Delta t \tag{2.1}$$

having as free parameter the constant α. Hence as shown in figure 2.9 from the interpolation results $\alpha = 0.01102 \pm 0.00004$.s

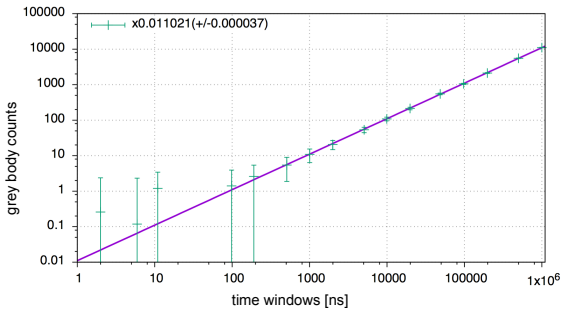

Figure 2.9: The number of SOP counts produced by the light emitted by a lamp at 2588 K ± 15 K and selected with a gaussian filter centered at 450 nm and with a FWHM of 40 nm is represented for each SOP time window with green cross. Each point is the result of an average over 100 measurements. Here, gray-body count stays for the measured signal minus the dark noise of the SOP (the background signal measured with the shutter closed).

The constant A, that relates the measured intensity and the temperature through eq 1.62, is given by A= $\alpha \cdot \Delta t \cdot (\exp(T_0/T_{lamp}) - 1)$. We recall that T_0 is known and it is equal to hc/λ_0 where h, c an λ_0 are Planck's constant, the speed of light and the centroid wavelength respectively. This interpolation method allowed to establish the

constant A more precisely than using only the average over 100 measurements at the sweep rate selected for the experiment.
However further adjustments of this formula are needed in order to consider changes in the experimental set-up. In particular a correction must be introduced when changing the slit width of the camera for the periodical checks of the optical path. The mechanic of the slit did not allow to re-close it to the same width with a 100% reproducibility. For this reason if the slit width used during a shock compression measurement was different from the one used for the calibration we corrected the constant A as it follows

$$A = \frac{FWHM_{shot}}{FWHM_{cal}} \cdot \alpha \cdot \Delta t \cdot (\exp(T0/T) - 1) \tag{2.2}$$

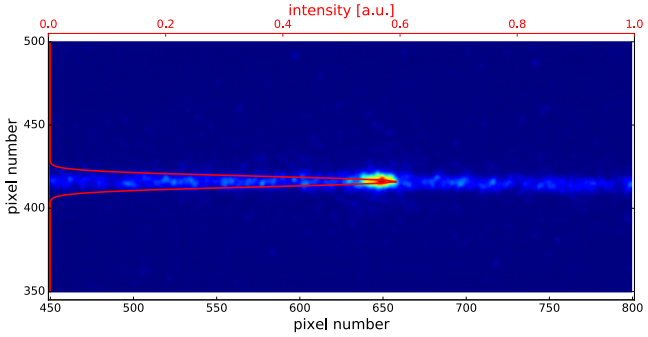

Figure 2.10: Example of a VISAR signal used to evaluate the slit width. The image is obtained using the VISAR in focus mode. The slit width is obtained with a gaussian interpolation.

The FWHMs represent the slit width as they were obtained fitting with a Gaussian function the line-out of images of the slit acquired in focus mode every time the slit was moved. Figure 2.10 represents one this acquisition and the Gaussian obtained from the interpolation of the vertical line-out of the image. $FWHM_{cal}$=7.868 px gives the slid width as it has been used for the calibration, while $FWHM_{shot}$ gives the slit width as used during a given shot. The maximum difference among a $FWHM_{shot}$ used for a measurements and $FWHM_{cal}$ of the calibration is $\sim$ 1 pixels and it implied a correction of $\sim$13% in the determination of the constant A.
During our experiment we performed streak acquisitions with gain equal to 63 and with two time windows: 20.694 ns and 11 ns. The respective calibration constants are A = 48540 $\pm$ 2320 and A = 25800 $\pm$ 1235. Errors are calculated from the propagation of the uncertainties on time windows (0.001 ns), lamp temperature (15 K), fit parameter α (0.000037) and FWHM of the slit width (1%).

Figure 2.11 represents the brightness temperature curves as a function of the corrected intensity $I/(1-R)$ for the two obtained calibration parameters. Coloured

areas represent the uncertainties coming from the errors on A and on T_0. The dashed and dot-dashed lines represent uncertainties considering the relative error on the corrected intensity of 10 % and 20 % respectively.

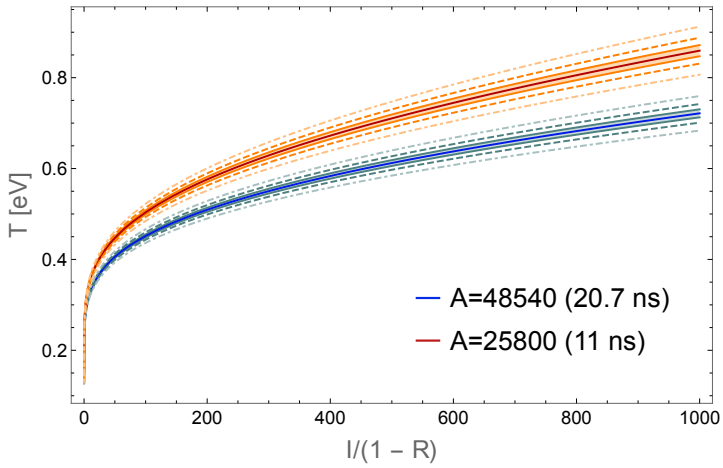

Figure 2.11: Brightness temperature T - corrected intensity I/(1-R) curves obtained from the calibration at LULI for a slit width $FWHM_s hot = 7.22$.

In order to validate our absolute calibration we performed some shots on SiO_2 as a reference material. The P-T curves that we obtained from SOP and VISAR data are in excellent agreement with previous results [Hicks et al., 2006; Spaulding et al., 2012; Millot et al., 2015] as shown in figure 2.12.

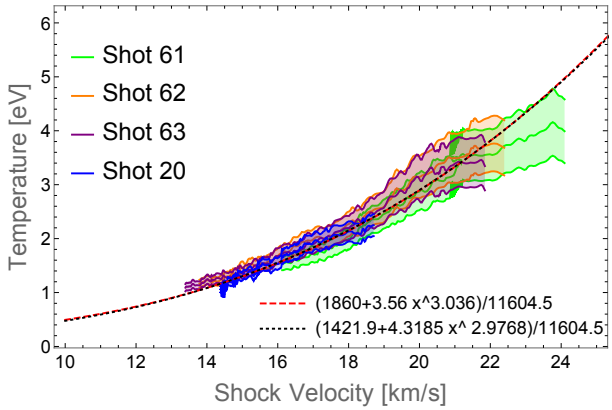

Figure 2.12: The SiO_2 T-Us curves obtained for different shots (20,63,61,62) at LULI are compared to T-Us interpolation of data from [Hicks et al., 2006] reported in literature [Brygoo, 2006; Millot et al., 2015]

GEKKO calibration At GEKKO we used α- quartz as in-situ reference for our SOP measurements. In particular we performed three calibration shots on targets with an SiO_2 $50\mu m$ thick layer measuring the SOP intensity and the shock velocity. To obtain the calibration constant A we interpolate the set of intensity and velocity data with the following relation:

$$\frac{I - I_{offset}}{1 - R_h(Us)} = \frac{A}{Exp[T0/(1860 + 3.56{U_s}^{3.056})] - 1} \tag{2.3}$$

that is obtained from equation 1.62 simply placing the well known temperature-shock velocity relation $\mathrm{T(Us)} = 1860 + 3.56 \cdot {U_S}^{3.036}$ (relation determined by [Brygoo, 2006] interpolating the T-Us data from [Hicks et al., 2006] that have been confirmed by various studies [Spaulding, 2010; Millot et al., 2015; Huser et al., 2015]). As a reflectivity we used the Hill function $R_h(Us) = 4.614 \cdot 10^{-3} + ((0.3073 - 4.614 \cdot 10^{-3}) \cdot Us^{9.73})/(Us^{9.73} + 24.185^{9.73})$ obtained interpolating R-Us data from [Hicks et al., 2006] and confirmed by [Millot et al., 2015; Spaulding, 2010; Qi et al., 2015].

Fig. 2.14 shows the interpolation for the three shots. Shots 39672 and 39703 were performed using the same gain value (40) for the SOP, while shot 39705 was performed with a higher value (55) in order to increase the signal for lower emission. Error bars are principally due to count fluctuations in the SOP ($\sim 15\%$ of the signal) and to the uncertainty on reflectivity. We converted the constant A obtained with shot 39705 to the one that corresponds to the gain value of shots 39672 and 39703 using the gain value - count relation previously characterised for the streaked camera that we used (see fig. 2.13).

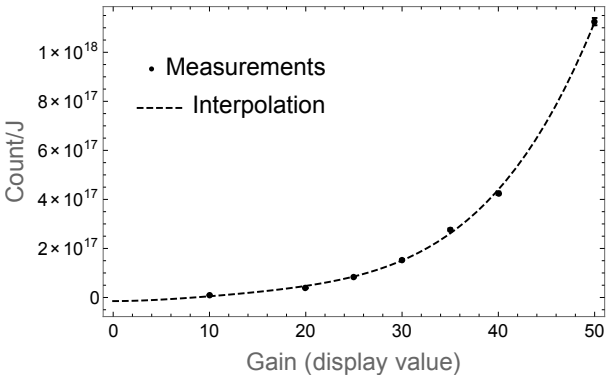

Figure 2.13: Gain value - count/J relation for the SOP streak camera.

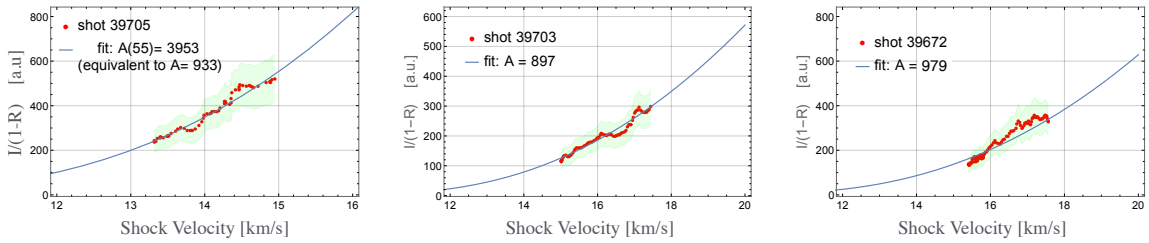

Figure 2.14: Red dots represent corrected intensity versus shock velocity curves obtained for three calibration shots on SiO_2 performed at GEKKO. The blue lines represent the interpolation used to get the calibration constant A.

Shot	gain	A measured	standard error
39672	40	979	22
39703	40	897	30
39705	55	3953	81

Table 2.2: Table showing the calibration constant A for each calibration shot.

The values of the constant A obtained with the interpolations are shown in the table 2.2. From an average of the three values we obtain $A = 937$ which is the result of this calibration. Figure 2.15 represents the brightness temperature curves as a function of the corrected intensity $I/(1-R)$ obtained for the constant A (for SOP gain = 40). The dashed and dot-dashed lines represent uncertainties considering the relative error on the corrected intensity of 10 % and 20 % respectively.

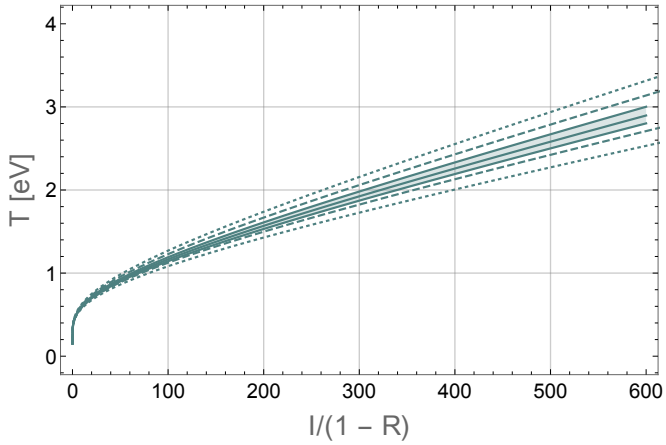

Figure 2.15: Brightness temperature T - corrected intensity I/(1-R) curves obtained from the calibration at GEKKO for a gain value equal to 40.

2.2.5 Sample preparation

The targets were made of multilayer pushers glued on 350 μm thick samples: MgO single-crystal (density= 3.58 g/cc, oriented for shock propagation in the 100 crystallographic direction), Mg_2SiO_4 single-crystal (Forsterite, density 3.2 g/cc) and $MgSiO_3$ glass (density= 2.74 g/cc). Mg_2SiO_4 and MgO single-crystal samples were manufactured respectively by Solix Crystal (Belarus) and by Base Optics. $MgSiO_3$ glass samples, instead, were prepared from powder mixture melted at high temperature and lapped at IMPMC with appropriate polishing machines to an optical flatness of $\lambda/4$. For MgO the refraction index are taken to be 1.7421 and 1.7216 for 0.532 and for 1.064 μm respectively [Stephens and Malitson, 1952]. Data on $MgSiO_3$ glass refractive index are scarce and contradictory: [Nesterchuk and Makarova, 1970], reports 1.51 while [Hanada et al., 1988] 1.56. For this reason we performed some ellypsometry measurements at the Center for Nanosciences and Nanotechnology (CNRS - Paris Sud University, Marcoussis, France) to characterise it. These measurements are reported in fig. 2.16. At 0.532 nm we measured 1.614., while for 1.064 nm extrapolated 1.6 with a polynomial fit. For Mg_2SiO_4 the ω and 2ω refraction index were 1.67 and 1.66 respectively.

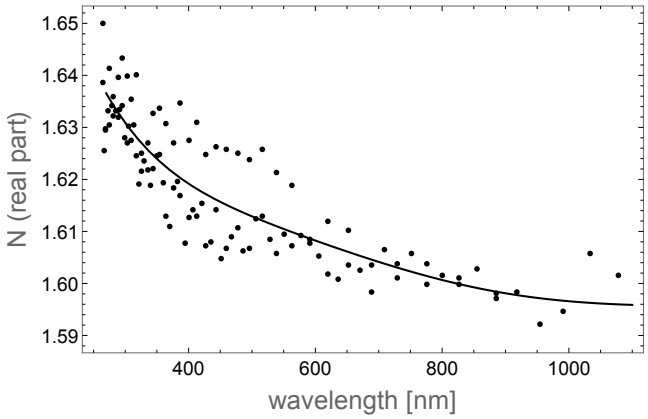

Figure 2.16: Ellipsometry measurements of the real part of the refractive index of $MgSiO_3$

All silicates were cut into 2×3 mm^2, 350 μm thick samples with diamond wire. They were then glued to multilayer pushers with a UV glue layer of around $1\mu m$- $2\mu m$. A 532 nm and 1064 nm anti-reflecting coating was applied to all the silicate samples in order to prevent the occurrence of residual reflections in VISAR measurements.

2.2.6 Target design

The choice of pushers is critical in decaying shocks experiments. Indeed there are two problems that can occur and need to be avoided: preheating and reverberations. The

preheating is issued by the X-ray emission from the coronal plasma produced by the drive laser-ablator interaction. The hotter the coronal plasma the more intense the X-ray emission and therefore its effect on the sample that can be significantly heated up. We will treat this problem in details in the following paragraph 2.2.6.1.
Reverberations are phenomena related to the occurrence of interfaces with a high impedance mismatch that strongly influence the hydrodynamic of a target complicating the interpretation of the detected signals, as we will see in paragraph 2.2.6.2.
In order to avoid these problems we selected and studied three configuration of targets with an ablator + shield + sample design:
1) 10 μm CH + 2 μm Au + 50 μm Al +sample;
2) 50 μm CH + 15 μm Fe + sample;
3) 75 μm CH + 3 μm Au + 25 μm Ti + sample;

2.2.6.1 Preheating

In this paragraph we present a study performed with MULTI radiative hydrodynamic code (which includes a description of the interaction between matter and radiation) in order to design pusher to prevent sample preheating. To reduce the preheating it is crucial to accurately choose the ablator (as interacting with the laser it produces the X-ray emitting plasma corona) and the shield layer (to stop the X-ray emitted by the corona). As ablator we chose CH in order to minimise the X-ray emission of the plasma corona (see sec. 1.0.1.5). As X-ray shields we choose high Z materials as Au, Al or Fe. In the following we give more details about the choice of our pushers.

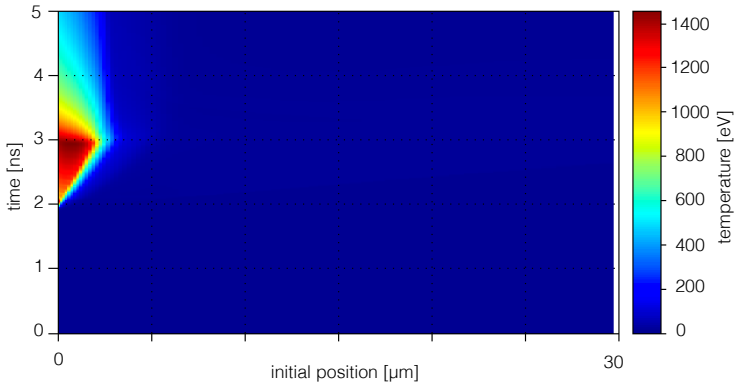

Figure 2.17: Color plot of the temperature versus time and initial position plane produced by a laser pulse of intensity 10^{14} W/cm$_2$ (time length 1.2 ns, focal spot 600 μm) focused on a CH target. The coronal plasma temperature reach values ∼1.4 eV.

During our experiment, depending on the drive laser intensity the plasma corona can reach temperatures > 1 keV. Such high temperature can induce a preheating. To stress out the need of a high Z material placed in between the CH ablator and the oxide sample we performed a radiative MULTI simulation with a 1.2 ns laser pulse of 10^{14} W/cm^2 focused onto a $50\mu m$ CH + $300\mu m$ MgO target [1]. Fig. 2.17 shows the corona temperature reached in the first 4μm of the CH ablator. The highest temperature reached is around 1.4 keV.

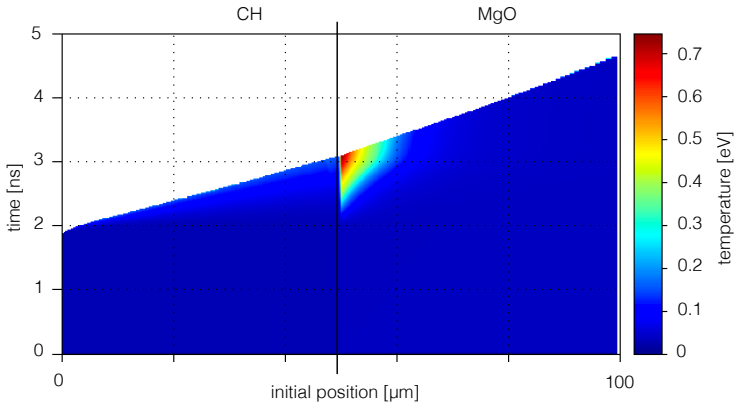

Figure 2.18: Color plot of the temperature versus time and initial position plane of a CH — MgO target produced by a laser pulse of 1.2 ns and 10^{14} W/cm^2 obtained with a MULTI simulation: the MgO is pre-heated. The color bar reduced to the range 0-0.75 eV in order to evidence the temperature gradient in the MgO layer.

The radiation of the plasma corona at 1.4 keV is intense enough to preheat the MgO layer as shown in fig. 2.18, that is a color plot obtained from the same simulation of fig. 2.17. A region of the MgO layer close to the CH layer is heated up to 0.7 eV[2]. Few tens of μm of MgO seem concerned by the X-rays preheating. From the graph one can see that the shock will propagate in a preheated sample for around 30 μm. In a decaying shock experiment this leads to difficulties in the interpretations of SOP and VISAR signal. First of all, the first microns of MgO can get opaque and this would imply a disappearance of the VISAR signal. Then, at a certain point the shock will enter in the transparent but still preheated MgO. Here the shock is still exploring

[1] We performed all this study performing the simulations with a drive laser of 10^{14} W/cm^2. Ensuring that with this value samples were not preheated, we made sure that during the experiment we could safely use laser intensities up to 10^{14} W/cm^2.

[2] In appendix B.1 we report a study of the preheating of CH+MgO samples varying the CH thickness. As the CH is not a good X-ray absorber, variations of its thickness do not produce significant changes. Indeed for the studied thicknesses (25 μm, 50 μm and 75 μm the MgO is always preheat up to ~ 0.7 eV.)

states along a preheated Hugoniot. Hence a big issue is that from the VISAR and SOP signal it won't be possible to understand whether the shock propagates in the unheated MgO. In other words it won't be possible to understand at which time the shock velocity profile and thermal emission profile respectively measured by VISAR and SOP refer to the principal Hugoniot.

The X-rays that preheat the MgO can be blocked by relatively thin layers of high Z material. Approximating the plasma corona as a black body, for a temperature of 1.4 KeV the Planck distribution of the spectral radiance for unit wavelength and for unit frequency have their maxima respectively at a wavelength $\lambda \sim 0.2$ nm and $h\nu = 2.82$ kT $\sim = 4$ KeV. However more precise models that include the plasma corona opacity can be considered. For optically thin media the opacity is described by the Planck opacity, while optically thick media can be described with the Rosseland opacity. For the Planck and the Rosseland models the process of radiative transfer is respectively dominated by high energetic photons at $h\nu = 2.85$ kT and $h\nu = 4$ kT. Therefore the radiative transfer process for optically thick media is dominated by more energetic photons than for a black body. On the contrary for optically thin media the Planck opacity predict the most energetic photons to have an energy close to those emitted by a black body. The plasma corona can be quite safely considered an optically thin medium at T=1.4 keV. To design our targets we therefore considered the transmission of the various layers for X-rays up to $\sim$ 10-15 keV.

In this energy range the high Z layers of our three chosen shields (2 μm Au + 50 μm Al ; 15 μm Fe; 3 μm Au + 25 μm Ti) significantly absorb the plasma corona X-rays (transmission spectra are shown in fig. B.2), though the transmission is not negligible for X-ray energy at 6-7 keV and >10 keV for the 15μm Fe and the 2μm Au+ 50μm Al shields respectively. However here, for safety we considered a quite extended energy range. The idea indeed was to obtain a general picture of the capability of such shields of blocking the plasma corona emission for preventing the preheating of the samples. Then we tested more precisely such pushers with hydrodynamic simulations to carefully verify whether preheating occurs or not.

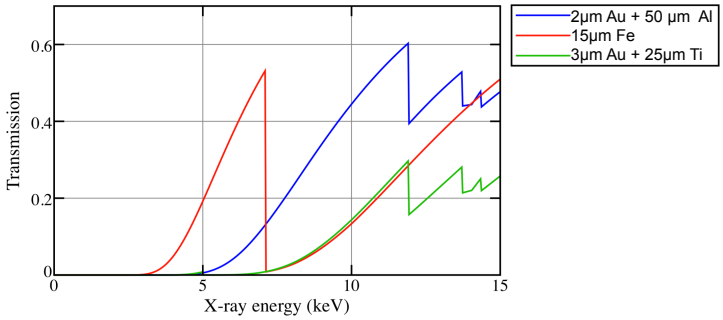

Figure 2.19: X-ray transmission versus energy curves for the three studied pushers.

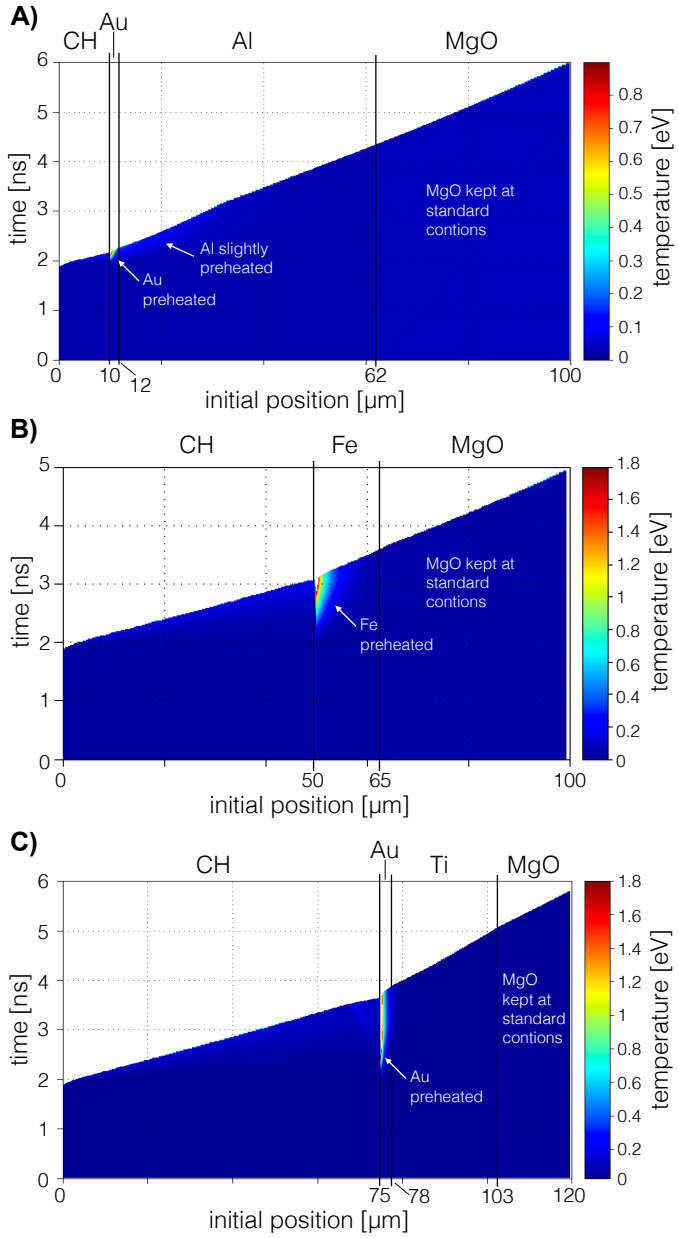

Figure 2.20: A), B) and C) represent respectively color plots of the temperature versus time and initial position plane of a 50μm CH|15μm Fe|MgO, 75μm CH| 3μm Au| 25μm Ti|MgO and 10μm CH |2μm Au| 50μmAl|MgO target produced by a laser pulse of 1.2 ns and 10^{14} W/cm^2 obtained with a MULTI simulation.

Figure 2.20 shows radiative MULTI simulations [3] performed with a 1.2 ns laser pulse with an intensity of 10^{14} W/cm^2 focused on targets composed of our pushers + MgO:
A) 10 μm CH + 2 μm Au + 50 μm Al +MgO ;
B) 50 μm CH + 15 μm Fe + MgO;
C) 75 μm CH + 3 μm Au + 25 μm Ti + MgO [4].
In all cases the x rays are absorbed by the high Z layers and do not reach the MgO, thus kept at standard condition. Therefore MULTI simulations which includes opacity tables of the CH predict no preheating.

2.2.6.2 Reverberations

The insertion of high Z layers inside our pushers introduces the other problem mentioned above (i.e. reverberations), as it implies the creation of interfaces with a high impedance mismatch. We have already described the shock behaviour at interfaces in section 1.0.2.5. However it is worth recalling that for a shock moving from a material A to a material B with impedance $Z_B > Z_A$ a shock is reflected and a shock is transmitted. Instead in the event of $Z_B < Z_A$ a rarefaction wave moving backward is generated and a shock is transmitted through the interface. The more important the difference in impedance the more intense the rarefaction wave or the reflected shock. These reflected shocks can be further reflected in the direction of the primary shock and in some cases they overtake the primary shock. This would affect the rear side diagnostic signals producing kinks on the measured profiles.
For this reason, we performed both hydrodynamic simulations and experimental tests verifying the occurrence of reverberations for our target configurations.

Hydrodynamic simulations In order to describe the phenomenon of the reverberations we consider first a target slightly different from those that we finally used in the experimental campaigns: 25 μm CH + 3 μm Au + 25 μm Ti + 300 μm MgO. If we simulate the hydrodynamic of this target irradiated by a 2.5 ns laser pulse with an intensity of $2.7 \cdot 10^{13}$ with MULTI (in this case neglecting radiative effects) we obtain the graph represented in figure 2.21. The simulation predicts a reverberating shock (or secondary shock) overtaking the primary one at around 6.5 ns.

[3] Multi simulations presented in this paragraph have been run using the .hetl opacity tables for the CH. We tested also the .TV table, results are shown in appendix B

[4] The reason for the differences in the CH layer thicknesses will be explained in the following paragraph

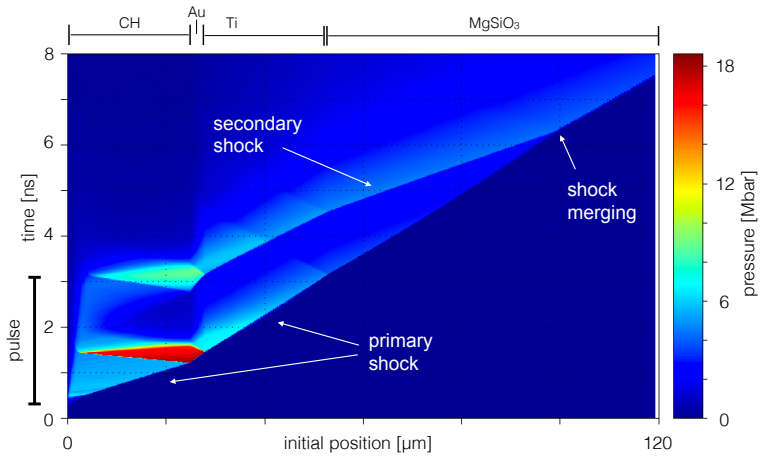

Figure 2.21: Color plot of the pressure versus time and initial position of a 25 μm CH + 3 μm Au + 25 μm Ti + 300 μm $MgSiO_3$ target compressed by a shock generated by a laser pulse of 2.5 ns and $2.4 \cdot 10^{13}$ W/cm^2 obtained with a MULTI simulation. In this case a second shock forms and reaches the first shock at 6.5 ns

As shown in figure 2.22 the shock enters in the $MgSiO_3$ with a pressure around 5.5 Mbar at its front. In such a case, $MgSiO_3$ is metallic and hence the VISARs would record the shock velocity of the shock. After $\sim$ 1 ns a second shock enters in the $MgSiO_3$ but diagnostics cannot see it because it's hidden by the first shock. Both shocks decay in time and the second reaches the first when the first is at 2.2 Mbar, which means that the first shock is reflecting or opaque. In other words until the time in which the second shock reaches the first shock the second shock is hidden by the first one. At the shock merging the pressure jumps from 2.2 Mbar to 4 Mbar. As the pressure increases the shock velocity increases too and the VISAR would observe a jump in the shock velocity. This jumps can be wrongly interpreted as phase transition signatures. (This jump in pressure or in the shock velocity can be derived if the pressures, shock velocities and eos of the two shocks are known. Otherwise from the measurements of the first shock and of the shock resulting from the merging it is possible to get the pressure and shock velocity of the secondary shock.)

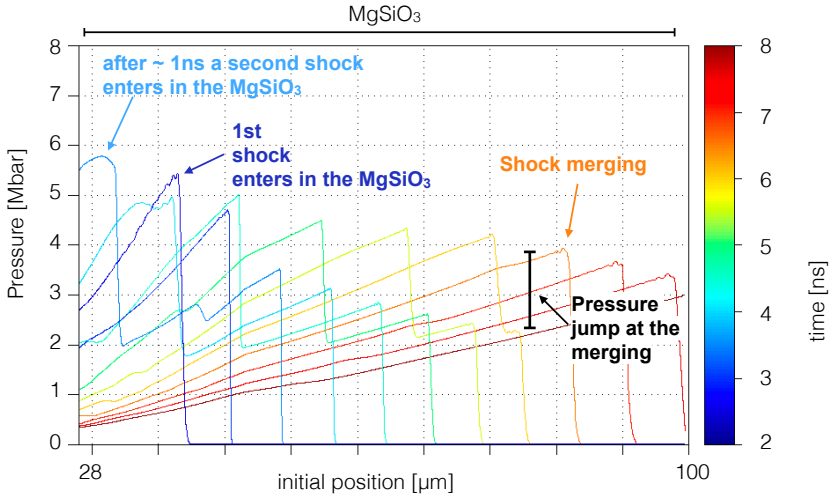

Figure 2.22: Pressure vs initial position curves of a CH — Au — Ti — $MgSiO_3$ target compressed by a shock generated by a laser pulse of 2.5 ns and $2.4 \cdot 10^{13}$ W/cm^2 obtained with a MULTI simulation.

In order to avoid the reverberations in the CH + 3 μm Au + 25 μm Ti pusher we used a 75 μm thick layer of CH. In this way no reverberating shock is produced (see fig 2.23). For this campaign we chose to thicken the CH ablator, another possibility would have been to shorten the drive pulse time length. However this pusher was used at Gekko where we could not play with the pulse temporal profile, since it was fixed at 2.5 ns.

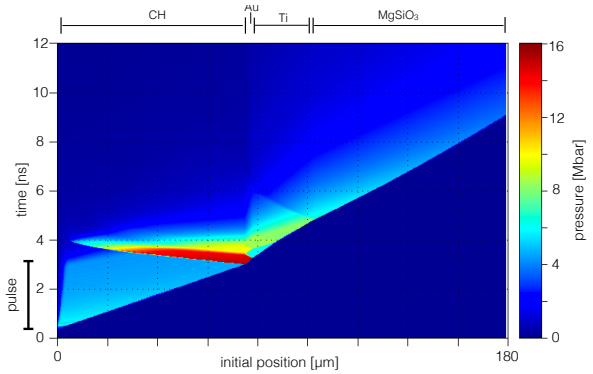

Figure 2.23: Hydrodynamic simulations for a target 75μmCH-3μmAu-25μmTi 350 μm $MgSiO_3$ with a 2.5 ns laser pulse with an intensity of 2.4 10^{13} W/cm2 are shown at the top and the bottom respectively. In this case there is no secondary shock merging with the first in the $MgSiO_3$ layer.

This study with hydrodynamic simulations has been performed for all the three pushers in order to choose the optimal thickness of the CH ablators in relations with the drive pulse duration. Our final choices were:

1) 10 μm CH + 2 μm Au + 50 μm Al;
2) 50 μm CH +15 μm Fe;
3) 75 μm CH + 3μm Au + 25 μm Ti.

Experimental test We tested our pushers using SiO_2 as a reference material. This experimental study allowed to establish that pushers 2 and 3 were suitable for our measurements, while pusher 1 was not appropriate for decaying shock experiment on thick silicate samples. Indeed with the pusher 1 and typical laser intensities used in silicate experiments, we observed a bump both in velocity and thermal emission signals. However at those thermodynamic conditions no phase transitions are expected. Furthermore the bump disappears for shots performed with pusher 2 and 3. This means that these bumps were due to hydrodynamic effects as reverberations. Examples of velocity and thermal emission profiles from a shot performed onto SiO_2 with pusher 1 (LULI shot 60) and a shot performed with pusher 2 (LULI shot 63), are represented in figure 2.24.

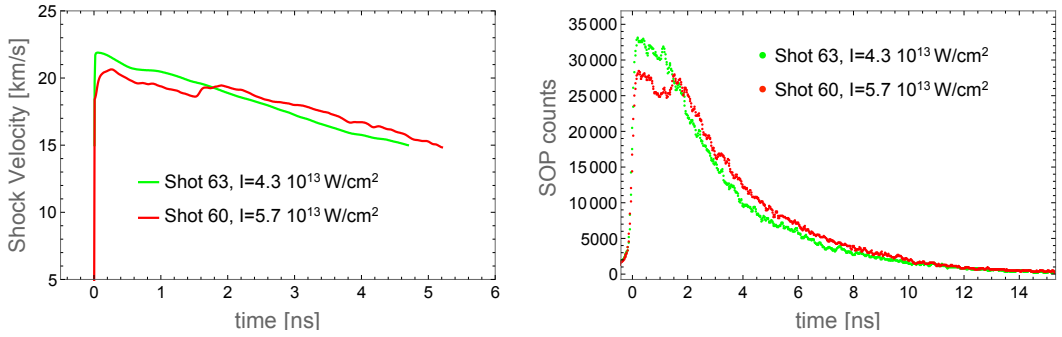

Figure 2.24: On the left, shock velocities profile for shot 60 (1.5 ns pulse of $5.7 \cdot 10^{13}$ W/cm^2) and 63 (1.5 ns pulse of $4.3 \cdot 10^{13}$ W/cm^2) obtained respectively with pusher 1 and pusher 2 on SiO_2 samples . Shot 60 exhibits a clear jump due to a reverberation since in quartz no transition is expected in the range of the measured velocities. Shot 63 indeed exhibits the typical behavior of a decaying shock propagation in a single phase. On the right, luminance profile for shot 60 and 63. As for the shock velocities, the luminance of shot 60 exhibits a clear jump due to a reverberation while shot 63 indeed exhibits the typical behavior of a decaying shock propagation in a single phase also for the thermal emission.

Conclusion The experimental tests performed on SiO_2 validated our hydrodynamic study on the pushers. We insist that a study of the hydrodynamic behaviour of the shocked sample is necessary in a decaying shock experiment. Indeed it allows to avoid misinterpretation of slope changes in the thermal emission or shock velocity profiles. Therefore for our experimental investigation we retained pusher 2 and 3 based on:

i) theory;
ii) hydrodynamic simulations;
iii) experimental test.

2.3 Results

2.3.1 General presentation and methods

Figure 2.25 shows examples of typical SOP and VISAR signals and their respective shock velocity Us, reflectivity R and thermal emission profiles for each studied material. The shown signals have been obtained with a 1.2 ns and 600 μm pulse of 726.7 J, a 1.2 and 600 μm pulse of 236 J and a 2.5ns and 600 μm pulse of 990J for MgO, Mg_2SiO_4 and $MgSiO_3$ respectively. VISAR shock velocity time profiles are represented by red lines, while the thermal emission time profile are represented by blue dots. The shock velocity profiles have been extracted from VISAR images using the NEUTRINO software developed by T. Vinci (LULI, Ecole Polytechnique).

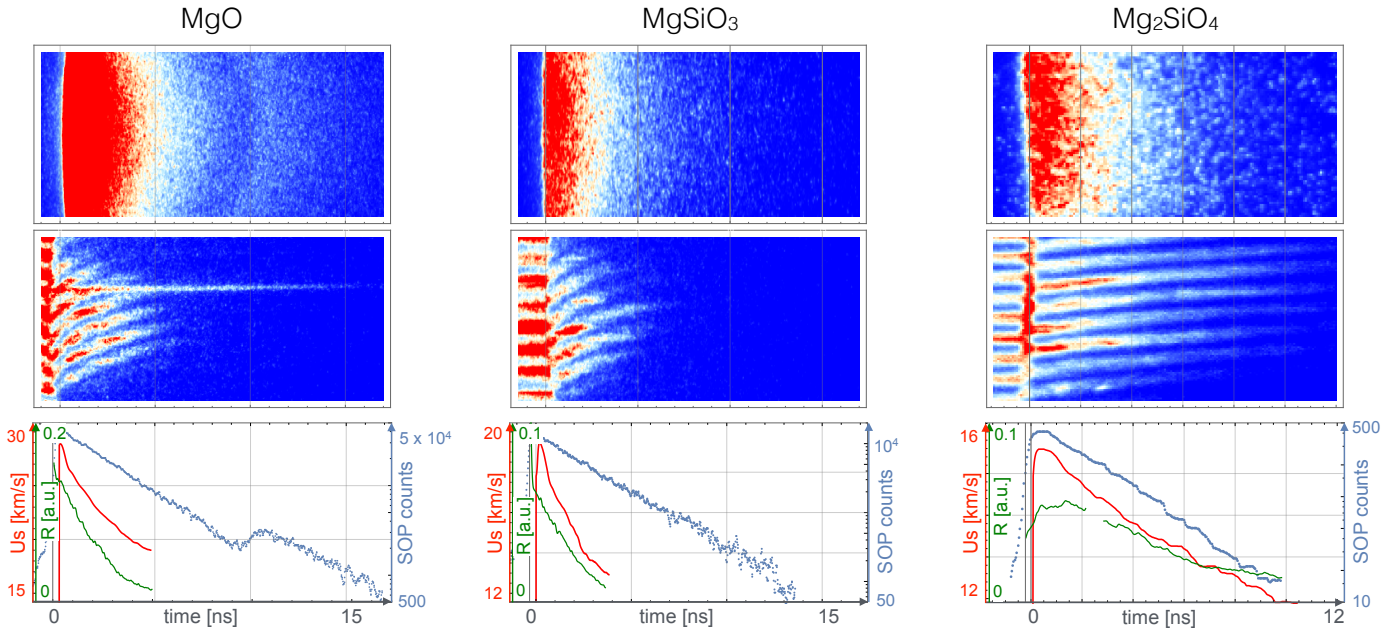

Figure 2.25: Typical SOP and VISAR signals are shown with thermal emission (blue dots), shock velocity U_s (red line) and reflectivity R (green dots) time profiles for each materials. The represented shots were performed with a 1.2 ns pulse with 726.7 J and 236 J for MgO and MgSiO3 respectively, and with a 2.5 ns pulse with 990 J Mg2SiO4.

The reflectivity $R(t)$ at the shock front is determined simply as $R(t) = R_r \times I_s(t)/I_r(t)$, where $I_s(t)$ and $I_r(t)$ are the intensities of the light reflected by the shocked

layer and by a reference surface of reflectivity R_r respectively. In our case, $I_r(t)$ was given by the reflection of the VISAR probe beam onto Fe, Al or Ti layers of the samples. We measured it with a VISAR streak camera acquisition of the signal reflected by the un-shocked target, as the magnesium oxide samples are transparent. We noticed that the Fe, Al and Ti R_r varies from tabulated values because of surface morphology. Hence we experimentally determine our R_r comparing them to a well known reflector (aluminium mirror). A fiducial system monitoring the laser energy as well as its temporal profile was used to correct for shot to shot fluctuations in the probe beam. In this way for Fe at $\omega = 532$ nm we get R_r =0.4 instead of the expected value 0.515, while for Al at $\omega = 532$ we obtain R_r =0.2 instead of 0.9. Al and Fe foils were provided by Goodfellow and we believe the reason of their low reflectivity is due to the production process that induces a strong morphological character to the foil surfaces. In order to determine the reflectivity at ω we considered the effect of the morphology to be the same at ω and 2ω. Therefore we calculated the reflectivity at ω simply considering that the ratio between the theoretical and the measured reflectivities is the same for both frequencies, obtaining $R_r(\omega)$= 0.47 and 0.21 for Fe and Al respectively. With these values of R_r we obtain the reflectivity data on SiO_2 shown in fig. 2.26 as an example. The reflectivity profiles are in agreement with data from literature [Hicks et al., 2006] thereby confirming the goodness of the R_r values we determined.
In the following we present the results obtained for each material.

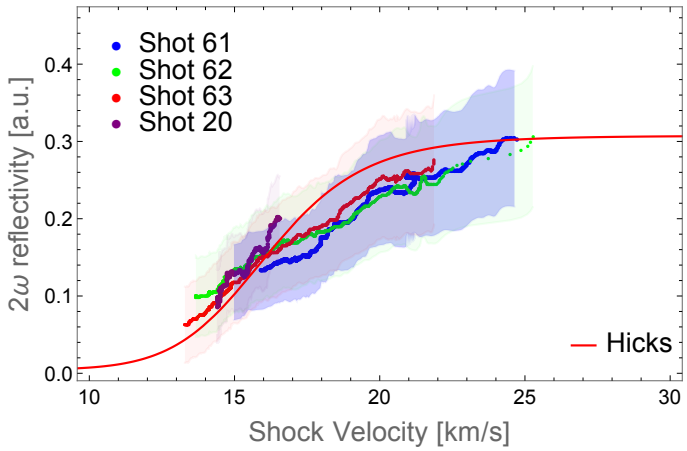

Figure 2.26: SiO_2 2ω reflectivity (coloured small dots) obtained at LULI in comparison with [Hicks et al., 2006] curve (red line).

2.3.2 MgO

2.3.2.1 SOP data

Typical MgO shock velocity (red curve), reflectivity (green curve) and thermal emission (blue curve) are shown in figure 2.25 on the left. While the shock velocity and reflectivity decay monotonically, the thermal emission profile exhibits a kink (at 11 ns for the shot shown in figure 2.25) which follows a monotonic decay without significant slope changes, as shown in figure 2.27.

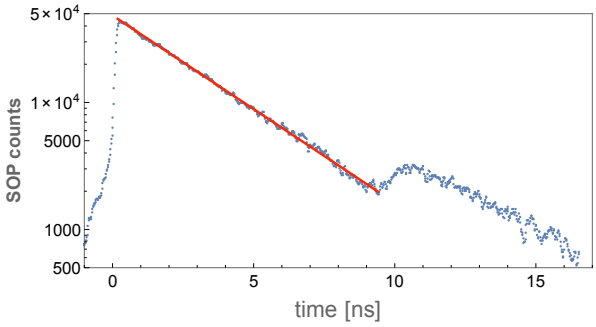

Figure 2.27: Example of a thermal emission time profile obtained at LULI for the MgO. This profile was obtained with a 1.2 ns laser pulse of 726.7 J and 600 μm

The kink has been observed for all shots as shown in figure 2.28. Thank to the study performed with hydrodynamic simulations and test shots on SiO_2, we can interpret such an abrupt variation in the thermal emission as a transition signature excluding that it is due to a reverberation.
Moreover, the curvatures of our thermal emission SOP data (see fig. 2.28) are typical of phase transition [Millot, 2016]. Let's explain this point. In a laser driven shock compression experiment, the ablation pressure is high and uniform only in the central region of the detected signal. On the contrary the edges of the SOP signals (related to the edges of the focal spot) corresponds to lower ablation pressures. This is because the edges of the focal spot only ideally represent a discontinuity, while in the real world they correspond to an intensity gradient which is clearly associated to an ablation pressure gradient. Therefore the shock velocity U_s is higher for higher pressure, i.e. in the center of the focal spot.In the same way, a possible reflected or secondary shock will be stronger and faster at the center. It follows that for a decaying shock, a phase transition occurs before at the edges than at the center, while a break out or a reverberation occurs before at the center than at the edges. These behaviours therefore translate into different SOP signal curvatures. Looking from the drive laser side the curvature is convex for a reverberation and concave for a phase transition. Therefore the observed curvatures support the interpretation of the observed kinks

as phase transition signatures.

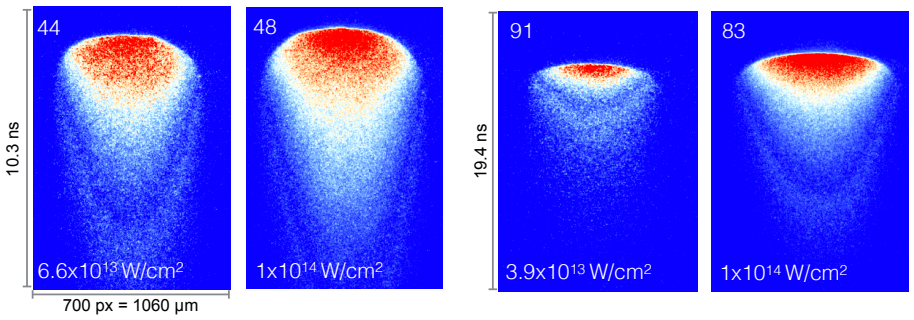

Figure 2.28: Thermal emission SOP signals obtained for four shots at LULI.

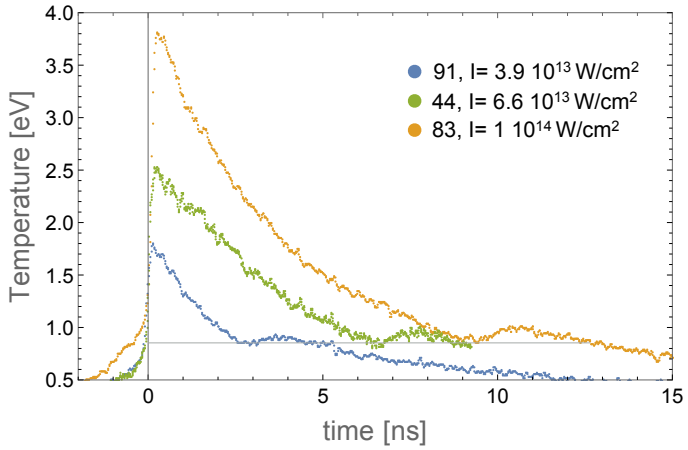

Figure 2.29: Temperature time profiles obtained for three shots showing the bump always at the same temperature.

Finally even with shocks generated with different laser pulses we observe the bump at the same thermal emission intensity, i.e. at the same temperature. This is shown in fig. 2.29 where we represent the temperature versus time obtained from the thermal emission signals of shots 91, 44 and 83 (performed respectively with a 1.2 ns laser pulse of 265 J, 448.6 J and 726.7 J and 600 μm focal spot on target type 2). Temperatures are obtained from the measured thermal emission and reflectivity using the curves presented in figure 2.11. The occurrence of the bump at the same temperature for different laser pulses excludes that the kink is produced by reverberating waves.

Indeed, in such a case, for different laser conditions, the bump would be expected to occur at different thermal emissions depending on the dynamic of the shock (velocity and decay rate). That is not the case and we can hence interpret the kink as a transition signature.
In conclusion, our thermal emission signals evidence the occurrence of a phase transition. This result is in partial agreement with [McWilliams et al., 2012], that observed two transition signatures on the thermal emission: a kink and a less pronounced but significant slope change occurring before the kink.

2.3.2.2 Evaluation of the thermodynamic conditions.

In order to interpret the nature of the transition it is necessary to obtain the thermodynamic conditions associated to the incident in the thermal emission (or temperature) decay. As we have already seen the temperature is obtained from the thermal emission and the reflectivity using the curves presented in fig. 2.11 in sec. 2.2.4. The pressure instead can be calculated from the shock velocity with an equation of state.

Shock velocity extrapolation The kink occurs in a nonreflecting regime where shock velocity cannot be measured (fringes disappear, see fig 2.25). Therefore, shock velocities to be associated with temperature in this regime are obtained using McWilliams et al. [2012] extrapolation method. In particular we fitted the velocity profiles with double exponential function that decays to the bulk sound speed[5]: $U_s(t) = 6.73 + A_1 Exp(-\alpha_1 t) + A_2 Exp(-\alpha_2 t.)$. A single or double exponential behaviour of the shock velocity has been observed for decaying shocks on various materials as diamond [Eggert et al., 2010], quartz [Hicks et al., 2006; Huser et al., 2015; Millot et al., 2015] , stishovite [Millot et al., 2015] and MgO [McWilliams et al., 2012]. Our extrapolation extends the $U_s(t)$ curve through the phase transition as the shock velocity decay usually does not exhibit significant changes at phase transitions with small volume changes. Examples of that are decaying shock studies of Diamond [Eggert et al., 2010] and SiO_2 [Hicks et al., 2006], where no changes in the decay rate through a phase transition have been observed. Moreover the extrapolation method has been considered valid for stishovite [Millot et al., 2015] and MgO [McWilliams et al., 2012]. Equation of state studies (Us-Up measurements) where no significant [McQueen et al., 1970] or very small [Root et al., 2015] changes at phase transitions have been observed further support the possibility of extending the extrapolation through phase boundary. We recall that Root et al. [2015] investigated MgO, the material studied here. Finally the accuracy of our extrapolation is confirmed by the

[5]The velocity decays toward the bulk sound speed as the more the shock strength decreases the more it approaches to the case of a small perturbation ($\Delta P/P0 << 1$, $\Delta\rho/\rho 0 << 1$, $\Delta u/c << 1$) propagating at the sound speed velocity (see sec 1.0.2.1)

fact that, as we will see in the following, it produces T-P curves which converges toward previous gas gun data [Svendsen and Ahrens, 1987]. The same conclusion is reached by [McWilliams et al., 2012].

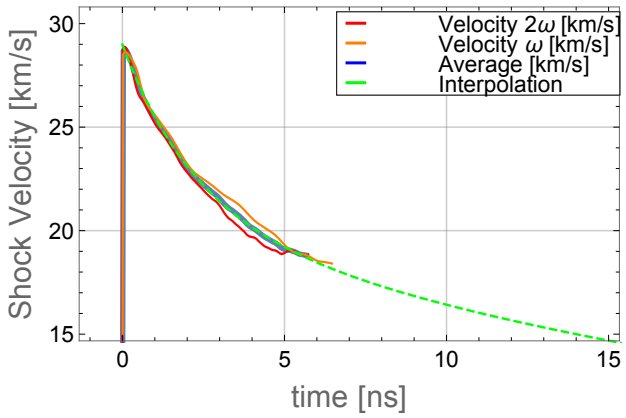

Figure 2.30: Temperature vs shock velocity curve obtained for shot 83 interpolated with a double exponential curve (green dashed line).

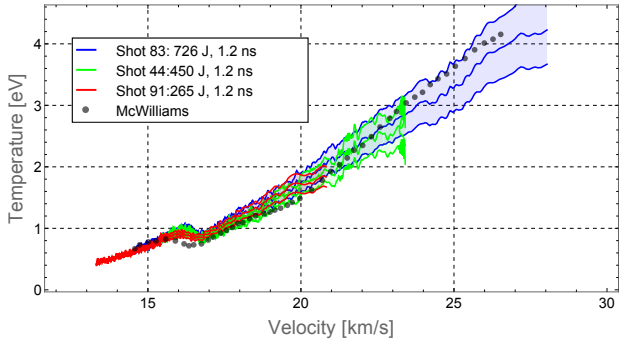

Figure 2.31: Pressure vs shock velocity curves obtained for shots 83 44 and 91 (coloured dots) in comparison with [McWilliams et al., 2012] (black dots).

Therefore this extrapolation performed with the double exponential function allowed to associate the shock velocity Us to the respective thermal emission and hence to the temperature T. We report in fig 2.31 some T-Us curves (coloured dots) explored by in comparison with a recent study [McWilliams et al., 2012] (black dots).

Equation of state: from Us to P In order to infer the pressure of our compressed samples we had to use an equation of state (EoS). To this aim we considered a recent experimental work: pressure values for MgO samples were obtained by interpolating the set of P-Us data reported in the supplementary material of [Root et al., 2015].

The interpolation is shown in fig. 2.32 in comparison with the Mie-Grüneisen-Debye equation-of-state model used by McWilliams et al. [2012]. The differences between the interpolation of the Root et al. [2015] data and McWilliams et al. [2012] in the liquid phase are small ($< 2.5\%$), while in the solid phase the measures of Root et al. [2015] do not exhibit significant changes as predicted by the model of McWilliams. For the liquid phase we verified that using these different P-Us relations the differences between the obtained P-T curves remain within the error bars 2.39.

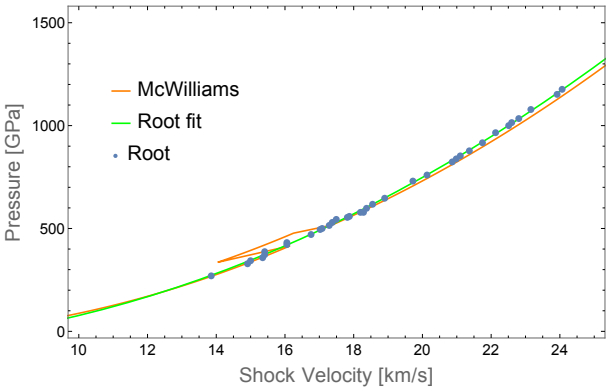

Figure 2.32: The interpolation of MgO P-Us data (blue dots) collected by [Root et al., 2015] is represented with a green line and is compared to the Mie-Grüneisen-Debye model reported by McWilliams et al. [2012] showing no significant differences

P-T curves In this way we finally obtained the thermodynamic conditions explored by our shocks. In particular the pressure - temperature curves (P-T curves) are represented in figure 2.33 in comparison with [McWilliams et al., 2012].

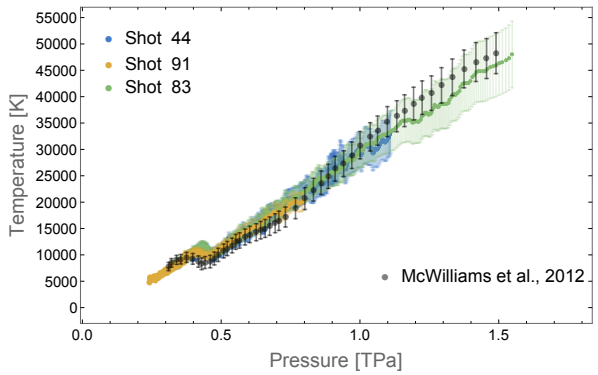

Figure 2.33: The experimental P-T curves measured along the Hugoniot at LULI (coloured dots) in comparison with McWilliams' et al [2012] results.

The P-T curves decays monotonically from the higher temperatures and pressures until 0.47 ± 0.04 TPa and 9860 ± 810 K (0.85 ± 0.07 eV), which hence represent the thermodynamic conditions where the shock crosses phase boundary/boundaries. Once again we point out that shocks generated with different laser pulses reproduce the bump at the same T-P conditions. We underline too that the bump is the only transition signature in our T-P curves, in contrast with [McWilliams et al., 2012] that observed two significant slope changes.

2.3.2.3 Interpretation of the phase transition nature

Recent calculations [Oganov et al., 2003; Wu et al., 2008; Cebulla and Redmer, 2014; Miyanishi et al., 2015; Root et al., 2015; Musella, 2016] agree on the prediction that the Hugoniot curve crosses melting and B1-B2 lines. In this context we interpret the bump as a signature of the melting of the B2 phase (see fig. 2.39). This interpretation is based on different arguments.
First, recent ab initio simulations predict an important discontinuity along the Hugoniot at the B2-melting boundary with a pressure change $\Delta P \sim 120$ GPa against, $\Delta P \sim 40$ GPa at the B1/B2 boundary [Miyanishi et al., 2015; Root et al., 2015]. As a shock can follow a thermodynamic path out of equilibrium (which is our case, as explained in the following point), we do not expect to reproduce exactly the ΔP calculated at the equilibrium but to have a more pronounced signature for melting than for the B1/B2 transition.

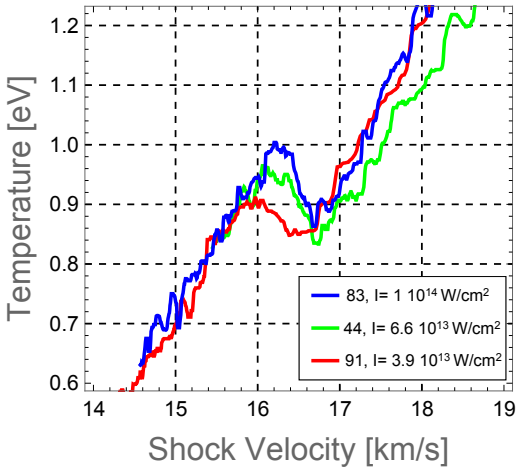

Figure 2.34: Zoom of the bump for the MgO P-T curves obtained with shot 83, shot 44 and shot 91 that have been performed with 1.2 ns laser pulse of 600 um diameter and energies of 726 J, 448 J and 265 J respectively. The bump varies for shots performed with different energies, suggesting that we are observing a non-equilibirum phenomenon.

Second, we observed that changing the laser intensity, and thus the decay dynamics (see fig. 2.35), the bump amplitude changed (fig. 2.34), supporting the idea of a non-equilibrium phenomenon. Moreover the shape of the bump is typical of superheating [Luo and Ahrens, 2004]. We underline that a decaying shock experiment is equivalent to a series of dynamic compressions of succeeding weaker shock strengths. This means that during the shock propagation different layers of the sample are compressed and heated from the same initial cold state. Features similar to the one we measured were attributed to superheating in previous laser and gas-gun experiments on alpha-quartz, stishovite and fused silica [Lyzenga et al., 1983; Hicks et al., 2006; Millot et al., 2015].

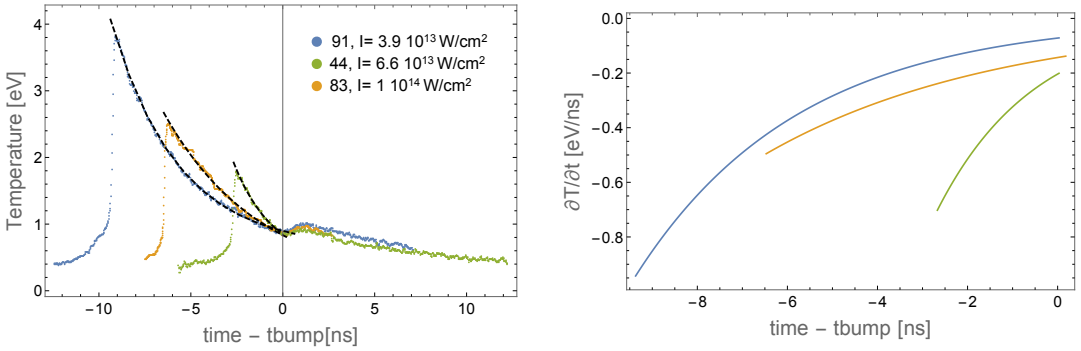

Figure 2.35: Left: temperature time profiles of shots 83, 44 and 91 versus time - t_{bump}, where t_{bump} is the bump time for each shot. The comparison evidenced that the temperature at the shock front decays differently for shots performed with different laser energies. Right: Derivative of the temperature over time.

Third, we investigated the possibility of detecting the B1/B2 transition. In general, SOP measurements of decaying shock are used to measure the thermal emission from a small volume behind the shock front. In general, this is the case when the shock is reflecting and the optical depth is negligible. On the contrary, if the optical depth is much larger, the thermal emission is also produced by an extended inhomogeneous region behind the shock, at off-Hugoniot conditions. Depending on the gradients behind the shock front, measurements will average over different thermodynamic states and smooth possible phase transition signatures. A scheme of the phenomenon is represented in fig. 2.36.

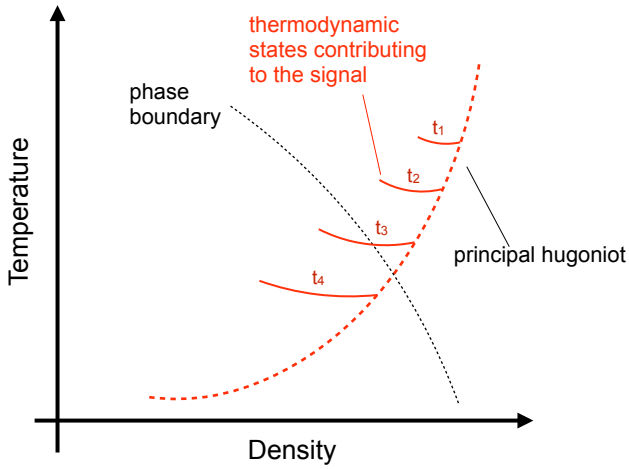

Figure 2.36: Scheme of the thermodynamic states contributing to an SOP signal for a decaying shock with non negligible optical depth.

To verify this third argument, we quantified pressure and temperature gradients with MULTI hydrodynamical simulations. On figure 2.37, we show the simulations performed on MgO with our experimental conditions. Pressure behind the shock varies fairly linearly with the sample initial position. In other words these simulations gives a pressure gradient fairly constant behind the shock front. For a numerical driven laser intensity of 3.5×10^{13}W/cm^2 we found for 600 GPa $\sim$ 7.5GPa/μm , for 470 GPa $\sim$ 5GPa/μm, for 325 GPa $\sim$ 3.2GPa/μm for 250 GPa $\sim$ 1.7GPa/μm. Instead for a laser intensity equal to 7.5×10^{13}W/cm^2 we obtained for 600 GPa $\sim$ 5.3GPa/μm and for 400 GPa $\sim$ 2.4GPa/μm. Concerning the temperature profiles, the temperature varies linearly only for a few tens of micrometers behind the shock front. Pressure and temperature gradients corresponding to the profiles of simulations reported in fig. 2.37 are shown in fig. 2.38.

To evaluate the optical depth, we performed some ab-initio calculations using the ab initio plane wave density functional theory (DFT) code ABINIT [Gonze et al., 2009]. We calculate the optical depth for the following conditions along the Hugoniot:

i) at 600 GPa, corresponding at the onset of reflectivity;

ii) at 470 GPa where our measurements detected the melting and the shock is opaque;

iii) at 325 GPa where ab initio calculations found in literature predict B1-B2 and where we did not detect any evidence of transition on P-T data.

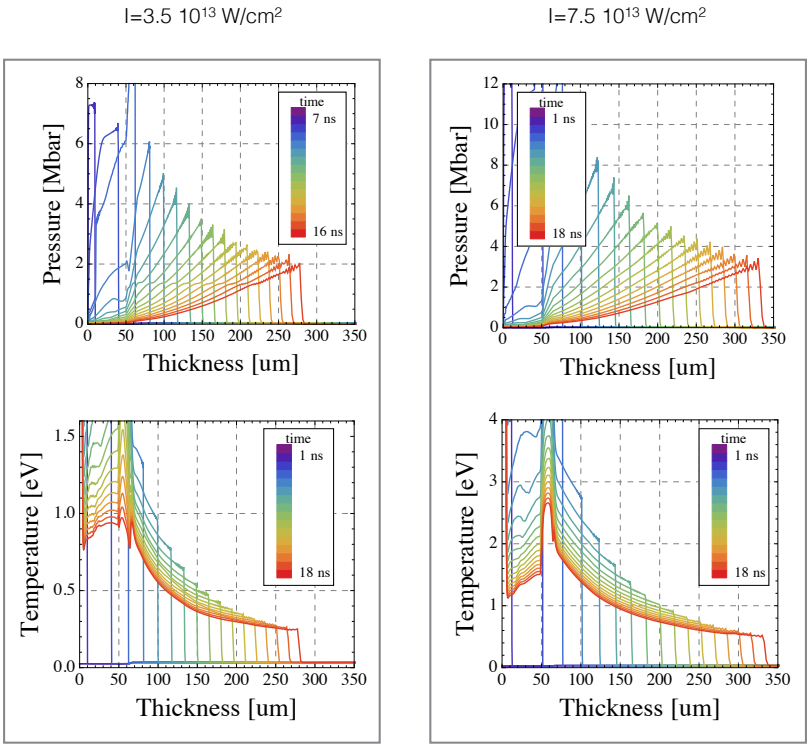

Figure 2.37: Pressure and temperature evolution in the 50μmCH — 15μmFe — 350μm MgO target calculated with hydrodynamics simulations for two different laser intensities. The equation of state used in simulation is QEOS. Since the shock is not sustained, pressure and temperature behind the shock do not have a uniform profile but increases and decreases respectively following the typical behavior related to the rarefaction wave.

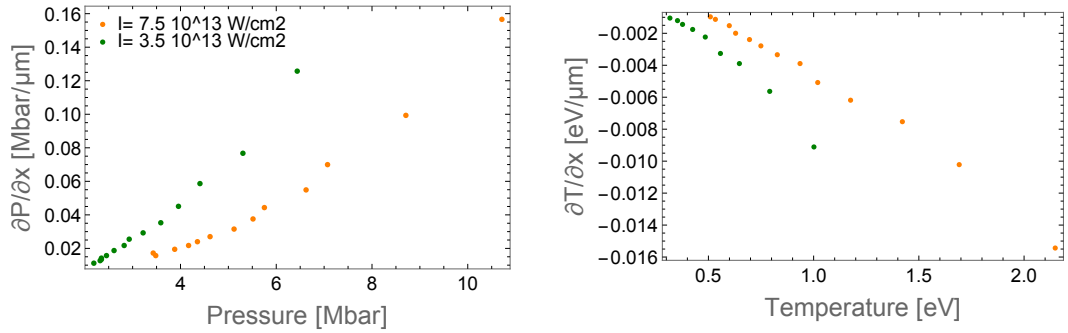

Figure 2.38: Pressure (left) and temperature (right) gradient behind the shock front.

For i) and ii) the optical depth is $\sim 0.5\mu$m and $\sim 1\mu$m respectively and the variation of pressure is negligible. For iii) it is significantly thicker, $\approx 10\mu$m. Using the gradients obtained with simulations shown in fig. 2.37, we obtained variations of pressure

and temperature of around 30 GPa and $\sim$ 110 K. Mainly because of the pressure variation, this means that the measured thermal emission comes from various states along the unloading adiabatic curve from different initial points on the Hugoniot and not from near shock-front. This implies that a possible phase transition signature will be smoothed and, since for the B1-B2 we do not expect a huge jump in the P-T conditions, we conclude that the decaying shock technique is not valid for measuring the B1-B2 phase transition in MgO. In addition the SOP noise is higher at lower T-P conditions. Hence the thermal emission data in these thermodynamic states are not suitable for a reliable phase transition detection along the Hugoniot.
Nevertheless, we still believe the data between 325 and 240 GPa to be representative of the P-T Hugoniot curve, considering the uncertainty of maximum 30 GPa and 100K given by the pressure variation in the probed volume. This reliability seems to be confirmed by the good agreement with previous theoretical [Svendsen and Ahrens, 1987; De Koker and Stixrude, 2009] and experimental works [Svendsen and Ahrens, 1987].

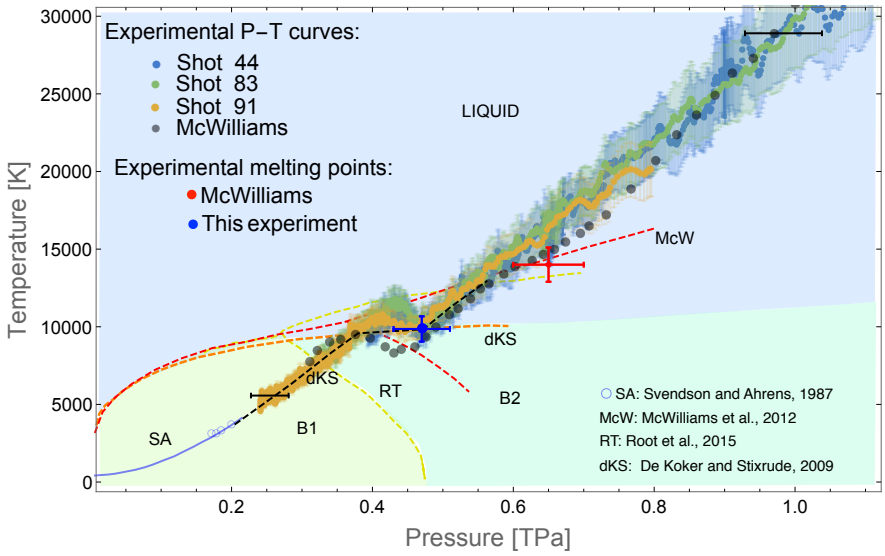

Figure 2.39: The experimental P-T curves measured along the Hugoniot at LULI (coloured dots) are represented in the MgO P-T diagram in comparison with previous experimental and theoretical P-T curves (black dots for [McWilliams et al., 2012]), and theoretical and experimental phase boundaries. Black horizontal bars represent the error on pressure.

To conclude this third point, we think that the detection of B1/B2 has been missed

mainly because of the small discontinuity predicted for this transition (according to theory). The smoothing effect mentioned above could have played an additional role. We therefore interpret the kink as superheated melting signature of the B2 phase. In the occurrence of superheating, the melting line is tangent to the minimum of the observed feature [Luo and Ahrens, 2004] and the melting point corresponds to the kink minimum. Nevertheless, a different scenario where the Hugoniot would cross liquid/B1 boundary, skipping the B2 phase, cannot be excluded. Direct structural investigations by using in-situ x-ray diffraction during the laser-driven compression experiments will be mandatory to resolve this issue.

Conclusions and implications Our measurements on MgO highlight a melting point at 0.47 ± 0.04 TPa and 9860 ± 810 K (0.85 ± 0.07 eV). This interpretation is partially in contrast with previous experimental results [McWilliams et al., 2012], where melting was determined at 0.65 ± 0.05 TPa and 14000 ± 1100 K along the Hugoniot, as inferred from a slope change in the P-T curve (pointed by the red cross in figure 2.39). Furthermore McWilliams et al. [2012] interpreted a feature at 0.44 ± 0.08 TPa and 9000 ± 700 K as a signature of the B1-B2 transition. However, while McWilliams et al. [2012] results are well fitted only by calculations by [Boates and Bonev, 2013], our interpretation is supported by the majority of the most recent ab initio calculations which predicts the melting line to pass through 0.47 TPa at ∼11750 K [Miyanishi et al., 2015; Root et al., 2015; Musella, 2016] and the B1-B2 coexistence line to lay ∼ 150 GPa lower [Oganov et al., 2003; Wu et al., 2008; Cebulla and Redmer, 2014; Miyanishi et al., 2015; Root et al., 2015] than McWilliams' et al. [2012] proposal.
Hence, our experimental melting point agrees with lower melting lines, e.g. [De Koker and Stixrude, 2009] than McWilliams et al. [2012] (see fig. 2.39) implying a lowering of super-Earths temperature profile [Stixrude, 2014; Gaidos et al., 2010]. Indeed recent models [Stixrude, 2014; Gaidos et al., 2010] assume the temperature at the core mantle boundary to be equal to the melting temperature of the mantle components. According to Stixrude this is justified by the fact that super-Earths at the end of their accretion process are likely to be completely molten. Then at the beginning of the cooling process, a super-Earth cools rapidly but when boundary layer temperature approaches the solidus the cooling loses efficiency and, thermally regulated by the boundary layer viscosity, the boundary layer temperature is kept nearly constant. This idea is illustrated in figure 2.40, that represents thermal profiles and core and mantle melting lines for planets with 1 and 10 Earth Masses. According to [Valencia et al., 2006], the core mantle boundary of a planet with 10 Earth Masses takes place at $\sim 1.4TPa$. Hence in order to determine planetary temperature profiles for super-Earths with masses up to 10 Earth Masses it is necessary to constrain mantle

component melting lines to extremely high pressure ($\sim 1.4TPa$).
Therefore in conclusion, the melting point highlighted by our measurements at 0.47 $\pm$ 0.04 TPa constitutes a precious constraint for the determination of melting lines and so of planetary temperature profiles.

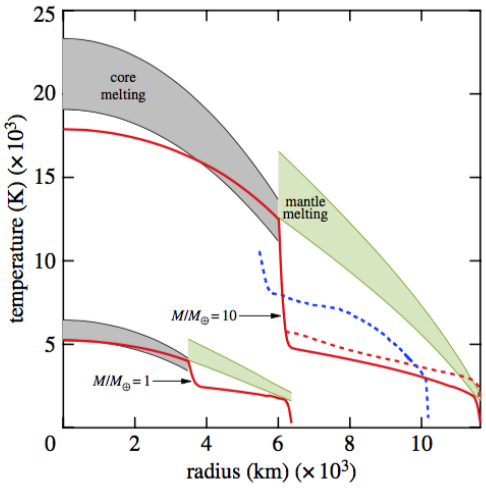

Figure 2.40: Temperature vs planet radius profiles for a 1 Earth mass and a 10 Earth masses planets proposed by [Stixrude, 2014]. Gray and green areas represent the core and mantle melting intervals respectively. Red dashed and blue dashed lines represents the thermal profiles obtained with dynamical simulations for a super-Earth of 8 Earth Masses by [Tackley et al., 2013] and [Van den Berg et al., 2010] respectively.

2.3.2.4 Reflectivity data

In this section we present the reflectivity data obtained with the VISAR interferometers. As we run VISARs at two different wavelengths, we determined the shocked MgO reflectivity at both $\lambda = 0.532\mu m$ and $\lambda = 1.064\mu m$. Fig. 2.41 represents the shocked MgO reflectivities (blue and orange lines) as a function of the pressure in comparison with literature data [McWilliams et al., 2012] (red dots). The two curves results from the average of the reflectivity profiles of the performed shots.

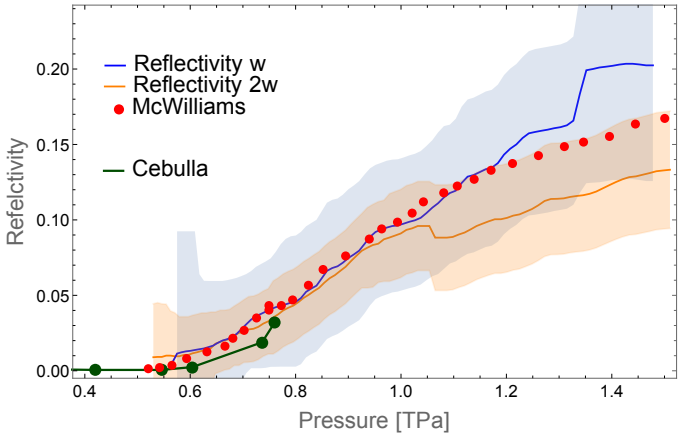

Figure 2.41: MgO reflectivity lines at 532 nm (orange) and at 1064 nm (blue), in comparison with previous experimental results (red dots) [McWilliams et al., 2012] and calculations (green dots) [Cebulla and Redmer, 2014].

As shown in figure 2.41, reflectivities start to smoothly increase at $\sim$ 0.55 TPa, i.e. at higher pressures than the measured melting point (at 0.47 TPa and 9860 K). This would suggest that melting is not directly associated with metallisation. We also observe that between 0.55 and 1 TPa, the reflectivity at 532 nm (R(2ω)) is similar to the reflectivity at 1064 nm (R(ω)), while for pressures higher than 1 TPa R(ω) $>$ R(2ω), saturating at $\sim$ 20% and $\sim$13% respectively. This behaviour suggests a transition between a semiconductor to a metal. In order to calculate the conductivity we applied two different models according to the pressure regime.

At 1.4 TPa (where reflectivities suggest a metallic behaviour), taking advantage from our 2 wavelength reflectivity measurements, we applied a Drude simple metal model [Goettel et al., 1989], while at lower pressures we applied a Drude-semiconductor model [Hicks et al., 2006; McWilliams et al., 2012; Millot et al., 2015].

Simple metallic Drude model Applying a simple metallic Drude mode [Goettel et al., 1989; Eggert et al., 2010] it is possible to obtain the reflectivity R as a function of the frequency ω and the conductivity σ. The Drude model classically treats the problem of the behaviour of electrons in solids [Jackson, 2007]. The motion of an electron driven by an electric field E(x,t) and bumped by the interaction with the ions is described by the following equation of the dynamics:

$$m[\ddot{x} + \dot{x}/\tau] = -eE(x,t) \tag{2.4}$$

where τ is the relaxation time. Considering the electric field varying $Exp[-i\omega t]$ it follows [Jackson, 2007] that the dielectric constant depends on the frequency ω as

$$\frac{\epsilon(\omega)}{\epsilon_0} = \epsilon_b - \frac{\omega_p^2\tau^2}{1+\omega^2\tau^2} + \frac{i\omega_p^2\tau}{\omega(1+\omega^2\tau^2)} \tag{2.5}$$

where ϵ_b is the bound electron contribution and the other two terms express the contribution of free electrons. The real ϵ_r and imaginary ϵ_i part of the complex dielectric function $\epsilon(\omega)$ can be expressed as a function of the real part n and imaginary part k of the refraction index $N = n + ik$ as it follows:

$$\epsilon_r = n^2 - k^2 \qquad \epsilon_i = 2nk \tag{2.6}$$

Finally the reflectivity R is described as

$$R(\omega) = \frac{|N(\omega) - n_0|^2}{|N(\omega) + n_0|^2} \tag{2.7}$$

where n_0 is the refraction index of the uncompressed MgO.
Hence we fit our data at 1.4 Tpa having as free parameters ϵ_b, the plasma frequency $\omega_p = \sqrt{n_e e^2/m\epsilon_0}$ (where n_e is the electron density and m the effective mass) and the relaxation time τ, that according to the Drude model [Jackson, 2007] are linked to the conductivity $\sigma_0 = \omega_p^2\tau\epsilon_0$.

Figure 2.42 represents the interpolation of the reflectivity data at 1.4 TPa. To fit the data the best fit parameters are $\epsilon_b = 1.44$ $\omega_p = 3.39 \cdot 10^{16} rad/s$ (corresponding to n_e=3.6 $\cdot 10^{29}$ 1/m^3) , $\tau = 1.3 \cdot 10^{-17} s$ which implies a conductivity $\sigma = 1.3 \cdot 10^5 S/m$ (see fig. 2.42 continuous line). However we found that the interpolation is good also for $\epsilon_b = 2.3$ $\omega_p = 9.13 \cdot 10^{15} rad/s$ (corresponding to n_e=2.6 $\cdot 10^{28}$ 1/m^3) and $\tau = 1.58 \cdot 10^{-16} s$ which gives a conductivity $\sigma = 1.2 \cdot 10^5 S/m$ (see fig. 2.42 dashed line).

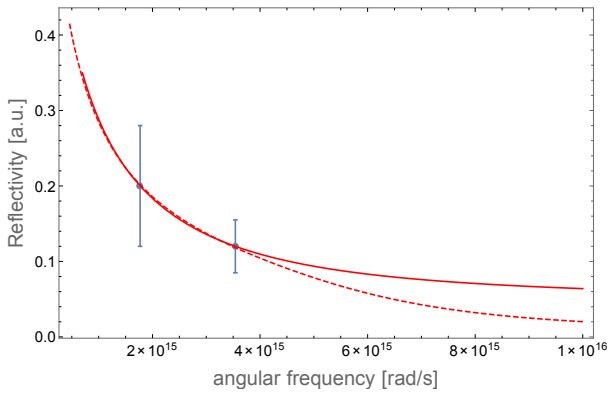

Figure 2.42: Reflectivities at 1.4 TPa interpolated by a classical Drude model. Continuos line is obtained with $\epsilon_b = 1.44$, $\omega_p = 3.39 \cdot 10^{16} rad/s$ and $\tau = 1.3 \cdot 10^{-17} s$, while the dashed line is obtained with $\epsilon_b = 2.3$, $\omega_p = 9.13 \cdot 10^{15} rad/s$ and $\tau = 1.58 \cdot 10^{-16} s$.

Drude-semiconductor model [McWilliams et al., 2012]] As [McWilliams et al., 2012]] we interpolate our reflectivity and inferred the respective conductivity using a Drude-semiconductor model [Hicks et al., 2006]. For the Drude model the refractive index can be written as

$$n = \sqrt{\epsilon_b + 4\pi i\sigma(\omega)/\omega} \tag{2.8}$$

where the conductivity $\sigma(\omega)$ is

$$\sigma(\omega) = (2n_e e^2\tau/m_{eff})/(1 - i\omega t) \tag{2.9}$$

where n_e is the carrier density, τ is the carrier relaxation time and m_{eff} is the carrier effective mass. In the Drude-semiconductor model the carrier density is assumed to depend on the temperature as for a semiconductor [Kittel, 2005]:

$$n_e = 2(m_{eff}k_bT/2\pi\hbar^2)^{3/2} f_{1/2}[-E_g/(2k_bT)] \tag{2.10}$$

where $f_{1/2}$ is the Fermi-Dirac integral[6] and E_g is the energy gap between the valence and conduction band [Kittel, 2005]. We assumed that scattering occurs at the Ioffe-Regel limit, i.e. that the scattering time τ is given by the ratio l/v_e between the interatomic distance $l = 2(3MV/4\pi N_A N_F)$ and the carrier velocity v_e (M, V N_A and N_F being the molar mass, the volume, the Avogadro number and the number of atoms in a formula unit respectively). The carrier velocity is given by :

$$v_e = \sqrt{(2k_bT/m_{eff})(f_{3/2}[-E_g/(2k_bT)]/f_{1/2}[-E_g/(2k_bT)])} \tag{2.11}$$

where $f_{1/2}$ and $f_{3/2}$ are again Fermi-Dirac integrals[7]. As before the reflectivity is given by the Fresnel formula 2.7.
The Fresnel formula is hence used to interpolate the measured reflectivities having ϵ_b, E_g and m_{eff} as unknown parameters. E_g was supposed to depend on the pressure with a sigmoidal function. Here the initial band gap value has been considered as a free parameter as in [McWilliams et al., 2012].

[6] $f_m(x) = 2/\sqrt{\pi}\int_0^\infty y^m/(1+e^{y-x})dy$

[7] Derivation of the carrier velocity expression: the carrier velocity is obtained from the average kinetic energy <E> that is defined as

$$< E >= \frac{\int_0^\infty g(E)f(E)EdE}{\int_0^\infty g(E)f(E)dE} \tag{2.12}$$

where f(E)= $1/(Exp(E/kT)+1)$ is the Fermi distribution and g(E)= $(8\sqrt{2}\pi m^{3/2}/h^3)\sqrt{E}$ represents the density of states of the conduction band. By substituting the expression of g(E) and f(E) in the integral one can show that eq. 2.12 is equivalent to $k_bT(f_{3/2}[-E_g/(2k_bT)]/f_{1/2}[-E_g/(2k_bT)])$.

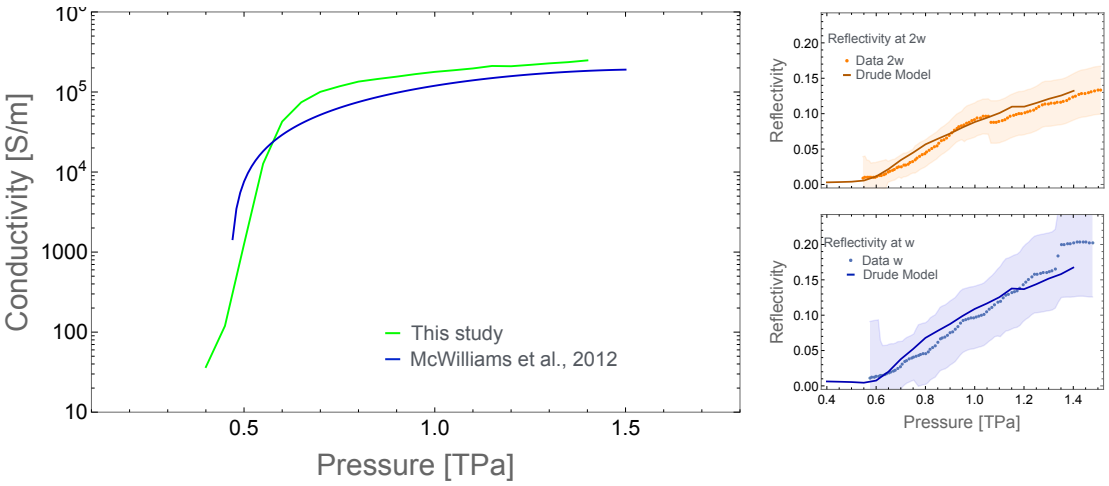

Figure 2.43: Left: Conductivity obtained with a Drude-semiconductor model in comparison with the conductivity obtained by [McWilliams et al., 2012]. Right: The graphs on the right show our data interpolated by the Drude-semiconductor model

Considering the initial band gap as a free parameter, the model predicts that a reflectivity of around 1% at around 0.55 TPa corresponds to a conductivity $\sim 10^4$ S/m. For pressure $P < 0.55$ TPa the conductivity is $< 10^4 S/m$. Hence our reflectivity data in the MgO liquid phase between 0.47 and ∼0.55 TPa corresponds to an electrical conductivity $< 10^4$ S/m and $\sim 10^2$ S/m at melting (0.47 TPa) using our conductivity calculations. These results are confirmed by more sophisticated ab initio calculations, which predict $\sim 7 \cdot 10^4 S/m$ for a 2 % reflectivity [Musella, private communication]. However conductivity values obtained with the Drude semiconductor model at low pressures <0.55 TPa depend on the extrapolation method. Indeed if we interpolate the reflectivity fixing the MgO band gap at its value (8eV) for pressure ∼0.47 TPa we obtain a conductivity $\sim 10^3$ S/m. Instead for pressures higher than 0.6 TPa the two interpolation methods do not produce significant difference in the conductivity profiles. At 1.4 TPa the model predicts a carrier density $n_e = 3.5 \cdot 10^{28}$ $1/m^3$ and a DC conductivity $\sigma_0 \sim 2\ 10^5$ S/m. We recall that with the simple metal Drude model at 1.4 TPa we found values in between $n_e = 3.6 \cdot 10^{29}$ $1/m^3$ and $2.6 \cdot 10^{28}$ $1/m^3$ and a DC conductivity σ_0 around 1.2-1.3 10^5 S/m.

Implications: electrical conductivity and geodynamo models The electrical conductivity is of particular importance for its link with the dynamo models for the generation of planetary magnetic field. Such models rely on the idea of hydromagnetic dynamo: an electrically conducting fluid moves across magnetic field lines and sustains the field via electromagnetic inductions. This situation is described by

Maxwell equations and the Ampere's law (neglecting the displacement current)

$$\nabla \times \vec{E} = -\frac{\partial \vec{B}}{\partial t} \tag{2.13}$$

$$\nabla \times \vec{B} = \mu_0 J \tag{2.14}$$

$$J = \sigma(E + \vec{v} \times \vec{B}) \tag{2.15}$$

By applying the curl to the Ampere's law and solving the system with the other two equations one can easily get the induction equation for the magnetic field:

$$\frac{\partial \vec{B}}{\partial t} = \eta \nabla^2 \vec{B} + \nabla \times (\vec{v} \times \vec{B}) \tag{2.16}$$

where $\eta = 1/\mu_0\sigma$ is the magnetic diffusivity (and σ the electrical conductivity). If the conducting fluid is at rest the induction equations becomes $\frac{\partial \vec{B}}{\partial t} = \eta \nabla^2 \vec{B}$, thus meaning that the electromagnetic field decay to zero in $\tau = L^2/(\pi^2\eta)$ (free decay time). L is the size of the magnetic field or equivanlty of the electrically conducting region. Instead considering the case of a moving conducting fluid, the magnetic Reynolds number, defined as $R_m = \nu L/\eta$ (where ν is the characteristic fluid velocity), is the parameter that gives the importance of the effect due to the fluid motion. Stevenson [2003] considered $R_m > 10$ - 100 sufficient for a moving electrically conducting fluid to sustain a magnetic field. Similarly [Gaidos et al., 2010] proposed $R_m > 40$.

Let's assume valid this criterion and let's consider the case of a terrestrial planet. Characteristic fluid velocities ν of a terrestrial magma ocean range typically between 4 and 40 m/s [Solomatov, 2000], while the size L of a terrestrial mantles is about 10^6 - 10^7 m. Then in order to satisfy $R_m > 10$ - 100 conductivities of few S/m are sufficient and therefore contributes to the magnetic field generation.
However $R_m > 10$ - 100 is not the only criterion proposed up to now. More specific studies considering the role of a long-lived basal magma ocean in the generation of the Earth's magnetic fields [Ziegler and Stegman, 2013], proposed D> 100 for the dynamo to be activated, where the Dynamo number D is equal to $(R_{m\,core} \cdot R_{m\,bmo})^{1/2}$. $R_{m\,core}$ and $R_{m\,bmo}$ are the magnetic Reynolds number of the core and of the basal magma ocean respectively. For a $R_{m\,core}$= 3500 (as $\nu_{core} = 5 \cdot 10^{-}4$ m/s [Holme and Olson, 2007] , σ_{core}= 1.5 $\cdot 10^6$ S/m [Pozzo et al., 2012] and L_{core}=3.5 $\cdot 10^6$ m) Ziegler and Stegman [2013] obtained a dynamo operating (D> 100) for 2 Gyr for σ = 1000 S/m and σ = 10000 S/m. A value of σ = 100 S/m was not sufficient for reaching D> 100.

In this context the values of DC conductivity σ_0 of liquid MgO that we found along the Hugoniot starting from 0.47 TPa and $\sim$ 10000K has temperatures probably to

large to be applied to an Earth-type planet. However, under the assumption that liquid MgO can occur in a planet, such conditions could be relevant to magma oceans of Super-Earths. According to our conductivity curve, MgO in magma oceans with pressures between 0.5-0.7 TPa and temperatures between 10000-15000K would significantly contribute to a dynamo process. Indeed in such case the conductivity σ varies between 10^3 to 10^5 S/m and it is much higher than the one expected in an Earth-like planet mantle (10^{-2} to 10^2 S/m). Nevertheless, at pressure lower than 0.5 TPa, i.e. very close to the melting line, the conductivity of MgO lowers quickly approaching values $<10^2$ S/m for which the contribution to the magnetic field generation would not be as significant. However as we have shown, the conductivity values obtained with the Drude semiconductor model at low pressure strongly depend on the reflectivity interpolation methods (on the choice of free parameters in particular). This results in an uncertainty of an order of magnitude over the conductivity predicted by the Drude model at conditions close to melting along the Hugoniot. Therefore we believe that such model can be used to obtain nothing more than a general picture of the conductivity behaviour. Moreover conductivity of liquid MgO has a limited geophysical relevancy. Indeed it is more likely to have liquids close to $MgSiO_3$ or Mg_2SiO_4 compositions in an Earth or Super-Earth magma ocean than liquid MgO. We will present in the following sections also the conductivity behaviour along the Hugoniot of $MgSiO_3$ or Mg_2SiO_4.
However MgO remains a good test material to be investigated, as it is simpler than $MgSiO_3$ or Mg_2SiO_4 to be studied with ab initio calculations. Therefore observations in MgO can be more easily theoretically verified. For example a question rising from this study is whether a region of low electrically conducting liquid MgO occurs at all pressures just above the melting line or if it is specific of the conditions along the Hugoniot explored in this study. In one of the next chapters, we will present an experimental XANES investigation of shocked MgO combined with an ab initio molecular dynamics study (AIMD). Such study will allow to investigate conductivity over a wide range of thermodynamic conditions. Unfortunately at the moment of the writing, calculation of electrical conductivity values are still ongoing.

2.3.3 $MgSiO_3$ glass

2.3.3.1 VISAR and SOP data

Fig. 2.25 and fig. 2.44 show typical SOP and VISAR data obtained on shocked $MgSiO_3$. Shock velocity and thermal emission profiles obtained from the data of fig 2.44 are represented in fig. 2.45. Our data stressed out that shock velocities decay monotonically between 18 km/s and $\sim$ 12 km/s. This is in contrast to a recent decaying shock experiment on $MgSiO_3$ glass where a shock velocity jump of 0.6 km/s was detected at around 16 km/s [Spaulding et al., 2012]. Such a jump has been considered as a signature of a liquid-liquid phase transition. Our data do not confirm the occurrence of this transition.

SOP data confirm the behaviour stressed by shock velocities. The SOP data exhibit two features due to defects of the SOP streak camera. These defects are the reason of the incidents that take place at $\sim$ 10 ns in the thermal emission profiles that therefore are not signatures of phase transition. Hence, apart from these incidents, thermal emissions decrease exponentially without exhibiting significant change of slope (see fig. 2.45). Again this is in contrast with [Spaulding et al., 2012], that observed a bump in the thermal emission associated to the velocity jump. In conclusion, at a first sight our VISAR and SOP data suggests that the shock propagates in a material without any distinct phase transition and do not confirm the occurrence of the liquid-liquid phase transition.

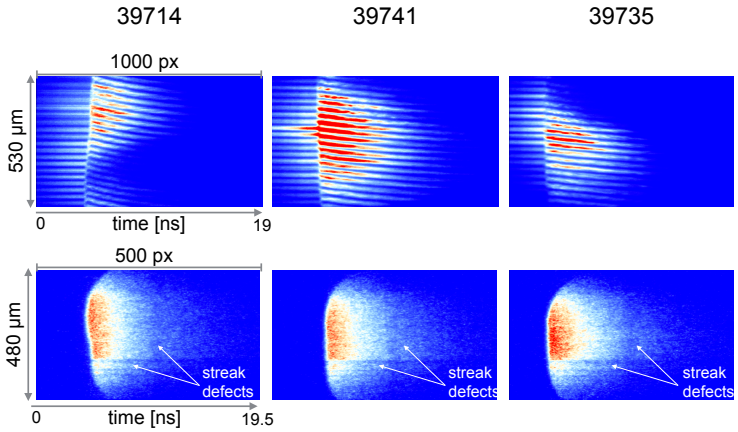

Figure 2.44: Typical VISAR and SOP signals obtained for the $MgSiO_3$.

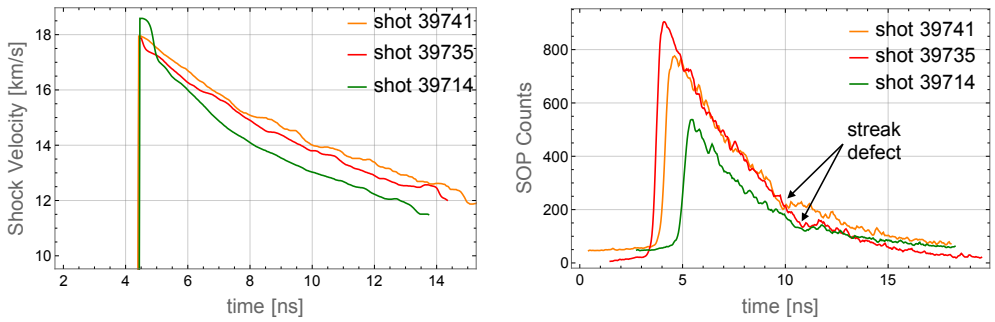

Figure 2.45: Shock velocity profiles and sop thermal emission.

2.3.3.2 Evaluation of the thermodynamic conditions

As for the MgO, in order to infer information on the $MgSiO_3$ phase diagram it is necessary to obtain the thermodynamic conditions explored by our shocks. Temperatures were obtained from the thermal emission and the reflectivity data using the curves presented in figure 2.11 and 2.15 for data collected at LULI and at GEKKO respectively. Pressure P instead have been obtained from shock velocity U_s using an equation of state.

Equation of state: from Us to P We obtain our P(Us) function from an interpolation of the Us-Up and P-Up literature data reported in [Spaulding et al., 2012] [8]. Since our thermal emission and shock velocity profiles do not present any signature of phase transitions, we performed the fit using a single function (a straight line for Up-Us and a parabola for P-Up). The interpolations of Up-Us and P-Up data are reported in Fig. 2.46 in comparison with QEOS model [More et al., 1988]. We verified that both the P-T curves calculated with interpolations and with QEOS lay inside the error bars of figure 2.47.

P-T curves explored by our shocks In this way we finally obtained the thermodynamic conditions explored by our shocks. $MgSiO_3$ glass P-T curves along the Hugoniot obtained at LULI and at GEKKO are shown in figure 2.47. The P-T curves decays monotonically from around 0.5 TPa- 20000 K in the liquid phase to 0.12 TPa -6300 K. We underline that the curves we obtained at GEKKO and at LULI, i.e. on two different facilities, are in good agreement each other and partially in agreement

[8] More specifically high pressure data were determined by Spaulding et al. [2012], low pressure data (< 200 GPa) are from [Mosenfelder et al., 2009; Akins et al., 2004; Luo et al., 2004].

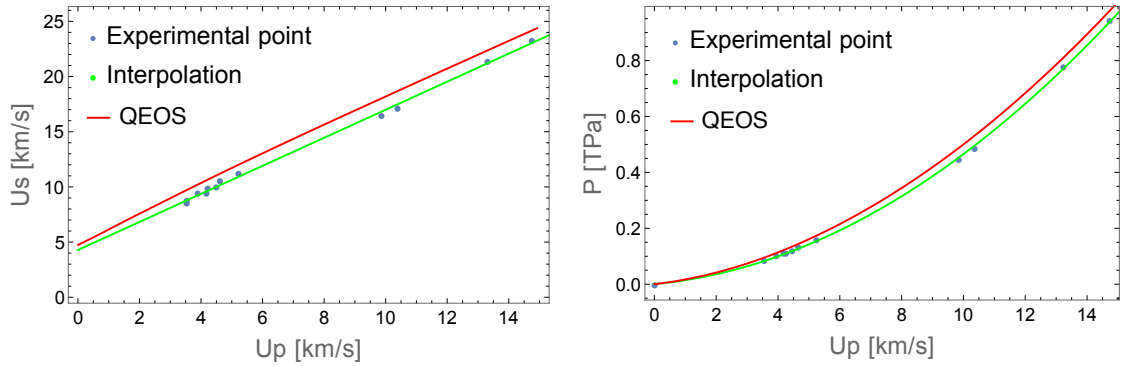

Figure 2.46: On the left, interpolation of $MgSiO_3$ Us-Up data reported in the supplementary material of [Spaulding et al., 2012] in comparison with the QEOS model [More et al., 1988]. On the right, interpolation of $MgSiO_3$ P-Up data reported in the supplementary material of [Spaulding et al., 2012] in comparison with the QEOS model [More et al., 1988]. Both the P-T curves calculated with interpolations and with QEOS lay inside the error bars of figure 3a.

with [Spaulding et al., 2012]. The reflectivity has been observed to increase above 0.16 TPa as pointed by the arrow in figure 2.47.

2.3.3.3 Interpretation

Our shocks start propagating in the melt region of the phase diagram [Shen and Lazor, 1995; Belonoshko et al., 2005; De Koker and Stixrude, 2009]. Hence our data suggest that the shocks propagated through one single liquid phase. This interpretation is strengthen by some considerations. First, we expect that in our targets no hydrodynamic effects could have affected shock decays. Moreover our results have been reproduced at two different facilities (LULI2000 and GEKKO). Furthermore below 0.4 TPa our Hugoniot data are in agreement with Spaulding et al. [2012]. The only disagreement concerns the feature at 0.4 TPa that has been proposed as a liquid-liquid phase transition by Spaulding et al. [2012]. However we remark that liquid-liquid transitions are rare (occurring e.g. in liquid phosphorous [Katayama et al., 2000]), and that for $MgSiO_3$ this phase transitions has not been reproduced by molecular dynamics calculations [Militzer, 2013]. Our data do not confirm neither the occurrence of dissociation, predicted, with different phase boundaries, by Boates and Bonev [2013] and [Umemoto et al., 2006]. Furthermore our P-T curve is consistent with low pressure steady shock data [Luo et al., 2004].
Our dataset does not rule out gradual changes in Si coordination number by oxy-

gen under extreme pressure or other structural transitions in the liquid state, but it implies that their possible effects on decaying shock would be too weak to produce distinct features in the data. The absence of transition signature until the detection limit suggests to set an upper limit for melting at 6300 ± 690 K at 0.12 TPa, that unfortunately does not allow to discriminate between the melting lines calculated by Belonoshko et al. [2005] and De Koker and Stixrude [2009].

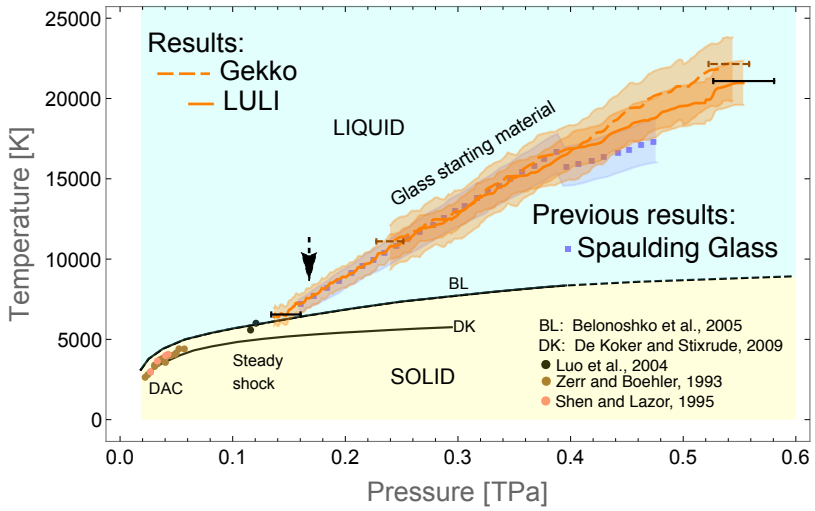

Figure 2.47: The experimental $MgSiO_3$ glass P-T curves measured along the Hugoniots at LULI (orange full line) and at Gekko (dotted orange line) are represented in $MgSiO_3$ phase diagram in comparison with previous experimental results (blue disk and square) [Spaulding et al., 2012]. Black lines represent theoretical melting lines.

2.3.3.4 Reflectivity data

Reflectivity data at λ=0.532μm of shocked $MgSiO_3$ glass are shown in fig. 2.48 in comparison with [Spaulding et al., 2012]. Reflectivity starts to increase at around 0.16 GPa and reaching a plateau at around 0.5 TPa. Our data confirm the behaviour observed by [Spaulding et al., 2012], although our reflectivity profiles along the Hugoniot are a bit lower than Spaulding's et al [2012] ones.

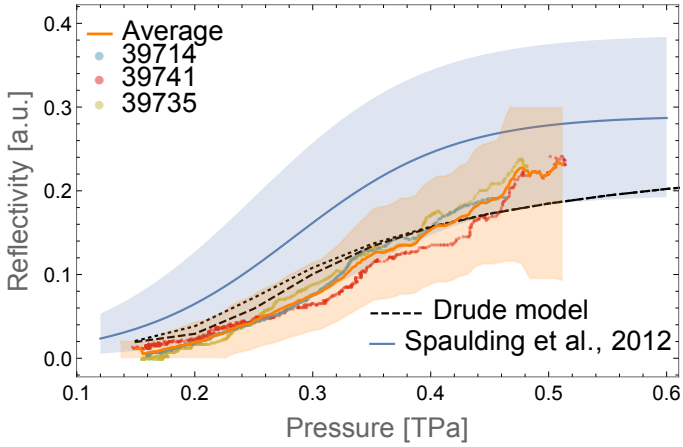

Figure 2.48: Reflectivity of $MgSiO_3$ glass along the Hugoniot in comparison with [Spaulding et al., 2012] (blue line). Black lines are the reflectivity profiles obtained with the Drude semiconductor model considering the initial band gap as a free parameter (dashed) and as equal to 9 eV [Umemoto et al., 2006] (dotted).

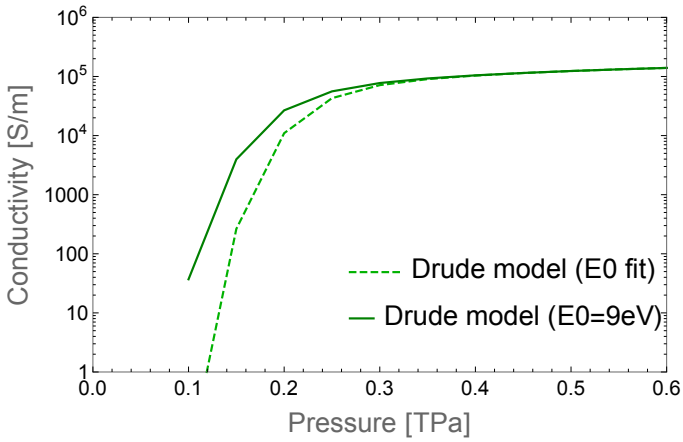

Figure 2.49: Conductivity of $MgSiO_3$ glass along the Hugoniot obtained with the Drude semiconductor model considering the initial band gap as a free parameter (dashed) and as equal to 9 eV Umemoto et al., science, 2006] (dotted).

Again as for MgO our data suggest that melting and reflectivity increase are not coincident, thus pointing at the presence of a poorly conducting liquid also in the $MgSiO_3$ phase diagram.
As for the MgO we interpolate our reflectivity with a Drude semiconductor model (dotted and dashed lines in fig. 2.48). The dotted line has been obtained with an initial band gap fixed and equal to 9eV, while the dashed line has been obtained having the initial band gap as a free parameter. The reflectivity profile represented by the dashed line better interpolates the data.

Fig. 2.49 represents the conductivity values occurring along the Hugoniot versus the pressure. Such conductivity curves correspond to the reflectivity profiles calculated with the Drude semiconductor model and represented in fig. 2.48. At conditions close to the melting line (0.12 TPa) both the conductivity profiles report values <100 S/m, though they present significant differences. Indeed the value obtained interpolating the reflectivity with the initial band gap as free parameter is significantly smaller < 10 S/m than the one obtained with E_0=9eV . For higher pressures the two curves approaches reaching a plateau of $\sim 10^5$ S/m.

2.3.3.5 Implications

Our data ruled out the occurrence of the liquid-liquid phase transition in the $MgSiO_3$ phase diagram between 0.15 and 0.55 TPa. The absence of such a transformation has important implications as pointed out in [Spaulding et al., 2012] it has been proposed to induce a geochemical differentiation in terrestrial planets. Indeed as the two liquids would have different densities, the other elements occurring in the mantle or in the magma ocean of the terrestrial planet would sink differently in the two liquids promoting a chemical differentiation in large planetary regions.
Moreover, though our data cannot completely exclude the occurrence of dissociation, they suggest a scenario where liquid $MgSiO_3$ is stable between 0.15 and 0.5 TPa. In such case for magma ocean at pressures higher than 150 GPa and temperatures over 5000 K the occurrence of separated MgO or SiO_2 cannot be attributed to dissociation of liquid $MgSiO_3$.
The Drude semiconductor model suggests that the liquid $MgSiO_3$ for conditions close to the melting temperature and at 120-150 GPa occurs in a low electrically conducting phase. For pressures > 0.2 TPa along the Hugoniot the conductivities approach values consistent with metallic or quasi metallic behaviours ($10^{14} - 10^{15}$ S/m). Assuming temperatures close to that of the Hugoniot, it appears that a magma ocean with a liquid composition close to $MgSiO_3$ at such high pressure (> 0.2 TPa) and temperature conditions would be sufficiently electrically conducting to contribute to the generation of a magnetic field. At lower pressure, the contribution of the liquid $MgSiO_3$ is more uncertain as our reflectivity profiles and Drude models stressed that the $MgSiO_3$ melts into a non-reflecting and probably poorly conducting liquid. However as we showed, the conductivity value obtained with the Drude model depends on the interpolation method and in particular on the choice of the free parameters. Therefore future studies to better constrain the conductivity of $MgSiO_3$ in the vicinity of the melting line are required.

2.3.4 Mg_2SiO_4

In this section we present the results obtained on Forsterite (Mg_2SiO_4 single crystal). As for the previous materials we present the SOP and VISAR data, the P-T conditions explored by the decaying shocks and the reflectivity data.

2.3.4.1 VISAR and SOP data

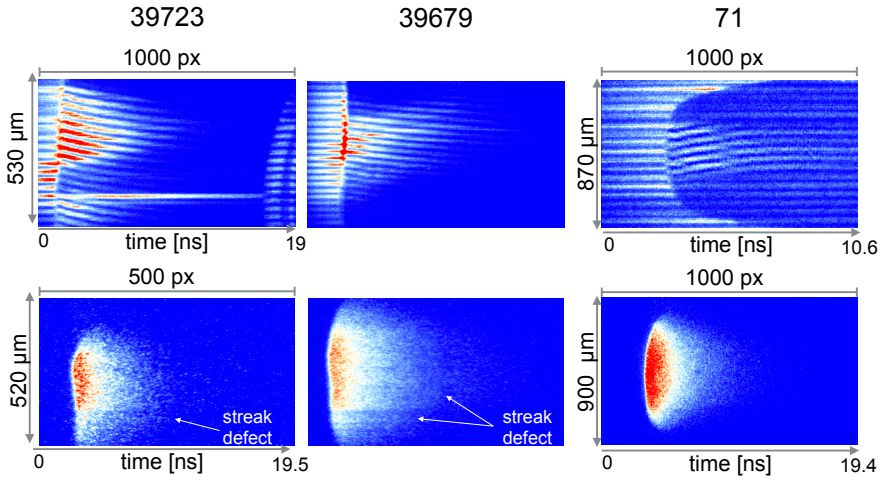

Figure 2.50: Examples of VISAR and SOP signals obtained for the Mg_2SiO_4. Here we shown data from two shots performed at GEKKO (39273 and 39679) and one shots performed at LULI (71).

Fig. 2.25 and fig. 2.50 show typical SOP and VISAR data obtained on shocked Mg_2SiO_4. In particular shots 39723 and 39679 were performed at GEKKO, while shot 71 was performed at LULI.
Shock velocity and thermal emission profiles obtained from the data of fig 2.50 are represented in fig. 2.51. As for the $MgSiO_3$, VISAR data exhibit only one abrupt fringe shift which corresponds to the time when the shock breaks into Mg_2SiO_4. Then fringes shift continuously which means that the shock velocity decrease smoothly. In particular our data stressed that shock velocities decay monotonically between 22 km/s and $\sim$ 12-10 km/s (see fig. 2.51). At LULI we lost fringes at around 18 km/s where they are less intense than ghost fringes coming from the interface Mg_2SiO_4 vacuum. The occurrence of these ghost fringes was due to a unsuccessful anti reflecting coating. Therefore for shots performed at LULI on Mg_2SiO_4 we extrapolate the shock velocity in order to get the temperature- shock velocity curves explored by our shocks.
Coherently with the shock velocity behaviour, the thermal emission signals decay

exponentially in time without significant slope changes. Hence our VISAR and SOP data suggests that shocks propagated in a single phase, with no evidence of dissociation or other phase transitions.
However these data cannot rule out the occurrence of phase transition with small volume change or latent heat release, as in such cases the phase transition does not produce significant imprints on VISAR or SOP data.

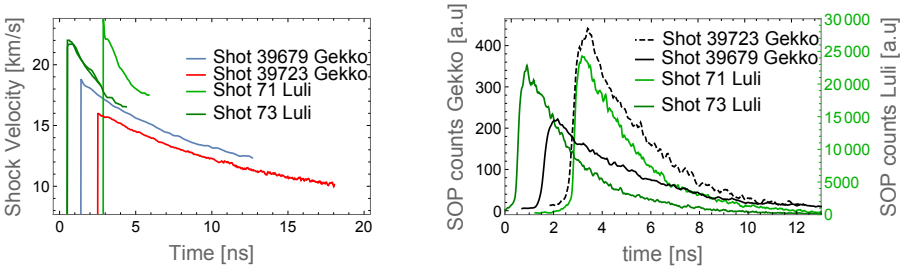

Figure 2.51: Shock velocity time profiles and sop thermal emission time profiles obtained from three shots on Mg_2SiO_4

2.3.4.2 T-Us curves

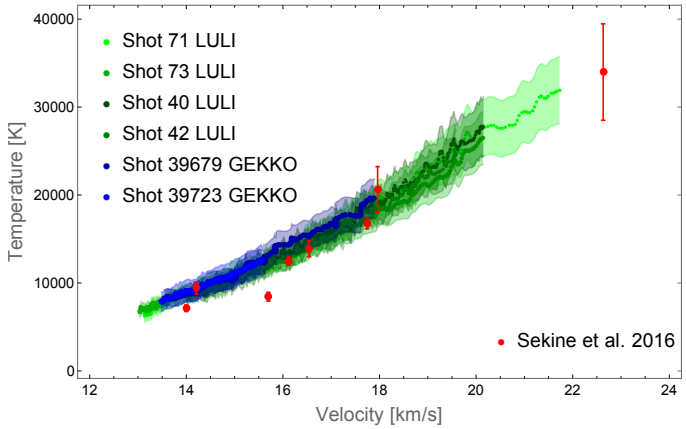

Figure 2.52: Temperature-shock velocity profiles (blue and green curves) in comparison with [Sekine et al., 2016] (red dots).

Temperatures were obtained from the thermal emission and the reflectivity data using the curves presented in figure 2.11 and 2.15 for data collected at LULI and at GEKKO respectively. In this way we obtained the T-Us curves explored by our shock in the

Mg_2SiO_4, represented in fig. 2.52 in comparison with steady shock data [Sekine et al., 2016]. As shown our decaying shocks span the phase diagram region containing the nine points of [Sekine et al., 2016]. We find an overall agreement between the two dataset, except for one point at 344 GPa (Us=15.7 km/s) and 8440 K, which has been interpreted as a clue of the occurrence of dissociated MgO. This feature, though, is not seen in our decaying shock measurements, which include six reproducible shots on two different facilities. Hence our data do not confirm the occurrence of the transition observed by Sekine et al. [2016].

2.3.4.3 Equation of state

Figure 2.53 shows the existing equation of state data [Mosenfelder et al., 2007; Sekine et al., 2016] obtained on Mg_2SiO_4 Forsterite in comparison with the QEOS model. For pressure $>$ 200 GPa the only available data are from [Sekine et al., 2016]. As our data do not exhibit clues of phase transitions we interpolate the data with a single function and we did not use Sekine's et al. [2016] model (red line). Moreover we believe that there is not enough statistics to justify an interpolation of Sekine et al. [2016] data with multiple functions. Thus the interpolation we obtained does not show significant differences from the P-Us curve predicted by the QEOS model (green line). Therefore to calculate the pressure from our shock velocity profiles we finally chose to use the curve predicted by the QEOS model.

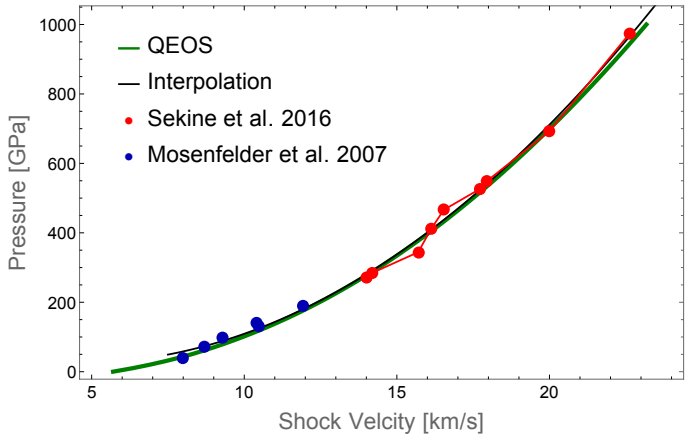

Figure 2.53: Mg2SiO4 relation between Pressure and shock velocity: Previous experimental point, QEOS model and quadratic fit.

2.3.4.4 Phase Diagram

With the QEOS equation of state we obtained the P-T curves shown in fig. 2.54 , where the shock pressure decays monotonically between 850 and 200 GPa crossing

the MgO melting line very close to the triple point. At these conditions the P-T curves do not exhibit any significant change of slope. In particular, the data do not show the melting signature detected at 0.47 TPa and 9860 K in MgO samples.
Hence there are two possible interpretation of these curves. These results either exclude the presence of crystalline MgO below its melt curve (i.e., Mg_2SiO_4 remains in a single undissociated phase, potentially because of the slow dissociation kinetic) or suggest that because of an eutectic behaviour in the MgO-SiO_2 or MgO-$MgSiO_3$ system, MgO concentration is not high enough to generate a detectable signature with decaying shocks. This conclusion contradicts what recently found [Sekine et al., 2016]. We already discussed this discrepancy in subsection 2.3.4.2. In particular we stated that this disagreement derives from the datum at $\sim$ 16 km/s. The origin of this difference calls for further EoS shock experiments to test the reproducibility of these steady shock data and to increase the sampling in this crucial region of the phase diagram. Preliminary results of such EoS studies have been presented at AGU fall meeting 2016 [Root et al., 2016] and at the 9th international workshop on warm dense matter 2017 [Townsend, 2017] and confirm our interpretation (no phase transition occurring along the Hugoniot in the studied pressure range).

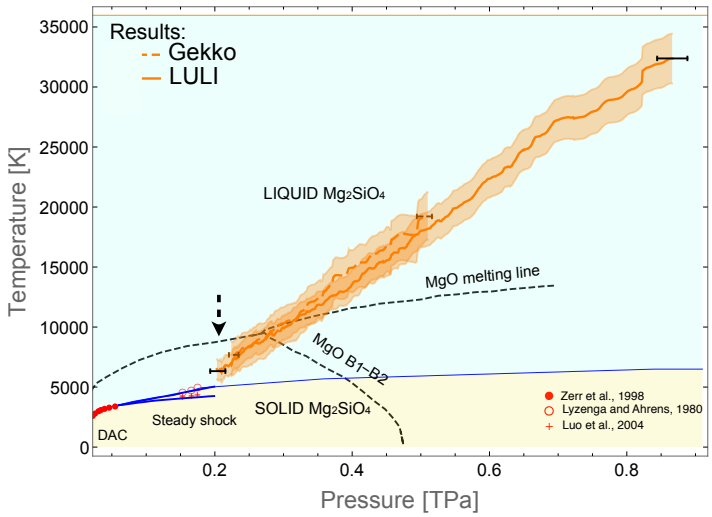

Figure 2.54: The experimental Mg2SiO4 P-T curves measured at LULI (orange full line) and at Gekko (dotted orange line) are represented in the Mg2SiO4 phase diagram. Dashed lines show MgO coexistence lines. MgO coexistence lines are from [Root et al., 2015]. Black and brown dashed horizontal bars represent the error on pressure for LULI and Gekko data respectively, for both materials. The arrows indicate the beginning of the reflecting segment along the Hugoniot.

2.3.4.5 Reflectivity data

We observed Mg_2SiO_4 reflectivity starting to increase at $\sim$ 10 km/s which corresponds to 0.2 TPa. No melting signatures have been detected down to 0.2TPa and 6300 $\pm$ 680K (SOP detection limit), in agreement with previous works [Lyzenga and Ahrens, 1980; Luo and Ahrens, 2004] which set forsterite melting between 150 GPa and 170 GPa along the Hugoniot. Therefore our data underline that as for MgO and $MgSiO_3$ melting does not coincide with the onset of reflectivity, suggesting the existence of a poorly conductive liquid in the Mg_2SiO_4 high-pressure phase diagram.

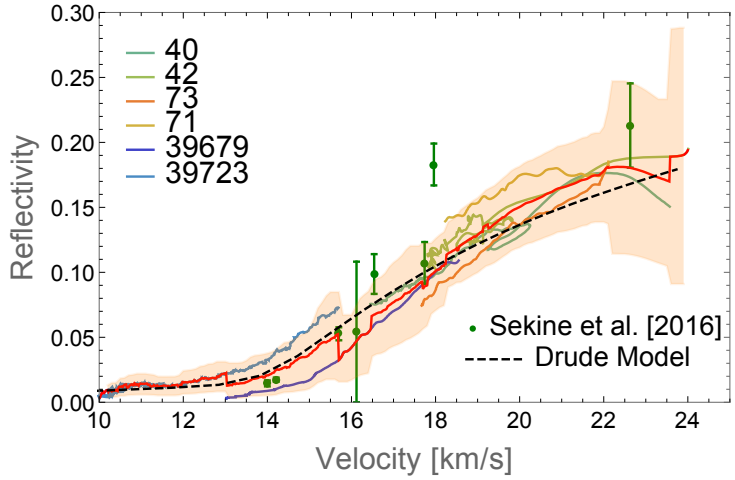

Figure 2.55: Coloured curves shown the Mg2SiO4 reflectivity vs shock velocity curves obtained from six shots performed at LULI and GEKKO. The red line represent the average and it is compared with [Sekine et al., 2016] (green dots). The dashed line represent the reflectivity obtained with the Drude semiconductor model

As for the $MgSiO_3$ and MgO we used the Drude semiconductor model to fit the reflectivity (black dashed line in fig. 2.55) and to calculate the conductivity along the Hugoniot fig. 2.56. Here we interpolate the reflectivity with an initial band gap of 8eV [Morin et al., 1977; Shankland, 1968]. Conductivity along the Hugoniot increases rapidly from values $\sim$ 10 S/m for conditions close to the melting line (0.15 TPa and 4000K) to values $\sim$ 1000 S/m at 0.2 TPa and 5500K and approaching a plateau of 10^5 S/m for pressures higher than 0.3 TPa and 10000K.

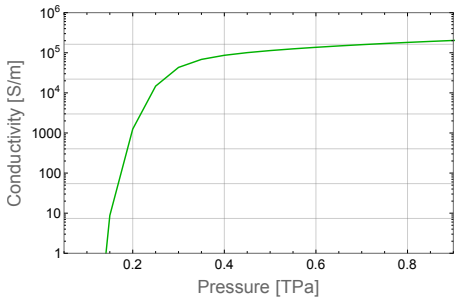

Figure 2.56: Conductivity obtained with the Drude semiconductor model

2.3.5 Implications

As we already mentioned the most reasonable scenario suggested by our data is that liquid Mg_2SiO_4 is stable between 200 and 800 GPa. However we already mentioned that our data cannot completely exclude the occurrence of phase transitions if implying small volume changes. Therefore a scenario where Mg_2SiO_4 liquid dissociated into MgO crystal and $MgSiO_3$ melt cannot be completely ruled out.
Further studies are mandatory to solve this issue. Indeed whether liquid Mg_2SiO_4 is stable or not is particularly important for the physics of impact phenomena and planetary stratification. Indeed in the scenario of the occurrence of liquid Mg_2SiO_4 dissociation under shock compression at around 300 GPa, planetary impacts at velocities of $\sim$ 13 km/s may produce MgO crystals. The density ratio between MgO crystals and the coexisting liquid could induce stratifications and the formation of a liquid region with a dominant $MgSiO_3$ composition. On the contrary the stability of liquid Mg_2SiO_4 between 200 and 800 GPa would exclude the occurrence of stratifications in MgO rich and $MgSiO_3$ layers.
Reflectivity profiles seem to suggest the occurrence of region of non reflecting and low electrically conducting Mg_2SiO_4 liquid in the phase diagram. Indeed with the Drude semiconductor model we found conductivity between 10-100 S/m for pressure between 150 and 180 GPa along the Hugoniot. A magma ocean of a super Earth with a liquid close to Mg_2SiO_4 composition, at a temperature of 5500 K and pressure of 0.2 TPa, liquid Mg_2SiO_4 would have a conductivity $\sigma_0 > 1000 S/m$ able to contribute to the generation of a magnetic field. However we believe that a more precise characterisation of the conductivity of liquid Mg_2SiO_4 in the region close to the melting line is required.

2.4 Conclusion

In this study, we have obtained pressure, temperature and reflectivity measurements along the Hugoniot of different compounds in the MgO-SiO_2 chemical system. We propose an upper limit of the melting point of MgO at 0.47 ± 0.04 TPa and 9860 ± 810 K (0.85 ± 0.07 eV). This is lower than several estimates of melting in this pressure range, and it implies lower temperature profiles for Earth-like and super-Earths [Stixrude, 2014; Gaidos et al., 2010]. As iron should be present in planetary mantles, future experiments on FeO and (Mg,Fe)O solid solutions should however be carried out in order to better constrain conditions of partial melting in this system. Moreover, molten MgO could play an important role in the case of deep magma oceans and/or in response to very large impacts, as well as in the putative cores of icy giant and gas giant planets (as for tidal dissipation [Remus et al., 2012]). The scenario proposed here with a lower temperature melting curve brings a new important input for modelling studies of these phenomena.
We have also shown that no detectable phase transition could be observed either in $MgSiO_3$ or in Mg_2SiO_4 in the range (0.12 TPa - 6300 K, 0.5 TPa-22000 K) and (0.2 TPa - 6300 K, 0.8 TPa-30000 K) respectively. The result on $MgSiO_3$ is in disagreement with previous experimental data [Spaulding et al., 2012] and calls for a novel interpretation of the behaviour of high pressure silicate liquids excluding a role of the liquid-liquid transition in planetary geochemical differentiation. Indeed such a liquid-liquid phase transition has been proposed to strongly affect the geochemical differentiation, with consequences for the bulk chemical composition of significant fractions of a planet in its early stages [Spaulding et al., 2012].
In addition, no signature of the occurrence of crystalline MgO could be detected in both $MgSiO_3$ and Mg_2SiO_4 data sets. Several hypotheses have been proposed to explain these observations, including the stability of the undissociated $MgSiO_3$ and Mg_2SiO_4 liquids. Nevertheless, due to the importance of this debate further direct structural investigations under dynamic compression are mandatory.
Interestingly, for all the studied materials, it has been observed that metallization and melting do not occur at coincident thermodynamic conditions (reflectivity starts to increase at P-T along the Hugoniot higher than melting), implying the presence of poorly electrically conducting liquid in the melting line vicinity. This result is extremely relevant for the models of magnetic field generation via dynamo mechanism in a molten silicate layer, where a strongly enough conducting liquid is necessary to sustain the magnetic field. In addition, this behaviour is different to what was established for SiO_2 (where along the Hugoniot reflectivity starts to increase at melting) [Spaulding, 2010; Hicks et al., 2006], pointing out a difference in the electronic structure changes at melting between MgO, $MgSiO_3$ and Mg_2SiO_4 on one hand and SiO_2

on the other hand. This is an extremely intriguing input for condensed matter studies and it encourages a deeper investigation of the high-pressure regime of these materials with x-ray diagnostics such as X-ray diffraction and X-ray absorption spectroscopy.

Chapter 3

XANES investigation of MgO in WDM regime.

Contents

3.1 Introduction

In this chapter we present the first X-ray Absorption Near Edge Spectroscopy measurements on shocked compressed MgO at the Mg K-edge in an extended range of densities and temperatures (0.2-2.5 eV and 3-6 g/cc). Measurements have been performed at LULI using a nanosecond laser pulse to drive the laser and a picosecond laser pulse to generate the probing X-rays. In particular in this study we determine structural and electronic properties of MgO melt, advancing in the comprehension of the metallisation mechanism of MgO.

We already discussed in sec. 2.1 how it is geophysically important to study MgO liquid properties like the density and phase boundaries at high pressures because of their implications on planetary differentiation and stratification, internal dynamics, planetary temperature profiles. Here we recall that MgO can occur in planetary interiors as a result of $MgSiO_3$ or Mg_2SiO_4 dissociations. It is therefore a fundamental planetary component whose knowledge is necessary to properly model the complexity of Earth-like, Super-Earth and giant planet interiors.
Another subject that worths a mention is its metallisation as liquid MgO has been proposed to significantly contribute to the Super-Earth's magnetic fields via dynamo mechanisms [McWilliams et al., 2012]. However our study [see chap. 2; Bolis et al., 2016] evidenced the possibility of having a low electrical conductivity melt in the MgO phase diagram and thus in planetary interiors. The consequence is that the contribution of MgO to the magnetic field generation is not ensured and it depends on the thermodynamic conditions at which MgO occurs in the planetary interior. However these hypotheses have been proposed on the basis of indirect methods (decaying shock technique), meaning that whether MgO melt coincides with MgO metallisation is still an open question.
XANES spectroscopy [Milne et al., 2014] combined to shock compression [Benuzzi-Mounaix et al., 2011] is a good technique to answer to this question as a XANES spectrum is linked to the electronic structure, the ionic local order, and in some cases to phase transitions [Harmand, 2009; Denoeud et al., 2014]. Indeed a XANES spectrum is a measure of the transitions from core electronic states to unoccupied electronic bands, that are correlated to the ionic structure. Therefore a XANES spectrum changes with the temperature T and the density ρ of the probed sample as well as at solid-solid or solid-liquid phase transitions, reflecting the changes in the local order and electronic structures of the probed sample. This means that structural transitions with ionic rearrangement producing significant changes in the electronic structure can be detected with XANES spectroscopy. An example of that is iron [Harmand, 2009] whose electronic band structure changes at melting induce a visible

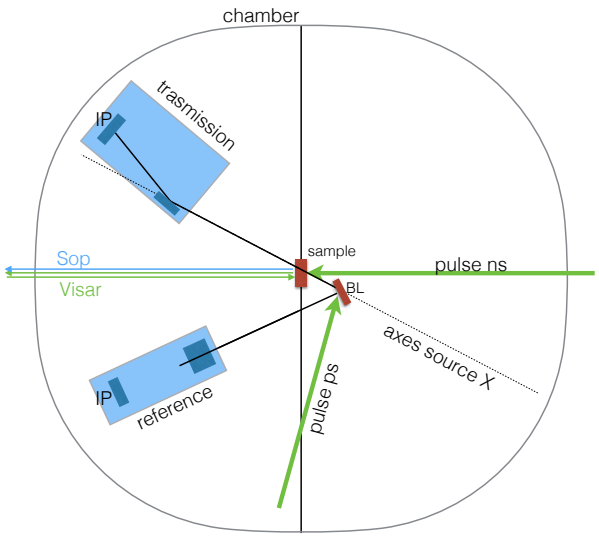

Figure 3.1: Conceptual layout of the key experimental elements in the vacuum chamber used at LULI

change on the Fe K pre-edge. Moreover this technique has been already successfully used to study the melt properties and metallisation of SiO_2 [Denoeud et al., 2014, 2016a], which sets an encouraging precedent for our study. To interpret the XANES spectra we used firs principle ab-initio simulations.

Here we spend some words to mention that measuring the XANES spectrum of shocked MgO is a non-trivial technical challenge because of the low X-ray transmission in the Mg K edge spectral region (@ 1.3 keV). To give an idea, for a 1 μm thick MgO crystal the transmission at 1.3 keV is about 20%, while the transmission for a 1 μm thick fused silica sample at the Si K edge energy (1.839 keV) is 64 % (i.e. more than three times). For this reason, particular attention has been paid in this campaign to experimental details in order to maximise the signal, as we will see in the following section.
After that we will present the XANES spectra obtained on shocked MgO and studied for varying temperatures, pressures and phases. With the help of ab-initio calculations, our experimental results give a picture of the metallisation mechanism of MgO and of the structural properties of liquid MgO.

3.2 Experimental setup

The experimental setup of this campaign is shown in fig. 3.1. We made use of both of the two beams available at the LULI2000 facility, rear side optical diagnostics and two spectrometers (a reference and a transmission spectrometer). One laser beam was used to drive the compression, the other to generate the X-rays. We will give a detailed description of the setup components in the following paragraphs. Fig. 3.2 represents a zoom of the target area with the details of the experimental geometry. The particular form of the mount S of the sample is for blocking the ps pulse reflected from the BL.

3.2.0.1 Laser beams

Drive beam The drive beam operated at 527 nm. The focal spot was smoothed with Hybrid Phase Plate to obtain a flat intensity profile of 600 μm. Energy was varied up to $\sim$ 50 J, thus obtaining laser intensity between 0.36-5.9 $\cdot 10^{13}$ W/cm^2 (on target 0.18-2.9 10^{13} W/cm^2). The time length was chosen to be relatively short: 0.3-0.5 ns. This choice took into account 1) the ablator thickness and two problems induced by the drive beam: 2) the coronal plasma X-rays emission and 3) the perturbation of the X-ray source.
1) The ablator thickness was kept very small (B 0.8 μm + CH 3.1 μm thick) to maximise the X-ray transmission (we will discuss more in details in sec. 3.2.1). Therefore the drive laser must be relatively short for generating a sharp plane shock wave and for avoiding pressure decrease due to reverberations and release waves.
2) The coronal plasma is kept hot by the ns pulse for all its duration. This means the longer the ns pulse the longer the coronal plasma emits energetic X rays (secondary X-rays or ns emission). These X rays go through the sample and contribute to the signal measured by the spectrometer. Hence the signal results from the superimposition of the X-rays from the main X-ray source (primary X-rays) and the X-rays from the corona. Hence a strategy to limit the contribution of the ns emission is to set its duration as short as possible.
3) The coronal plasma emission can perturb the X-ray source too, altering the spectrum of the primary X-ray beam. Therefore the longer the drive beam the longer the interaction with the X-ray source.
We will treat these problems more in details in section 3.3.2.3.

X-ray source- ps beam A 3 ps laser beam with a focal spot of $\sim$ 50 μm was used to generate the X-rays. The delivered energy was $\lesssim$ 20 J, implying intensities up to 3.4 10^{17} W/cm^2. Such short intense pulse was focalised to a solid target, thus generating an hot and dense plasma. This plasma is sufficiently hot to emits X-rays via various

mechanisms: K_α emission induced by super-thermal electrons, Bremsstrahlung emission and K, M, L shell emission lines related to electronic transitions.
The MgO K-edge lies at $\sim$ 1.3 keV. Hence to perform a X-ray absorption experiment to resolve the near edge structures, it was necessary to use an X-ray beam spectrally flat between 1.25 and 1.4 KeV. To this aim we chose to focalise the 3 ps beam on Samarium (Z= 62) or Gadolinium (Z= 64) sheets, as the M shell emission of these elements at standard conditions satisfy the request of spectral flatness between 1.25 and 1.4 keV.

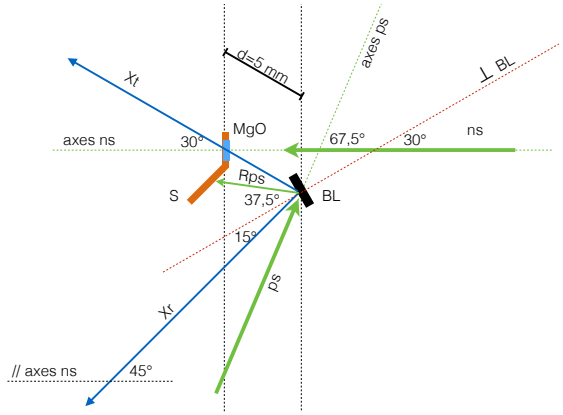

Figure 3.2: Details of the geometry of the experimental set-up.

3.2.0.2 Spectrometers

As mentioned previously, two spectrometers have been used during this experiment. These instruments have been developed at CELIA (Université Bordeaux 1) by F. Dorchies and already successfully used at LULI for studying the K edge of shocked Al [Lévy et al., 2012] and of Si in shocked SiO_2 [Denoeud et al., 2014, 2016a]. For this experiment spectrometers have been re-adapted by F. Dorchies to measure the Mg K edge which is located at lower energy (1.3 keV) than those of Al (1.559 keV) and Si (1.839 keV). Changes have been made also in order to maximise the the number of photons that reach the IPs, as the MgO X-ray transmission at 1.3 keV is lower than for Al and SiO_2 at 1.559 and 1.839 keV respectively.

Before presenting the details and the design of such spectrometers, we comment the necessity of having two of them. Indeed in order to measure an absolute absorption spectrum it is necessary to know both the X-ray source spectrum (reference spectrum)

and the spectrum transmitted through the sample (transmission spectrum). Indeed ideally, if measuring a sample composed by a unique MgO layer, the absorption spectrum would be given by $\mu(E) \propto -ln(I_t(E)/I_i(E))$ (see sec. 1.0.6), where $\mu(E)$ is the absorption, I_t the intensity of the transmitted beam (measured by the transmission spectrometer), and I_i the intensity of the X-ray source emission (in our case measured by the reference spectrometer). Unfortunately it is not as straightforward and corrections to I_t and I_i are needed in order to take into account the complexity of the experiment (i.e. we already mentioned the problems due to the ns emission) and the fact that we are obliged to use a multilayer target (B— CH — MgO — Diamond — CH, see sec. 3.2.1 for details). The necessity of two spectrometers comes from the instability of the X-ray source, that is due to different reasons: the energy of the ps pulse is not constant shot to shot, the angle between the BL and the sample is not reproductible at 100% and the pointing of the ps can slightly vary with consequences on the intensity irradiated to BL . Therefore the X-ray source emission spectrum (or reference spectrum) has been measured for each shot by the reference spectrometer.

Spectrometer design The designs of the transmission and reference spectrometers are shown respectively in fig. 3.3 top and bottom. The spectrometers, which are identical, are both composed of a RbAP crystal (with a d-spacing of 13.06 A) with a truncated-conic geometry, a lead shield of around 3 mm (with a hole to let pass the signal) and an Image Plate (IP) to collect the X-rays shielded by a 15 μm thick beryllium filter.
RbAP crystals were chosen for their high reflectivity in order to maximise the signal on the IPs. These crystals substitute the KAP crystals used in previous experiments on Al and SiO_2 which have a 3 times lower reflectivity. RbAP crystals were provided by Saint Gobain S.A. . Crystal size is 40 mm x 40 mm, while the maximum and the minimum curvature radius are 104.4 mm and 119 mm respectively.

The truncated-conic geometry allows to maximise the signal measured by the IP. Indeed in this way the X-rays are focused onto a vertical axes perpendicular to the detection axes, as shown fig. 3.4. Unexpectedly we noticed that the focal plane of the reference spectrometer was not perpendicular to the detection axes. This was due to a problem in the mechanical stage mounting which was forced probably causing a light twist of the mounting. This is why the IP plane is tilted of 38 $\pm$ 2 degrees (as shown in fig. 3.3) in order to image the X-ray source on the IP without distortions.
The 15 μm beryllium filters are used to shield the IP detectors from the background noise due to optical and UV radiation. Again the thicknesses of these filters have been reduced as much as possible in order to maximise the X-rays that reach the IPs (in previous experiment on Al and SiO_2 using the same spectrometers the Be filters

were 23 μm thick).
Moreover always for maximising the signal on IPs, we chose to not shield the spectrometer crystals from debris coming from the shocked sample, contrarily to what has been done in previous experiment on Al and SiO_2 with a $8\mu m$ thick polypropylene film.
In order to have a spatial resolution of the MgO samples we placed the IP at a distance D from the focal plane. The magnification of the sample is hence given by the ratio D/d= 30mm/5mm = 6, with d the distance between the target and the source X. gives a zoom of the shocked region of the sample.
The MgO samples were tilted so that there was an angle of 30 degrees between the normal of the sample surface and the X-ray axes (fig. 3.3, fig. 3.2). This angle was imposed by the fact that we wanted rear side optical diagnostics to be perpendicular to the sample surface (fig. 3.2). This implies that the probed region of the MgO sample was an isosceles trapezoid (see fig. 3.5). The sizes of the trapezoid depends simply on the geometry of the spectrometer (see fig. 3.3). In our case we got: 230 μm along the spectral dispersion axis (see fig. 3.5), 610 μm along the spatial axis "low energy side" (i.e. the sample side closer to the spectrometer crystal) and 550 μm along the spatial axes "high energy side" (i.e. the sample side further to the spectrometer crystal).

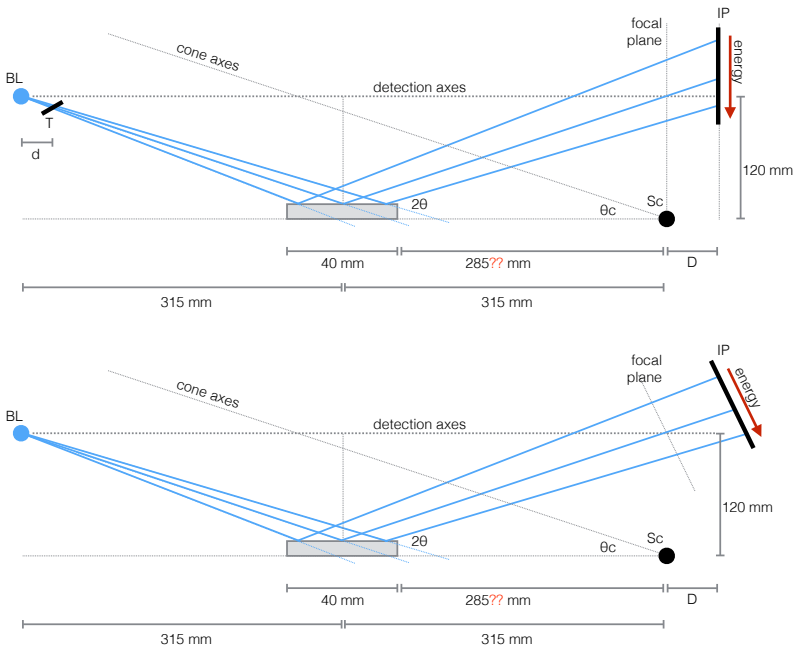

Figure 3.3: Geometry of the transmission and reference spectrometer are shown respectively at the top and at the bottom.

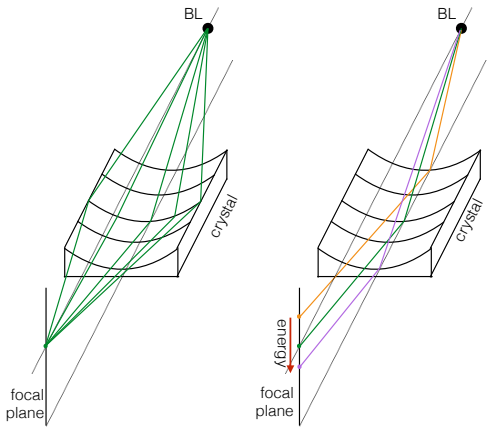

Figure 3.4: Conceptual layout of truncated-conic crystals.

Therefore the size along the "spatial" axes (vertical axes in the figure) is almost the same as the diameter of the shocked region of the sample, varying between 550 and 610 μm according to the X-ray energy. It was then crucial to center the probed region on the "shocked" region of the sample with extreme precision, to get the signal entirely from the compressed sample. This is another of those adjustments made for maximising the intensity of the signal. The centring along the other axes is less delicate as the height of the trapezoid is 230 μm.
Because of its importance we report in appendix C the centring process along the vertical axes (see fig. C.1.1), which allowed us also to give an estimation of the spatial resolution (see C.1.2)

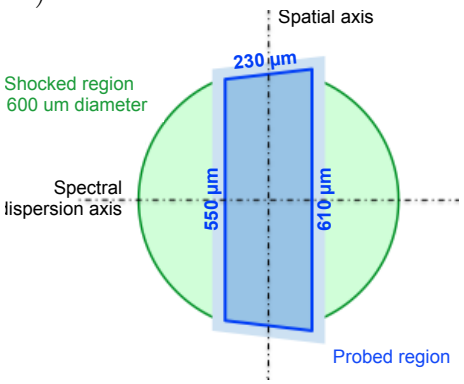

Figure 3.5: Representation of the sample area shocked by the drive beam (green circle, 600 μm of diameter) and probed by the X-rays (blue isosceles trapezoid: heigth = 230 μm along the horizontal axes; longer side= 610 μm along the vertical axes; shorter side = 550 μm along the horizontal axes.)

3.2.1 Target design

We designed our targets taking into account of various constraints among which the most important was maximising the transmission signal and the contrast of the Mg K-edge at 1.31 keV (first constraint). As already mentioned the X-ray transmission in the MgO is quite low for energies immediately beyond the Mg K-edge. To make an example the transmission for a 1 μm thick MgO crystal at 1.31 keV is 20 %. Moreover other layers need to be added to the MgO sample in order to generate the shock (an ablator) and to keep the sample compressed (higher impedance layers), thereby further reducing the transmission of the target.

Indeed the target has been designed also in order to compress the MgO layer to conditions in a extended region of the T-ρ diagram (second constraint) as we wanted to study the behaviour of the spectra as a function of the density and of the temperature. Moreover the hydrodynamic conditions had to be kept uniform and constant for a time long enough to guarantee a precise diagnostic (third constraint). Indeed it is true that the probe pulse is very short (3 ps), but, as we will see, the uncertainty about the time delay between the pulses is $\pm$ 25 ps. Hence the MgO layer had to be kept compressed to uniform conditions for a significantly long time window (i.e. 100-200 ps) in order to avoid a huge uncertainty on the probed thermodynamic conditions. Finally the target design had to be compatible with SOP measurements (fourth constraint).

Concerning the first three constraints, we tested with the MULTI code various target configurations that guarantee an acceptable transmission. We finally chose the best compromise between a target with a good X-ray transmissivity and a target that allows to compress uniformly the MgO layer and to reach easily the desired thermodynamic conditions.

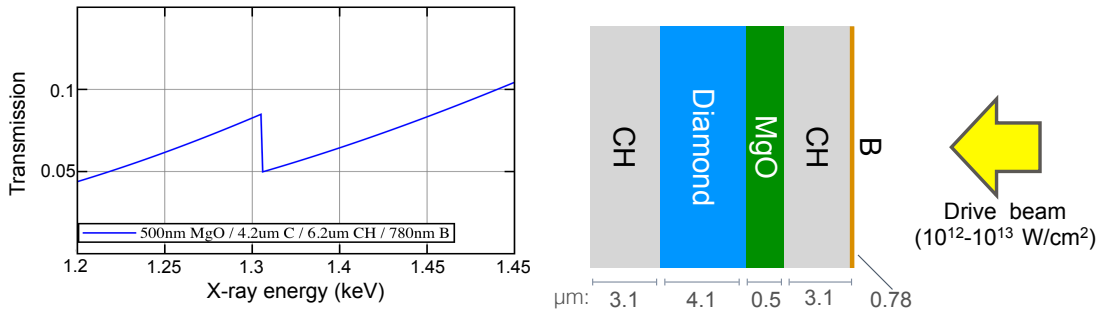

Figure 3.6: Target transmission (on the left) and target design (on the right).

Our final choice was a multi-layer target of 0.8 μm B + 3.1 μm CH + $\sim$0.5 μm

MgO + $\sim$ 4.1 μm Diamond + 3.1 μm CH. The drive laser was focused on the B side. This target is represented in fig. 3.6 on the right and its X-ray transmission in fig. 3.6 on the left. The B layer is placed to prevent laser light to directly reach and in case damage rear side diagnostics. The diamond layer, which has a higher impedance than MgO, has been inserted in the sample in order to generate a reflecting shock counter-propagating into MgO. This allows to reach higher pressure and to keep the sample compressed uniformly and for a relatively long time. Indeed for its properties, diamond allows to confine and sustain a sample at high pressure. Moreover diamond fulfils the technical requirement of having a layer hard enough (also if thin) to be coated with the MgO film. The last CH layer (the one on the rear side) was inserted in the target to satisfy the fourth constraint. Indeed CH gets quickly hot along the Hugoniot and this allowed, at least for the shots performed with the highest laser intensities, to measure a thermal emission signal, which has been used to tune the hydrodynamic simulations. Indeed as we will see in paragraph 3.3.1.2 the thermodynamic conditions have been obtained with hydrodynamic simulations performed with the MULTI code.

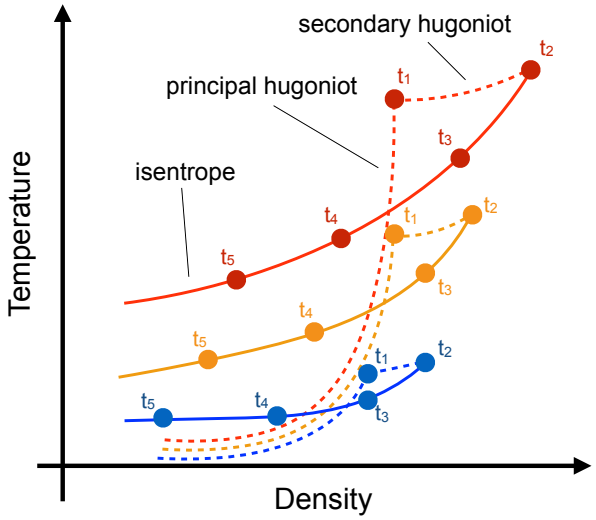

Figure 3.7: Scheme of the experimental strategy of this campaign. The laser intensity and the time delay set the conditions measured with the absorption spectroscopy.

The MgO phase diagram is explored here by tuning the laser intensity and the time delay between the drive and ps beam, i.e. between the shock wave and the X-ray. The laser intensity sets the the thermodynamic conditions of the MgO layer at the shock front, i.e. along the standard or secondary (relative to the shock reflected by

the Diamond) Hugoniot. In fig. 3.7 different laser intensities corresponds to different colours. Playing with the time delay between the drive and probe pulses, it is possible to probe the thermodynamic conditions in t_1, t_2 or along the continuos line that represents the isentrope starting from the point reached by the reflected shock along the secondary Hugoniot. The thermodynamic states along the secondary Hugoniot between t_1 and t_2 cannot be explored, as between t_1 and t_2 the sample is partially compressed by the secondary shock and partially in release from the compression of the first shock. Then at t_2 is completely compressed by the second shock, and for longer times the thermodynamic states lie on the isentrope which starts from the conditions in t_2.

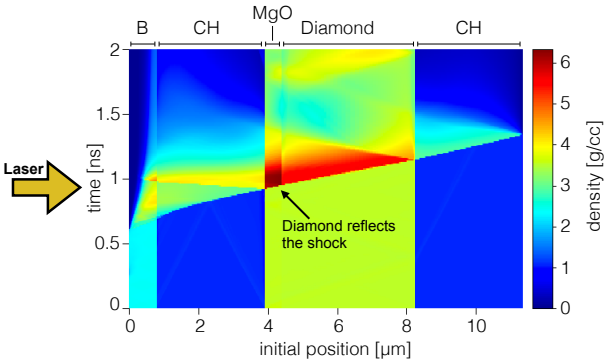

Figure 3.8: Hydrodynamic simulation of a XANES target irradiated by a laser with intensity 0.78 10^{13} W/cm^2

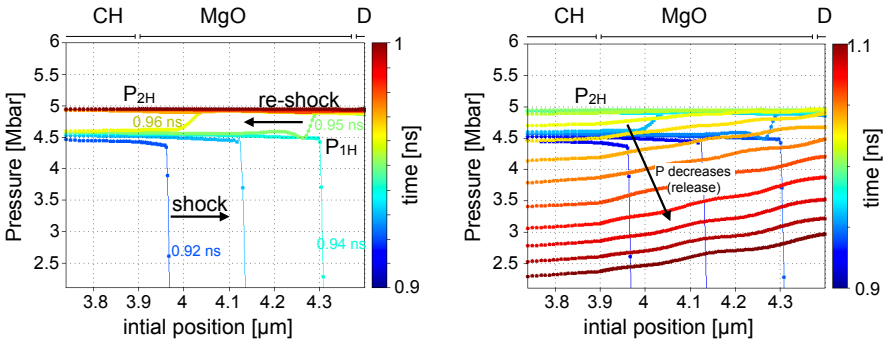

Figure 3.9: Pressure profiles for various time obtained with the hydrodynamic simulation of a XANES target irradiated by a laser with intensity 0.78 10^{13} W/cm^2

As examples, fig. 3.8 and fig. 3.9 represent the results of hydrodynamic simulations performed with MULTI for a 300 ps long drive beam of 7.8 10^{12} W/cm^2

irradiated on the target already presented in this paragraph. The color plot showing the density over time and initial position gives a clear picture of the hydrodynamic of our targets. The laser (irradiated on the B side) generates the shock that compressed the CH and successively the MgO. At the MgO-Diamond interface a secondary shock is reflected further compressing the sample and generating the thermodynamic states along the secondary hugoniot, as represented in fig. 3.7. However the reason why we placed the Diamond layer in our sample is not only for reaching higher density states but primarily to keep the sample compressed for an acceptably long time. The dynamic of the primary and secondary shock in the MgO layer are represented in the pressure lineouts of fig. 3.9. Pressures P_{1H} and P_{2H} points respectively at the principal Hugoniot and secondary Hugoniot states schematised in fig. 3.7. The secondary hugoniot state P_{2H} is reached at 0.97 ns and kept at constant pressure for around 30-40 ps (left of fig. 3.7). At higher times (see the right of fig. 3.7) the pressure decreases quite rapidly: 2.5 Mbar in 100 ps. It is therefore difficult to tune the delay time to systematically study the second hugoniot states. However the diamond layer allows to keep the MgO sample compressed between 4 and 5 Mbar for around 100 ps, giving the opportunity of probing high pressure states.

Sample preparation and characterisation MgO have been coated on polycrystalline CVD Diamond films of a thickness around $4\mu m$ by Diamond Materials which provided also a characterisation of the MgO and diamond layers. Being the sample thicknesses very small, they needed to be characterised with high precision. The MgO density have been determined measuring the thickness of a MgO film deposited on a silicon wafer of known mass, the mass difference after the MgO deposition and the deposition area. The measurement yields a value of 3.364 g/cc which is slightly different from the density of crystalline MgO (3.58 g/cc). The MgO and CVD diamond thicknesses have been measured with respectively sub-nanometric ($\pm$0.1 nm) and nanometric ($\pm$1 nm) precision.
CH and B layers have been successively coated by Scitech Precision, UK.

3.3 Analysis

3.3.1 Evaluation of the thermodynamic conditions

3.3.1.1 Characterisation of the time delays

Time delays between the drive and the ps beam have been measured with two Hamamatsu R1328U series ultra-fast photodetectors. The photodetectors, connected to a scope, measure the time profile for each beam before the vacuum chamber. These photodetectors allowed to measure the time delay with a precision within ± 25 ps, which corresponds to the rise time of the photodetector. We defined our time delays as the difference between the time at the FWHM of the measured drive beam time profile and the maximum of the measured probe beam time profile. This definition is arbitrary, we could have chosen the difference between the two maxima or between the two positions at half maximum. The important is to use the same definition when determining the delays from the scope signals and when evaluating the probed thermodynamic states with hydrodynamic simulations.

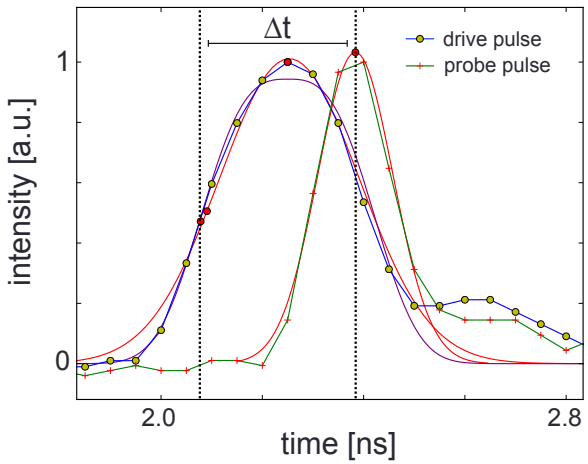

Figure 3.10: Ns and ps beam as measured by the photodetector for shot 43. The pulses are interpolated with gaussian or gaussian-type function in order to extract parameters as the maximum or the FWHM (pointed by red dots). The measured delay is pointed by dotted lines.

To obtain the probe beam maximum we interpolate its profile with a gaussian. While to obtain the time at half maximum of the drive beam we interpolate the profile with a gaussian or with a higher order gaussian according to the pulse shape

(a1 · Exp (- Abs((x-b1)/c1)^3) recorded by the scope. An example of the measured time profiles (blue line with yellow dots and green line with red crosses for the drive and the probe beam respectively) and of their interpolations (red lines for gaussian functions, purple line for higher order gaussian) is shown in fig. 3.10. As shown the 3 ps probe pulse appears much larger on the profile collected by the scope because of the response time of the photodetector.

3.3.1.2 Evaluation of the thermodynamic conditions with MULTI hydrodynamic simulations

The main tool we used to obtain the hydrodynamic conditions explored by our shocks was the code MULTI. The parameters needed by MULTI to perform the simulations are the drive pulse conditions (intensity irradiated on target, time length and pulse shape) and, concerning the target, the composition, the thicknesses, the atomic numbers, the opacity and the equation of state.

Numerical drive pulse parameters As numerical pulse time shape we used the profile measured by the photodetector. Concerning the laser intensity, it is a bit more complicated. Indeed at LULI the laser energy is measured before the pulses go through the phase plates and compress the samples. As we already pointed out in the decaying shock chapter, because of the phase plate only a fraction of the laser energy reaches the target. Depending principally on the loss due to the phase plate and on the energy coupling between the laser and the target, the ratio between the measured intensity and the intensity irradiated on target remained constant during this experiment. To determine this ratio we performed hydrodynamical simulations tuning the laser intensity in order to reproduce shock velocity measurements in a well-known material (e.g., SiO_2).

Using SOP to constraint the simulations Moreover to further constrain our MULTI hydrodynamic simulation we measured, when possible, the thermal emission of the target shown in 3.6 with an SOP. Such measurements allow to determine the shock transit times in the sample layers. Then we verified that simulations reproduced the measured transit times.

However measuring transit time of extremely thin layers as those of our target is quite challenging. Indeed it requires a high time resolution. This introduces a further complication as the higher the sweep time of the streak camera the lower the number of photons collected by a pixel. Therefore the compromise we chose was to use a 1.12 ns time windows synchronised to measure the thermal emission coming from the last CH layer.

Emission from the last CH layer was the only one detected by our SOP (for intense enough drive beams: I $>10^{13}$ W/cm^2, see fig. C.2 in appendix C). Shock compressed MgO and Diamond were respectively too thin and too cold to produce exploitable thermal emissions in this campaign. The absence of emission of the CH on laser-side is likely due to some opacification of CH layer due to the plasma corona emission [Theobald et al., 2006]. Moreover as time windows were short it was quite complicated to tune the timing to measure the signal coming from the entire sample, including the first CH layer. Hence, we chose to synchronise the streak camera to the last CH layer.

This method allowed us to determine the transit time for shots performed with a laser intensity $> 10^{13} W/cm^2$ [1], i.e. for around 20 shots. For these shots we obtained a good agreement[2] between the measured transit time and those obtained from the simulations, validating also the ratio between the measured intensity and the intensity irradiated on target determined with the shots on SiO_2.

Fig. 3.11 shows an example of an SOP measurements (300 ps and 21.66 J at 2w). The measured transit time corresponds to the one in the last layer of the CH.

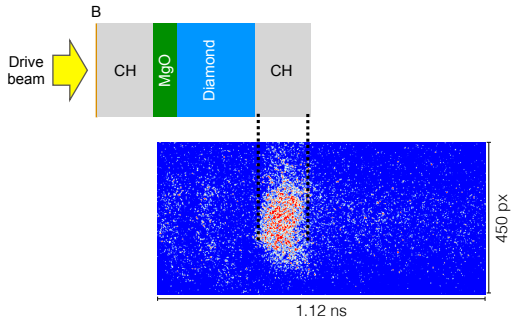

Figure 3.11: SOP signal of the thermal emission from the last CH layer measured for shot 43.

Simulation outputs Simulations were performed using the SESAME 7592 and SESAME 7834 tables for CH and Diamond respectively. Concerning MgO we used QEOS equation of state and out of equilibrium opacity tables. Although the applicability limits of the QEOS model are known[3] (mostly for what concerns the evaluation

[1] Fig.C.2 in appendix shows some SOP signals for various drive laser intensities

[2] $\Delta t/t \sim 5$ % depending on the intensity of the drive beam, where Δt is the difference between measured and computed transit times and t is the transit time.

[3] An example of this applicability limit is evidenced by the difference between the MgO QEOS hugoniot and the MgO hugoniot reported by [Root et al., 2015] and [Bolis et al., 2016]

of the temperature and of heat transfer), this model can be used to obtain a satisfying estimation of the thermodynamic conditions explored in a sample.
As mentioned, to determine the thermodynamic conditions in the MgO layer at the probe time for each shot we performed a simulation using the numerical intensity determined as described before and the time profile measured by the photodetector of the drive beams. Then the thermodynamic conditions have been obtained from a line-out of the MgO layer temperature and density at the time probed by the X-rays.

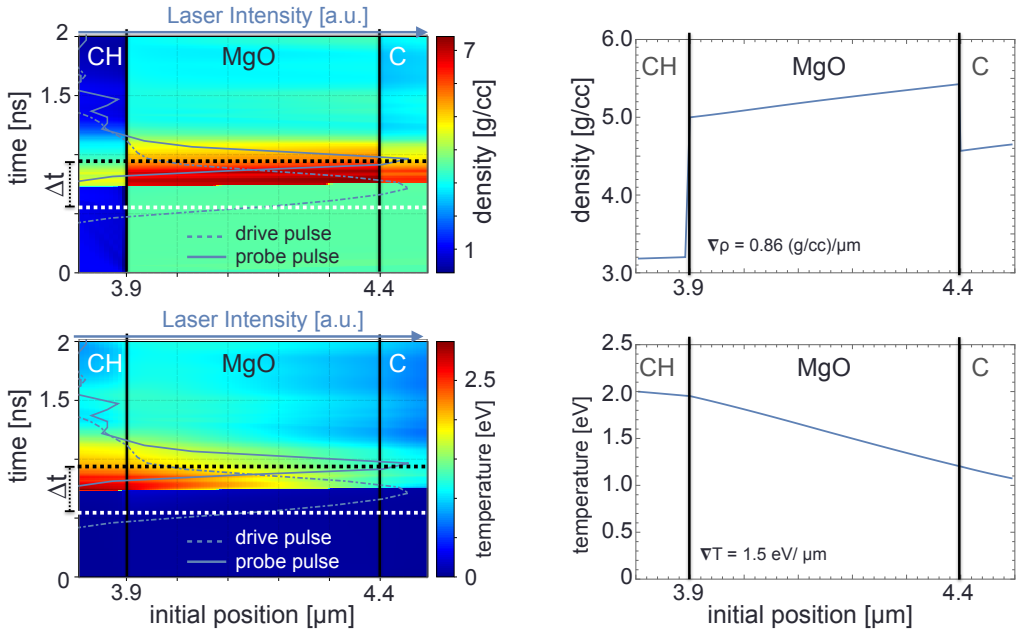

Figure 3.12: Example multi simulations for a shot with a drive beam of 1.82 10 13 W/cm2 and a time delay of 410 ps. On the left: density and temperature color plots versus time and initial position. Drive and probe pulses are represented by blue curves. The hydrodynamic conditions probed by the ps pulse are pointed by the black dotted line. On the right: density and temperature spatial profile measured by the probed beam (i.e. density and temperature line-outs of the color plots along the dotted black lines.)

We report an example to illustrate the method with more clarity. Figure 3.12 shows the temperature and density obtained in the MgO layer with MULTI simulation for arbitrary drive laser intensity and probe beam- drive beam time delay (in this case $1.8 \cdot 10^{13} W/cm^2$ and 410 ps). The continuos and dashed blue curves on the color plots (on the left) represent respectively the probe and the drive beam time profiles. The time delay has been measured from the FWHM of the drive beams pointed by the white dashed lines. The time position of the probe beam time profile, obtained from the measurement with the photodetector, is pointed by the black dashed lines.

Finally the density and the temperature profiles measured by the probe beam are obtained from line-outs along the black line in the color plots on the left of the figure. We report such profiles on the right of the figure. The density profile is almost homogeneous while the temperature profile exhibits a larger gradient. This temperature gradient is caused by two phenomena. The first is an inhomogeneous preheating of the sample due to the X-rays emitted by the plasma corona. The second phenomenon can be understood looking at fig. 3.12 on the left. The CH layer gets very hot when compressed by the shock. It follows an heat transfer from the CH to the MgO, that causes the temperature inhomogeneity in the MgO layer. Both effects are expected to be more significant for high laser intensities.

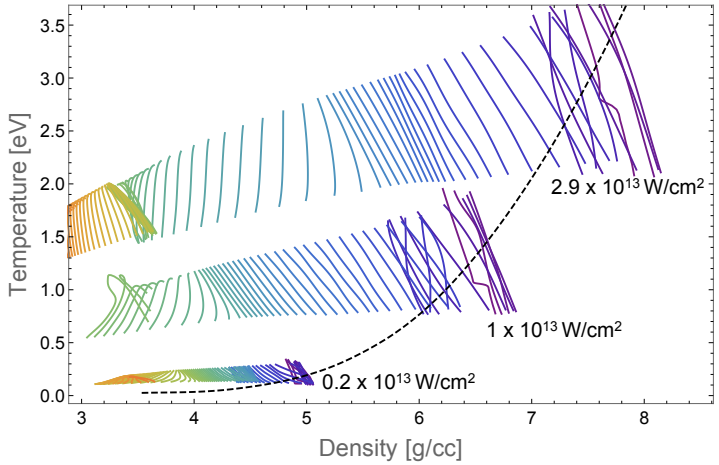

Figure 3.13: Time evolution of the thermodynamic conditions in the MgO layer obtained with MULTI simulations performed with drive laser pulses with intensities of $0.2{\cdot}10^{13}$ W/cm^2, $1{\cdot}10^{13}$ W/cm^2, $2.9{\cdot}10^{13}$ W/cm^2. Each set of lines correspond to the intensity pointed at its bottom right. Each line represents an instantaneous of the thermodynamic conditions in the MgO layer and are taken each 10 ps. Each color represent a time and the discretisation is 10 ps.

In order to understand how this temperature gradient depends on the laser intensity and evolves in time, we performed simulations for various laser intensities and we looked at the evolution of the thermodynamic conditions in the MgO layers for relatively long time windows. Fig. 3.13 represents in the T-ρ diagram the time evolution of the thermodynamic conditions of the MgO layer obtained with the simulations for three laser intensities: $0.2 \cdot 10^{13}$ W/cm^2, $1 \cdot 10^{13}$ W/cm^2, $2.9 \cdot 10^{13}$ W/cm^2. Each line represents the T-ρ conditions in the MgO layer at a certain time. The time delay

between each line is 10 ps. This graph points that the temperature is almost uniform for an intensity of $0.2{\cdot}10^{13}$W/cm^2, while it is significantly inhomogeneous for $1{\cdot}10^{13}$ W/cm^2 and $2.9{\cdot}10^{13}$ W/cm^2. On the contrary the density gradient does not depend as strongly on the laser intensity and it is more linked to the hydrodynamic (like e.g. the occurrence of re-shock). Moreover this graph underlines that the temperature decreases much slower than the density with time, as expected for a material in release. The time evolutions of the density and temperature gradients are shown in graph 3.14.

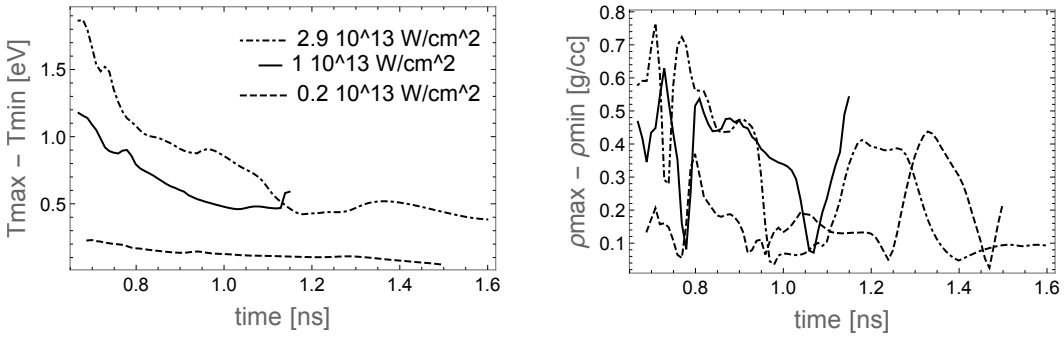

Figure 3.14: Time evolutions of the density and temperature gradients in the MgO layer of the sample obtained with MULTI simulations for three laser intensity: $0.2{\cdot}10^{13}$ W/cm^2, $1{\cdot}10^{13}$ W/cm^2, $2.9{\cdot}10^{13}$ W/cm^2.

A consequence of the behaviour shown here is that the uncertainty over the temperature is linked to this temperature inhomogeneity, while the uncertainty over the density is linked to the uncertainty in the time delay as the density decreases with time quite fast. We report in fig. 3.15 the method used to evaluate the error bars from our simulations. The red line represents the T-ρ conditions in the MgO layer at the probe time. Green lines represent the conditions in a time window corresponding to the time delay uncertainty. It is clear from the figure that the error on the temperature mainly depends on the temperature gradient, while the error on the pressure mainly depends on the uncertainty on the time delay. Therefore to reduce uncertainties on the pressure, it is necessary to improve the method of determination of the time delays, while the only way to reduce the uncertainty on the temperature is to design another target, putting a material between the CH and MgO with a good X-ray transmission at 1.3 keV but that shields the X-rays from the plasma corona (impossible for X-rays emitted at energy close to the Mg K edge energy) and does not get too hotter than the MgO for a given laser intensity.

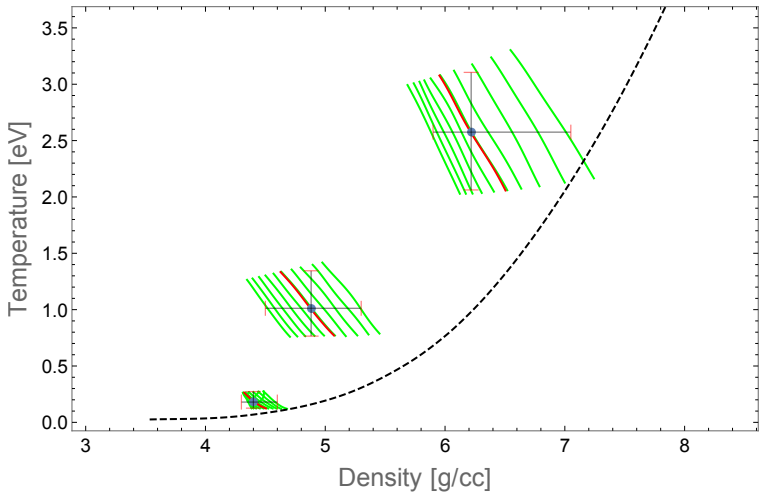

Figure 3.15: Evaluation of the error bars for three shots (68, 76 and 84)

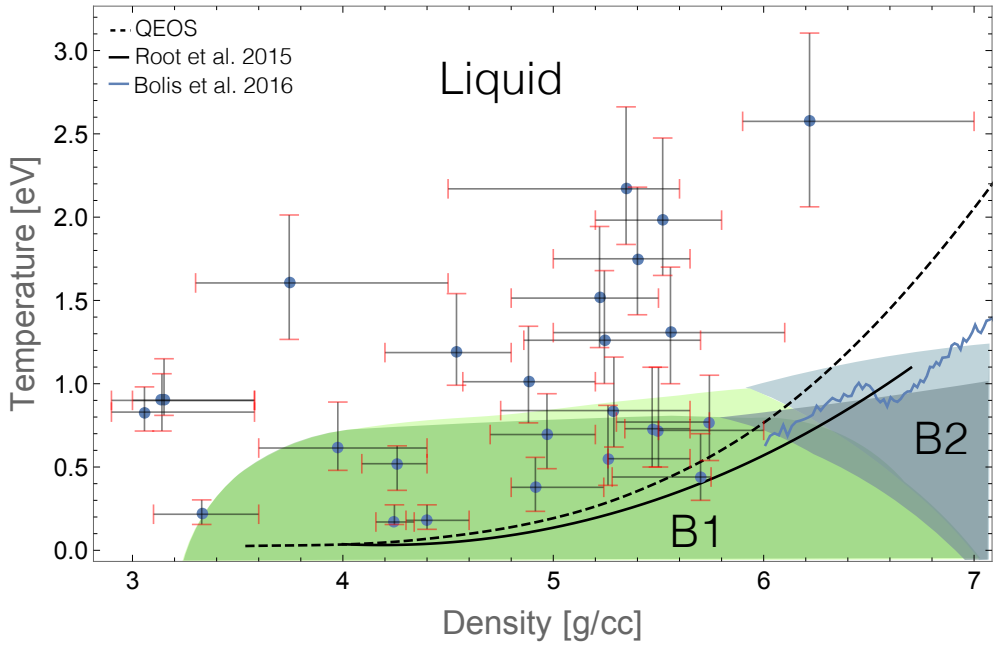

Figure 3.16: Thermodynamic conditions probed with the absorption spectroscopy (blue dots) represented on the MgO phase diagram. The dotted line represent the QEOS shock hugoniot in the ρ-T plane, while the black continuos line represent the one proposed by [Root et al.]. The blue curve represent the points explored by [Bolis et al., 2016].

Finally fig. 3.16 presents the hydrodynamic conditions explored, as deduced by MULTI simulations. As shown, all our explored conditions lie at lower densities than

the Hugoniot. This is because, as we already mentioned, it is quite difficult to tune the timing to probe the secondary hugoniot states. The explored density range varies between 3 and 6 g/cc, while the temperature range varies between 0.2 and 2.5 eV. As shown, most spectra have been collected for conditions in the liquid phase of MgO. Then a significant number has been collected in the B1 solid phase, and there are few points close to the B1-B2 phase boundaries. The large range of explored densities and temperatures will allow to characterise general behaviour of the spectra with increasing temperature, increasing density and different MgO phases in order to infer a general picture of the MgO structural and electronic property changes in the phase diagram.

3.3.2 Analysis of the XANES spectra

3.3.2.1 Spectral calibration and spectral resolution

The spectral calibration has been performed using the K shell tabulated lines of various elements: Mg, Na (first order line) and Cl (second order line). To this aim we performed some shots with the probe beam only and using MgO and NaCl samples as back-lighters.
The spectral resolution is limited by various elements:

- typically the FWHM of the rocking curve of an RbAP crystal is $\sim$ 1 eV [Beck et al., 1995];
- the size of the X ray source which contributes to the final spectral resolution with 0.2 eV;
- the IP scanner spatial resolution and the reproducibility of the IP position shot to shot contributes to a broadening of the spectral resolution of 0.5 eV.

Therefore the minimum ΔE that theoretically we can resolve is $\sim$ 1.1 eV. In sec 3.4.1.1 we will experimentally determine the spectrometer response comparing the MgO XANES spectra measured in this experiment and the MgO xanes spectra measured at a synchrotron [Yoshimura et al., 2013] (where they could resolve down to 250 meV at 1300 eV).

3.3.2.2 Calculation of the spectra procedure

The analysis of the data collected by the spectrometers has been performed by F. Dorchies and N. Jourdain (CELIA, Bordeaux), using a method similar to [Levy et al., 2010]. We report here a description of the procedure followed to obtain the XANES absorption spectra:

1) For each shot we collected a signal both with the reference spectrometer and with the transmission spectrometer. The reference spectrometer collects the signal as it is produced by the X-source, while the transmission spectrometer collects the signal produced by the X-ray source and transmitted through the sample at TCC (chamber center).

2) The first issue to solve is to get rid of the imprints of the crystal reflectivity defects collected on the IP. To this aim a signal for both the spectrometers has been collected during a shot without the target at TCC. Dividing the signal obtained with targets at TCC by such signals, allows to get reference and transmission spectrometer images without the crystal defect imprints.

3) Then the corrected transmission signal is divided by the corrected reference signal. This ratio corresponds to the target transmission T_{target}. This process is repeated for each shot as the X-ray source is not stable shot to shot. The $-lnT_{target}$ gives the absolute absorption of the target A_{target}.

4) As we want to determine the absorption of the MgO layer we need to take out from A_{target} the contributions given by the CH, B and diamond layers, that do not absorbe the X-rays constantly in the considered range of energies but contribute with a monotonic slope to the total absorption. This background was determined and subtracted looking at the slope before the Mg K edge in the A_{target} absorption spectra. We hence obtain the absorption of the MgO layer A_{MgO}.

5) Further corrections are needed for the shots performed with intense drive beam. We will detail such corrections in the following.

3.3.2.3 Problems caused by the "ns emission"

As the shock wave generation requires a drive beam with a high intensity, the temperature of the plasma corona produced during the drive laser - target interaction is quite high ($\sim$ 1 keV). This implies a significant emission from plasma corona in the X-UV spectral region that causes two problems. The first problem is due to the X-ray emission that is collected by the transmission spectrometer after the propagation through the shocked sample ("ns emission problem"). The second problem is due to the X-UV emission that goes toward the backlighter vaporising its surface.

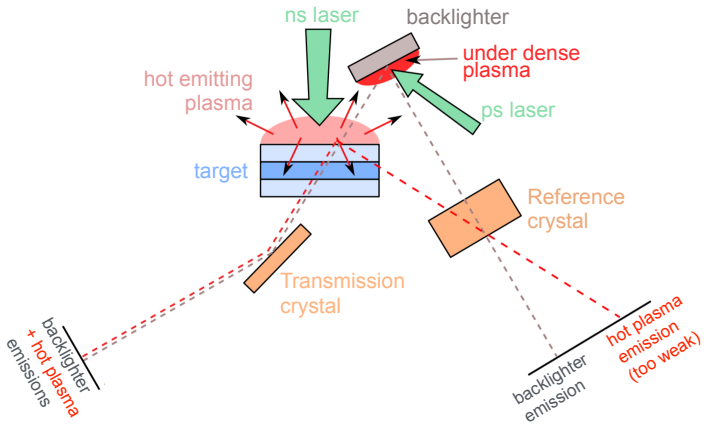

Figure 3.17: Conceptual scheme of the problems induced by the ns emission.

First problem: "ns emission" through the sample As we already said the plasma corona is heated up to high temperatures ($\sim$ 1 keV) and this causes a not negligible ns emission in the energy range we are interested in (1.26-1.4 eV). The ns emission transmitted through the sample is collected by the transmission spectrometer. The problem is that the ns emission follows the same axis as the X-rays produced by the backlighter. Therefore it generates a signal spatially superimposed to the one produced by the backlighter. Thus such a contribution of the ns emission must be subtracted from the measured signal in order to obtain the absorption spectra of ps backlight.
This problem had been identified also in other experimental campaigns [Festa, 2013; Denoeud, 2014] and it was solved thanks to the detection of the ns emission on the reference spectrometer. Unfortunately in the present experiment, this was not possible. Indeed in our experiment, the backlight emission (that arrives directly at the reference spectrometer and therefore with high intensity) induces a noise on the reference spectrometer that masks the ns emission. Therefore in order to characterise the contribution of the ns emission we used the transmission spectrometer performing some shots with only the drive beam on the MgO sample for various laser intensities. The spectral shape of the signals was very stable shot to shot only varying in amplitude. Such stability of the spectral shape implies that the ns emission can be subtracted if its amplitude is known. Unfortunately the amplitude of the ns contribution with respect to the signal did not depend only on the laser energy, but also on the target thicknesses and on the fluctuations of the X-ray source. Therefore it has been necessary to characterise the amplitude of the contribution of the ns emission shot to shot from the signal measured during the ps + ns shots.

To this aim, coherently with the fact that the ns emission source (the plasma corona) is closer to the transmission spectrometer than the X-ray source we noticed that the signal contribution produced by the ns beam only and ps beam only were spatially different (see fig. 3.18 on the left). Analysing the spatial profile of the signals produced for ns+ps beam shots we noticed that the more the amplitude of the ns emission the more the spatial shape of the signal approaches the one obtained with the ns beam only and vice-versa.

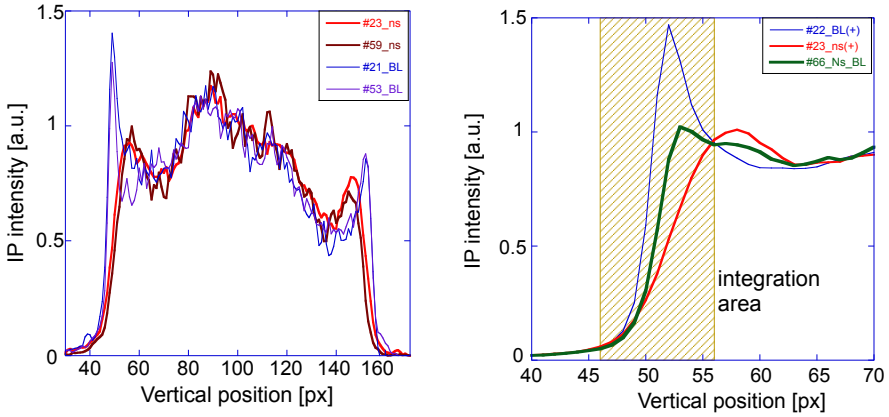

Figure 3.18: On the left: vertical lineouts of the transmission spectra obtained in a region of 50 pixels around the Mg K edge for two shots performed with the ps beam only (21 and 53) and two shots performed with the ns beam only (23 and 59). On the right: zoom on the vertical lin-eot edge for a shot performed with the ps beam only (blue), a shot performed with a ns beam only (red) and a shot performed with both beams (green).

Hence we evaluated the amplitude of the ns emission from a quantitative estimation of the differences in the normalised spatial line-outs of the signal. To this aim, we integrated the area subtended by the edges of the lineouts, as shown in fig. 3.18 on the right. We define the ns emission amplitude parameter η which values 0 for shot performed with only the ps beam, and 1 for shot performed only with the ns beam:

$$\eta = 1 - (I_{MeasPeak} - I_{NsPeak})/(I_{BcklPeak} - I_{NsPeak}) \tag{3.1}$$

where $I_{MeasPeak}$ represents the result of the integral of the edge of the ns+ps shot under analysis, I_{NsPeak}= 4.33 $\pm$ 0.54 pixels and $I_{BcklPeak}$ = 8.95 $\pm$ 0.35 pixels are obtained from the average of the integrals calculated for the shots performed with the ns beam only and the ps beam only respectively. Therefore the corrected transmission of the MgO layer is given by $T_{MgOcorr} = (T_{MgO} - \eta \cdot T_{ns})$ where T_{ns} is the normalised transmission of the ns emission characterised with the drive beam only shots. With

the natural logarithm $-ln(T_{MgOcorr})$ we obtain the normalised absorption corrected $A_{MgOcorr}$ from the ns emission.
The ingenious procedure to characterise the ns emission and to correct the measured spectra has been ideated, performed and successfully tested for shots with ps beam only and for shots with ns beam only (for which we know the results: 0 and 1 respectively) by F. Dorchies and N. Jourdain.

3.3.2.4 Second problem: "ns emission" toward the backlighter

This problem emerges from the interaction between the X-UV emission from the plasma corona and the backlighter. This emission irradiates the backlighter with a significant flux. With a 100 J laser pulse we can obtain a flux $\sim$ 1-2 J/cm^2 (considering that the 10% of the laser energy is converted in X-ray-UV). Such a flux is sufficiently high to vaporise and/or ionise a layer of the backlighter and after some hundreds ps a low density layer forms. Hence the ps beam interacts with an underdense plasma which induces an X-ray emission with steeper emission lines. Moreover the emission lines are anisotropically re-absorbed by the plasma itself.
Such a problem has been already observed during a similar experiment on SiO_2 [Denoeud, 2014]. Therefore we verified whether this phenomenon occurred by performing some measurements with the reference spectrometer driving shocks on MgO targets. Figure 3.19 compares the reference spectrometer signals obtained without a sample at TCC and driving a shock on a sample (drive pulse: 110 J, 600 μm and 500 ps; delay between the pulses= 600 ps). For both shots we used a Sm backlighter. As shown in the figure the reference spectrum obtained with the shocked targets exhibits some lines that do not occur for the shot with the probe beam only.

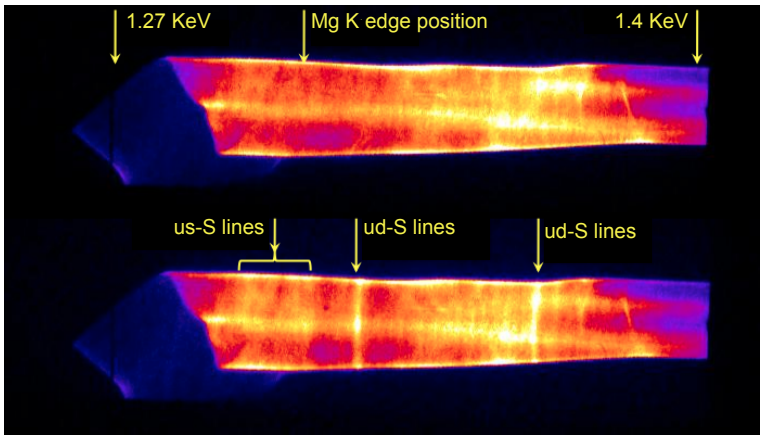

Figure 3.19: Reference spectrometer signals obtained with a Sm backlighter without a sample at TCC (top) and driving a shock on a sample (bottom).

A possibility to solve/reduce this problem was to place the backlighter further than 5 mm from the TCC. However this implies a smaller flux of the X-ray produced by the backlighter through the sample and hence less signal on the transmission spectrometer. As we were already low in the transmission intensity we decided to choose another strategy.
We looked for a material that does not present these lines in the explored spectral range. We found out that Gadolinium satisfied our necessities. Indeed performing a measurement on shocked MgO (drive beam: 110 J, 600 μm and 500 ps; delay between the pulses= 600 ps) with the Gd emission we did not observe any under dense plasma lines.
We therefore chose Gd as the backlighter for this experiment.

3.4 Results

In this section we present the XANES spectra obtained during this experimental campaign.
The section is organised as it follows:

- Subsec. 3.4.1 presents:
  - the spectrum obtained on MgO at standard conditions in comparison with literature results;
  - an evaluation of the MgO preheating induced by plasma corona using XANES.
- Subsec. 3.4.2 presents:
  - XANES spectra obtained on shocked MgO along isotherms and isochores;
  - a preliminary interpretation of the spectra behaviour based on a comparison with SiO_2.

3.4.1 Cold spectra, comparison with literature and evaluation of the preheating

3.4.1.1 Reproducibility of cold spectra and comparison with literature

XANES spectra obtained with three independent measurements on MgO at standard conditions are shown in fig. 3.20, exhibiting a good reproducibility. Moreover at the left of fig 3.20 they are compared with results obtained on synchrotron [Nemausat et al., 2015; Yoshimura et al., 2013]. Our spectra are normalised to the high energy part (@ 1.4 eV) of the spectra.
The spectra are qualitatively in good agreement although there are two significant differences:

1) our data do not exhibit the feature A evident on the synchrotron data. However a synchrotron signal has a better energy resolution (e.g. [Yoshimura et al., 2013]: 250 meV/1300 eV = $2 \cdot 10^{-4}$) with respect to the one of our measurements. Therefore we convolved the synchrotron spectra with a gaussian varying the FWHM in order to reproduce our data. We found that the results of a convolution with a gaussian with FWHM=3.53 eV reproduce well our data, as shown in fig. 3.20 on the right. We can see that with the convolutions the difference relative to peak A disappears. This means that with our resolution we cannot resolve peak A. We can consider this gaussian as the response of our spectrometer and its FWHM = 3.53 eV as its resolution. Such estimation of the

resolution gives a higher values than the theoretical one reported in paragraph 3.3.2.1).

2) the structures of the spectra of Yoshimura et al. [2013] have different amplitudes than ours. We believe that this is due to a different normalisation. Indeed we normalised to the furthest region of our spectra (around 1.4 keV), i.e. in a spectral region not characterised by Yoshimura et al. [2013].

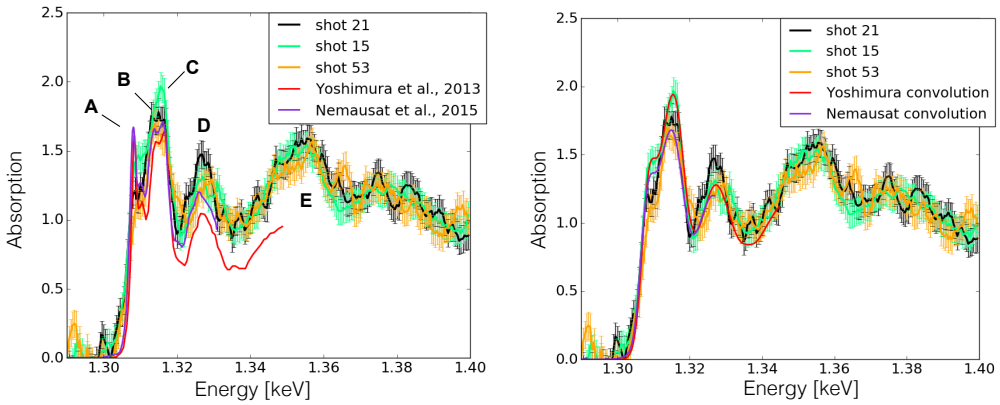

Figure 3.20: Absorption spectra of MgO at standard conditions compared with spectra measured at synchrotron [Nemausat et al., 2015; Yoshimura et al., 2013] (on the left), and compared with the same spectra convolved with a gaussian with a FWHM=3.53.

3.4.1.2 Study of preheating

For high drive intensities the MgO could be preheated by the X-rays emitted by the plasma corona. We already discussed the importance of such preheating for our study: MULTI simulations reported in sec. 3.3.1.2 evidenced that the temperature gradient in the MgO layer is in part due to the MgO preheating.
Fig. 3.21 shows the MULTI temperature profiles of MgO before the shock arrival for different drive laser intensities: $0.2{\cdot}10^{13}$ W/cm^2, $1{\cdot}10^{13}$ W/cm^2, $2{\cdot}10^{13}$ W/cm^2 and $2.7{\cdot}10^{13}$ W/cm^2. As shown, the higher the laser intensity the stronger the effect of preheating.
However the estimation of preheating obtained with hydrodynamic code depends on the opacity tables used in the code. Therefore its reliability is correlated to the goodness of the opacity model used to calculate the tables. Then it is worth to estimate preheating with another independent method.

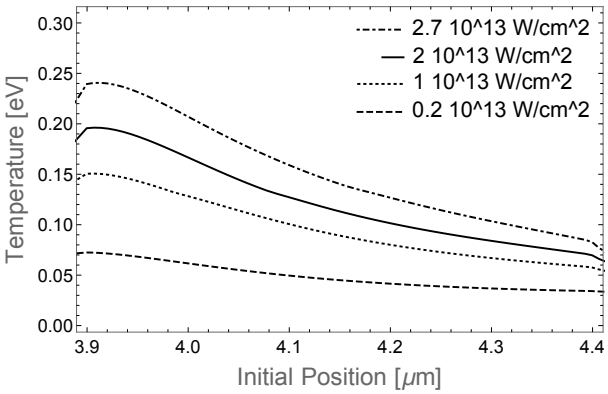

Figure 3.21: MULTI temperature profile versus MgO initial position for time just before (around 10 ps before) that the shock enters in the MgO for various laser intensities: $0.2{\cdot}10^{13}$ W/cm^2, $1{\cdot}10^{13}$ W/cm^2, $2{\cdot}10^{13}$ W/cm^2 and $2.7{\cdot}10^{13}$ W/cm^2.

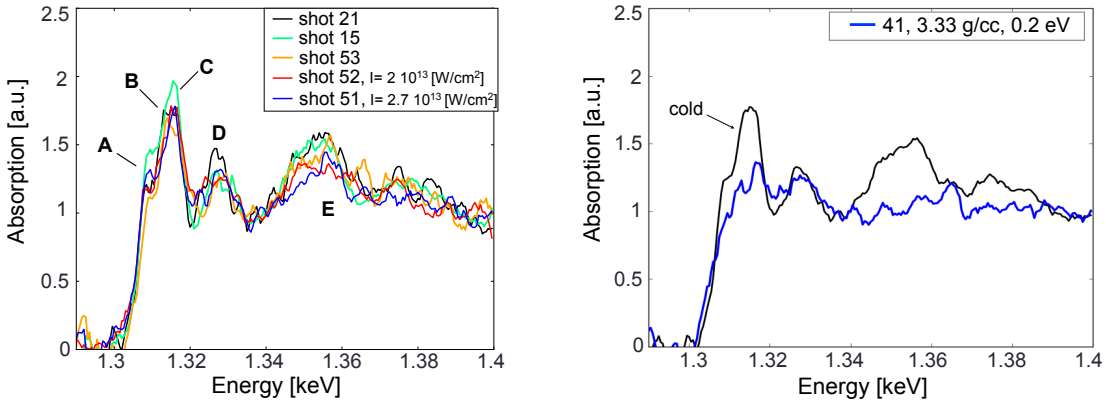

Figure 3.22: On the left study of the preheating: absorption spectra of MgO at standard conditions are compared to those obtained with shots 51 and 52 performed with a drive beam intensities 2.7 10^{13} W/cm^2 and 2. 10^{13} W/cm^2 respectively and time delays set to probe the MgO before that was reached by the shock. On the right: comparison between a XANES spectra at standard conditions and a spectra obtained for MgO at 3.3 g/cc and 0.2 eV

To this aim, we performed an experimental investigation using XANES. We performed two shots (51 and 52) probing MgO just before the shock arrival. Drive laser intensities used for shots 51 and 52 were $2.7{\cdot}10^{13}$ W/cm^2 and $2{\cdot}10^{13}$ W/cm^2 respectively. The spectra obtained with shots 51 and 52 are shown in fig. 3.22 (left) in comparison with standard MgO spectra (15, 21, 53). Spectra 51 and 52 exhibit all the structures of the spectra at standard conditions. The only difference is that peak E is less pronounced, especially for shot 51. Fig. 3.22 on the right compares a XANES

spectrum of MgO at standard conditions (s.c.) and a XANES spectrum of MgO at 3.3 g/cc - 0.2 eV (obtained in this experimental campaign). The figure evidences that differences from the spectrum at s.c. are more important for the spectrum at 3.3 g/cc - 0.2 eV than for spectra 51 and 52. We can therefore conclude that the preheating for shot performed with the highest laser intensities (I=$2.7{\cdot}10^{13}$ W/cm^2) is << 0.2 eV. This result suggest that MULTI simulations overestimate the effect of preheating.

3.4.2 Spectra of shock compressed MgO: reproducibility, behaviours along isotherms and isochores.

As already mentioned, in this section we present the XANES spectra obtained on shocked compressed MgO. The large amount of explored conditions allowed us to study separately the effect of the temperature and the effect of the density on the XANES spectra. In this analysis there are two key points that are linked to important physical processes:

1) K-edge energy position and broadening;

2) spectral structures.

K-edge energy position are related to the energy difference between core states (E_{1s}) and the lowest unoccupied states. In the case of a dielectric the lowest unoccupied states belong to the conduction band. Therefore, for a dielectric, XANES measures the transition from core state to the conduction band (see fig. 3.23 on the right). In the case of a metal, lowest unoccupied states are energetically located close to the Fermi energy and therefore XANES measures electronic transitions from core states to the Fermi energy[4] (see fig. 3.23 on the left). In some cases, changes in the position of the edge are correlated to transition from a dielectric to a metal [Denoeud et al., 2014].
The K-edge broadening is correlated to the broadening of the conduction band edge. XANES spectral structures derive from two contributions: the shape of the unoccupied electronic bands and the multiple scattering. Patterns produced by the multiple scattering are linked to the local order of the investigated sample. Therefore XANES spectral structures may give structural information at a local level about the investigated sample.

[4]In this thesis as typical of WDM literature we will speak of Fermi level or Fermi energy also for T> 0.

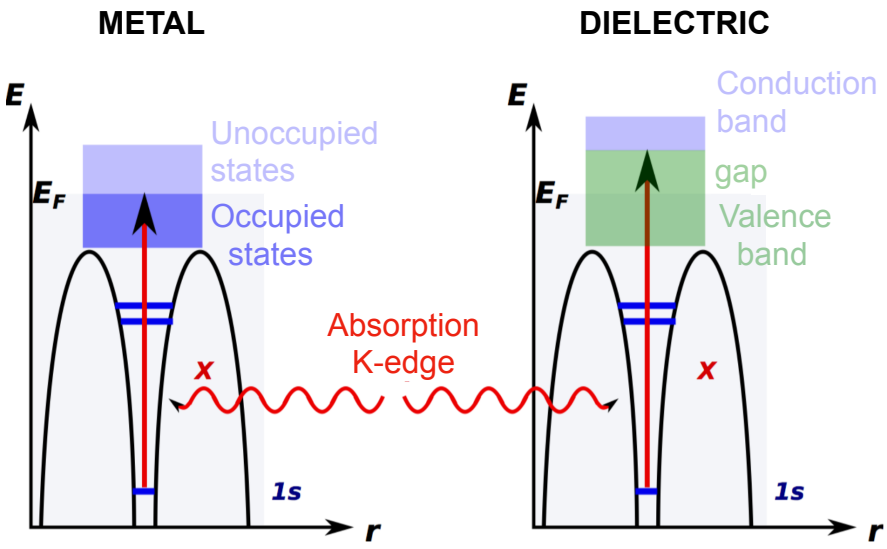

Figure 3.23: Scheme of XANES for a dielectric and a metal.

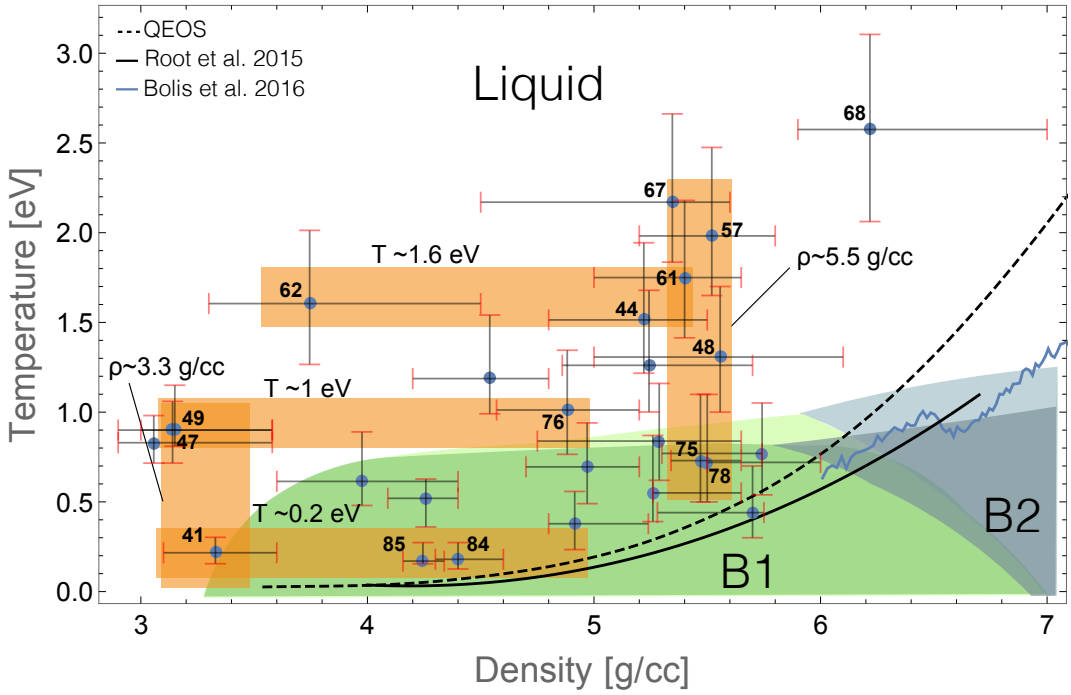

Figure 3.24: Thermodynamic conditions probed with the absorption spectroscopy (blue dots) represented on the MgO phase diagram. The orange areas point the selected isochores and isotherms.

After a brief discussion about the reproducibility of our spectra, we will present the measured spectra. For studying the effect of the temperature we will analyse spectra along selected isochores, while for studying the effect of the density we will look at spectra along selected isotherms. As isotherms we selected a set of probed conditions at 0.2 eV, ∼1 eV and ∼1.6 eV, while as isochores we selected series of spectra for ρ ∼3.3 g/cc (i.e. close to the MgO sample standard density) and $\rho \sim$ 5.5 g/cc. The selected isotherms and isochores are represented in fig. 3.24.

3.4.2.1 Reproducibility of shocked MgO spectra

The reproducibility of the spectra obtained on shocked MgO can be tested comparing the spectra whose thermodynamic conditions are similar. Fig. 3.25 shows the XANES spectra of MgO at $\sim$ 3.1 g/cc and $\sim$ 10000 K. The shown spectra are in excellent agreement validating this experimental approach for XANES spectroscopy on laser shocked MgO.

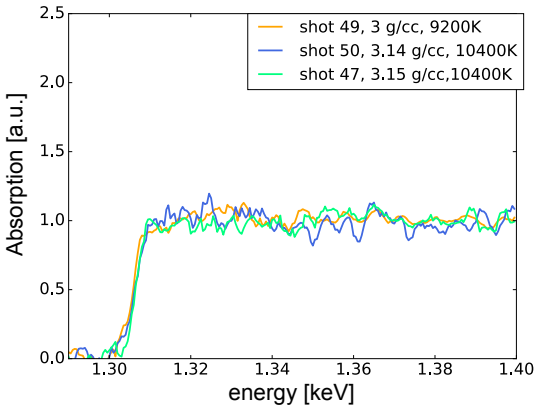

Figure 3.25: On the left: Absorption spectra measured during shots 50, 47 and 49 which compressed the MgO to the same thermodynamic conditions: $\sim$ 3 g/cc and $\sim$ 10000K.

3.4.2.2 XANES spectra behaviours along isochores and isotherms

Behaviour as a function of the density Fig. 3.26 presents the spectra of MgO at conditions along the isotherm at $\sim$ 0.2 eV in comparison with the spectrum of MgO at standard condition (black line). Shots 84 and 85 produced conditions in the B1 solid phase. Conditions obtained with shot 41 are very close to the boundary between the B1 and the liquid phase. This may imply that this spectrum is a superimposition of the contributions from the B1 phase and from the liquid phase. However all the

spectra clearly present structures B-C (slightly blue-shifted for shots 41 and 85) and spectra 41 and 84 exhibit also peak D. These measurements are coherent with spectra measured for MgO in the solid phase and demonstrate that our method is capable of detecting XANES structures for shock compressed MgO.

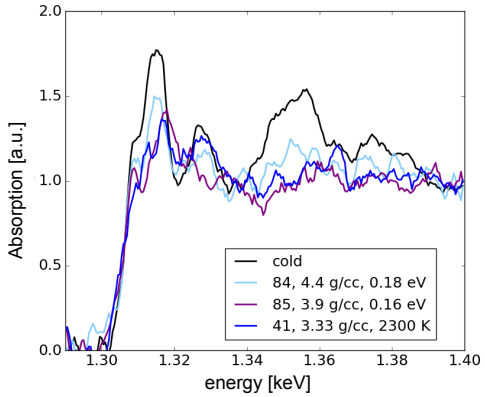

Figure 3.26: Xanes spectra obtained along the isotherm at 0.2 eV, i.e. in the solid phase.

Fig. 3.27 shows the spectra obtained along two isotherms above the melting line: at $\sim$ 1 eV (i.e. just above the melting line) and at $\sim$ 1.6 eV. All the spectra are compared to the spectra of MgO at standard conditions (black line). It is interesting that no one of the reported spectra exhibits any of the structures typical of the cold or solid MgO. On the contrary all the spectra in the liquid are flat. This also means the density increase does not re-structure any of the shown spectra. Moreover these series do not exhibit K edge shifts nor broadenings.

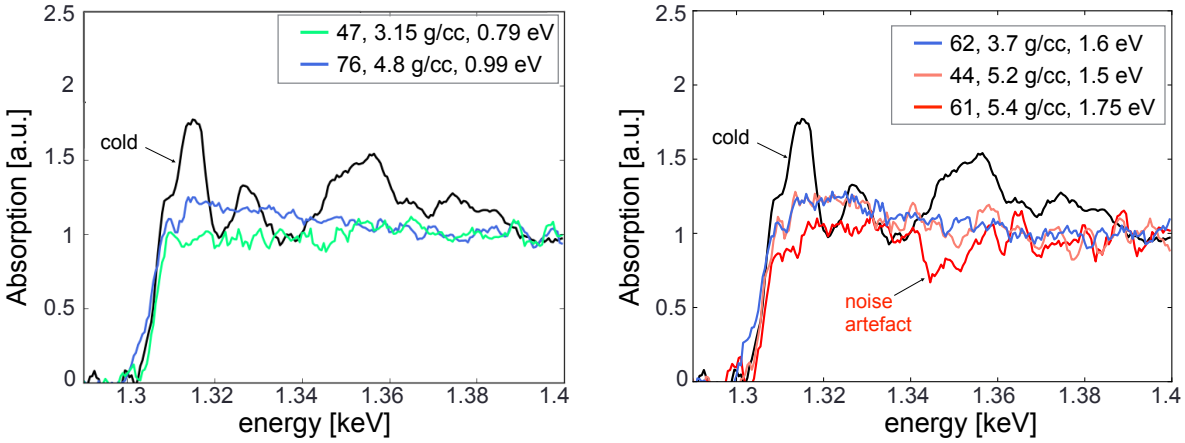

Figure 3.27: Xanes spectra obtained along the selected isochores: $\sim$ 1 eV on the left, $\sim$ 1.6 eV on the right

Interestingly, the only series that present structured spectra is the one in the solid phase, while spectra in liquid MgO are unstructured already at 1 eV. Therefore liquid spectra seem to be characterised by the absence of structures in the probed energy range. To further investigate this point we looked at the behaviour of the spectra with increasing temperature.

Behaviour as a function of the temperature To investigate the effect of the temperature we selected spectra along two isochores: at $\sim$ 3.3 g/cc (i.e. close to the standard density of MgO) and at $\sim$ 5.5 g/cc. The selected spectra are shown in fig. 3.28. All the spectra are compared to the spectra of MgO at standard conditions (black line).

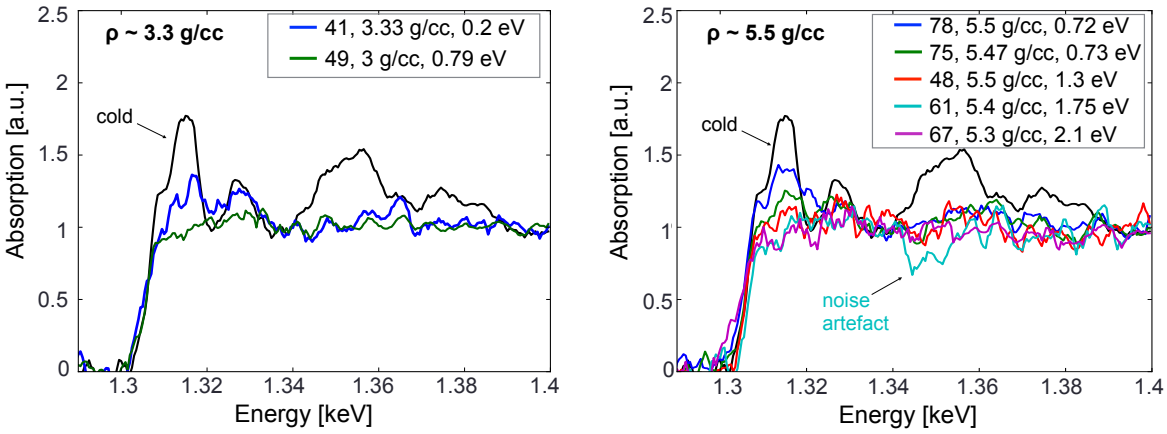

Figure 3.28: Xanes spectra obtained along the selected isochores: $\sim$ 3.3 g/cc on the left, $\sim$ 5.5 g/cc on the right

The series of spectra at $\sim$ 3.3 g/cc evidences that the temperature has the effect of reducing the spectral structures. As shown before, spectrum at 0.2 eV (shot 41) exhibits slight structures corresponding to peak B-C and D. The spectrum at higher temperature 0.79 eV (shot 49, for sure in the liquid phase) is not structured at all. The two spectra exhibit the Mg K edge always at the same energy and there is not a significant broadening of the edge.
Isochore at $\sim$ 5.5 g/cc presents a similar behaviour. Spectrum 75 (obtained on solid MgO, B1 phase) clearly exhibits a structure corresponding to the merge of peak B and C. For higher temperatures, structures disappear. Again spectra in the liquid phase (corresponding to shots 48, 61 and 67) are flat. As in the isochore at $\sim$ 3.3 g/cc,

all the spectra shows the Mg K edge at the same energy. The spectrum measured at the highest temperature (shot 67, at $\sim$ 2.1 eV) shows a slight edge broadening (the foot of the edge redshifts of about $\sim$ 4.5 eV).

Sum up and conclusion The main observations presented in this section for spectra along isotherms and isochores are summarised in table 3.1.

Summary Table

	Effect of T	Effect of ρ
Edge shift:	No	No
Edge broadening:	slight for T>2.1 eV	No
Spectral shape:	Loss of spectral structures	No structuration
Spectra in the liquid:	Flat	Flat

Table 3.1

We already mentioned that the position of the XANES K-edge is given by the energy difference between the core states and the lowest unoccupied states. Therefore the fact that the K-edge lies always at the same energy points that such difference does not change. The density is expected to modify both the energies of core state E_{1s} and of lowest unoccupied states E_{lus}. Therefore our observations would suggest that E_{1s} and E_{lus} vary of the same quantity for a density increase. What concerns the temperature is a bit more interesting. Indeed the temperature is not supposed to modify the energy of core states. Assuming that this is the case, the fact that the K-edge lies always at the same energy for spectra in the liquid and in the solid phase would imply that the lowest unoccupied state does not move significantly in energy ($<$ 3.5 eV, as our resolution is $\sim$ 3.5 eV/1300 eV) at melting.
Concerning the flatness of the spectra in the liquid phase, we already commented that structures on the XANES spectra are linked to multiple scattering and therefore to the local order of the investigated sample. The absence of structures in the XANES spectra of liquid therefore may suggest that liquid MgO is locally disordered.

3.4.2.3 A first qualitative interpretation from a comparison with SiO_2.

In this section, we give a preliminary interpretation on the basis of a comparison between the behaviours observed here for the MgO and those recently observed for the SiO_2 [Denoeud et al., 2014, 2016a].
Denoeud [2014], Denoeud et al. [2014, 2016a] investigated the electronic and structural properties of shock compressed SiO_2 with XANES and ab initio molecular dynamics AIMD. Similarly to our study, Denoeud et al. [2014, 2016a] investigated separately

the effects of the temperature and the density on the XANES spectra (in this case @ the Si K-edge). Such studies contributed to advance in the comprehension of the metallisation behaviour of SiO_2 [Denoeud et al., 2014] and in the understanding of the structural changes occurring in liquid SiO_2 under the effect of the density [Denoeud et al., 2016a].
The behaviours of SiO_2 XANES spectra for increasing temperature or densities are significantly different from those observed here for the MgO. Differences mainly concern two points:

- spectral structures in the liquid phase (for increasing density)
- edge behaviour (for increasing temperature)

Spectral structures.
Differently from MgO, the XANES spectra of SiO_2 in the liquid phase show structures. They exhibit a peak at $\sim$ 1.34 keV which corresponds to the first peak of the cold spectrum (see fig. 3.29, from [Denoeud et al., 2016a]). Such peak is linked to the Si-O correlations and its occurrence in the liquid phase suggests that atoms are still locally organised as Si-O polyhedra (tetrahedra at standard density). In addition to that, Denoeud et al. [2016a] observed that the density has the effect of blue-shifting this first peak (see fig. 3.29). AIMD evidenced that such shift occurs together with a change in the Si-O coordination number [Denoeud et al., 2016a]. This underlines the link between the first peak and the Si-O correlation.

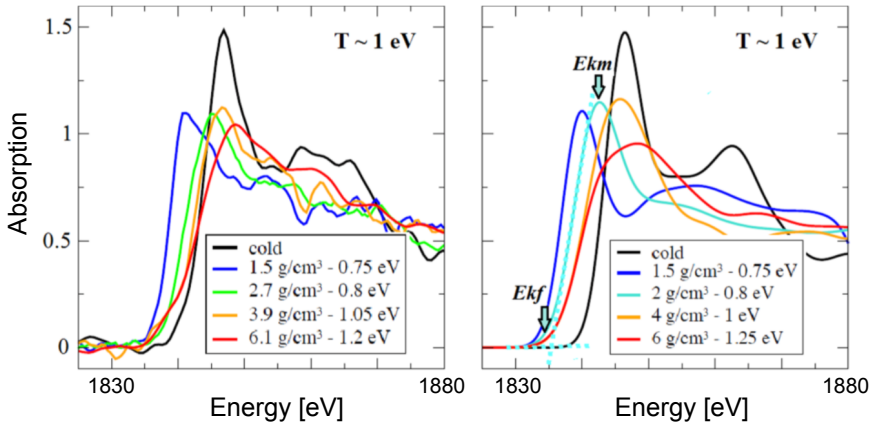

Figure 3.29: Experimental (left) and theoretical (right) SiO_2 XANES spectra for different densities and fixed temperature ($\sim$ 1eV) as reported in [Denoeud et al., 2016a].

We mentioned that XANES spectral structures are produced by multiple scattering. This happens if the contributions of the local environments sum to each other constructively. This occurs for solids, where the local environments are always the same,

or for liquid with a local order (as the SiO_2 liquid at ambient pressure that is organised in SiO_4 tetrahedra). Indeed resonances are due to angular ordering which is maintained by the covalent or semi-covalent polyhedral structures (tetrahedra, octahedra, exc.) On the contrary, for a liquid disordered at a local level, multiple scattering contributions of local environments may not sum constructively. This results in the absence of structures in the XANES spectra. This could be the case for the MgO, in which ionic bonds with weak charges of the cations may not be strong enough to conserve a local order. Therefore differences between MgO and SiO_2 may be significantly linked to the different strength of cation-oxygen bonds. Contrarily to SiO covalent bonds or ionic with a high charge on Si ions, ionic Mg-O bonds with a low charge on Mg are not strong enough to maintain rigid polyhedral structures in the liquid phase.

Edge behaviour.
Denoeud et al. [2014] evidenced a red-shift of the Si K-edge of liquid SiO_2 with respect to the spectrum of the solid. This behaviour has been interpreted in terms of the closure of the electronic band gap. In particular [Denoeud et al., 2014] stressed that the redshift corresponds to a gap closure mechanisms that would occur by populating the gap with a high density of defect states (see fig. 3.31 right) associated to a relatively smaller shift of the energy of the core level.

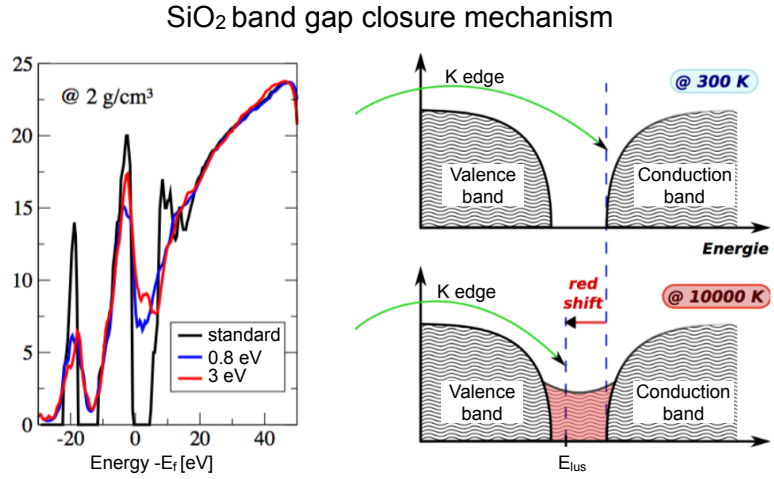

Figure 3.30: Band gap closure mechanism of SiO_2 as induced by the melting. From [Denoeud, 2014]

The loss of Si-O correlations occurring at melting induces these new electronic states energetically located in the band gap, that fill or partially fill the gap (according to the temperature). The amplitude of the redshift depends on the position of the new lowest unoccupied states (E_{lus}) which are associated to new defect configurations in

the liquid phase with respect to the one of the solid phase (see fig. 3.30) and of the relatively small shift in the energy of the core level state.
The absence of an energy shift of the Mg K edge resolvable with our 3.5 eV energy resolution reflects a smaller difference in the shifts between the first unoccupied state and the core energy level. Therefore for SiO_2, high temperature has the effect of creating local environments with stronger changes in the electronic structures if compared to what happens for MgO. For SiO_2 temperature induces the creation of new electronic states in all the band gap[5]. Instead for MgO liquid the absence of a significant K-edge energy shift suggests that new electronic states may form in the vicinity of the valence and conduction bands. For this reason we will call the MgO band gap closure mechanism "band widening mechanism" or "mechanism by band widening".

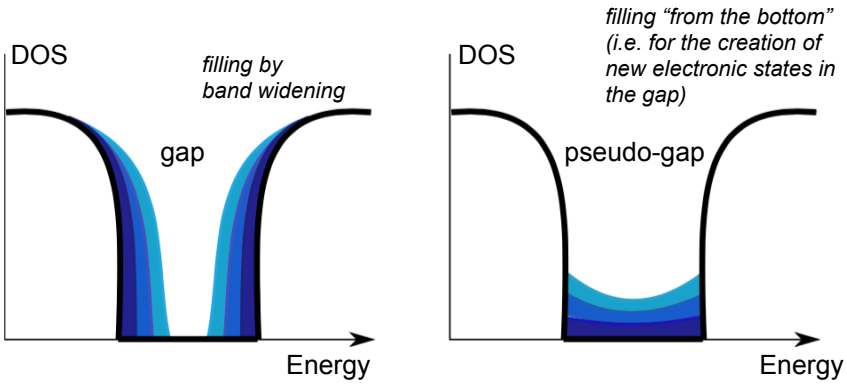

Figure 3.31: Band gap closure mechanisms induced by creation of new electronic states in the gap. The effect can appear as a widening of the conduction and valence bands (left) or a filling of the gap from the "bottom" (right).

In order to get further insights about these differences and to be able to interpret our observations in MgO, we used ab-initio simulations (performed by V. Recoules). Details will be presented in the following section.

[5] At the same time, the permanence of a majority local order in the liquid (rigid SiO_x structures, x depends on the density) is the reason why the valence and conduction bands remain narrow also in liquid SiO_2 (see fig. 3.30)

3.5 Interpretation with ab initio calculations

To understand the behaviour of measured XANES spectra, we used ab initio molecular dynamics (AIMD) simulations. AIMD is a well adapted method for studying matter in the WDM regime and it has been already successfully applied to various materials [Recoules and Mazevet, 2009; Denoeud et al., 2014; Mazevet et al., 2015; Dorchies et al., 2015; Denoeud et al., 2016a]

Fig. 3.32 represents the grid of calculated spectra. AIMD spectra and measured spectra do not lie exactly at the same ρ-T conditions. However it is possible to individuate isochores and isotherms along similar temperatures and densities respectively. This allows to compare the behaviour of experimental and theoretical spectra for increasing density or temperature. We will show that trends predicted by AIMD are the same as those that we observed experimentally. This will allow to use DoS and pair correlation functions predicted by AIMD for interpreting the behaviour of the experimental spectra with increasing temperature and density.

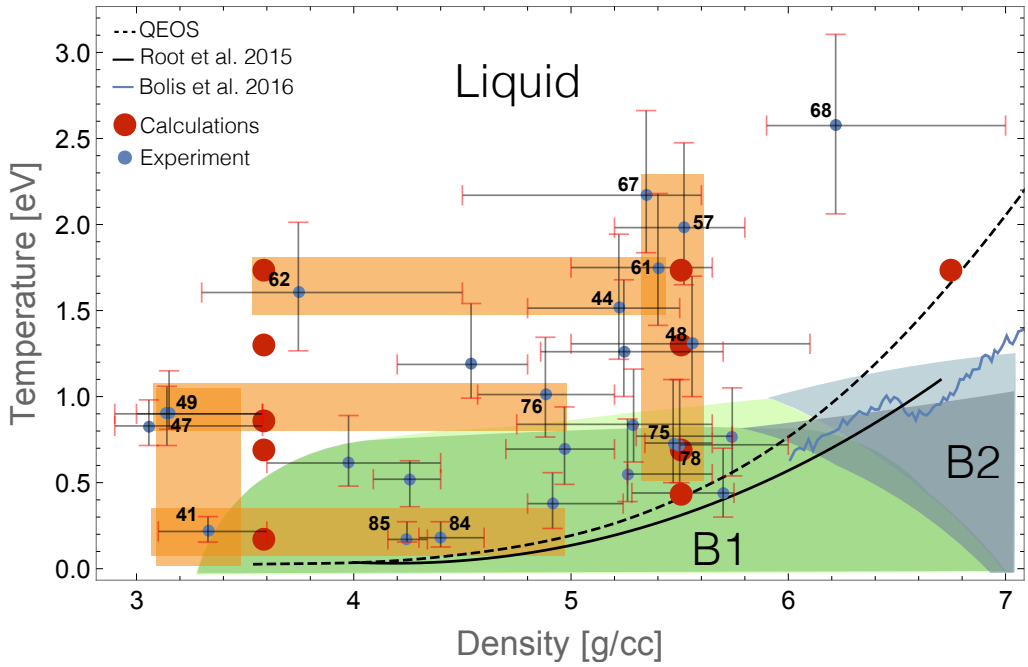

Figure 3.32: Phase diagram of MgO representing the conditions probed experimentally with XANES spectroscopy (blue dots) and investigated with AIMD (red dots).

We recall here the main experimental observations to explain:

1) The flattening of the spectra with increasing temperature and in particular for conditions above the melting line.

2) The absence of shift or broadening of the K-edge with increasing temperature.

3) The absence of shift or broadening of the K-edge with increasing density.

4) The absence of any structuration induced by the density in spectra of liquid MgO.

In order to explain points 2) and 3) we will use the density of states (DoS), as the position of the K edge measured with XANES spectroscopy is linked to the energy difference between core states and lowest unoccupied states. Looking at the evolution of the DoS will allow to explain the behaviour of the edges for increasing temperature and density.
Points 1) and 4) instead are linked to structural properties of liquid MgO. We already commented that the absence of structures in XANES spectra could be a hint that MgO melts into a disordered liquid even at the local scale. We will further investigate the structural properties of liquid MgO looking at AIMD pair correlation functions. Unfortunately pair correlation functions cannot tell us directly if Mg and O atoms are bonded or not in structures or molecules. However they give us information about the local order in the liquid.

This section is organised as it follows.

- in subsec. 3.5.1 we compare the experimental and theoretical XANES spectra obtained for MgO at standard conditions.
- in subsec 3.5.2 we present the analysis and a microscopic interpretation of the spectra behaviour along the isochores at 3.59 g/cc and 5.5 g/cc (effect of the temperature).
- in subsec 3.5.3 we present the analysis and a microscopic interpretation of the spectra behaviour along the isotherms at 0.86 eV and 1.72 eV

3.5.1 Comparison between theoretical and experimental XANES spectra at standard conditions

Fig. 3.33 compares theoretical (red) and experimental (black) XANES spectra obtained in this study for MgO at standard conditions (s.c.). It also represents the experimental XANES spectrum from [Nemausat et al., 2015] (blue line) of MgO at (s.c.). The calculation reproduces the energy position for all the calculated peaks (A, B, C, D). As already discussed, our spectra do not exhibit peak A because our spectrometers cannot resolve it.
For what concerns the amplitude of the peaks, calculations overestimate the amplitude of peak B and C and underestimate the amplitude of peak D. The same problem has been reported by [Nemausat et al., 2015], whose calculations reproduced exactly the energy positions of the peaks in the experimental spectra but not their amplitude. Despite this difference in the structure amplitudes, the agreement between experiment and calculation is qualitatively good.

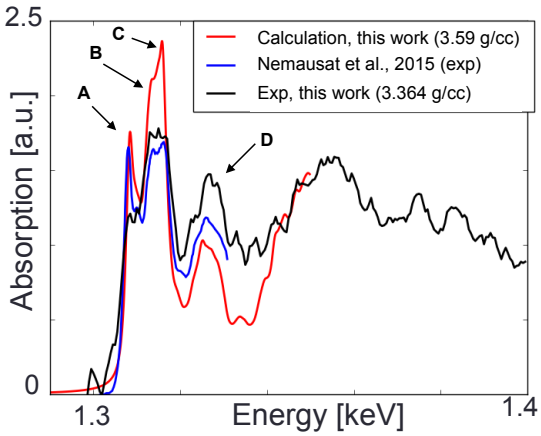

Figure 3.33: Comparison between theoretical XANES spectra and experimental ones from this work and from [Nemausat et al., 2015] for MgO at ambient conditions

3.5.2 Interpretation of the behaviour along two isochores: study of the effect of the temperature.

In this subsection we focus on the interpretation of the behaviour of the spectra for increasing temperature at fixed density. We will present the analysis for two isochores: one at $\sim$ 3.59 g/cc and one at $\sim$ 5.5 g/cc.

3.5.2.1 Isochore at 3.59 g/cc

Comparison between XANES spectra calculation and experiment Fig. 3.34 shows the comparison between experimental (on the left) and theoretical (on the right) XANES spectra along the isochore at 3.59 g/cc. Calculated and experimental spectra evidence the same behaviour. Spectra in the solid and in the liquid phases are respectively structured and flat and there is no evidence of a shift of the K-edge. The only difference between experiment and calculations is the slight edge broadening (the foot of the edge moves of $\sim$ 2.4 eV) predicted by calculations. Such broadening is however below our experimental resolution.
Therefore, thanks to this qualitative agreement between AIMD and experimental spectra, we can use AIMD pair correlation functions and the DoS for interpreting our experimental observations.

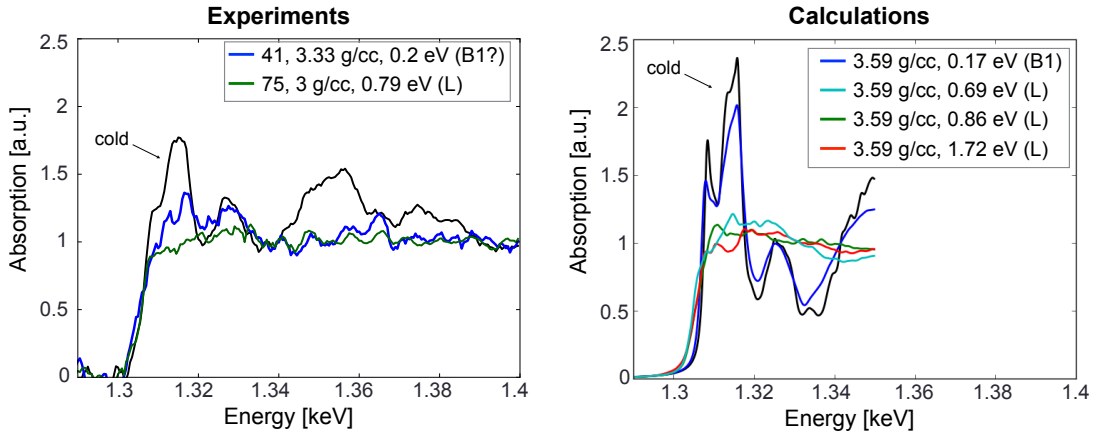

Figure 3.34: Experimental XANES spectra (left) and spectra obtained with ab-initio calculation for various temperature along the isocore at 3.59 g/cc. B1 and L denotes B1 solid phase and the liquid phase.

Density of States and electronic properties. Fig. 3.35, fig. 3.36 and 3.37 represent respectively the total, the occupied and the unoccupied DoS corresponding to calculated spectra along the isochores at 3.59 g/cc. The temperature evolutions of the total DoS (fig. 3.35) exhibit a *band gap closure* by widening of the valence and conduction bands (see sec. 3.4.2.3 for definition), in agreement with what reported in a recent theoretical work [Musella, 2016]. This widening suggests that defects populate the energy band gap like in SiO_2 but that in MgO, unlike in SiO_2, the electronic structures of these defects are electronically close to normal MgO. This is also intuitively coherent with a smaller edge shift and confirms the hypothesis presented

in sec. 3.4.2.3 (see fig. 3.31). Moreover these calculations seems to suggest that, as in SiO_2, melting and band gap closure are correlated in MgO. Indeed at 0.17 eV (i.e. solid phase) the conduction band shifts and widens significantly reducing the gap, but without closing it. Instead for conditions above the melting the effect is more significant and the band gap is then closed. Evaluations of the conductivity are ongoing to verify whether MgO melts into a reflecting liquid along the Hugoniot or not as observed in the decaying shock experiment (chapter 2).

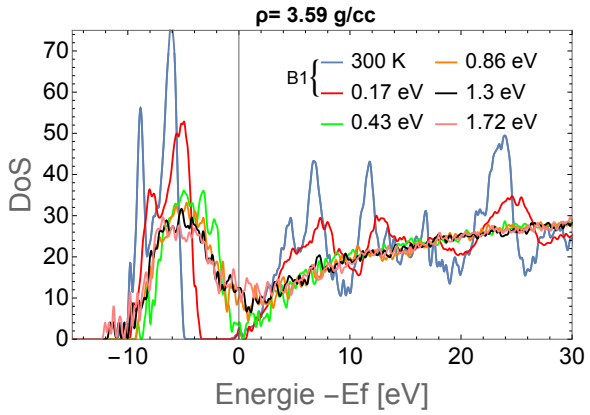

Figure 3.35: Density of states for various temperature along the isocore at 3.59 g/cc.

The *K edge evolution* reflects the behaviour of the bands. Indeed we recall that XANES is a measurement of transition from core to first empty states. Therefore broadening and shift of the Mg K edge can be explained looking at the evolution of the unoccupied density of states for increasing temperatures shown in fig. 3.36.
The conduction band broadens slightly (the foot of the edge moves of $\sim$ 3 eV, see fig. 3.34 on the right) with the temperature and at melting. This therefore explains our experimental observations: with a resolutions of 3.5 eV /1300 eV we could not resolve such broadening.
Concerning the shift of the K edge, its occurrence depends on the changes of the energy position of the first unoccupied states relatively to the core states. Calculations do not predict a significant variation (< 2.5 eV) of the lowest unoccupied state energy for spectra in the liquid phase[6] with respect to those in the solid. As the temperature is not expected to have a significant effect on the energy of core states neither, this explains the experimental observation that the Mg K edge has the same energy both for spectra in the liquid and in the solid phases. Moreover this evidences that for

[6]For spectra in the liquid phase calculated energies of the lowest unoccupied states are closed to the Fermi energy

MgO the widening of the bands does not imply a significant shift of the energy of the lowest unoccupied states in the studied temperature range. This is consistent with the fact that the electronic structure of the defect states is not so different from that of normal MgO.

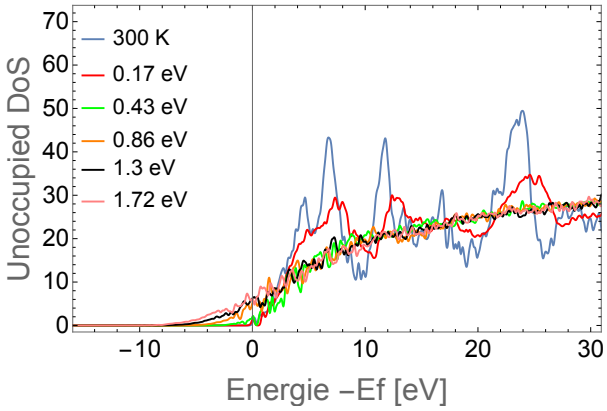

Figure 3.36: Unoccupied DoS for various temperature along the isocore at 3.59 g/cc.

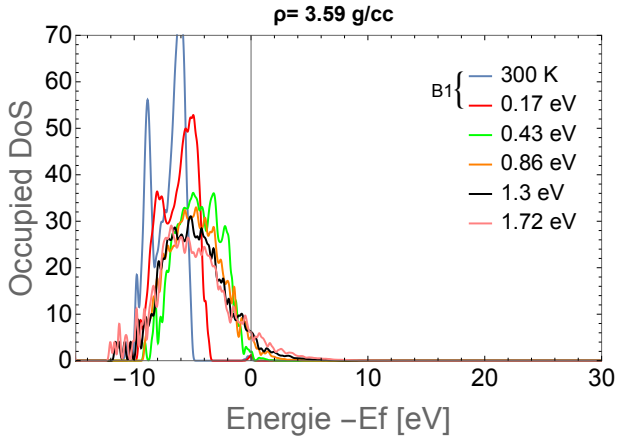

Figure 3.37: Occupied DoS for various temperature along the isocore at 3.59 g/cc.

In conclusion to this paragraph, we can say that AIMD allowed us to explain the physical origin of the behaviour of K-edge of MgO observed experimentally along the isochore at 3.3 g/cc. The absence of an abrupt shift at melting is due to the MgO metallisation mechanism from band widening (associated to disorder with electronic structure close to that of normal MgO) with a small shift of the E_F (or chemical potential) relative to energies of core level.

Mg-O pair correlation function and ionic structure The Mg-O pair correlation function g(r) for thermodynamic states along the isochore at 3.59 g/cc are shown

in fig. 3.38. The blue curve represents the g(r) for thermodynamic condition in the solid B1 phase (0.17 eV) exhibiting narrow peaks as typical for a crystal. The position of first peak at 3.9 bohr radii (or 2.08 angstrom) corresponds to the Mg-O distance in the B1 phase.
All the other g(r) reported in fig. 3.38 correspond to conditions in liquid MgO. The melting and the temperature have the effect of lowering, broadening the pair correlation function peaks. Moreover melting transition and temperature both shift the first and the second peak toward lower and larger radii respectively. In particular for temperature higher than 1.3 eV the first peak position moves toward lower radii. Moreover, as typical, the minimum between the two peaks for pair correlation function corresponding to the liquid phase has a finite value (>0). We can therefore say that these calculated g(r) are typical of a transition from a solid to a liquid.
The occurrence of a first peak in the liquid g(r) corresponds to a maximum in the probability of finding an O atom. We underline that a maximum in the local order is not necessarily a signature of a liquid locally organised in rigid structures with well defined bon angles as in SiO_2. The absence of structures in the MgO liquid XANES spectra seems to suggest the contrary, i.e. that MgO liquid is locally disordered. In this context, the different behaviour of the first peaks of MgO and SiO pair correlation functions may help in interpreting the structural properties of the two liquids (see fig. 3.38). Contrarily to what happens in the MgO g(r), for increasing temperature the first peak of the Si-O g(r) does not shift to lower radii, but it gets just lower in amplitude and broader [Denoeud, 2014]. This could suggest that in liquid SiO_2 a significant number of rigid Si-O structures is conserved as the probability maximum of finding an O atom is always at the same distance from the Si atom. Instead in the MgO, the gradual shift of the first peak of g(r) with temperature suggests the absence of rigid structures in the MgO liquid. MgO liquid may be unstructured or characterised by a distribution of MgO_x structures with a variety of angular distributions. Such a scenario would be coherent also with the band widening observed with DoS.

Therefore XANES spectra and AIMD (pair correlation functions and DoS) suggest that MgO is a disordered liquid at a local level as far as O-Mg-O bond angles are concerned. This would be coherent with the ionic nature of MgO bonds that would unlikely force Mg and O atoms to be organised in angularly well defined structures. Calculations of the Mg-O angular distribution functions are ongoing to verify this point. Therefore this study suggests that the structural properties of liquid MgO significantly differ from those of liquid SiO_2, where the covalent nature of the bonds forces the Si and O atoms to be organised in rigid Si-O polyhedra (tetrahedra at standard density).

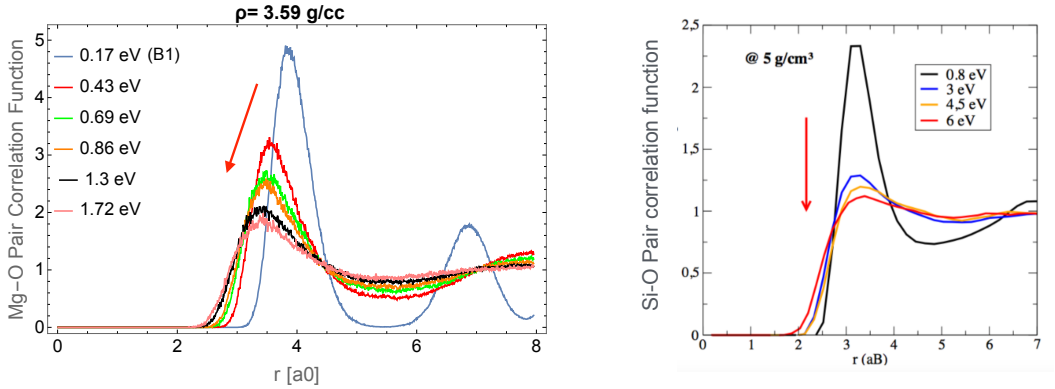

Figure 3.38: Left: Mg-O pair correlation functions for various temperature along the isochore at 3.59 g/cc. Right: Si-O correlation functions for various temperature along the isochore at 5 g/cc from [Denoeud, 2014].

3.5.2.2 Isochore at 5.5 g/cc

Fig. 3.39 shows the comparison between experimental and theoretical XANES spectra for the isochore at 5.5 g/cc.

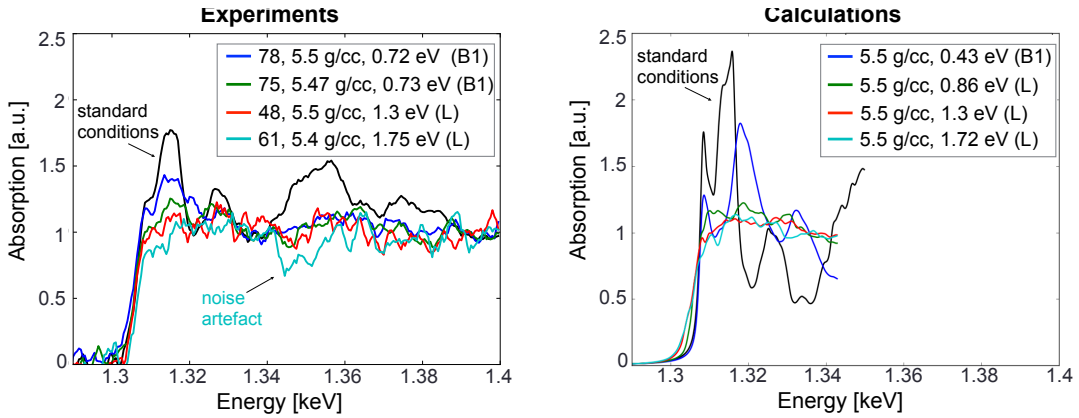

Figure 3.39: Experimental XANES spectra (left) and spectra obtained with ab-initio calculation for various temperature along the isocore at 5.5 g/cc. L and B1 denote respectively conditions in the B1 solid and liquid phases.

The theoretical spectrum at 5.5 g/cc and 0.43 eV (i.e. in the solid phase B1) presents a blueshift of peaks B-C and D. As for the isochore at 3.59 g/cc, in the melt phase calculated spectra exhibit the same qualitative behaviour that we observed experimentally (i.e. a loss of all the structures and the absence of K edge shift).

Therefore we use again DoS and pair correlation functions predicted by AIMD to investigate the microscopic origin of such behaviours.

Density of States and electronic properties Fig. 3.40, fig. 3.41 and 3.42 represent respectively the total, the occupied and the unoccupied DoS for the spectra along the isochore at 5.5 g/cc. As for the isochore at 3.59 g/cc, the DoS reported here for the isochore at 5.5 g/cc evidence a band gap closure mechanism by band widening which is complete for spectra corresponding to liquid MgO. Fermi energy for the considered temperatures along the isochores at 5.5 g/cc does not vary significantly (< 2.7 eV, i.e. below our experimental resolution). This is coherent with our experimental observations of no shift for increasing temperatures, also for conditions above the melting line (see previous paragraph for details), provided that the shift in the energy core levels follows a trend close to that of the Fermi energy.

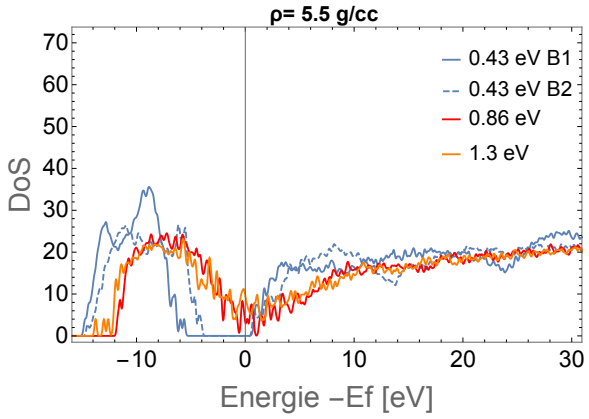

Figure 3.40: Density of states for various temperature along the isochore at 5.5 g/cc.

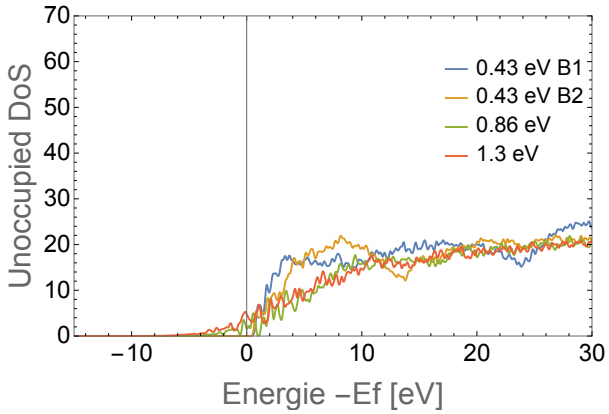

Figure 3.41: Unoccupied DoS for various temperature along the isochore at 5.5 g/cc.

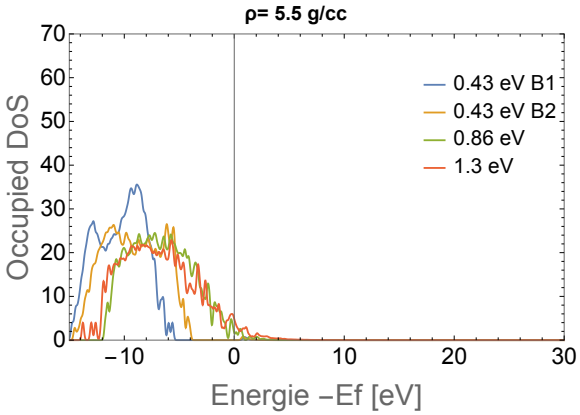

Figure 3.42: Occupied DoS for various temperature along the isochore at 5.5 g/cc.

Mg-O pair correlation function and ionic structure Fig. (3.43) on the right represents the Mg-O g(r) of liquid MgO for three temperatures at 5.5 g/cc: 0.86 eV, 1.3 eV and 1.75 eV. As for the pair correlation functions shown for the isochore at 3.59 g/cc the temperature has the effect of lowering, broadening and shifting the peaks. As before the shift of the first peak toward lower radii combined with the absence of structures on the corresponding XANES spectra are coherent with angular disorder in MgO (unlike SiO_2).

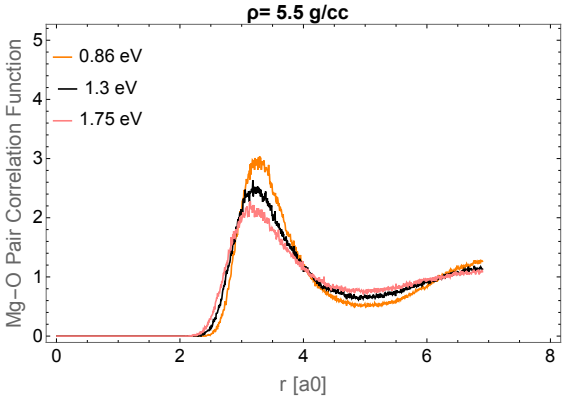

Figure 3.43: Mg-O pair correlation function for various temperature along the isocore at 3.59 g/cc (left) and 5.5 g/cc (right).

Section sum up

To sum up, in this section we obtained information about the physical processes that govern the evolution of the K-edge for increasing temperatures. In particular the DoS evolution is coherent with the absence of shifts of the Mg K-edge at melting and at higher temperature, as well as with the fact that the edge does not broaden significantly for the studied conditions. Moreover DoS evidenced that the band gap closes by a band widening due to the increase of disorder and that the melting seems to coincide with the closure of the gap. Finally the combination of pair correlation functions and XANES spectra suggests that MgO melt has not a strong structural behaviour as the SiO_2. This behaviour is coherent with the ionic nature of the MgO bondings.

3.5.3 Interpretation of the behaviour along the isotherms at 0.82 eV and 1.72 eV: study of the effect of the density.

Comparison between XANES spectra calculation and experiment Fig. 3.44 and fig. 3.45 show the comparison between experimental and theoretical XANES spectra for the isotherms at 0.82 eV and at 1.72 eV.

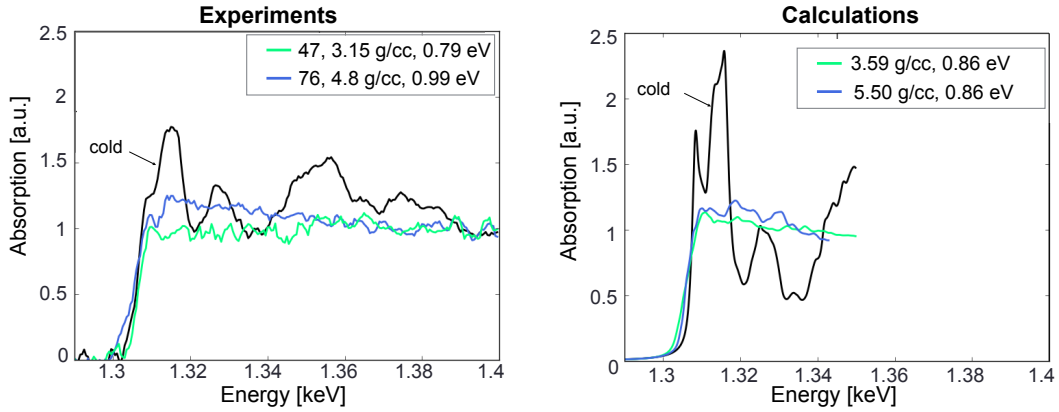

Figure 3.44: Experimental XANES spectra (left) and spectra obtained with ab-initio calculation for various temperature along the isocore at 0.86 eV.

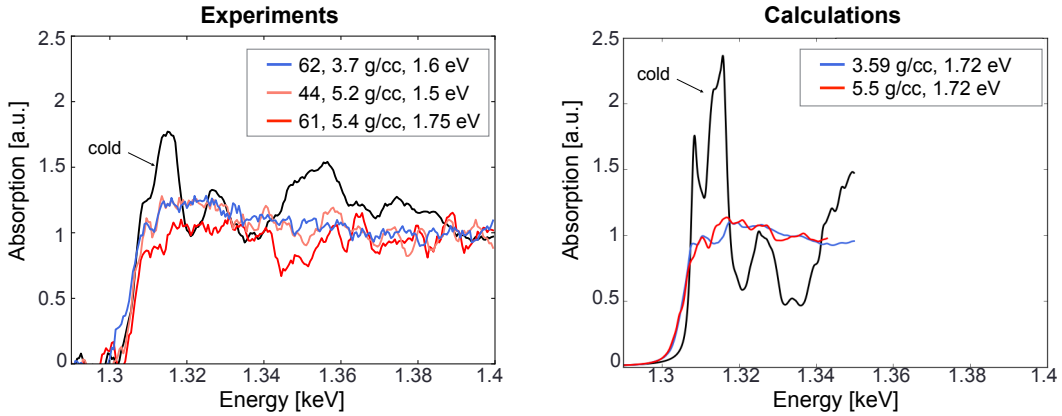

Figure 3.45: Experimental XANES spectra (left) and spectra obtained with ab-initio calculation for various temperature along the isocore at 1.72 eV.

Theoretical and experimental spectra exhibit the same behaviour. Neither simulations nor the experiment evidence an effect of the density on the XANES spectra in liquid MgO for both isotherms. Density does induce neither the occurrence of structures on the spectra nor a shift of the K-edge. To investigate the absence of the shift we will

look at the AIMD DoS. The fact that the density does not induce any structuration on the spectra suggests that ionic non-compact nature and angular disorder do not change significantly with the density. To further investigate the liquid structure of MgO with increasing density, we look at the pair correlation function.

Mg-O pair correlation function and ionic structure The Mg-O pair correlation function g(r) for thermodynamic states along the isotherms at 0.86 eV and 1.72 eV are shown in fig. 3.46.
The density has the effect of increasing the the maximum of the first and second peaks as well as of decreasing the minimum between the two peaks. Moreover the FWHM of the first peak decreases. This means that for higher densities the probability of finding an O atom at a given distance from an Mg atom is localised in a smaller volume. This is not inconsistent with maintaining large angular disorder in liquid MgO. Indeed as evidenced in the previous paragraph, density has not the effect of generating structures on the XANES spectra. Moreover we already discussed that the presence of a maximum in the g(r) does not necessarily correspond to well defined polyhedra. Concerning the peak positions, fig. 3.46 evidences a shift toward lower radii. The most likely scenario that follows from these calculations is that the density, on average, has the effect of reducing the distances between the Mg and O atoms in the ionic liquid and of increasing short range order, but not of inducing the formation of well defined polyhedra.

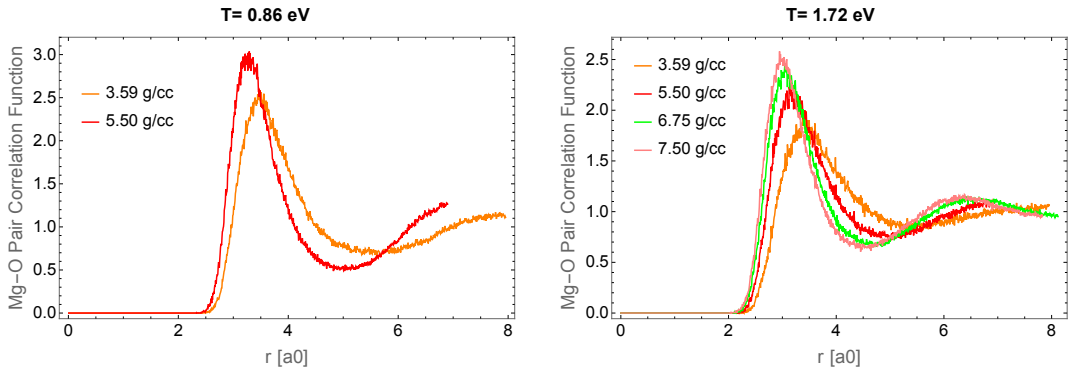

Figure 3.46: Mg-O pair correlation function for various temperature along the isotherm at 0.86 eV (left) and 1.72 eV (right).

Density of states and electronic structure Fig. 3.47 presents the total DoS at densities 3.59 g/cc and 5.5 g/cc for temperature T=0.86 eV (on the left) and T=1.29 eV (on the right.). In both cases the density has the effect of lowering the DoS in the band gap and shifting toward lower energies the valence band. To better understand

this behaviour and its implications we can look at the occupied DoS (see fig. 3.48). Fig. 3.48 allows to better appreciate that the density has the effect of shifting and also widening the valence band. Moreover the density lowers the occupied DoS above the Fermi level. This could mean that density lowers the conductivity (as observed e.g. by [Mazevet et al., 2015] for SiO_2). Calculations of the conductivity values corresponding to the reported DoS are ongoing and will allow to verify this hypothesis. AIMD calculations also evidence that the difference E_F-E_{1s} does not change significantly for increasing density. This explains the absence of a shift of the K-edge with the density.

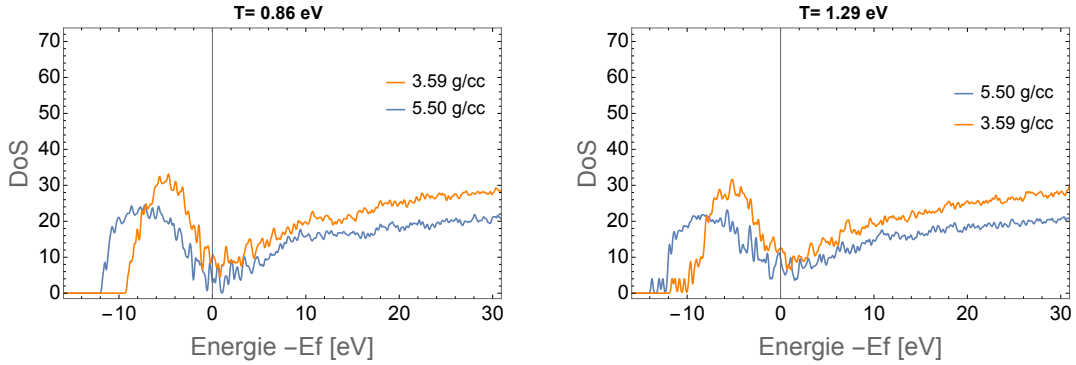

Figure 3.47: Total density of states along two isotherms: 0.86 eV (on the left) and 1.29 eV (on the right)

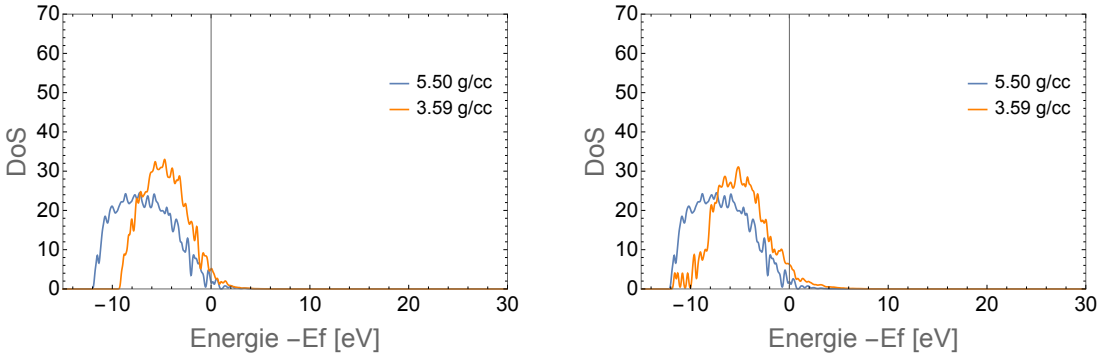

Figure 3.48: Occupied density of states along two isotherms: 0.86 eV (on the left) and 1.29 eV (on the right)

Section sum up

To sum up, in this section we presented the structural properties of liquid MgO and their changes for increasing densities. The XANES spectra and the AIMD seem to suggest that the density has not the effect of structuring the MgO liquid. Moreover we explained that the absence of the K-edge shift for increasing density is due to the fact that the difference between E_F and the energy of the 1s band (E_{1s}) does not change. Finally DoS suggests that conductivity decreases with density. This hypothesis will be verified with calculations of the corresponding conductivity (such calculations are ongoing at the moment of the writing of this thesis).

3.6 Conclusion and implications

In this chapter we reported first XANES measurements of the Mg K edge of shocked compressed MgO in an extended region of the phase diagram. Such experimental measurements have been technically challenging for various reasons as we reported in this chapter. The principal reason was the fact that the K-edge of the Mg in the MgO lies at relatively low energy ~ 1.3 eV, implying a low transmission of the various experimental components (target layers, spectrometer filters, etc.). We therefore improved as much as possible the experimental set up to maximise the signal collected by the detectors (re-designing the spectrometers and designing a well adapted target).

The experimental campaign successfully provided a high number of exploitable spectra at various temperatures and pressures. This allowed us to analyse the effects of melting, temperature and density on the XANES spectra. In particular we observed two behaviours that required an interpretation:

1) a flattening of the spectral structures typical of the solid for spectra in the liquid phase;

2) the absence of any shift and broadenings of the K edge detectable within the 3.5 eV energy resolution of our spectrometers.

In order to interpret such observations we performed ab-initio simulations of the XANES spectra, DoS and pair correlation functions. The calculated XANES spectra exhibit the same behaviours as observed in the experiment.
The analysis of the theoretical Density of States allowed us to explain that the absence of any shift or strong broadening with increasing temperature was linked to the band gap closure mechanisms. We stressed out that the temperature has the effect of narrowing the gap by creating electronic states energetically located inside the gap in the vicinity of conduction and valence bands (phenomenon that appears as a band widening). We also observed that the gap is closed for conditions above the melting line. Calculations are ongoing to obtain conductivity values corresponding to the theoretical spectra reported here. This would allow to verify what we observed in the decaying shock experiment, i.e. whether MgO melts into a reflecting liquid along the Hugoniot or not. DoS allowed also to stress that the absence of shift for increasing density is coherent to the fact that the difference E_F - E_{1s} does not change. This absence of shift is intuitively consistent with the electronic similarities between defects that populate the band gap and normal MgO.
The absence of structures in XANES spectra in the liquid phase suggest that MgO melts into a liquid characterised by wide distributions of O-Mg-O angles. We investigated the local order of this liquid and the effect of temperature and density on such

a local order with the AIMD pair correlation functions. The results are consistent but the distribution of angles remain to be calculated and compared to SiO_2.

Chapter 4

X-ray diffraction investigation of shock compressed $MgSiO_3$ glass and Forsterite

Contents

4.1 Introduction

In this chapter we present an XRD investigation of the structural changes occurring along the Hugoniot of $MgSiO_3$ glass and Forsterite between 0-150 GPa and 0-90 GPa respectively, i.e. mostly for conditions corresponding to solid phases. This study provides complementary information to the results presented in chapter 2, where we investigated along the Hugoniot the properties of liquid $MgSiO_3$ and Mg_2SiO_4 for pressures P>120 GPa and P>200 GPa respectively[1]. Decaying shock were well adapted to study melting and melt properties, but may have problems to study polymorphic phase transitions at lower pressures (see shock splitting at phase transition in sec. 1.0.2.8). Moreover interpretation of the phases detected with decaying shock studies is not always trivial, as based on indirect observations. This is particularly true for the conditions studied here, where shock front are opaque and instant shock velocity cannot be measured. XRD instead directly accesses to the structural properties of a sample and it allows to determine the nature of the probed phase.
In order to have both bright X-ray source adapted to perform XRD on amorphous materials and high power optical lasers to drive the shock, we performed the experiment at MEC end-station of the LCLS free electron laser. The results that we obtained suggest that $MgSiO_3$ glass is kept in amorphous phase up to melting and that shocked Fo yields an amorphous phase.

The reason of this study are manifold. The knowledge of $MgSiO_3$ and Mg_2SiO_4 phase diagram at pressure and temperature conditions up to $\sim$ 200 GPa and $\sim$ 5000K is crucial for both solid and liquid phases. Indeed phase transitions and dissociation reactions of solid silicates are at the basis of our understanding of the structure of the upper mantle. At the same time melt properties are relevant for phenomena linked to mantle dynamics and planetary evolution. In the vicinity of the CMB partial melts of these magnesium oxides might exist and strongly influence the mantle dynamics [Stixrude and Karki, 2005]. Densities of these liquids are required for establishing their buoyancy with respect to the coexisting solids. Finally the knowledge of melting boundaries and melt properties are necessary to correctly model the Earth's chemical differentiation and its implications [Thomas and Asimow, 2013], as well as to explain seismic anomalies as ULVZ (ultra low velocity zones) [Thomas and Asimow, 2013].

Phase transitions and structural changes occurring below the melting have been widely investigated with static compression. These studies provide a quite complete picture of phase transitions occurring in the Earth's mantle at conditions along the

[1] 120 GPa and 200 GPa correspond also to melting upper limits that we set in chapter 2 for $MgSiO_3$ and Mg_2SiO_4 respectively.

Earth's geotherm. They evidence that phase transitions in $MgSiO_3$ and Mg_2SiO_4 and their polymorphs are responsible for the major seismic discontinuities in the upper Earth's mantle, clearly detected at 410, 520 and 670km. Olivine $(Mg,Fe)_2SiO_4$ has been observed to transform into Wadsleyite (Wds) at around 14-15 GPa, that corresponds to a depth of 410 km in the Earth mantle (T $\sim$ 1700K [Katsura et al., 2004]). Wds in turn transforms into Rwd at around 17-18 GPa, i.e at a depth of 520 km (T $\sim$ 1800K [Katsura et al., 2004]). Deeper in the mantle, at around 670 km (P $\sim$ 23 GPa, T $\sim$ 1850K [Katsura et al., 2004]), Rwd dissociates into bridgmanite (Pv) $(Mg,Fe)SiO_3$ and ferropericlase (Mg,Fe)O, that are the most abundant solid phases in the lower mantle [Knittle and Jeanloz, 1987]. In the lowest region of the Earth's mantle, i.e. at P $\sim$ 125 GPa (T $\sim$ 2500K [Tsuchiya et al., 2004]), a polymorph of $MgSiO_3$ is still present, as bridgmanite transforms to Mg-postperovskite (Ppv) [Murakami et al., 2004]. Regions deeper in the Earth's mantle correspond to higher pressures and temperatures where magnesium silicates are probably partially melted. Unfortunately DAC cannot access these extreme conditions. Indeed, usually maximum pressure achieved by DAC are $\sim$ 200 GPa. Moreover technical difficulties need to be solved for uniformly heating samples compressed with DAC to the high temperatures typical of Mg-rich silicate melts ($>$ 3500 K at 100 GPa). These difficulties are among the reasons why data on structural properties of silicate melts are missing.

Other reasons concern the difficulty up to recent times in coupling short and intense X-ray sources adapted for XRD to shock compression. Indeed solid-liquid boundaries of $MgSiO_3$ and Mg_2SiO_4 phase diagrams can be easily reached with shock compression. But up to now, Hugoniots of $MgSiO_3$ and Mg_2SiO_4 in the solid regime up to melting have been studied mainly with optical diagnostics. Among these studies, we can cite [Marsh, 1980; Luo et al., 2004; Mosenfelder et al., 2009; Akins et al., 2004] that provided equations of state P-ρ from the measurements of shock velocity U_s and fluid velocity u_p . Some of these studies also obtained an estimation of melting boundary from thermal emission measurements (in addition to U_s and u_p) [Luo et al., 2004; Luo and Ahrens, 2004]. However in these studies structural informations are missing. Phase diagrams on Hugoniot are determined on the basis of theoretical models or calculations. Direct characterisation of the phases occurring along the Hugoniot are therefore still required.
The advent of facilities like MEC that couples ultrafast X-ray diffraction to shock loading constitutes a turning point, opening the way for a direct characterisation of the structural changes occurring under shock compression. This also opens other exciting possibilities in addition to those linked to planetary interior structures. This type of facilities indeed is well adapted for investigating impact phenomena. Indeed, despite under different timescales, a shock experiment naturally mimics what happens during a meteorite impact. Therefore full comprehension of the crystallographic and

structural changes of major planetary constituents occurring under shock or dynamic loading would pave the way for a correct interpretation of the geologic histories of sites strongly impacted by meteorites [Jaret et al., 2015].

There are further motivations than geophysical for studying the structural properties of $MgSiO_3$ and Mg_2SiO_4 under shock compression. Indeed the relevance of dynamic compression for geophysics data is still matter of debate. In this context the major issue concerns the maintenance of metastable states along the Hugoniot. This research has so far been limited by the absence of a structural probe able to determine the structures along the Hugoniot curves. Facilities as MEC now provide new opportunities for important advances. As widely characterised with DAC, phase diagrams of $MgSiO_3$ and Mg_2SiO_4 up to $\sim$ 150 GPa are good candidates for evaluating the differences between static and dynamic phase diagrams.

In this chapter we will first present our current knowledge of $MgSiO_3$ and Fo Hugoniot. Then we will give some details about the experimental set-up and the samples. Finally we will present the XRD data obtained on shock compressed $MgSiO_3$ glass and Fo crystal and a preliminary discussion about the structural properties.

4.1.1 $MgSiO_3$ glass and Mg_2SiO_4 Forsterite Hugoniot

In this section we review the shock studies that provide our current knowledge on the $MgSiO_3$ glass and Fo Hugoniot in the pressure range 0-150 GPa and 0-200 GPa respectively.

$MgSiO_3$ glass Hugoniot There are two main motivations for studying $MgSiO_3$ glass in addition to its crystalline polymorph Enstatite. The melting along the $MgSiO_3$ glass Hugoniot occurs at lower pressure with respect to the En Hugoniot. Therefore it is easier to study the melting with shock compressed $MgSiO_3$ glass than En. The second reason lies in the fact that silicate glasses have long been considered as high pressure liquid analogs. For this reason and since they are experimentally more accessible that the liquids, they have been widely investigated [Williams and Jeanloz, 1988; Kubicki et al., 1992; Meade et al., 1992; Sato and Funamori, 2008; Murakami and Bass, 2010]. However a characterisation of the melt properties is still missing and the equivalence of glass and liquid behaviour at high pressure is not established yet. Therefore the analogy between high pressure glasses and liquids need to be experimentally tested. Facilities as MEC are extremely well suited to perform such a study. X-rays of the LCLS XFel are intense enough to obtain structure factors of liquid or amorphous phases. This in combination with high power laser, provide the means to measure structure factors of amorphous and liquid phases occurring along

the Hugoniot. This would allow to characterise liquid and glass at close thermodynamic conditions. The Hugoniot of $MgSiO_3$ up to ∼200 GPa has been investigated by various experiments [Marsh, 1980; Luo et al., 2004; Mosenfelder et al., 2009; Akins et al., 2004] that measured the shock velocity U_s and fluid velocity u_p. The Hugoniot data obtained in these studies are represented in fig. 4.1 on the left.

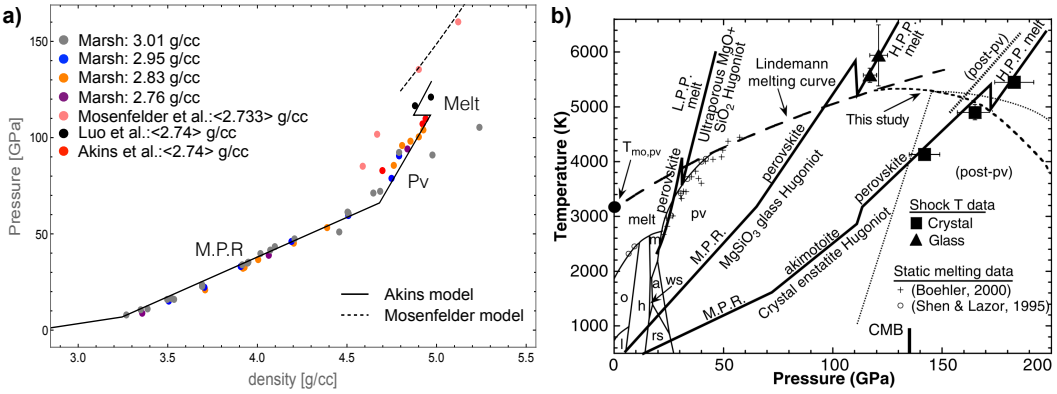

Figure 4.1: a) $MgSiO_3$ Shock P-ρ data from various gas gun and laser driven shock compression experiments (coloured dots), interpolated theoretical Hugoniot obtained with Mie-Gruneisen models from [Akins et al., 2004] and for the liquid [Mosenfelder et al., 2009] (black and dashed lines respectively). b) $MgSiO_3$ P-T phase diagram from [Akins et al., 2004].

Shock data have been interpolated by Akins et al. [2004] and Mosenfelder et al. [2009] with Mie-Grüneisen models. Interpolation are represented in the P-ρ diagram by black continuos and dashed lines in fig. 4.1 on the left. Mie-Grüneisen models also allow to calculate the P-T curve corresponding to the Hugoniot. The P-T curve calculated by Akins et al. [2004] (corresponding to the continuos black line in fig. 4.1 on the left) is shown in fig. 4.1 on the right. According to this interpretation, the Hugoniot of $MgSiO_3$ glass can be divided in three regime: 1) a mixed phase region (M.P.P.) composed of a mixture of enstatite (En) and other higher pressure phases as majorite up to ∼ 70 GPa, 2) a transition to Pv starting at ∼ 70 GPa and extending up to 110 GPa, 3) a melting region at 110 GPa with a drop in the temperature of about 700 K [Akins et al., 2004; Mosenfelder et al., 2009]. This phase diagram is shown in fig. 4.1-a. The same scenario is shown in the P-T phase diagram in fig. 4.1-b, together with enstatite and ultraporous $MgO+SiO_2$ Hugoniots. In this diagram measurements of T together with U_s and u_p (for $MgSiO_3$ glass and Enstatite Hugoniots) indicate a temperature substantially lower than what is calculated for solid-state Hugoniot. This would suggest that the data correspond to molten or partially molten Hugoniot states being the temperature difference due the the latent heat of melting. The

curves obtained by Akins et al. [2004] support such interpretation, although both interpretations are based on indirect methods.

Mg_2SiO_4 Forsterite Hugoniot. The Hugoniot data of shocked Fo obtained during various experimental campaigns [Wett and Ahrens, 1983; Jackson and Ahrens, 1979; Syono et al., 1981a; McQueen and Simmons, 1968; Mosenfelder et al., 2007] are reported in fig. 4.2-a (the graph is taken from [Mosenfelder et al., 2007]).

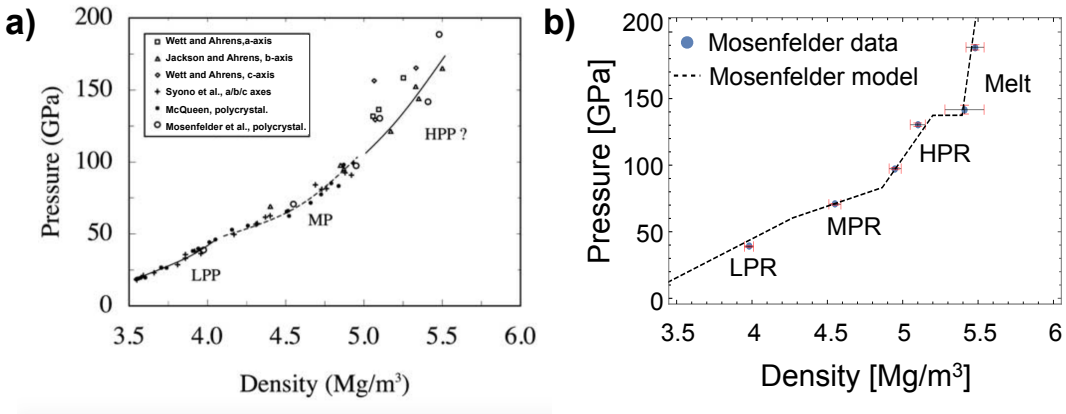

Figure 4.2: a) from [Mosenfelder et al., 2007] Fo shock P-ρ data from various gas gun and laser driven shock compression experiments. b) The Fo theoretical Hugoniot obtained with a Mie-Gruneisen proposed by [Mosenfelder et al., 2007]

These data combined with temperature pressure data from [Luo et al., 2004] have been interpolated by Mosenfelder et al. [2007] with a Mie-Gruneisen-Debye model starting from a Birch-Murnagam 4th order isentrope. The theoretical interpolation of Hugoniot data is shown in fig. 4.2-b. As shown, [Mosenfelder et al., 2007] individuated four regimes:

1) a low pressure phase - plastic regime (LPP), where Forsterite is kept in a metastable state up to ∼50GPa;

2) a mixed phase regime (MP) occurring between 50 and 90 GPa, where Forsterite partially transforms into an assemblage MgO Periclase (Pe) + $MgSiO_3$ Pv;

3) an high pressure phase regime (HPP) between 90 and 130 GPa, composed of an assemblage $MgSiO_3$ Pv + MgO Pe [2].

[2]Interpretation of the nature of regimes HPP and MP is also based on data on recovered samples [Syono et al., 1981b] that show a partial breakdown of forsterite to MgO + amorphous $MgSiO_3$, the latter considered to represent former Pv.

4) a melt regime occurring above 140 GPa, composed of a liquid phase denser than the solid.

This interpretation is partially contested by [de Koker et al., 2008a], who studied Mg_2SiO_4 with ab initio calculations. De Koker et al. [2008a] proposed that under shock compression Mg_2SiO_4 appears as post-perovskite ($MgSiO_3$ solid phase) + periclase (MgO solid phase) assemblage below 150 GPa, transforming into periclase + liquid $MgSiO_3$ at 150-170 GPa and melting into pure Mg_2SiO_4 liquid above 170 GPa. These differences in the interpretation of the higher part of the Hugoniot are also due to the scattering exhibited by the data at pressure above 100 GPa (see fig. 4.2). A direct diagnostic as XRD would allow to understand the nature of the phases occurring along the Hugoniot and to discriminate between the different hypotheses.

4.2 Experimental set-up

The experimental set-up used at the Matter in Extreme Conditions (MEC) end-station at the X-FEL of LCLS is shown in fig. 4.3. At MEC we used the 50 fs long X-Fel pulse at 8 keV (single photon energy) and 1-3 mJ (pulse total energy) as probe beam for the x-ray diffraction. Cornell-SLAC Pixel Array Detectors (CSPADs) [Philipp et al., 2011] were used to collect diffraction patterns. To drive the shock in the samples we used two 10 ns long laser pulses, while two VISAR systems allowed to measure the average shock velocity in the sample. Targets were mounted on special motorised holder that allowed to perform shots with a high repetition rate.
As shown the x-ray diffraction was performed in transmission geometry.
In the following we give some details of the various components of the experimental set-up.

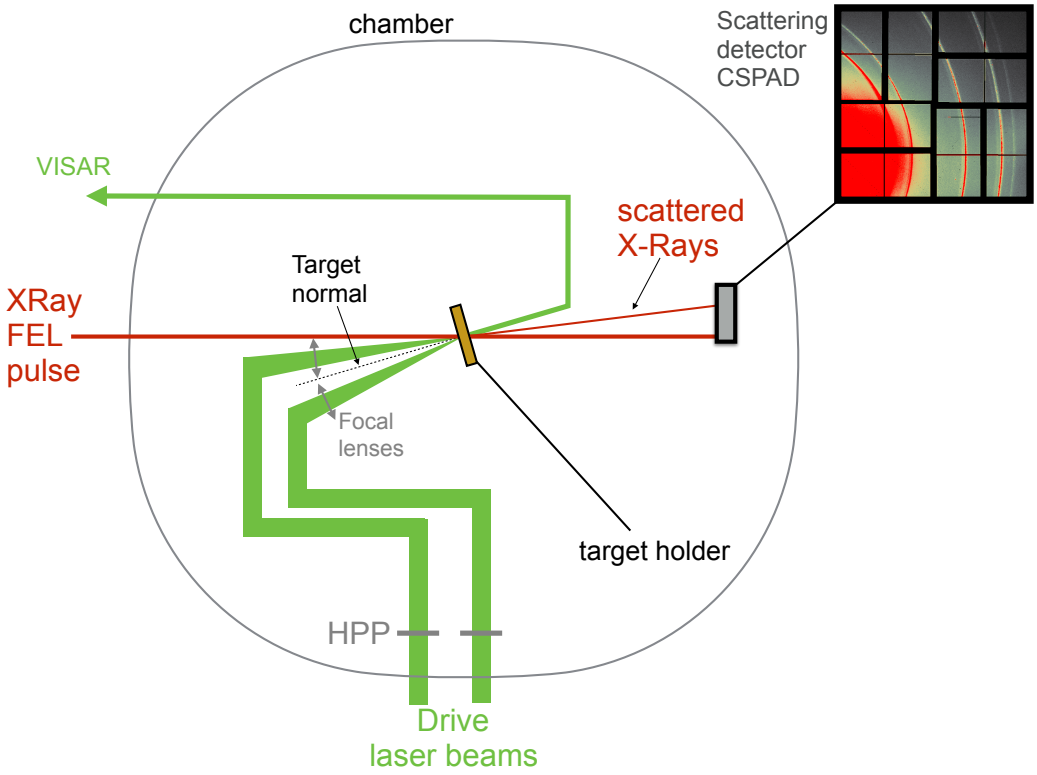

Figure 4.3: Experimental setup of the X-ray diffraction experiment performed at the MEC end-station at LCLS.

Drive beams At MEC we used the two available frequency-doubled Nd:Glass laser beams (wavelength = 0.527 μm) to shock compress the samples. The pulses were $\sim$

10 ns long and the focal spots were smoothed with Hybrid Phase Plates in order to obtain flat intensity profile of 100-250 μm. As at LULI2000 and GEKKOXII facilities, at MEC the drive laser energy is measured before the pulse goes through the phase plates and compress the samples. Because of optical system transmissivity, only a fraction of the measured energy reaches the target that was not determined in this experiment. In any case, in this work absolute energy values are not crucial, and we are more interested in relative values for different shots. The temporal profile was quasi-squared in order to provide an uniform loading of the sample. Indeed since XRD probes the bulk target it is crucial that the sample is brought to uniform conditions. To this aim the target design is optimised for MEC laser characteristics with the help of hydrodynamic simulations (see fig. 4.2). An example of the drive laser time profile is shown in fig. 4.4.

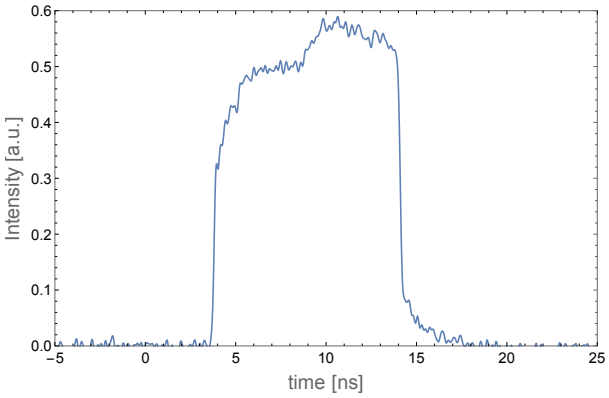

Figure 4.4: Typical drive laser time profile used during this experimental campaign.

X-ray pulse To obtain the x-ray diffraction of the compressed sample we used the X-Fel x-ray pulse at wavelength 8 keV. Thanks to the self amplified spontaneous emission (SASE) mechanisms the X-ray pulse of an X-Fel is by nature quasi-monochromatic. At LCLS the monochromaticity $\Delta E/E$ is $\sim 1{\cdot}10^{-3}$. The pulse energy provided at MEC varied between 1-3 mJ, corresponding to a bunch of $\sim 10^{12}$ photons. Thanks to its monochromaticity and high intensity the LCLS X-ray pulse provided at MEC is a perfect tool for single shot X-ray diffraction.
A system of three silicon carbide coated mirrors[3] and beryllium compound refractive lenses allowed to guide and focus the X-ray beam over a 50 μm diameter spot spatially overlapped to the target area irradiated by the drive lasers. To spatially overlap the X-ray and optical beams at the target a Ce:YAG scintillator is placed at the desired

[3]Silicon carbide coated mirrors are also used to spectrally and spatially filter the gamma rays, bremsstrahlung and broad spectrum undulator radiation present on top of the free-electron laser beam.

interaction point. The fluorescence signal produced by the optical laser or the X-rays is then imaged with microscope systems with a spatial resolution of 18μm. The two beams are then overlapped with motorised focusing lenses.

X-ray pulse parameters

Photon energy:	8 keV
Pulse energy:	1-3 mJ
Pulse duration:	50 fs
Spot size:	50 μm
Monochromaticity ΔE/E:	$1{\cdot}10^{-3}$

Table 4.1

In order to obtain diffraction patterns of entirely shock compressed samples we tuned the delay time between the X-ray and drive beams. The X-rays beam timing is determined by the X-Fel electron beam timing, which is correlated to the radio frequency fields in the electron accelerator cavity of LCLS [Minitti et al., 2015]. Optical lasers are locked to the accelerator RF distribution, thus having the same reference than the X-ray pulse. This configuration allows to synchronise the X-ray pulse and the optical lasers as well as well as to tune their time delay.
For this experimental campaign we set the zero delay (or absolute time zero t_0) between the synchronised X-ray pulse and optical lasers was set at the overlap between their leading edges.

Samples The samples were designed in order to obtain shocked conditions as uniform as possible to be probed by X-rays. They consisted in multilayer targets made of an ablator (10 μm polypropilene), a 2μm Ti shield and the samples: $MgSiO_3$ glass and natural Fo single-crystal 95μm $\pm$ 15μm thick. The Ti shield was coated to the sample and the polypropilene ablator was glued (on the Ti side) with 2μm- 3μm of UV glue.
The $MgSiO_3$ glass samples (density= 2.74 g/cc) were prepared from powder mixture melted at high temperature and lapped at IMPMC of the UPMC university in Paris. Appropriate polishing to an optical flatness of $\lambda/4$ was obtained. The natural forsterite Mg_2SiO_4 single-crystals (density 3.22 g/cc) were polished in the same way. All silicates were cut into 2 x 2 mm^2 samples with a diamond wire.

The target has been designed to maximise the target volume fraction uniformity compressed by the shock wave generated with the MEC laser. To this aim we performed MULTI hydrodynamic simulations for various target configurations. In particular we run the code using the measured drive pulse time profiles for a higher

precision. We found that multi-layer targets of 10 μm CH+ 2μm Ti+ 95 μm $MgSiO_3$ glass or Fo satisfy the uniformity requirement. $MgSiO_3$ and Mg_2SiO_4 thicknesses also maximise the XRD signal since $\sim$ 100 μm correspond to optical depth at 8 keV [Rygg et al., 2012]. Fig. 4.5 shows a color plot of the pressure in the time-initial position plane obtained with an intensity of $4 \cdot 10^{12}$ W/cm^2 irradiated for a $MgSiO_3$ glass target. The dashed white line shows that at late times the shock traveled almost at constant velocity. Fig. 4.6 shows pressure versus initial position curves for times close to the time break out. These line-outs evidence that the $MgSiO_3$ is uniformly compressed at 0.8 Mbar.
This study proves that with a good timing between the drive laser pulse and the probe X-ray beam it is possible to obtain X-ray diffraction of a uniformly compressed sample. Moreover it stresses that the transit time of the shock in the sample layer can be used to obtain the average velocity that in turn with an equation of state will give the pressure.

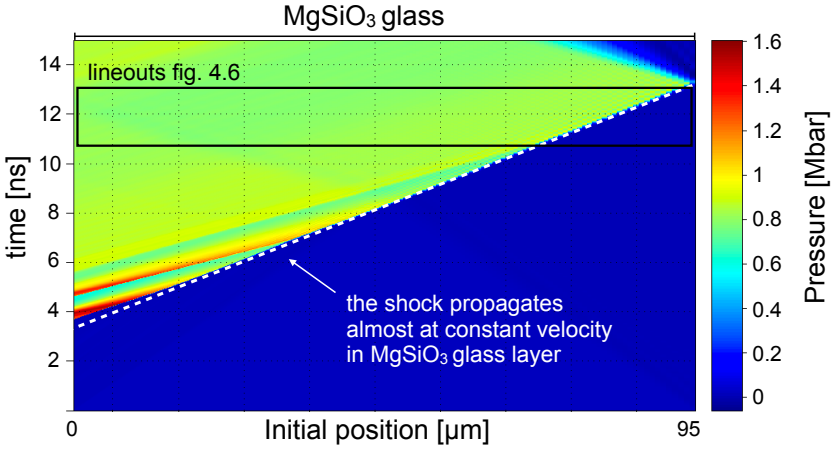

Figure 4.5: Color plot of the pressure in the time-initial position plane obtained with MULTI hydrodynamic simulation for a 10 ns long drive pulse of $4 \cdot 10^{12}$ W/cm^2 irradiated on a 10 μm CH+ 2μm Ti+ 95 μm $MgSiO_3$ glass target.

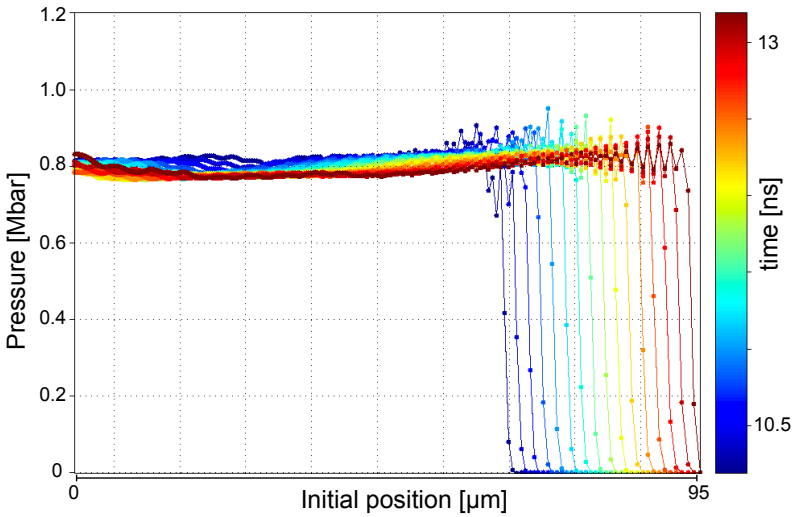

Figure 4.6: Pressure versus initial position curves for times close to the time break out obtained with MULTI hydrodynamic simulation for a 10 ns long drive pulse of $4 \cdot 10^{12}$ W/cm^2 irradiated on a 10 μm CH+ 2μm Ti+ 95 μm $MgSiO_3$ glass target. Uniform pressures of 0.8 Mbar are obtained over the whole samples.

VISAR A VISAR system was implemented in the set up. The VISARs have been operated at 532 nm with sensitivities of 0.99 km/(s·fringe) and 3.32 km/(s·fringe). Shock waves generated in this campaign were not strong enough to metallise $MgSiO_3$ glass and Fo sample. Therefore we could not measure the instant shock velocity. However, being the samples transparent at standard conditions, we could use the VISAR to measure the break out time t_{BO} and the transit time Δt of the shock in the Fo and $MgSiO_3$ glass layers. Figure 4.7 shows a typical VISAR signal used to determine Δt and t_{BO}. The VISAR data show that as the shock crosses the Ti-sample interface t_{int} , both $MgSiO_3$ and Fo become opaque. The intensity of the interference fringes drastically drops after time t_{int} as the signal only comes from reflection on the sample vacuum interface not AR coated (ghost fringes). At the shock breakout (t_{BO}) the ghost fringes are lost.
Transit time allowed us to obtain the mean shock velocity. Mean thermodynamic conditions are then inferred assuming the EoS known.
Break out time was also used to estimate the time delay between the shock and the XFEL pulse (to this aim the time zero of the streak camera was set at the absolute time zero). This allows to estimate if the sample is entirely or partially compressed by the shock or if it is in release at the X-ray probing time.

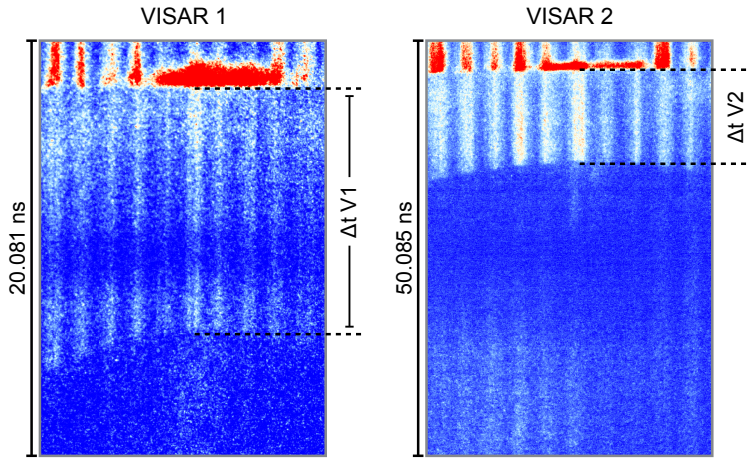

Figure 4.7: Example of VISAR signals used to measure the transit and the break out times.

X-ray diffraction detector Cornell-SLAC Pixel Array Detectors (CSPADs) [Blaj et al., 2014] were used to record the X-Ray diffraction patterns. The detector is composed of 500 μm thick silicon diodes. The charges produced by the diodes when irradiated by the X-rays are converted to a digital signal by pixilated application specific integrated circuits (ASICs) [Philipp et al., 2011] that constitute the unit module of CSPAD detectors used at LCLS. A single ASIC is composed of 194 x 185 pixels of size 110 μm x 110 μm and the CSPAD used at MEC during this experiment was composed of 16 ASICs organised in a square and composing a detector of 758 x 758 pixels. The size of such detector was therefore $\sim$ 8 cm x 8cm ASIC circuits have a high quantum efficiency (0.97 (i.e. 97%?)) and a signal to noise ratio equal to 7 for 8 keV X-rays. Moreover they are characterised by a readout speed that matches the LCLS high repetition rate: 120 Hz.
CSPAD background noise measured with an acquisition in the dark is subtracted from raw data pixel by pixel. Pixels too noisy have been automatically masked.
For eached probed sample we collected both an un-shocked sample XRD pattern (X-ray only shot) as a reference and a shocked sample XRD pattern (X-ray + drive beam shot).
The limited size of the detector in addition to the geometry of the experimental set-up allowed to explore 2θ in the range 21-65°.

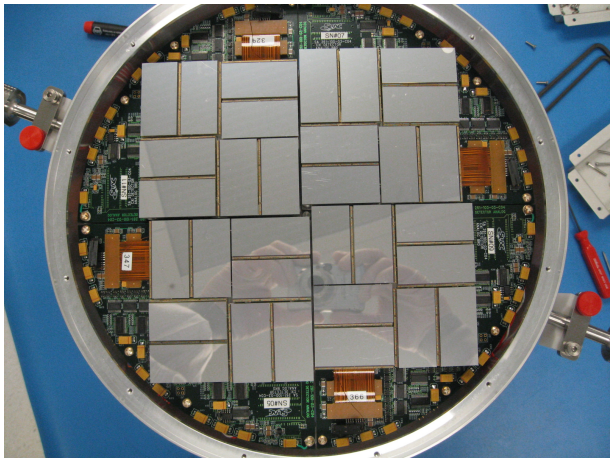

Figure 4.8: Example of the CSPAD composed of four quadrant of 16 ASICs available at the CXI instrument at LCLS. The CSPAD used during this experimental campaign correspond to one quadrant of the one shown in this figure. The 32 reflecting rectangular units are the 500 μm thick silicon diodes. Each diode is mounted on two ASIC units.

4.3 Data

In this section we present the XRD data obtained on $MgSiO_3$ glass and Fo.
The section is divided in three part:

- in sec. 4.3.1 we briefly describe the process of data reduction necessary to extract quantitative information from the CSPAD patterns (sec. 4.3.1);
- in sec. 4.3.2 we present the XRD pattern of uncompressed and shock compressed $MgSiO_3$;
- in sec. 4.3.3 we present the XRD pattern of uncompressed and shock compressed Fo.

4.3.1 Data reduction

The 2D diffraction signals recorded by the CSPAD detectors need to be reduced into diffraction spectra intensities as a function of 2θ angle or of the scattering vector $q = 4\pi sin\theta/\lambda$. To this aim and to extract quantitative information from the spectra we used the Dioptas software developed by Prescher and Prakapenka [2015].
The first step of the data reduction consists in determining the relation between the coordinates (x,y) of the detector and the (2θ,ϕ) angles of the diffracted beam. To this aim we performed X-ray measurement on unshocked polycrystalline CeO_2 and LaB_6, that present multiple Debye-Scherrer rings at known d-spacings and can be used as references. Indeed for a known X-ray wavelength and by interpolating the Debye-Scherrer rings of a known spectrum (see fig. 4.9-a), Dioptas software finds automatically the function f(x,y)= (2θ, ϕ). With this function f it is possible to transform the CSPAD signal into a spectrum in coordinates (2θ, ϕ), as the one represented in fig. 4.9-b. This system of coordinates allows to visualise the Debye-Scherrer rings on vertical lines.
Finally the integration over ϕ of the intensity in the (2θ, ϕ) coordinates gives the intensity as a function of 2θ (fig. 4.10-a). Fig. 4.10-b reports the XRD integrated spectrum obtained with a LaB_6 sample. Peak positions correspond to expected values [Pecharsky and Zavalij, 2009] and confirm the goodness of the calbration.

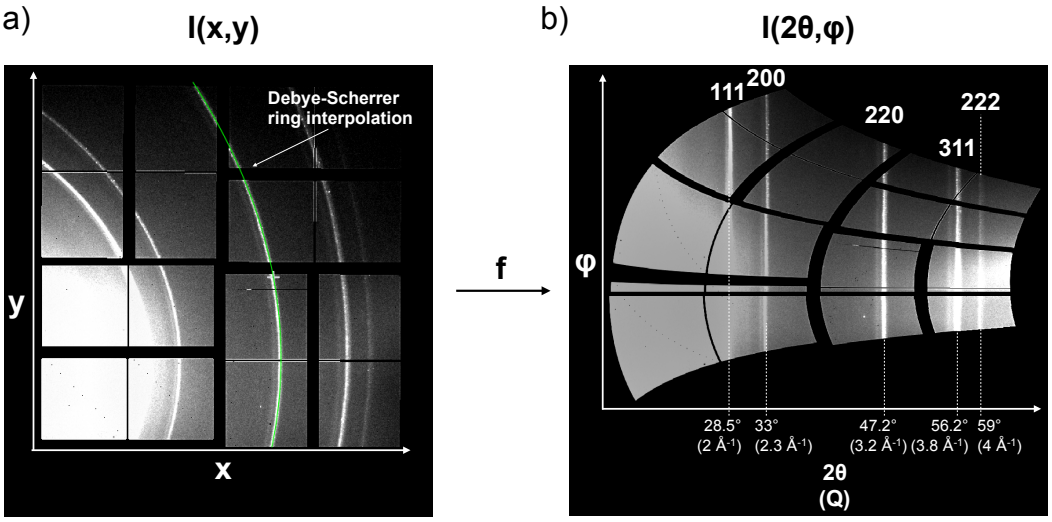

Figure 4.9: a) Diffraction signal of a CeO_2 sample at standard condition as measured by the CSPAD detector. b) The diffraction signal shown on the left represented in (2θ, ϕ) coordinates.

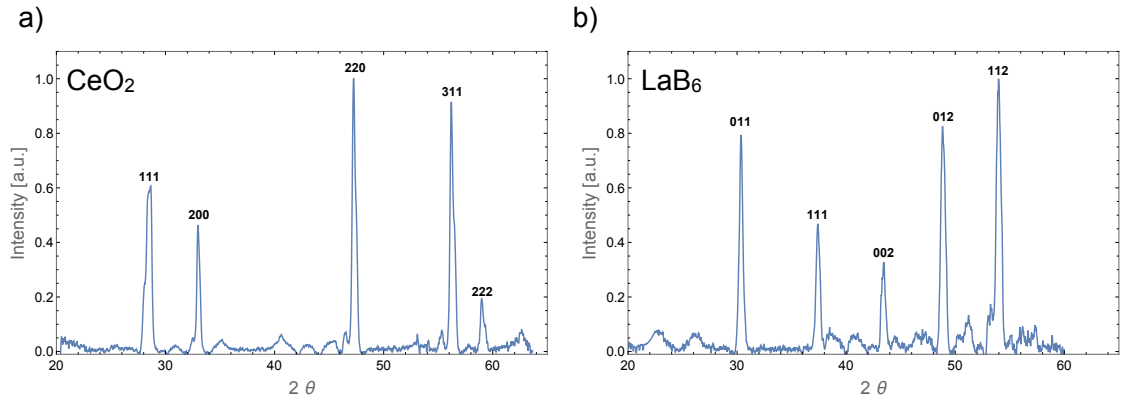

Figure 4.10: a) Integrated spectrum corresponding to XRD pattern shown in figure 4.9 obtained with a CeO_2 sample. b) Integrated spectrum obtained with a LaB_6 sample. Peak positions correspond to expected values [Pecharsky and Zavalij, 2009].

The experimental configuration used in this campaign allows to access a range of 2θ between 21-65°, corresponding to a range of Q $\sim$ 1.5-4.4 $Å^{-1}$.

4.3.2 $MgSiO_3$ glass XRD patterns

X-ray diffraction pattern at standard conditions Fig. 4.11-a shows the XRD pattern obtained for the 10μm Polypropilene + 2μm Ti + $MgSiO_3$ glass target at

standard conditions in (x,y) coordinates. On the right it is shown the corresponding integrated XRD pattern versus scattering vector q.
The shown XRD pattern (fig. 4.11-a) exhibits two Debye-Scherrer rings that are pointed by the white arrows. These rings correspond to the peaks of the integrated XRD signal (fig. 4.11-a) represented with dashed lines and result from the contribution of the Ti shield to the X-ray diffraction pattern. In particular, as evidenced in fig. 4.11-a, the rings correspond to lattice planes 100 and 101.
At the same time the raw XRD signal exhibits a broad ring (fig. 4.11-a) with a broad peak centred at q=1.87 $Å^{-1}$ in fig. 4.11-b. This broad structure results from the contribution of $MgSiO_3$ glass. Such contribution is represented in fig. 4.11 with the continuous line. Our spectrum is compared with results from recent XRD studies on cold $MgSiO_3$ glass [Wilding et al., 2004b,a] in fig. 4.11 on the right, showing good agreement.

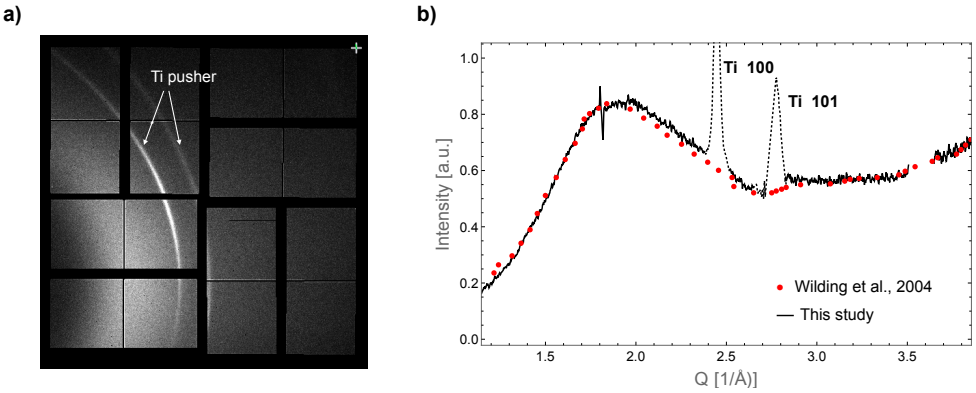

Figure 4.11: X-ray diffraction signal of $MgSiO_3$ glass at standard conditions as measured by the CSPAD (a) and intensity profile vs scattering vector Q in comparison with results from [Wilding et al., 2004b,a] (b).

Shocked $MgSiO_3$ glass X-ray diffraction pattern. Fig. 4.12 represents a selection of the XRD diffraction patterns obtained on shocked $MgSiO_3$ glass with drive laser pulses of different intensities. Laser shock - X-ray probe delays were tuned in order to probe at time close to the shock break out time. XRD signals are represented in (2θ, ϕ) coordinates. On top of the figure, the cold signal is reported as a reference for the other patterns. The first peak of the cold spectrum is pointed by a red arrow. Integrated spectra corresponding to those shown in fig. 4.12 are shown in fig. 4.13 versus the scattering vector.

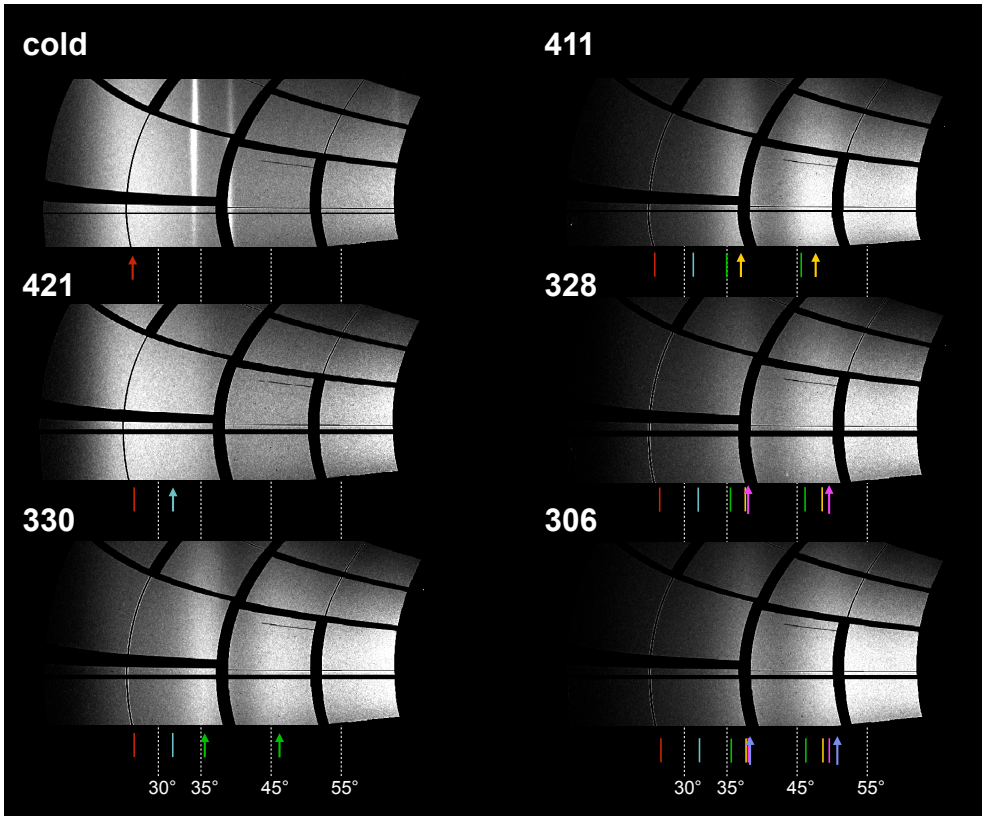

Figure 4.12: XRD patterns of shocked $MgSiO_3$ glass

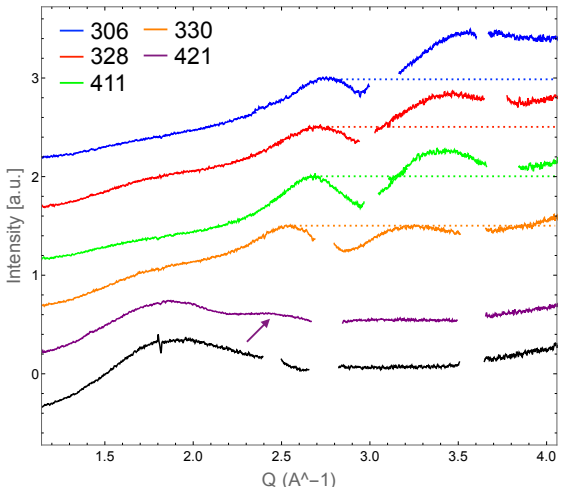

Figure 4.13: X ray diffraction spectra obtained on shocked $MgSiO_3$ glass for increasing laser intensities (coloured lines) are compared with the spectrum at standard conditions (black line).

Fig. 4.12 and fig. 4.13 evidence that shock compression induces two effects on the XRD spectra:

- a shift of the first peak toward higher q or 2θ;
- the emergence of a second peak at ~ 3.3 Å^{-1}, growing in amplitude and shifting toward higher q for increasing laser intensities.

Shifts of the first and second peak are pointed by coloured arrows in fig. 4.12 and are evident also from integrated spectra of fig. 4.13. Horizontal dotted lines in fig. 4.13 underline the amplitude increase of the second peak with respect to the first one.
Integrated spectra of the shot at the lowest intensity (421, purple curve fig. 4.13) differs from the cold for a slight curvature pointed by the purple arrow and centred at q=2.45 Å^{-1}. This curvature points at the effect of the shock of shifting the first peak of the XRD signal. The similarity with the cold underlines that spectrum 421 receives also a contribution from the uncompressed region of the sample. The spectrum corresponding to the highest laser intensity (shot 306) evidences the shift of the first peak up to 2.76 Å^{-1} and the shift of the second peak to 3.55 Å^{-1}. Moreover it shows that the amplitude of the second peak increased, being higher than the one of the first peak.
Peak positions of all the XRD patterns obtained on $MgSiO_3$ glass are resumed with corresponding shot numbers and nominal laser intensities in table 4.2.

shot	Nominal intensity [10^{13} W/cm^2]	First peak [Å^{-1}]	Second peak [Å^{-1}]
421	0.24	2.46	–
330	0.51	2.53	3.22
329	0.64	2.5	3.23
410	1.59	2.67	3.42
411	1.64	2.68	3.39
333	1.6	2.67	3.45
307	1.8	2.7	3.46
328	1.55	2.7	3.44
306	3.53	2.76	3.55

Table 4.2

4.3.3 Fo XRD patterns

Fo at ambient conditions Fig. 4.14 shows the raw (a) and integrated (b) x-ray diffraction pattern obtained on Ch+Ti+Fo target at standard conditions. The Fo crystal layer contributes to the spectrum with bright spots as expected for single crystals. Lattice planes contributing to the observed peak are pointed in fig. 4.14-b. We individuate contributions from lattice planes 211, 141, 202, 241. As for the spectrum obtained on $MgSiO_3$ glass, the two Debye-Scherrer rings are due to the Ti layer, and in particular to the lattice plane 100 and 101.

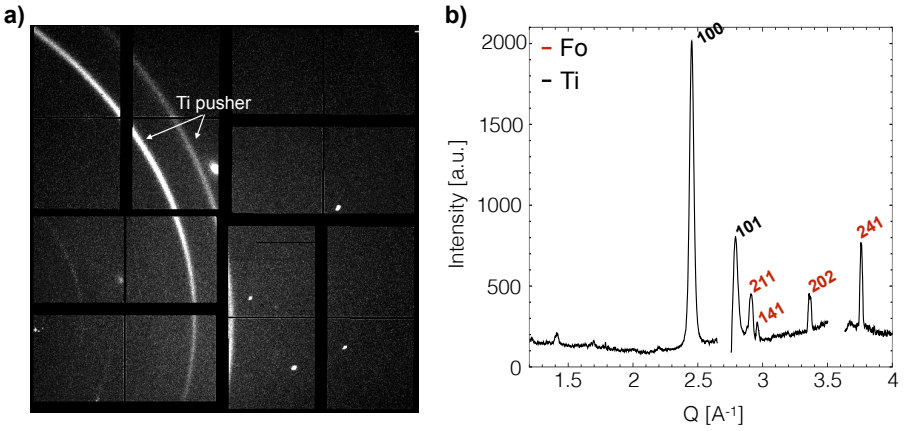

Figure 4.14: Left: measured CSPAD diffraction signal from Fo at standard conditions. Right: the X-ray diffraction spectrum extracted from the signal shown on the left.

Xrd spectra of shocked Fo. Fig. 4.15 shows the Xrd patterns in (2θ, ϕ) coordinates measured for shocked Fo. The figure evidences that measured spectra can be divided in two classes:

- XRD signals corresponding to shots with lower laser intensities (273, 272, 274, 335 in red) exhibit broad bright spots typical of a crystalline phase.
- spectra corresponding to higher drive laser intensities (shots 334, 312, 336, 311, 310 in green) present two broad Debye-Scherrer rings, as typical of XRD signals produced by amorphous or liquid phases. We can also notice the resemblance of this patterns with those observed for shocked $MgSiO_3$ glass (see fig. 4.12).

Spectra corresponding to shots 310 and 334 exhibit uniform Debye-Scherrer rings over the range of accessed ϕ angles. For the other spectra (311, 312 and 336), Debye-Scherrer rings are not uniform and there are bright spots superimposed (see arrows in fig. 4.15). This may indicate a coexistence of amorphous (or liquid) and crystalline phases, but it can also be due to the probing of low compressed material.

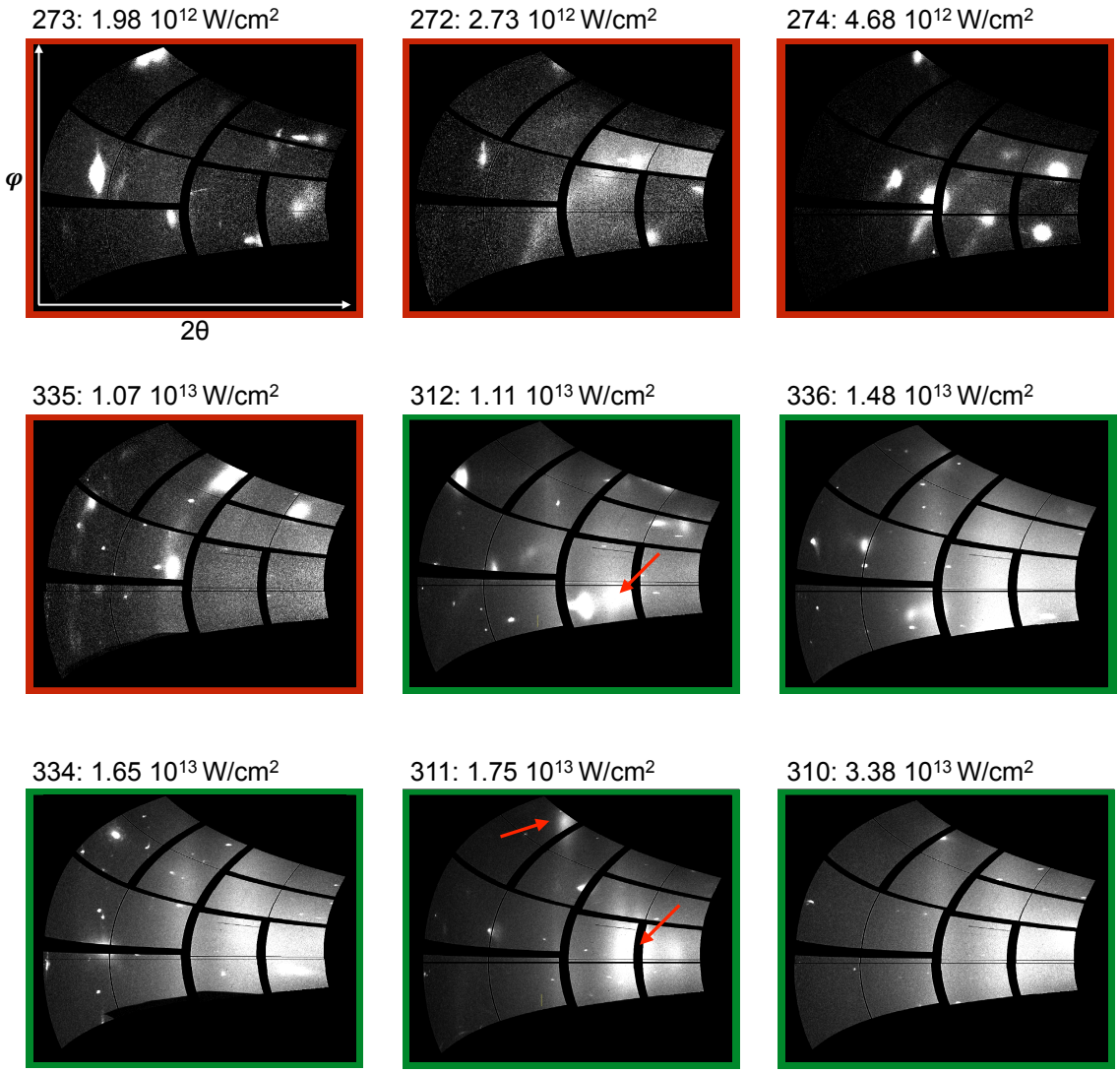

Figure 4.15: XRD patterns of shocked Fo obtained with different laser intensities (intensities increase from left to right)

Fig. 4.16 shows the integrated X-ray diffraction spectra of the amorphous or liquid phase produced with shots 334, 336 and 310. Shots 334 and 336, performed with similar drive laser parameters, produce spectra in good agreement whose peak positions are 2.7 $Å^{-1}$ and ∼3.4 $Å^{-1}$. At the same time for shot 310, which has been performed with the highest laser intensity, we obtained a spectrum with peaks shifted to higher q (2.76 $Å^{-1}$ and ∼3.52 $Å^{-1}$). Peak positions of the XRD patterns obtained

for shocked Fo with the corresponding drive laser intensities are resumed in table 4.3. Comparing this table with table 4.2 it is possible to appreciate that peak positions of the liquid or amorphous phase obtained from shocked Fo are similar to those observed for shocked $MgSiO_3$ glass. Moreover the table evidences that the more intense the drive laser the more the peaks shift toward higher q, as observed also for the $MgSiO_3$ glass.

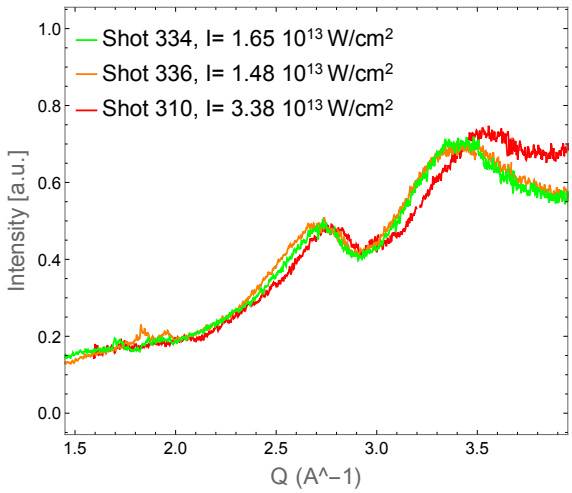

Figure 4.16: Glass contribution to the X-ray diffraction spectra of shots 334, 336 and 310.

shot	Nominal laser intensity [10^{13} W/cm^2]	Peak one [Å^{-1}]	Peak two [Å^{-1}]
312	1.11	2.63	3.29
336	1.48	2.7	3.4
334	1.65	2.7	3.38
311	1.75	2.7	3.34
310	3.38	2.76	3.52

Table 4.3

4.4 Analysis

In order to understand the XRD diffraction data and their link with sample structures we evaluate the contribution of the pusher to the diffraction patterns and we estimate the pressure regimes attaint in the different shots.

4.4.1 Contribution of shocked Ti to XRD patterns.

To verify the contribution of shocked Ti to the XRD pattern, we performed a shot (430) tuning the X-Rays - drive laser delay (1.5 ns) in order to probe the sample just before that the shock enters in the $MgSiO_3$ layer, which occurs at 1.67 ns. In this way the $MgSiO_3$ was uncompressed at probe time, while the Ti layer was almost completely compressed . Fig. 4.17 shows the reference (X-rays only) XRD pattern (a) in comparison with the one obtained with shot 430 (b). The XRD pattern of the shock compressed sample does exhibit neither the Ti lines nor other structures at higher q, but only the broad peak typical of uncompressed $MgSiO_3$ glass. This means that the structures observed in fig. 4.17 do not result from the contribution of compressed Ti but are due to compressed $MgSiO_3$. We can therefore interpret the XRD spectra shown in figures 4.12 and 4.15 as coming from amorphous or liquid $MgSiO_3$ and Mg_2SiO_4.

shot	Time at Ti-$MgSiO_3$ interface [ns]	X probe time [ns]
430	1.67	1.5 ns

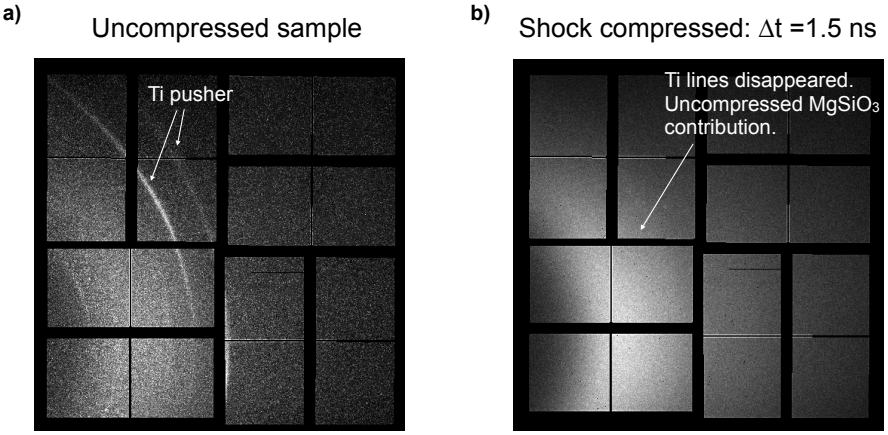

Figure 4.17: a) Reference measurements showing the xrd pattern of the unshocked sample (shot 430). Ti contributions is evident in the two sharp lines (pointed by the white arrows) and the $MgSiO_3$ glass contributes with the typical broad peak. b) XRD pattern of the same target of the reference signal shown on the left shock compressed and with a drive laser probe delay time equal to 1.5 ns (shot 430).

4.4.2 Estimation of the pressures

As seen in sec. 4.2, hydrodynamic simulations show that the shock propagates at quasi constant velocity uniformly compressing the sample. This allows to determine the shock velocity from a measurements of the transit time for known sample thicknesses.
Shock velocities are related to the pressure through equation of states that we discussed in sec. 4.1.1. We can therefore use these P-U_s relations to infer hydrodynamic conditions reached in the target.
Method for obtaining transit time from VISAR data has been reported in sec 4.2. Measured transit times, break out times and shock velocities are listed in table D.3 reported in appendix D.

$MgSiO_3$ glass P-Us. For $MgSiO_3$ glass we interpolate the P-Us shock data obtained on $MgSiO_3$ glass (density 2.74 g/cc) [Mosenfelder et al., 2009; Luo et al., 2004; Akins et al., 2004] and on porous $MgSiO_3$ (density 2.76-2.83 g/cc) [Marsh, 1980] that we already discuss in sec. 4.1.1. We did not considered the data series on porous $MgSiO_3$ at 2.171 g/cc reported in [Marsh, 1980] because, as already suggested by Mosenfelder et al. [2009], it seems to be affected by systematic errors being in disagreement with all the other dataset.

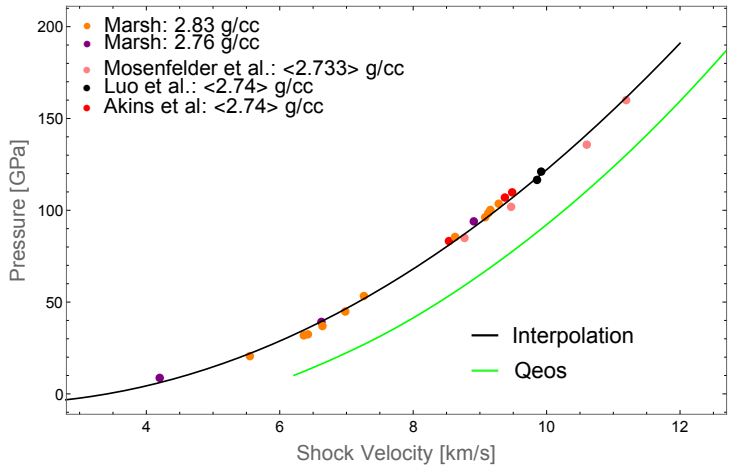

Figure 4.18: P - U_s shock data of $MgSiO_3$ (coloured dots) with the interpolation used in this study to calculate the pressure from the shock velocity (black line).

The P(U_s) function interpolating the selected literature data is represented in fig. 4.18 by the black line. The green line shows the P-Us relation obtained with the QEOS model, that has been used as equation of states of the $MgSiO_3$ glass for the

hydrodynamic simulations. QEOS is based on a Thomas-Fermi model and therefore is reliable for high temperature conditions. At low temperatures QEOS is not accurate as evidenced by the comparison with EoS data (see fig. 4.18). However, we remark that in this study hydrodynamic simulations have been used for qualitatively investigating the uniformity of the hydrodynamic conditions behind the shock front and not to determine the probed P-T conditions shot to shot. These are inferred from the fit function for the measured shock velocities.

Fo P-Us. For Forsterite we used the theoretical EoS proposed by Mosenfelder et al. [2007] that we reported in sec. 4.1.1. The model is represented by the red line in fig. 4.19 in a P-Us diagram together with the EoS data [Wett and Ahrens, 1983; Syono et al., 1981a; Marsh, 1980; Mosenfelder et al., 2007] that we already discussed in 4.1.1.

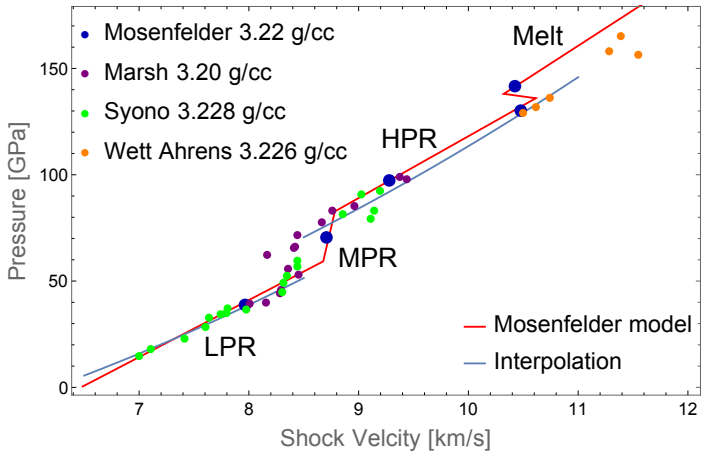

Figure 4.19: P - Us shock data of Fo (coloured dots) with the model [Mosenfelder et al., 2007] used in this study to calculate the pressure from the shock velocity (red line)

Estimated velocities and pressures Using the measured transit times (for the method see sec. 4.2) we obtained the mean shock velocities. Then with the reported P-U_s relations we estimated the pressure conditions reached in our samples and we associated a pressure regime to the XRD spectra presented before. Uncertainties on pressures are about 30% and derives from uncertainties on mean shock velocities of 16 %.

$MgSiO_3$ pressure estimation
Fig. 4.20 reports the evolution of shocked $MgSiO_3$ glass integrated XRD spectra through the different pressure regimes. We identified three regimes:

i) Low pressure regime with 10 GPa<P<50 GPa corresponding to a solid region of the Hugoniot: spectrum 421 ;

ii) Intermediate regime with 50 GPa<P <104 GPa corresponding to conditions still below the melting line: spectra 329, 330;

iii) High pressure regime or liquid regime with P>104 GPa which represent the Hugoniot segment above the melting: spectra 328 and 306;

Some shots (like 411) correspond to pressures close to the melting boundary, but uncertainty on the pressure does not allow to determine if they correspond to a solid or liquid phase.

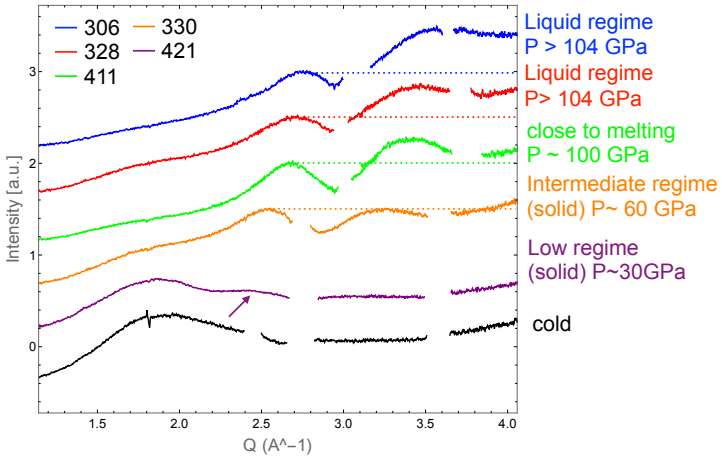

Figure 4.20: X ray diffraction spectra obtained on shocked $MgSiO_3$ glass. Labels indicate the pressure regime or phase corresponding to the spectrum.

We start to have evidence of the second peak from spectra in the intermediate regime at pressure $\sim$ 60 GPa. The increase in amplitude of this peak with respect to the first is evidenced by dotted coloured lines in fig. 4.20. For spectra in the intermediate regime (P $\sim$ 60 GPa) the second peak amplitude is equal or similar to the first peak amplitude. Then for spectra at conditions close to the melting (P $\sim$ 100 GPa) the second peak is higher that the first one. For spectra in the liquid regime (P>104 GPa) the amplitude of the second peak is even higher and the minimum between the two peaks is less pronounced than for spectra at conditions close to the melting.

Mg_2SiO_4 pressure estimation
Fig. 4.21 reports the shocked Fo XRD spectra classified according to their pressure regime.

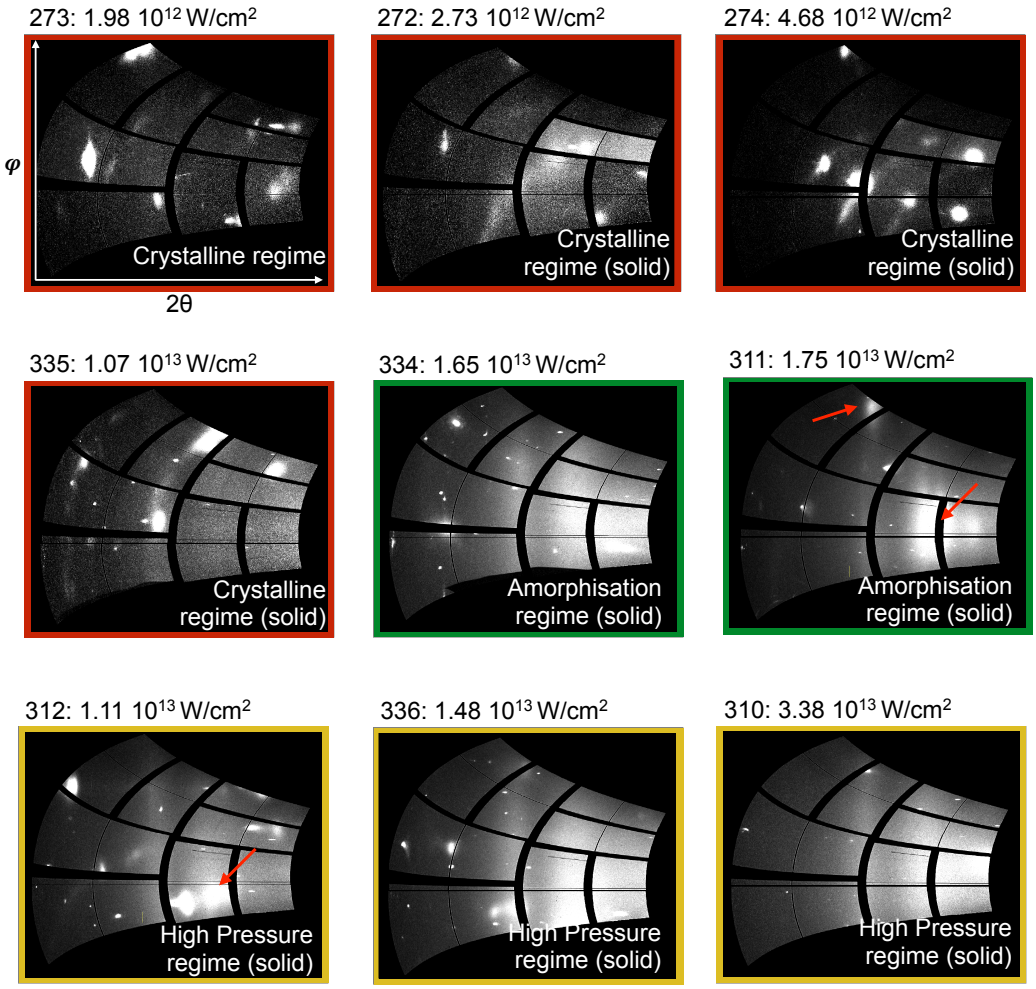

Figure 4.21: XRD patterns of shocked Fo classified according to their pressure regime.

We individuated three regimes:

i) Crystalline regime (red squares in fig. 4.21) with pressures $\sim$ 30 GPa corresponding to conditions along the Hugoniot in the solid phase. Spectra 273, 272, 274 and 335 belong to this regime. At these conditions spectra present broad bright spots that points at the occurrence of a crystalline phase.

ii) Amorphisation regime (green squares in fig. 4.21) with pressures $\sim$ 50 GPa, that still correspond to conditions below the melting (that along the Hugoniot occurs at 150 GPa). Spectra 334 and 311 belong to this regime. Spectra in this regime present broad Debye-Scherrer rings as typical for liquid or amorphous samples. The fact that estimated pressures here are well below melting boundary would suggest that these signals result from the contribution of an

amorphous phase.

iii) High pressure regime (yellow squares in fig. 4.21) with pressure $\sim$ 90 GPa. Spectra 310, 312 and 336 belong to this regime. The most likely scenario supported by our observations and pressure estimations is that spectra in this regime still corresponds to conditions below the melting line.

This analysis suggests that the spectra presenting Debye-Scherrer rings correspond to a solid amorphous phase. This result represents the first evidence of Fo amorphization under shock compression and calls for a revision of the calculated phase diagram proposed by Mosenfelder et al. [2007] and of the interpretation of recovery data of shocked Fo [Syono et al., 1981b]. Shock amorphization is a phenomenon that has been already observed for B_4C [Zhao et al., 2016]. Similarly picosecond amorphization of SiO_2 stishovite under tension has been recently reported by [Misawa et al., 2017].

4.5 Interpretation

In this section we will present an interpretation of the XRD signal observed for the $MgSiO_3$ glass and Fo. Our experiment accessed to a short q range (1.5-4.4 $Å^{-1}$). For this reason it is not possible to Fourier transform our integrated XRD signal to obtain total distribution functions. Therefore to interpret the structural properties linked to the observed XRD signals we could not use measured total distribution functions, but we must rely on comparison with theoretical studies that calculates total structure factors S(q) and corresponding partial structure factors and pair correlation functions g(r). Unfortunately, to our knowledge, there are no theoretical studies of this kind for conditions along the Hugoniot. Therefore we will compare our observations with calculations and experiments on $MgSiO_3$ and Mg_2SiO_4 compressed at ambient temperature.
We will first interpret the structure of $MgSiO_3$ glass and Fo at standard conditions and the structural changes these materials undergo under high pressure.

4.5.1 $MgSiO_3$ glass, Fo and Mg_2SiO_4 glass at standard conditions.

Interpretation of the XRD pattern of $MgSiO_3$ glass at standard conditions and underlying structural properties. Thanks to recent experiments and theoretical molecular dynamics MD studies [Ghosh et al., 2014; Wilding et al., 2004b,a; Kohara et al., 2004, 2011] the structural properties of $MgSiO_3$ glass at standard conditions are well known. DFT studies [Kohara et al., 2011] predict the $MgSiO_3$ glass to be composed of SiO_4 tetrahedra and MgO_x polyhedra (among which MgO_4 is the most abundant). This is consistent with average coordination numbers of Si-O and Mg-O correlations found experimentally [Wilding et al., 2004a] and theoretically [Ghosh et al., 2014] (SiO and MgO coordinations are 4.0 ± 0.1 and 4.5 ± 0.1 respectively). Both SiO_4 tetrahedra and MgO_x are connected in networks with broad ring size distributions.
MD studies also allow to interpret XRD pattern of $MgSiO_3$ glass at standard conditions. Indeed with MD it is possible to calculate the partial pair correlation functions $g_{\alpha\beta}$ and therefore through Fourier transform the partial structure factors $S_{\alpha\beta}$, where α and β denote the atomic species. Then the total structure factor results from the sum of all the partial structure factors weighted over the products $b_\alpha b_\beta \sqrt{C_\alpha\, C_\beta}$ where C_α gives the concentration of species α and b_α is the scattering length (that in the case of the X-rays is proportional to the atomic structure factor):

$$S_{tot}(q) = \frac{\sum_{\alpha\beta} b_\alpha(q)\, b_\beta(q) \sqrt{C_\alpha\, C_\beta}\; S_{\alpha\beta}(q)}{\sum_{\alpha\beta} b_\alpha^2(q) C_\alpha} \tag{4.1}$$

Therefore MD studies allows to interpret the structures of the total structure factor on the basis of the various α-β correlations.

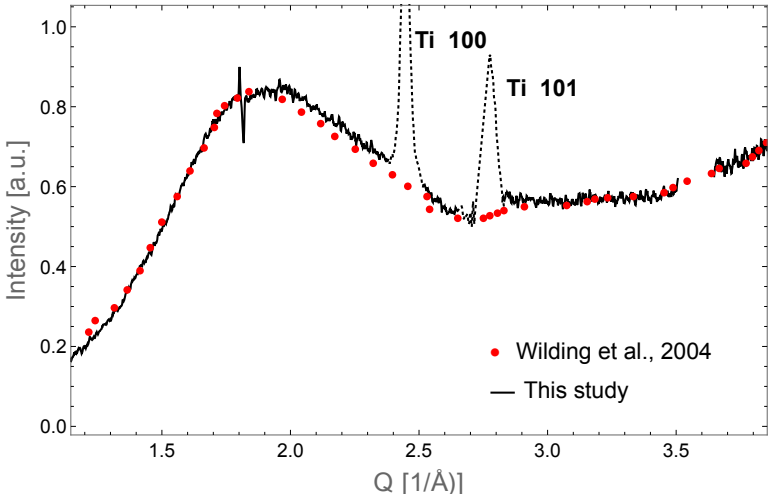

Figure 4.22: Integrated X-ray diffraction signal of $MgSiO_3$ glass at standard conditions (versus scattering vector q) in comparison with results from [Wilding et al., 2004a].

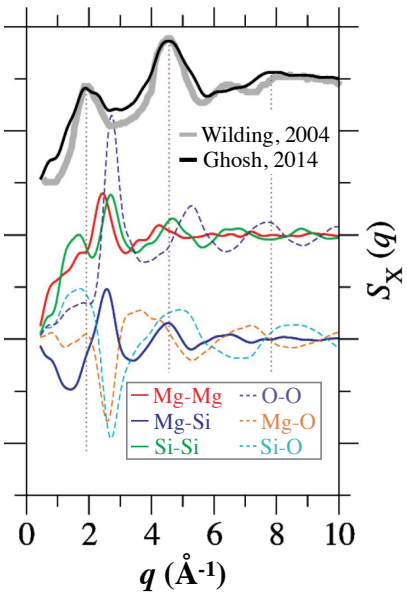

Figure 4.23: X-rays total (black lines) and partial (coloured lines) structure factors obtained with first principle ab-initio calculations by [Ghosh et al., 2014]. The theoretic total structure factors are compared with the experimental ones obtained by Wilding et al. [2004a]. Figure from [Ghosh et al., 2014].

Theoretical X-ray total structure factor S(q) obtained by Ghosh et al. [2014] is represented in fig. 4.23, showing good agreement with experimental S(q) of [Wilding et al., 2004a] and therefore with our XRD spectrum of $MgSiO_3$ glass at standard conditions (fig. 4.22). We can therefore interpret our XRD spectra on the basis of partial structure factors calculated by Ghosh et al. [2014] with AIMD and shown in fig. 4.23. It follows that the first peak of XRD spectra at 1.87 $Å^{-1}$ is mainly due to Si-O and Mg-O (cation-anion) correlations. Mg-Mg and Si-Si correlations are instead the main contribution of the second peak of the XRD structure factor, whose beginning corresponds to the rise in the XRD intensity signal that we observe for q > 3.5 $Å^{-1}$.

Forsterite XRD pattern at standard conditions and underlying structure As already reported in sec. 4.3.3 the spectrum obtained on Fo at standard conditions exhibit single spots at q vectors corresponding to various Fo lattice plane. The analysis of the peak positions for these spectra is coherent with tabulated values for Fo lattice plane (see fig. 4.14).

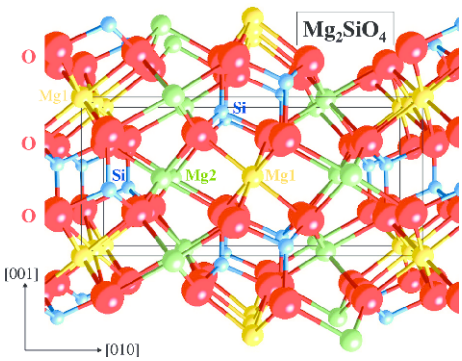

Figure 4.24: Crystal structure of Forsterite. Image taken from [Mitchell, 2008]. Red spheres represents oxygen atoms, green and yellow spheres represent magnesium atoms, blue spheres represent Si atoms.

The comprehension of the structural properties of Fo at standard conditions will help in the interpretation of the structural changes induced by shock compression. The crystal structure of Fo is orthorhombic, with unit cell of sizes a = 4.75 Å, b = 10.2 Å, c = 5.98 Å. Fo is composed by SiO_4^{4-} anions and Mg^{2+} cations. As in quarts, Si (blue spheres in fig. 4.24) and O (red spheres in fig. 4.24) atoms are organised in a SiO_4 tetrahedra. In this tetrahedra each O atoms is linked to the Si with a covalent bond, thus implying that each O has a residual partial negative charge. Such negative

charge exerces a repulsive force between the oxygens, which leads to the tetrahedral shape. Mg^{2+} cations can occupy two different MgO_6 octahedral sites (yellow and green spheres in fig. 4.24) and are linked to SiO_4^{4-} anions through ionic bonds. In Fo crystal SiO_4 structures are isolated, not directly linked to each other. This has been proved by various Raman spectroscopy studies (e.g [Durben et al., 1993]).

	$MgSiO_3$ glass	Mg_2SiO_4 glass	Fo
Structure	SiO_4 network + MgO_x network	MgO_x network +isolated SiO_4 or Si_2O_7	Orthorombic with isolated SiO_4
CN_{MgO}	4.5	5	6
CN_{SiO}	4	4	4
MgO_x structures	mainly x =4	x=4,5,6..	only x= 6
SiO_x structures	x=4	x=4	x=4
SiO_4 connectivity	network	isolated SiO_4 + Si_2O_7 dimers	isolated SiO_4
MgO_x connectivity	MgO_x network	MgO_x network	MgO_6 crystalline network
MgO_x morfology	uniform polyhedra	relatively uniform tetrahedra, distorted polyhedra	uniform tetrahedra

Table 4.4

Mg_2SiO_4 glass structure at ambient conditions In the previous section we reported the observation of an amorphous phase obtained from shocked Fo. In order to interpret its structural properties, it will be helpful to comprehend the structure of the Mg_2SiO_4 glass at standard conditions. Recent theoretical [Kohara et al., 2011] and experimental studies [Kohara et al., 2004; Wilding et al., 2004a,b] provide a picture of the Mg_2SiO_4 glass structure at standard conditions. These studies found an Mg_2SiO_4 glass structure significantly different from both Fo crystal and $MgSiO_3$

glass structures. Peculiarly with respect to other silicate glasses, the network is provided by distorted MgO polyhedra connectivity surrounded by isolated and dimerised SiO_4 tetrahedra. Indeed differently from Fo crystal, Si_2O_7 dimers are present in the Mg_2SiO_4 glass. Finally MgO networks are composed of different polyhedra (uniform MgO_4 tetrahedra, distorted MgO_5 and MgO_6 polyhedra present in 3:5:2 ratio) with respect to $MgSiO_3$ glass where the key unit are MgO_4 uniform tetrahedra and to Fo crystal where networks are formed by uniform MgO_6 octahedra.

Tab 4.4 resumes the structural properties of $MgSiO_3$ glass, Mg_2SiO_4 glass and Fo crystal.

4.5.2 $MgSiO_3$ glass, Fo and Mg_2SiO_4 glass structural changes under shock compression: interpretation of the XRD signals

In this section we present a preliminary interpretation of the structural properties at the basis of the observed XRD patterns for shocked $MgSiO_3$ glass and Fo. Unfortunately there are no theoretical works on the structural properties of these material along the Hugoniot. For this reason our interpretations will rely on the existing MD and experimental studies of statically compressed $MgSiO_3$ and Mg_2SiO_4 glasses.

4.5.2.1 Shocked $MgSiO_3$ glass: interpretation of the XRD pattern and structural changes for conditions below the melting line.

We recall that the two main effects induced by shock compression on our XRD patterns are: a shift of the first peak of the cold XRD spectrum toward high q; the emergence, grow (with respect to the first peak) and shift of a second peak at ~ 3.3 $Å^{-1}$. Here we focus on the interpretation of these behaviours for conditions below the melting line. To this aim we compare our XRD patterns with MD studies performed by Ghosh et al. [2014] on $MgSiO_3$ glass compressed at ambient temperature.
Ghosh et al. [2014] calculated with MD neutron and X-ray structure functions for $MgSiO_3$ under ambient temperature compression. The X-ray S(q) obtained by Ghosh et al. [2014] for P= 0 GPa, 14 GPa and 170 GPa are shown in fig. 4.25. These X-ray S(q) evidence that pressure induces:

i) a shift of the first peak toward high q (q= 1.85 $Å^{-1}$ at 0, q=2.5 $Å^{-1}$ at 14 GPa and q=2.8 $Å^{-1}$ at 170 GPa);

ii) the emergence, grow (with respect to the first peak) and shift of a second peak. Second peak lies at q= 3.2 $Å^{-1}$ at 14 GPa and q= 3.8 $Å^{-1}$ at 170 GPa.

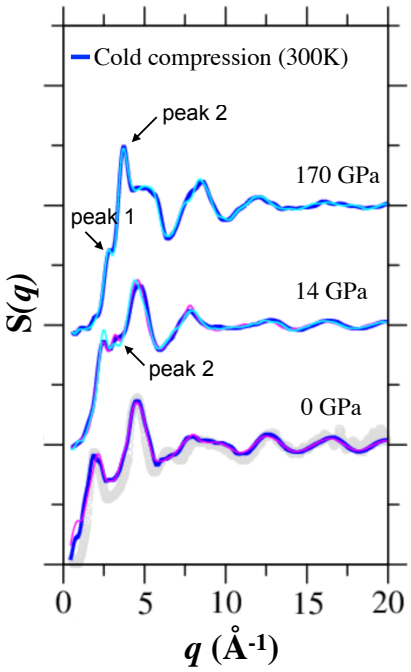

Figure 4.25: X-ray S(q) of $MgSiO_3$ at P= 0 GPa, 14 GPa and 170 GPa. Image from [Ghosh et al., 2014].

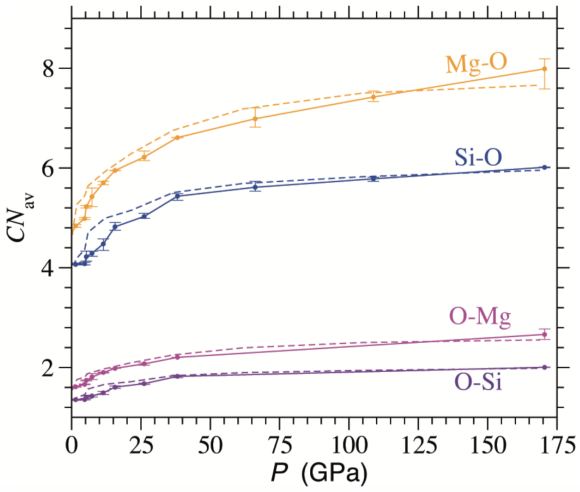

Figure 4.26: Average coordination numbers of $MgSiO_3$ obtained by [Ghosh et al., 2014] for pressures between 0 and 175 GPa. Image from [Ghosh et al., 2014]

Therefore X-ray structure factors calculated by [Ghosh et al., 2014] for ambient temperature compression and our XRD patterns observed for shock compression exhibit

the same qualitative behaviour. In addition to that, peak positions predicted by [Ghosh et al., 2014] are similar to those observed in our experiment. Differences mainly concern the contrast between the first and the second peaks and may be due to the effect of the temperature in shock compression (along the Hugoniot P∼100 GPa corresponds to T ∼ 5000K). However the qualitative agreement suggests that shock compression produces similar structural changes to those predicted for a compression at ambient temperature in [Ghosh et al., 2014] and that temperature has not a dominant effects at the studied conditions. In such a case the structural configurations explored by $MgSiO_3$ glasses at pressures between 0 and 100 GPa along the Hugoniot span from the one dominated by a network of SiO and MgO tetrahedra (0 GPa) to those dominated by environments with higher Si-O and Mg-O coordination numbers (Ghosh et al. [2014] predict sixfold SiO and sevenfold MgO environments at 100 GPa, see fig. 4.26). Moreover, the pressure has the effect to increase the connectivity of SiO_x structures with respect to the un-shocked glass [Ghosh et al., 2014]. Molecular dynamics studies of $MgSiO_3$ glass along the Hugoniot are required in order to confirm is this scenario predicted for ambient temperature compression is really valid also for shock compression. A deeper comprehension of the structural changes induced by shock compression can provide new insights for a better understanding of the microscopic origins of the macroscopic properties (e.g. changes in the compressibility) occurring along the Hugoniot.

4.5.2.2 Shocked Fo: interpretation of the XRD pattern and structural changes

Intepretation of the nature of the crystalline phases in the low pressure regime Efforts have been made to identify the crystal phases underlying to these signals. E.g. the XRD pattern probed during shot 273 has been interpolated using a fit (see fig .4.27) calculated with a LeBail refinement (performed with the diffraction refinement program GSAS) that seems to identify phase fractions of compressed forsterite (pink tick marks in fig.4.27) and wadsleyite[4] (light blue tick marks in fig. 4.27) [Gleason private communication]. However the small range of q that we accessed does not allow to identify the phases with reasonable certainty.
Thanks to the energy upgrade of LCLS and to the advent of European XFEL, endstations as MEC will allow to perform experiments over an extended q range (1.5-6 $Å^{-1}$) thus entirely accessing to second peak. This would allow to interpret the crystal structure that produces our XRD pattern with more confidence.

[4]Wadsleyte structure belongs to the orthorombic crystal system as Fo. However an important difference from Fo crystal, is that Wadsleyite structures sees the occurrence of linked SiO_4 tetrahedra, i.e. of Si_2O_7 units

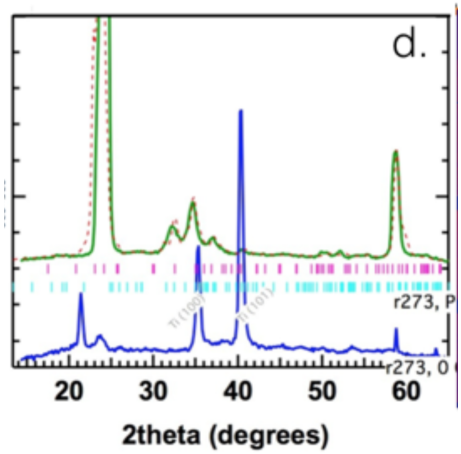

Figure 4.27: Integrated xrd pattern of shot 273 (see fig. 4.15) (green line) and of its reference signal (blue line). The red dashed line represents a LeBail refinement for calculated fit identifying phase fractions of compressed forsterite (pink tick marks) and Wd (light blue tick marks).

Interpretation of the XRD patterns in the amorphization and high pressure regimes. There are two possibilities to explain XRD patterns in the amorphisation and high pressure regime. In the first scenario the signal results from Fo dissociated into MgO + glassy $MgSiO_3$ (hypothesis 1)). In the second scenario, the signal results from amorphous Mg_2SiO_4 (hypothesis 2)).
An analysis of the bright spots occurring in spectra 312, 336, 334, 311 and 310 (i.e. for the spectra that evidence an amorphous phase) did not evidence the occurrence of dissociated crystalline MgO that in case would exhibit diffraction peaks in the explored q range[5]. Therefore our data seem to suggest that shocked Fo yields Mg_2SiO_4 glass in disagreement with the interpretation proposed in [Syono et al., 1981b]. However we cannot exclude hypothesis 1) with reasonable confidence. Future experiments accessing to a larger q range would allow to discriminate between these two hypotheses with stronger certainty.

[5]A crystallisation under shock compression is expected to produce various crystal grains randomly oriented with high chances to be detected.

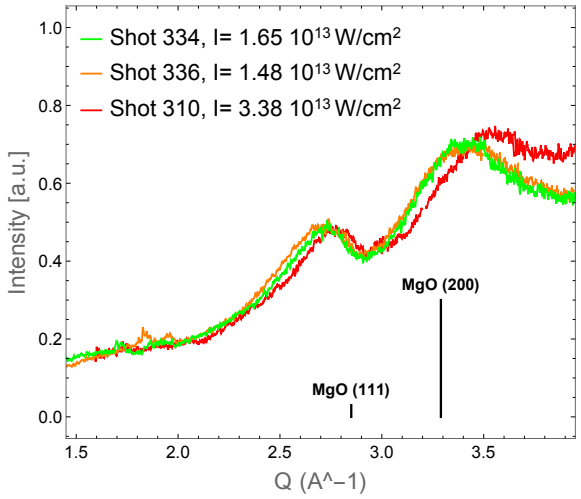

Figure 4.28: Glass contribution to the X-ray diffraction spectra of shots 334, 336 and 310. Black lines represent tabulated peak positions of MgO lattice planes 110 and 200 at 90 GPa.

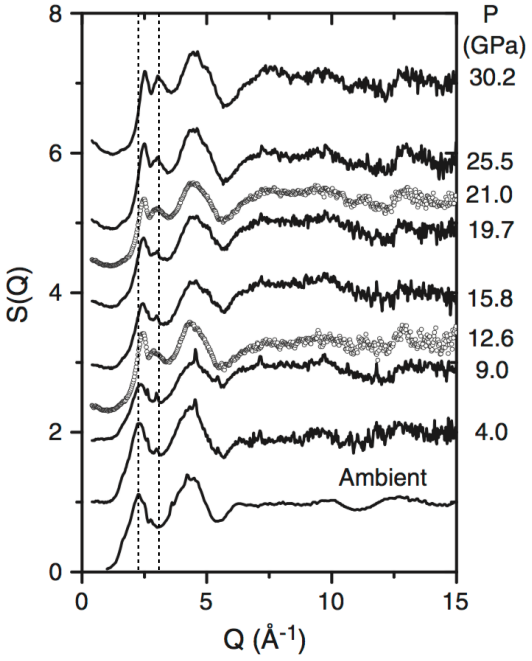

Figure 4.29: Mg_2SiO_4 X-ray structure factors up to 30.2 GPa. Image from [Benmore et al., 2011].

In the following we discuss the case of amorphous Mg_2SiO_4 glass (hypothesis 2)), as it is the most probable case according to our data. Unfortunately there are no theoretical studies on Mg_2SiO_4 glass that provide the structural properties at the pressures reached in this experiments (0 - $\sim$ 90 GPa). A recent XRD experiment [Benmore et al., 2011] on Mg_2SiO_4 glass compressed at ambient temperature reports and analyses structure factors up to 30.2 GPa (see fig. 4.29). Fig. 4.29 evidences that pressure induces a shift of the first peak at 2.3 $Å^{-1}$ (pointed by the first dashed line) and the emergence of a second peak at 3.1 $Å^{-1}$. Also the second peak shifts toward higher q for increasing pressures (see second dashed line). These behaviours are similar to those that we observed on our XRD spectra. Therefore if we assume that the XRD signal corresponds to an Mg_2SiO_4 amorphous phase, we can interpret the emergence and shft of the second peak and the shift of the first one in our XRD patterns on the basis of what have been proposed by Benmore et al. [2011]. In such case, the second peak in shock compressed Mg_2SiO_4 glass would arise from the contributions of O-O and Mg-O correlations. The shift of the first peak instead points at changes in the correlations Mg-Mg, Mg-Si and Mg-O.
In particular, static compression induces on Mg_2SiO_4 glass an increase of the Mg-O coordination from 5 to $\sim$ 7 in a range of pressure between 7 and 30 GPa. This would suggest, for the glass obtained from shocked compressed Fo, the occurrence of a higher number of high coordinated and connected MgO_x environments with respect to the glass at ambient pressure.
Instead, the effect of pressure on the Si-O correlations of Mg_2SiO_4 glass is not yet well understood. Unfortunately X-ray diffraction studies of Benmore et al. [2011] did not allow to determine changes in the Si-O correlations. These have been determined with neutron diffraction by Wilding et al. [2012] on a MgO-SiO_2 glass with 38% concentration (concentration close to Mg_2SiO_4 that has 33% of SiO_2). This study reports that a pressure increase from 0 to 8.6 GPa induces a significant increase in the connectivity of Si-O bonds. In other words Wilding et al. [2012] evidences that pressure induces a network formation for the studied glass. This may suggest that compression has a similar effect also on the Mg_2SiO_4 glass inducing the formation of SiO_4 networks. This is also suggested by the similarity of observed XRD patterns of the amorphous phases obtained from shocked $MgSiO_3$ glass and Fo.
However Raman studies by Shim and Catalli [2009] suggest that isolated SiO_4 tetrahedra in the Mg_2SiO_4 glass at standard conditions hardly transforms in SiO_x polyhedra with higher coordination (e.g. SiO_6 octahedra) for compression up to 80 GPa. We can imagine that the same would still applies for the transformation induced by the shock from Fo crystal[6] to Mg_2SiO_4 glass. In such a scenario the densification mechanism would be significantly different from the one of $MgSiO_3$ glass as the dominating

[6]We recall that Fo crystal are characterised by isolated SiO_4 tetrahedra as the Mg_2SiO_4 glass

SiO_x environments remain isolated SiO_4 tetrahedra[7].
Therefore two scenarios of the effects of shock compression are possible. In one case, pressure may induce formation of SiO_4 network as for the $MgSiO_3$ glass. For the other, the compaction due to compression may not be able to connect the isolated SiO_4 tetrahedra. In both cases pressure induces an increase in the Mg-O connectivity forming MgO networks. More theoretical investigation at higher pressure are required for discriminating between these hypotheses and for understanding whether and at which pressures compressed Mg_2SiO_4 glass could form SiO_4 networks as the other silica rich glasses.

[7]Effect of the pressure on Si-O correlation is neither understood for the Mg_2SiO_4 liquid. Ab initio simulation studies of de Koker et al. [2008b] predict and increase of the Si-O coordination with a pressure change from 0 to 20 GPa, while for Adjaoud et al. [2008] Si-O coordination is constant in the same pressure range.

4.6 Conclusion

We presented X-ray diffraction measurements on shocked Fo and $MgSiO_3$. Despite being preparatory, this study evidenced for the first time that shocked compressed $MgSiO_3$ glass is kept in an amorphous state up to the melting, contrarily to the interpretation for which shock compressed $MgSiO_3$ glass yields crystal Pv [Akins et al., 2004; Mosenfelder et al., 2009]. A quantitative analysis of the structural changes of the glass along the Hugoniot evidenced an agreement with the changes predicted by Ghosh et al. [2014] for compression a ambient temperature. This would suggests that such changes are mainly induced by the pressure, that would have a bigger effect than the temperature. Further theoretical and experimental studies are however required to advance in this field. The results obtained on Forsterite evidences that shocked Fo yields an amorphous phase at ~ 50 GPa. This observation calls for a reinterpretation of the phase diagrams proposed by Mosenfelder et al. [2007]. However the scarcity of the data and the limited q range that we access, requires additional experimental campaigns to provide a better characterisation of the total structure factors. Moreover a higher number of measurements would allow to increase the statistic of probed pressure conditions and therefore to determine phase boundaries. At the same time, theoretical studies of the structural properties of $MgSiO_3$ and Mg_2SiO_4 for conditions along the Hugoniot are required for a precise interpretation of XRD data.
The observation of shock formed Mg_2SiO_4 glass calls for investigations on the solid-amorphous transition mechanism and dynamics, which is a topic of primary interest for meteorite impact science. Indeed the correct interpretation of amorphous phases observed in meteorite craters requires a precise knowledge of glass formation mechanisms [Jaret et al., 2015].

Conclusions and perspectives

Conclusions

The main purpose of this project was characterising the phase diagrams and physical properties of MgO, $MgSiO_3$ and Mg_2SiO_4 at thermodynamic conditions relevant for planetary science.
To this aim, we performed three experimental campaigns using laser driven shock compression for reaching high pressure conditions. As diagnostics we used:

- rear side optical diagnostics for characterising decaying shocks in MgO, $MgSiO_3$ and Mg_2SiO_4 phase diagram for pressures between 0.2-1.4TPa, 0.12-0.5 TPa, 0.2-0.8 GPa respectively (first campaign);
- XANES spectroscopy for characterising MgO in a wide region of the phase diagram up to $\sim$ 500 GPa and $\sim$ 30000 K (second campaign);
- X-ray diffraction on shock compressed $MgSiO_3$ and Mg_2SiO_4 for pressures between 0-150 GPa and 0-90 GPa respectively (third campaign).

The ensemble of these experiments enriches our knowledge of the studied MgO-SiO_2 systems at high pressure.
The first campaign aimed at studying the occurrence of phase transitions along the Hugoniot of MgO, $MgSiO_3$ and Forsterite (Mg_2SiO_4 crystalline phase) between 0.2-1.2 TPa, 0.12-0.5 TPa, and 0.2-0.85 TPa respectively, with the decaying shock technique. The target of this campaign were carefully designed in order to avoid to misinterpret reverberating shock as phase transition signatures. To this aim, an hydrodynamic simulation study has been performed and tested with shots on a reference material. Therefore our study provided reliable information about the occurrence of phase transitions in the MgO, $MgSiO_3$ and Mg_2SiO_4 phase diagrams. In particular we proposed a new experimental melting point for the MgO that put into question previous estimates of the melting line; we did not evidence the occurrence of any phase transition between 0.12-0.5 TPa and 0.2-0.85 TPa for the $MgSiO_3$ and Mg_2SiO_4 respectively. These latter two points respectively solved the controversy on the $MgSiO_3$ liquid-liquid phase transition and ruled out the occurrence of Mg_2SiO_4 dissociation in

MgO+ $MgSiO_3$ as proposed in [Sekine et al., 2016]. Such results have been recently confirmed by [Davies, AGU Fall meeting] and [Root, AGU Fall meeting]. For all the studied materials, we observed that the reflectivity increase and melting do not occur at coincident thermodynamic conditions. This may suggest that MgO, $MgSiO_3$ and Mg_2SiO_4 melts into poor electrical conductor (along the Hugoniot) with implications for what concerns the modelling of magnetic field generation via dynamo mechanisms.

Despite decaying shock results are of good quality (tested with the reproducibility on different facilities), such a study needs to be integrated by studies with X-ray diagnostics. Indeed decaying shock is an indirect method for detecting transitions with no access to structural informations and it is not adapted for studying transitions with a small volume change for example. For this reason, we performed experiments also with X-rays diagnostics that directly access to microscopic information.
We experimentally investigated MgO in the WDM regime with XANES spectroscopy (second campaign). The campaign has been performed at LULI2000 and focused on investigating electronic and structural properties of MgO. This experiment provides the first exploitable XANES spectra of shocked MgO, which is a not negligible technical success. XANES spectra have been collected over a wide pressure and temperature range and this allowed to study the behaviour of the spectra for increasing temperature and density. In order to interpret our spectra we used ab-initio molecular dynamics AIMD. We obtained theoretical spectra that exhibit the same behaviour of the experimental ones. Calculated density of states and pair correlation functions (g(r)) evidences the metallisation mechanism and the liquid properties of liquid MgO:

- the gap closes for increasing temperature by valence and conduction band widening;
- the liquid MgO is disordered at a local level.

The third campaign has been performed at the MEC end station of LCLS (SLAC). Using the X-FEL X-ray beam and the drive laser available at MEC we performed X-ray diffraction measurements on shocked Forsterite and $MgSiO_3$ glass for pressures between 0-90 GPa and 0-150 GPa respectively. Despite being preparatory, this study reports first direct observations of the structural changes occurring along the Hugoniot of Fo and $MgSiO_3$, evidencing the unexpected occurrence of an amorphous phase along the Fo Hugoniot. A qualitative analysis of the structural changes of the XRD patterns observed for shocked Forsterite and $MgSiO_3$ glass has been performed comparing our observations with theoretical results obtained on $MgSiO_3$ glass [Ghosh et al., 2014] and experimental [Benmore et al., 2011] and theoretical [Adjaoud et al., 2008] studies on Mg_2SiO_4. Unfortunately our study does not allow to precisely locate the occurrence of Fo amorphisation in the Mg_2SiO_4 phase diagram. A possibility is that this amorphisation corresponds to the phase transformation from MPR to HPR

proposed by [Mosenfelder et al., 2007] to occur at $\sim$ 50 GPa along the Hugoniot. The results obtained here can help in the comprehension of impact phenomena as meteorites for which the knowledge of the structural transformations occurring under shock compression is crucial.

In conclusion this thesis provide precious information about MgO, $MgSiO_3$ and Mg_2SiO_4 phase diagram at geophysically relevant conditions that would allow to make some other steps forward in the modelling of Earth-like and Super-Earth interiors.

Perspectives

This study left a variety of interesting and important open questions that worth to be faced with systematic studies. We report here those that we consider most significant:

- Further theoretical and experimental studies on the structural properties of shock compressed $MgSiO_3$ glass and Forsterite are needed. With energy upgrade of LCLS and the advent of European X-Fel, future experiments will allow to measure XRD spectra over a wider range of q thus providing a better characterisation of the phases that occur along the Hugoniots. This will allow, for example, to interpret with more certainty whether shocked Fo yields amorphous Mg_2SiO_4 or MgO + amorphous $MgSiO_3$. Moreover the mechanism and kinetics of the transition from Fo to Mg_2SiO_4 glass need to be investigated since it is of extreme importance for the comprehension of meteorite craters [Jaret et al., 2015]. Theoretical MD dynamic studies on $MgSiO_3$ and Mg_2SiO_4 at conditions along the Hugoniot are required for a deeper comprehension of the structural changes induced by shock compression.
- Our study provided precious information for advancing in the knowledge of the properties of $MgSiO_3$ and Mg_2SiO_4 in a wide region of the phase diagram. However the geophysically relevant high pressure (P> 4-5Mbar) and low temperature (<10000K) region of $MgSiO_3$ and Mg_2SiO_4 phase diagrams still need to be investigated. $MgSiO_3$ and Mg_2SiO_4 at these extreme conditions are thought to be present in Super-Earth mantles or giant planet cores. Here, these materials are thought to undergo to polymorphic transformations and dissociation reactions, that have never been experimentally observed. Whether Ppv $MgSiO_3$ transforms into another polymorph or whether and at which conditions $MgSiO_3$ dissociates into the constituent oxides MgO and SiO_2, for examples, are questions that need to be answered. Future experiments on largest high power laser facilities (NIF, LMJ[8]) with quasi-isentropic compression are needed to achieve

[8]In this context, a proposal of our group to perform X-ray diffraction on ramp compressed Fe at

these conditions and answer these questions.

- The last point opens to another perspective. Ideally X-ray diffraction would be the best diagnostic to couple to quasi-isentropic compression in order to study the polymorphic transitions or dissociation reactions at the conditions cited before. Unfortunately the optical lasers now available at X-Fel do not have enough power to ramp compress materials to the required high pressure - low temperature conditions. Therefore it is necessary to develop XRD diagnostics for the facilities (NIF, LMJ) where such conditions can be achieved. To this aim, during this thesis we started the development of a diagnostic for X-ray diffraction in transmission geometry at LULI2000. Preparatory campaign provided XRD patterns on shocked Al[9]. Some experimental adjustments still need to be performed, like a better shielding from background noise. Continuing with the development of this diagnostic is mandatory to prepare future experiments on larger facilities (LMJ).
- There is another strategy to study the transitions that occurs in the high pressures and low temperature regions of $MgSiO_3$ and Mg_2SiO_4 phase diagrams and it is based on the concept of chemical pressure in analogue compositions. For example, the $MgSiO_3$ analogue $CaTiO_3$ undergoes to the same polymorphic transition as $MgSiO_3$ but at lower pressure (Pv to Ppv at 100 GPa [Trunin et al., 1971]). Therefore the same transitions occurring in $MgSiO_3$ or Mg_2SiO_4 can be investigated at intermediate scale facilities (e.g LULI2000 and GEKKOXII with easier accessibility than NIF or LMJ) with experiment on analogue compounds.

- Another natural perspective of this study is to experimentally investigate the more complex materials that really occurs in planetary interiors: $(Fe, Mg)SiO_3$ and $(Fe,Mg)_2SiO_4$. An exciting possibility is to study the Fe K-edge of shocked $(Fe, Mg)SiO_3$ and $(Fe,Mg)_2SiO_4$ with EXAFS spectroscopy. This will be possible at the ESRF synchrotron, where recently a high power laser has been installed at the beam-line ID24. The feasibility of EXAFS measurements on shock compressed matter at ID24 has already been proven with an experiment on Fe [Torchio et al., 2016].

LMJ is already scheduled

[9]first time of exploitable XRD pattern in transmission geometry on shocked samples at LULI

Appendix A

MULTI Code

This code deals with the problem of hydrodynamic motion coupled to intense radiation field. In other words it solves the following system of equations:

$$\frac{d\rho}{dt} = -\rho \boldsymbol{\nabla} \cdot \boldsymbol{u} \tag{A.1}$$

$$\rho \frac{d\boldsymbol{v}}{dt} = -\nabla P - \boldsymbol{R} \tag{A.2}$$

$$\rho \frac{de}{dt} = -P \boldsymbol{\nabla} \cdot \boldsymbol{v} \ \boldsymbol{\nabla} \cdot \boldsymbol{q} - Q + S \tag{A.3}$$

$$f(P, \rho, e) = 0 \tag{A.4}$$

$$\Big(\frac{1}{c}\frac{\partial}{\partial t} + \boldsymbol{n} \cdot \nabla\Big) I(\boldsymbol{r}, \boldsymbol{n}, \nu, t) = \eta(\boldsymbol{r}, \boldsymbol{n}, \nu, t) - \chi(\boldsymbol{r}, \boldsymbol{n}, \nu, t) I(\boldsymbol{r}, \boldsymbol{n}, \nu, t) \tag{A.5}$$

where the first three equations represent the hydrodynamic problem coupled to the radiation through the terms Q, R respectively represent the total emission rate per unit volume of energy, the total emission rate per unit volume of momentum and S represents the external energy sources like the laser pulse. The fourth equation is the equation of state. Finally the fifth equation is the radiation transport equation where $I(\boldsymbol{r}, \boldsymbol{n}, \nu, t)$ represents the radiation intensity at coordinates $\boldsymbol{r}$, time t, and with a wave-vector $\boldsymbol{n}$ and frequency ν and η and χ are the emissivity and opacity respectively. The code solves this problem in the planar case modeling the electronic heat conduction using Spitzer limited flux treatment. The laser energy is absorbed via inverse bremsstrahlung. The results obtain with this simulation of course depends on the equation of state and opacity used. Usually for our simulations we used the SESAME equation of state and QEOS equation of state when SESAME was not available.

Appendix B

Hydrodynamic simulations to evaluate preheating with different opacitites

B.1 Appendix to the preheating problem

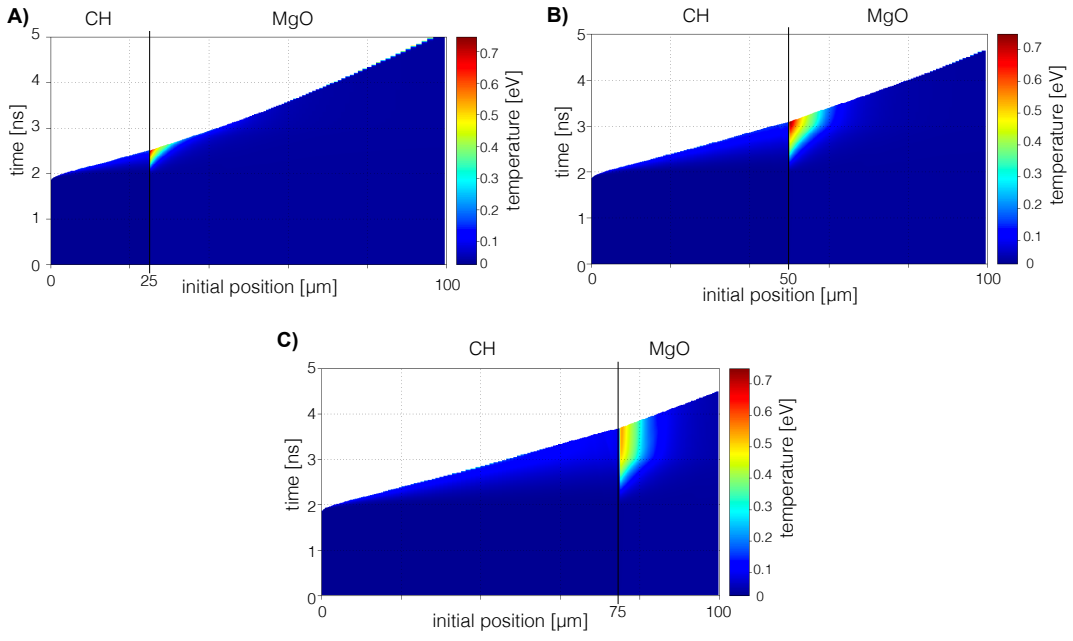

Figure B.1: preheating of MgO for different CH thicknesses

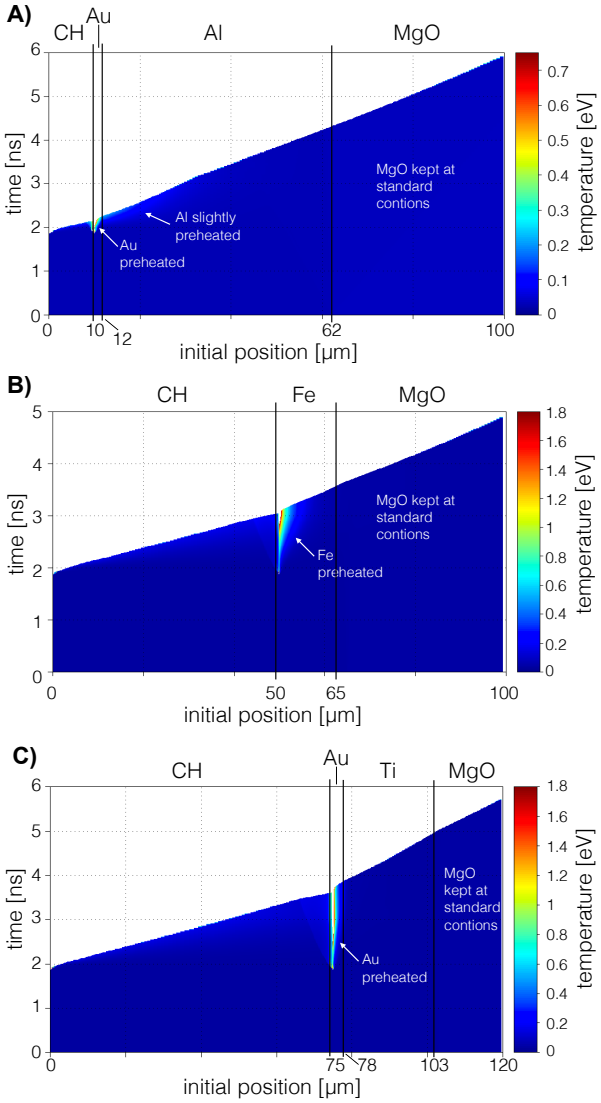

Figure B.2: A), B) and C) represent respectively color plots of the temperature versus time and initial position plane of a 50μm CH|15μm Fe|MgO, 75μm CH| 3μm Au| 25μm Ti|MgO and 10μm CH |2μm Au| 50μmAl|MgO target produced by a laser pulse of 1.2 ns and 10^{14} W/cm^2 obtained with a MULTI simulation with tables TV for the opacity of CH.

Appendix C

Supporting information to chapter 3.

C.1 Vertical alignment and spatial resolution

C.1.1 Vertical alignment

In order to refine the vertical alignement of the spectrometer we follow the procedure that we report here. We placed a Vanadium wire with a diameter of 100 μm at TCC along the "spectral" axes. We then performed three shots (shots 10, 12 and 13) varying the wire position respect to TCC and we looked at the wire shadows on the IP signals (shot 10 was performed also as calibration shot with a NaCl target). The wire position relative to the TCC was 0, + 125 μm and + 85 μm for shots 10, 12 and 13 respectively. The signals, normalised with a shot performed with the backlighter only (shot 11) are reported in fig. C.1. As it is easy to see from the figure, the wire is not always perfectly horizontal. For this reason, for the alignement we selected a region of $\sim$ 10 eV around MgO K edge. The vertical lineouts obtained from this selected integration area for the three shots are shown in fig. C.1. The closest wire shadow to the IP center is the one relative to shot 13 which corresponds to a distance between the wire and the TCC of + 85 μm. We selected this configuration and we aligned the targets to this position.
We do not report the horizontal alignment as it has been performed with the same technique and it was less delicate than the vertical (see the geometry of the probed region and the shocked region shown in fig. 3.5)

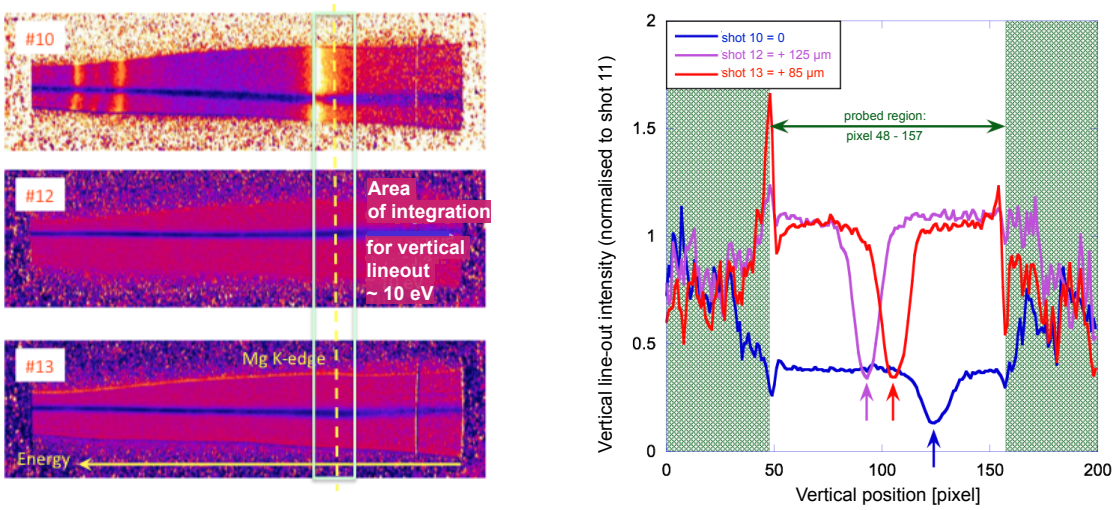

Figure C.1: Left: vertical alignment signals. Right: Vertical line-out from the area of integration shown on the left for the three alignment shots.

C.1.2 Spatial resolution

The spatial resolution of our spectrometer can be deduced from the shadows of the wire that we used for the vertical alignment. From fig. C.1 we see that the wire shadow edge is broadened of about 10 $\pm$ 2 pixels which corresponds to a spatial resolution of 55 $\pm$ 11 μm. Considering the geometry of the spectrometer as it is shown in fig. 3.3, this resolution corresponds to a source X of a diameter equal to 66 $\pm$ 13 μm. This is reasonable since we defocused our ps beam in order to get a focal spot on the backlighter of about 50 μm of diameter.

C.2 SOP signals

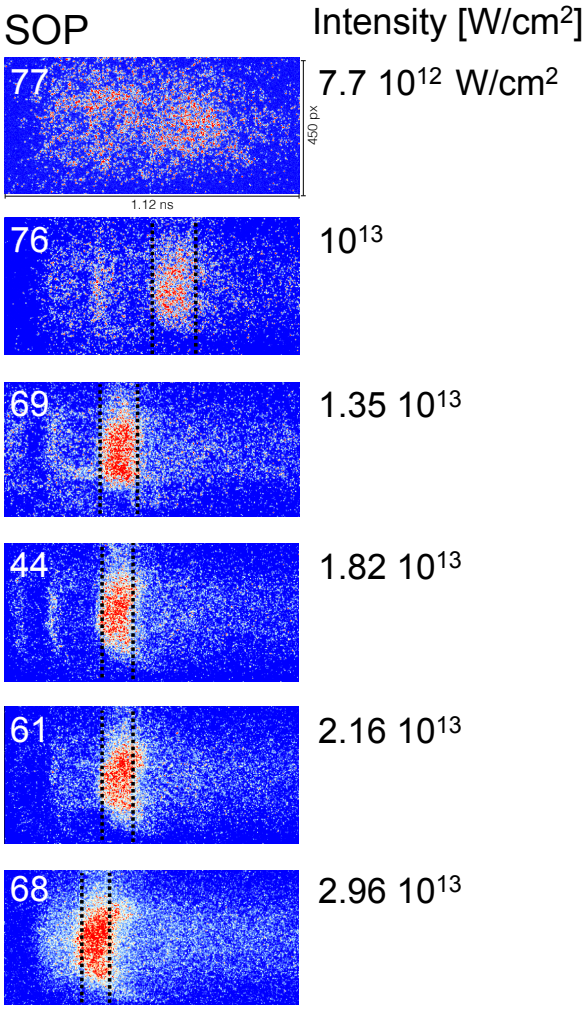

Figure C.2: SOP signal for various drive laser intensities. For laser intensity $< 10^{13}$ the thermal emission signal is not exploitable and transit time cannot be characterised.

Appendix D

Transit times, break out times, mean shock velocities and X-ray probe times.

Table D.1 summarises break out time and X-ray probe time for the shots performed on $MgSiO_3$ glass.

Shot	**Break out time [ns]**	**X probe time [ns]**
306	8.04	8
307	10.96	10
328	9.91	9
329	12.96	9
330	14.79	12
333	10.22	9
410	11.98	9
411	10.22	11
421	25	10

Table D.1

Tab. D.2 summarises break out times and X-ray probe times corresponding to shots on Fo.

shot	Time break out [ns]	X-ray probe time [ns]
273	14.78	12
272	15.23	12
274	14.35	12
335	12.19	11
312	12.84	12
336	11.01	11
334	13	12
311	12.1	10
310	10.68	7

Table D.2

Table D.3 summarised the measured transit and break out time and the shock velocity for each shot.

Shot	**Transit time [ns]**	**Us [km/s]**	δ **Us**	**break out time [ns]**	**Material**
306	8.17	11.63	2.18	8.04	MgSiO3 glass
307	11.07	8.58	1.61	10.96	MgSiO3 glass
328	8.85	10.75	2.02	9.91	MgSiO3 glass
329	13.01	7.3	1.37	12.96	MgSiO3 glass
330	13.12	7.24	1.36	14.79	MgSiO3 glass
331	11.31	8.41	1.58	11.24	MgSiO3 glass
332	9.82	9.68	1.82	9.73	MgSiO3 glass
333	10.38	9.16	1.72	10.22	MgSiO3 glass
410	11.53	8.24	1.55	11.98	MgSiO3 glass
411	11.17	8.51	1.6	11.63	MgSiO3 glass
412	12.86	7.39	1.39	13.46	MgSiO3 glass
269	11.05	8.59	1.61	13.89	MgSiO3 glass
310	10.23	9.28	1.74	10.68	Fo
334	12.1	7.86	1.47	13	Fo
336	10.27	9.27	1.74	11.01	Fo
311	12.01	7.92	1.49	12.1	Fo
312	10.59	8.99	1.69	12.84	Fo
335	10.86	8.76	1.64	12.19	Fo
272	12.8	7.43	1.39	15.23	Fo
273	12.01	7.93	1.49	14.78	Fo
274	13.14	7.23	1.36	14.35	Fo

Table D.3

Bibliography

Adjaoud, O., Steinle-Neumann, G., and Jahn, S. (2008). Mg 2 sio 4 liquid under high pressure from molecular dynamics. *Chemical Geology*, 256(3):185–192.

Akins, J. A., Luo, S.-N., Asimow, P. D., and Ahrens, T. J. (2004). Shock-induced melting of mgsio3 perovskite and implications for melts in earth's lowermost mantle. *Geophysical Research Letters*, 31(14).

Anisimov, S. and Kravchenko, V. (1985). Shock wave in condensed matter generated by impulsive load. *Zeitschrift für Naturforschung A*, 40(1):8–13.

Beck, L., Stemmler, P., and Legrand, F. (1995). Measurement of the x-ray spectrometric properties of cesium hydrophthalate (csap) crystal with the synchrotron radiation. *Review of scientific instruments*, 66(2):1601–1603.

Belonoshko, A. B., Skorodumova, N., Rosengren, A., Ahuja, R., Johansson, B., Burakovsky, L., and Preston, D. (2005). High-pressure melting of mgsio 3. *Physical review letters*, 94(19):195701.

Benmore, C., Soignard, E., Guthrie, M., Amin, S., Weber, J., McKiernan, K., Wilding, M., and Yarger, J. (2011). High pressure x-ray diffraction measurements on mg 2 sio 4 glass. *Journal of Non-Crystalline Solids*, 357(14):2632–2636.

Benuzzi-Mounaix, A., Dorchies, F., Recoules, V., Festa, F., Peyrusse, O., Levy, A., Ravasio, A., Hall, T., Koenig, M., Amadou, N., et al. (2011). Electronic structure investigation of highly compressed aluminum with k edge absorption spectroscopy. *Physical review letters*, 107(16):165006.

Benuzzi-Mounaix, A., Koenig, M., Huser, G., Faral, B., Batani, D., Henry, E., Tomasini, M., Marchet, B., Hall, T., Boustie, M., et al. (2002). Absolute equation of state measurements of iron using laser driven shocks. *Physics of plasmas*, 9(6):2466–2469.

Blaj, G., Caragiulo, P., Carini, G., Carron, S., Dragone, A., Freytag, D., Haller, G., Hart, P., Herbst, R., Herrmann, S., et al. (2014). Detector development for the linac coherent light source. *Synchrotron Radiation News*, 27(4):14–19.

Boates, B. and Bonev, S. A. (2013). Demixing instability in dense molten mgsio 3 and the phase diagram of mgo. *Physical review letters*, 110(13):135504.

Boehly, T., Hicks, D., Celliers, P., Collins, T., Earley, R., Eggert, J., Jacobs-Perkins, D., Moon, S., Vianello, E., Meyerhofer, D., et al. (2004). Properties of fluid deuterium under double-shock compression to several mbar. *Physics of plasmas*, 11(9):L49–L52.

Bolis, R., Morard, G., Vinci, T., Ravasio, A., Bambrink, E., Guarguaglini, M., Koenig, M., Musella, R., Remus, F., Bouchet, J., et al. (2016). Decaying shock studies of phase transitions in mgo-sio2 systems: Implications for the super-earths' interiors. *Geophysical Research Letters*, 43(18):9475–9483.

Brown, J. M. and McQueen, R. G. (1986). Phase transitions, grüneisen parameter, and elasticity for shocked iron between 77 gpa and 400 gpa. *Journal of Geophysical Research: Solid Earth*, 91(B7):7485–7494.

Brygoo, S. (2006). *Chocs laser sur le diamant, l hélium et l hydrogène: une etude experimentale de la"Warm Dense Matter.* PhD thesis, Ecole Polytechnique X.

Cauble, R., Phillion, D., Hoover, T., Holmes, N., Kilkenny, J., and Lee, R. (1993). Demonstration of 0.75 gbar planar shocks in x-ray driven colliding foils. *Physical review letters*, 70(14):2102.

Cebulla, D. and Redmer, R. (2014). Ab initio simulations of mgo under extreme conditions. *Physical Review B*, 89(13):134107.

Celliers, P., Bradley, D., Collins, G., Hicks, D., Boehly, T., and Armstrong, W. (2004a). Line-imaging velocimeter for shock diagnostics at the omega laser facility. *Review of scientific instruments*, 75(11):4916–4929.

Celliers, P., Collins, G., Hicks, D., Koenig, M., Henry, E., Benuzzi-Mounaix, A., Batani, D., Bradley, D., Da Silva, L., Wallace, R., et al. (2004b). Electronic conduction in shock-compressed water. *Physics of Plasmas*, 11(8):L41–L44.

Collins, G., Celliers, P., Da Silva, L., Cauble, R., Gold, D., Foord, M., Budil, K., Stewart, R., Holmes, N., Ross, M., et al. (1998a). Equation of state measurements of hydrogen isotopes on nova. *Physics of Plasmas*, 5(5):1864–1869.

Collins, G., Da Silva, L., Celliers, P., Gold, D., Foord, M., Wallace, R., Ng, A., Weber, S., Budil, K., and Cauble, R. (1998b). Measurements of the equation of state of deuterium at the fluid insulator-metal transition. *Science*, 281(5380):1178–1181.

Coppari, F., Smith, R., Eggert, J., Wang, J., Rygg, J., Lazicki, A., Hawreliak, J., Collins, G., and Duffy, T. (2013). Experimental evidence for a phase transition in magnesium oxide at exoplanet pressures. *Nature Geoscience*, 6(11):926–929.

Da Silva, L., Celliers, P., Collins, G., Budil, K., Holmes, N., Barbee Jr, T., Hammel, B., Kilkenny, J., Wallace, R., Ross, M., et al. (1997). Absolute equation of state measurements on shocked liquid deuterium up to 200 gpa (2 mbar). *Physical review letters*, 78(3):483.

De Koker, N. and Stixrude, L. (2009). Self-consistent thermodynamic description of silicate liquids, with application to shock melting of mgo periclase and mgsio3 perovskite. *Geophysical Journal International*, 178(1):162–179.

de Koker, N. P., Stixrude, L., and Karki, B. B. (2008a). Thermodynamics, structure, dynamics, and freezing of mg 2 sio 4 liquid at high pressure. *Geochimica et Cosmochimica Acta*, 72(5):1427–1441.

de Koker, N. P., Stixrude, L., and Karki, B. B. (2008b). Thermodynamics, structure, dynamics, and freezing of mg 2 sio 4 liquid at high pressure. *Geochimica et Cosmochimica Acta*, 72(5):1427–1441.

Denoeud, A. (2014). *Etude de la matière dense et tiède à l'aide de diagnostics X-Applications aux intérieurs planétaires*. PhD thesis, Ecole Polytechnique.

Denoeud, A., Benuzzi-Mounaix, A., Ravasio, A., Dorchies, F., Leguay, P., Gaudin, J., Guyot, F., Brambrink, E., Koenig, M., Le Pape, S., et al. (2014). Metallization of warm dense sio 2 studied by xanes spectroscopy. *Physical review letters*, 113(11):116404.

Denoeud, A., Mazevet, S., Guyot, F., Dorchies, F., Gaudin, J., Ravasio, A., Brambrink, E., and Benuzzi-Mounaix, A. (2016a). High-pressure structural changes in liquid silica. *Physical Review E*, 94(3):031201.

Denoeud, A., Ozaki, N., Benuzzi-Mounaix, A., Uranishi, H., Kondo, Y., Kodama, R., Brambrink, E., Ravasio, A., Bocoum, M., Boudenne, J.-M., et al. (2016b). Dynamic x-ray diffraction observation of shocked solid iron up to 170 gpa. *Proceedings of the National Academy of Sciences*, 113(28):7745–7749.

Dorchies, F., Festa, F., Recoules, V., Peyrusse, O., Benuzzi-Mounaix, A., Brambrink, E., Levy, A., Ravasio, A., Koenig, M., Hall, T., et al. (2015). X-ray absorption k edge as a diagnostic of the electronic temperature in warm dense aluminum. *Physical Review B*, 92(8):085117.

Du, Z. and Lee, K. K. (2014). High-pressure melting of mgo from (mg, fe) o solid solutions. *Geophysical Research Letters*, 41(22):8061–8066.

Dubrovinskaia, N., Dubrovinsky, L., Solopova, N. A., Abakumov, A., Turner, S., Hanfland, M., Bykova, E., Bykov, M., Prescher, C., Prakapenka, V. B., et al. (2016). Terapascal static pressure generation with ultrahigh yield strength nanodiamond. *Science advances*, 2(7):e1600341.

Duffy, T., Madhusudhan, N., and Lee, K. (2015). 2.07 mineralogy of super-earth planets.

Durben, D. J., McMillan, P. F., and Wolf, G. H. (1993). Raman study of the high-pressure behavior of forsterite (mg˜ 2sio˜ 4) crystal and glass. *American Mineralogist*, 78(11):1143–1148.

Eggert, J., Hicks, D., Celliers, P., Bradley, D., McWilliams, R., Jeanloz, R., Miller, J., Boehly, T., and Collins, G. (2010). Melting temperature of diamond at ultrahigh pressure. *Nature Physics*, 6(1):40–43.

Festa, F. (2013). *Etude expérimentale et théorique de la structure électronique de l'aluminium en conditions extrêmes par spectroscopie d'absorption X*. PhD thesis, Ecole Polytechnique X.

Fiquet, G., Guyot, F., and Badro, J. (2008). The earth9s lower mantle and core. *Elements*, 4(3):177–182.

Gaidos, E., Conrad, C. P., Manga, M., and Hernlund, J. (2010). Thermodynamic limits on magnetodynamos in rocky exoplanets. *The Astrophysical Journal*, 718(2):596.

Garban-Labaune, C., Fabre, E., Max, C., Fabbro, R., Amiranoff, F., Virmont, J., Weinfeld, M., and Michard, A. (1982). Effect of laser wavelength and pulse duration on laser-light absorption and back reflection. *Physical Review Letters*, 48(15):1018.

Ghosh, D. B., Karki, B. B., and Stixrude, L. (2014). First-principles molecular dynamics simulations of mgsio3 glass: Structure, density, and elasticity at high pressure.

Gillon, M., Triaud, A. H. M. J., Demory, B.-O., Jehin, E., Agol, E., Deck, K. M., Lederer, S. M., de Wit, J., Burdanov, A., Ingalls, J. G., Bolmont, E., Leconte,

J., Raymond, S. N., Selsis, F., Turbet, M., Barkaoui, K., Burgasser, A., Burleigh, M. R., Carey, S. J., Chaushev, A., Copperwheat, C. M., Delrez, L., Fernandes, C. S., Holdsworth, D. L., Kotze, E. J., Van Grootel, V., Almleaky, Y., Benkhaldoun, Z., Magain, P., and Queloz, D. (2017). Seven temperate terrestrial planets around the nearby ultracool dwarf star trappist-1. *Nature*, 542(7642):456–460.

Gleason, A., Bolme, C., Galtier, E., Lee, H., Granados, E., Dolan, D., Seagle, C., Ao, T., Ali, S., Lazicki, A., et al. (2017). Compression freezing kinetics of water to ice vii. *Physical Review Letters*.

Gleason, A., Bolme, C., Lee, H., Nagler, B., Galtier, E., Milathianaki, D., Hawreliak, J., Kraus, R., Eggert, J., Fratanduono, D., et al. (2015). Ultrafast visualization of crystallization and grain growth in shock-compressed sio2. *Nature communications*, 6.

Goettel, K. A., Eggert, J. H., Silvera, I. F., and Moss, W. C. (1989). Optical evidence for the metallization of xenon at 132 (5) gpa. *Physical review letters*, 62(6):665.

Gonze, X., Amadon, B., Anglade, P.-M., Beuken, J.-M., Bottin, F., Boulanger, P., Bruneval, F., Caliste, D., Caracas, R., Côté, M., et al. (2009). Abinit: First-principles approach to material and nanosystem properties. *Computer Physics Communications*, 180(12):2582–2615.

Gray, D. and Kilkenny, J. (1980). The measurement of ion acoustic turbulence and reduced thermal conductivity caused by a large temperature gradient in a laser heated plasma. *Plasma Physics*, 22(2):81.

Gray, D., Kilkenny, J., White, M., Blyth, P., and Hull, D. (1977). Observation of severe heat-flux limitation and ion-acoustic turbulence in a laser-heated plasma. *Physical Review Letters*, 39(20):1270.

Guillot, T. (2005). The interiors of giant planets: Models and outstanding questions. *Annu. Rev. Earth Planet. Sci.*, 33:493–530.

Hanada, T., Soga, N., and Tachibana, T. (1988). Coordination state of magnesium ions in rf-sputtered amorphous films in the system mgo? sio2. *Journal of non-crystalline solids*, 105(1-2):39–44.

Harmand, M. (2009). *Spectroscopie d'absorption X résolue en temps pour l'étude de la matière dense et tiède*. PhD thesis, Université Sciences et Technologies-Bordeaux I.

Harmand, M., Ravasio, A., Mazevet, S., Bouchet, J., Denoeud, A., Dorchies, F., Feng, Y., Fourment, C., Galtier, E., Gaudin, J., et al. (2015). X-ray absorption spectroscopy of iron at multimegabar pressures in laser shock experiments. *Physical Review B*, 92(2):024108.

Hicks, D., Boehly, T., Eggert, J., Miller, J., Celliers, P., and Collins, G. (2006). Dissociation of liquid silica at high pressures and temperatures. *Physical Review Letters*, 97(2):025502.

Holme, R. and Olson, P. (2007). Large-scale flow in the core. *Treatise on geophysics*, 8:107–130.

Huser, G., Recoules, V., Ozaki, N., Sano, T., Sakawa, Y., Salin, G., Albertazzi, B., Miyanishi, K., and Kodama, R. (2015). Experimental and ab initio investigations of microscopic properties of laser-shocked ge-doped ablator. *Physical Review E*, 92(6):063108.

Jackson, I. and Ahrens, T. J. (1979). Shock wave compression of single-crystal forsterite. *Journal of Geophysical Research: Solid Earth*, 84(B6):3039–3048.

Jackson, J. D. (2007). *Classical electrodynamics*. John Wiley & Sons.

Jaret, S. J., Woerner, W. R., Phillips, B. L., Ehm, L., Nekvasil, H., Wright, S. P., and Glotch, T. D. (2015). Maskelynite formation via solid-state transformation: Evidence of infrared and x-ray anisotropy. *Journal of Geophysical Research: Planets*, 120(3):570–587.

Karato, S.-i. (2011). Rheological structure of the mantle of a super-earth: Some insights from mineral physics. *Icarus*, 212(1):14–23.

Katayama, Y., Mizutani, T., Utsumi, W., Shimomura, O., Yamakata, M., and Funakoshi, K.-i. (2000). A first-order liquid–liquid phase transition in phosphorus. *Nature*, 403(6766):170–173.

Katsura, T., Yamada, H., Nishikawa, O., Song, M., Kubo, A., Shinmei, T., Yokoshi, S., Aizawa, Y., Yoshino, T., Walter, M. J., et al. (2004). Olivine-wadsleyite transition in the system (mg, fe) 2sio4. *Journal of Geophysical Research: Solid Earth*, 109(B2).

Kittel, C. (2005). *Introduction to solid state physics*. Wiley.

Knittle, E. and Jeanloz, R. (1987). Synthesis and equation of state of (mg, fe) sio3 perovskite to over 100 gigapascals. *Science*, 235:668–671.

Knudson, M., Hanson, D., Bailey, J., Hall, C., and Asay, J. (2003). Use of a wave reverberation technique to infer the density compression of shocked liquid deuterium to 75 gpa. *Physical review letters*, 90(3):035505.

Koenig, M., Faral, B., Boudenne, J., Batani, D., Benuzzi, A., Bossi, S., Remond, C., Perrine, J., Temporal, M., and Atzeni, S. (1995). Relative consistency of equations of state by laser driven shock waves. *Physical Review Letters*, 74(12):2260.

Koenig, M., Faral, B., Boudenne, J. M., Batani, D., Benuzzi, A., and Bossi, S. (1994). Optical smoothing techniques for shock wave generation in laser-produced plasmas. *Physical Review E*, 50(5):R3314.

Koenig, M., Henry, E., Huser, G., Benuzzi-Mounaix, A., Faral, B., Martinolli, E., Lepape, S., Vinci, T., Batani, D., Tomasini, M., et al. (2004). High pressures generated by laser driven shocks: applications to planetary physics. *Nuclear fusion*, 44(12):S208.

Kohara, S., Akola, J., Morita, H., Suzuya, K., Weber, J., Wilding, M., and Benmore, C. (2011). Relationship between topological order and glass forming ability in densely packed enstatite and forsterite composition glasses. *Proceedings of the National Academy of Sciences*, 108(36):14780–14785.

Kohara, S., Suzuya, K., Takeuchi, K., Loong, C.-K., Grimsditch, M., Weber, J., Tangeman, J., and Key, T. (2004). Glass formation at the limit of insufficient network formers. *Science*, 303(5664):1649–1652.

Kubicki, J., Hemley, R., and Hofmeister, A. (1992). Raman and infrared study of pressure-induced structural changes in mgsio3, camgsi2o6, and casio3 glasses. *The American mineralogist*, 77(3-4):258–269.

Lévy, A., Dorchies, F., Benuzzi-Mounaix, A., Ravasio, A., Festa, F., Recoules, V., Peyrusse, O., Amadou, N., Brambrink, E., Hall, T., et al. (2012). X-ray diagnosis of the pressure induced mott nonmetal-metal transition. *Physical review letters*, 108(5):055002.

Levy, A., Dorchies, F., Fourment, C., Harmand, M., Hulin, S., Santos, J., Descamps, D., Petit, S., and Bouillaud, R. (2010). Double conical crystal x-ray spectrometer for high resolution ultrafast x-ray absorption near-edge spectroscopy of al k edge. *Review of Scientific Instruments*, 81(6):063107.

Löwer, T., Sigel, R., Eidmann, K., Földes, I., Hüller, S., Massen, J., Tsakiris, G., Witkowski, S., Preuss, W., Nishimura, H., et al. (1994). Uniform multimegabar

shock waves in solids driven by laser-generated thermal radiation. *Physical review letters*, 72(20):3186.

Luciani, J., Mora, P., and Virmont, J. (1983). Nonlocal heat transport due to steep temperature gradients. *Physical review letters*, 51(18):1664.

Luo, S.-N. and Ahrens, T. J. (2003). Superheating systematics of crystalline solids. *Applied physics letters*, 82(12):1836–1838.

Luo, S.-N. and Ahrens, T. J. (2004). Shock-induced superheating and melting curves of geophysically important minerals. *Physics of the Earth and Planetary Interiors*, 143:369–386.

Luo, S.-N., Ahrens, T. J., Çağın, T., Strachan, A., Goddard III, W. A., and Swift, D. C. (2003). Maximum superheating and undercooling: Systematics, molecular dynamics simulations, and dynamic experiments. *Physical Review B*, 68(13):134206.

Luo, S.-N., Akins, J. A., Ahrens, T. J., and Asimow, P. D. (2004). Shock-compressed mgsio3 glass, enstatite, olivine, and quartz: Optical emission, temperatures, and melting. *Journal of Geophysical Research: Solid Earth*, 109(B5).

Lyzenga, G. A. and Ahrens, T. J. (1980). Shock temperature measurements in mg2sio4 and sio2 at high pressures. *Geophysical Research Letters*, 7(2):141–144.

Lyzenga, G. A., Ahrens, T. J., and Mitchell, A. C. (1983). Shock temperatures of sio2 and their geophysical implications. *Journal of Geophysical Research: Solid Earth*, 88(B3):2431–2444.

Marsh, S. (1980). Shock hugoniot data. *Univ. of California at Los Angeles Press, Los Angeles*.

Mazevet, S., Tsuchiya, T., Taniuchi, T., Benuzzi-Mounaix, A., and Guyot, F. (2015). Melting and metallization of silica in the cores of gas giants, ice giants, and super earths. *Physical Review B*, 92(1):014105.

McQueen, R., Marsh, S., Taylor, J., Fritz, J., and Carter, W. (1970). The equation of state of solids from shock wave studies. *High velocity impact phenomena*, 293:294–417.

McQueen, R. and Simmons, G. (1968). Shock-wave data and equations of state. In *Seismic Coupling, Advanced Research Project Agency Meeting*, pages 53–106.

McWilliams, R. S., Spaulding, D. K., Eggert, J. H., Celliers, P. M., Hicks, D. G., Smith, R. F., Collins, G. W., and Jeanloz, R. (2012). Phase transformations and metallization of magnesium oxide at high pressure and temperature. *Science*, 338(6112):1330–1333.

Meade, C., Hemley, R. J., and Mao, H. (1992). High-pressure x-ray diffraction of sio 2 glass. *Physical Review Letters*, 69(9):1387.

Militzer, B. (2013). Ab initio investigation of a possible liquid–liquid phase transition in mgsio 3 at megabar pressures. *High Energy Density Physics*, 9(1):152–157.

Miller, J., Boehly, T., Melchior, A., Meyerhofer, D., Celliers, P., Eggert, J., Hicks, D., Sorce, C., Oertel, J., and Emmel, P. (2007). Streaked optical pyrometer system for laser-driven shock-wave experiments on omega. *Review of Scientific Instruments*, 78(3):034903.

Millot, M. (2016). Identifying and discriminating phase transitions along decaying shocks with line imaging doppler interferometric velocimetry and streaked optical pyrometry. *Physics of Plasmas*, 23(1):014503.

Millot, M., Dubrovinskaia, N. a., Černok, A., Blaha, S., Dubrovinsky, L., Braun, D., Celliers, P., Collins, G., Eggert, J., and Jeanloz, R. (2015). Shock compression of stishovite and melting of silica at planetary interior conditions. *Science*, 347(6220):418–420.

Milne, C., Penfold, T., and Chergui, M. (2014). Recent experimental and theoretical developments in time-resolved x-ray spectroscopies. *Coordination Chemistry Reviews*, 277:44–68.

Minitti, M. P., Robinson, J. S., Coffee, R. N., Edstrom, S., Gilevich, S., Glownia, J. M., Granados, E., Hering, P., Hoffmann, M. C., Miahnahri, A., et al. (2015). Optical laser systems at the linac coherent light source. *Journal of synchrotron radiation*, 22(3):526–531.

Misawa, M., Ryuo, E., Yoshida, K., Kalia, R. K., Nakano, A., Nishiyama, N., Shimojo, F., Vashishta, P., and Wakai, F. (2017). Picosecond amorphization of sio 2 stishovite under tension. *Science Advances*, 3(5):e1602339.

Mitchell, T. E. (2008). Dislocations in ceramics. *Ceramics Science and Technology. Volume 2: Materials and Properties*, pages 379–436.

Miyanishi, K., Tange, Y., Ozaki, N., Kimura, T., Sano, T., Sakawa, Y., Tsuchiya, T., and Kodama, R. (2015). Laser-shock compression of magnesium oxide in the warm-dense-matter regime. *Physical Review E*, 92(2):023103.

Mochizuki, T., Yabe, T., Okada, K., Hamada, M., Ikeda, N., Kiyokawa, S., and Yamanaka, C. (1986). Atomic-number dependence of soft-x-ray emission from various targets irradiated by a 0.53-μm-wavelength laser. *Physical Review A*, 33(1):525.

Mora, P. (1982). Theoretical model of absorption of laser light by a plasma. *The Physics of Fluids*, 25(6):1051–1056.

More, R., Warren, K., Young, D., and Zimmerman, G. (1988). A new quotidian equation of state (qeos) for hot dense matter. *The Physics of fluids*, 31(10):3059–3078.

Morin, F., Oliver, J., and Housley, R. (1977). Electrical properties of forsterite, mg 2 si o 4. *Physical Review B*, 16(10):4434.

Mosenfelder, J. L., Asimow, P. D., and Ahrens, T. J. (2007). Thermodynamic properties of mg2sio4 liquid at ultra-high pressures from shock measurements to 200 gpa on forsterite and wadsleyite. *Journal of Geophysical Research: Solid Earth*, 112(B6).

Mosenfelder, J. L., Asimow, P. D., Frost, D. J., Rubie, D. C., and Ahrens, T. J. (2009). The mgsio3 system at high pressure: Thermodynamic properties of perovskite, postperovskite, and melt from global inversion of shock and static compression data. *Journal of Geophysical Research: Solid Earth*, 114(B1).

Murakami, M. and Bass, J. D. (2010). Spectroscopic evidence for ultrahigh-pressure polymorphism in sio 2 glass. *Physical review letters*, 104(2):025504.

Murakami, M., Hirose, K., Kawamura, K., Sata, N., and Ohishi, Y. (2004). Post-perovskite phase transition in mgsio3. *Science*, 304(5672):855–858.

Musella, R. (2016). *Ab initio simulations of MgO and MgSiO3 for planetary modelling*. PhD thesis, Sorbonne Paris Cité.

Nemausat, R., Cabaret, D., Gervais, C., Brouder, C., Trcera, N., Bordage, A., Errea, I., and Mauri, F. (2015). Phonon effects on x-ray absorption and nuclear magnetic resonance spectroscopies. *Physical Review B*, 92(14):144310.

Nesterchuk, N. and Makarova, T. (1970). The formation of aqueous magnesium silicate in the interaction of solutions of magnesium chloride and sodium metasilicate. *Russian Chemical Bulletin*, 19(10):2053–2055.

Nguyen, J. H. and Holmes, N. C. (2004). Melting of iron at the physical conditions of the earth's core. *Nature*, 427(6972):339–342.

Oganov, A. R., Gillan, M. J., and Price, G. D. (2003). Ab initio lattice dynamics and structural stability of mgo. *The Journal of chemical physics*, 118(22):10174–10182.

Panero, W. R., Benedetti, L. R., and Jeanloz, R. (2003). Equation of state of stishovite and interpretation of sio2 shock-compression data. *Journal of Geophysical Research: Solid Earth*, 108(B1).

Pecharsky, V. K. and Zavalij, P. Y. (2009). *Fundamentals of powder diffraction and structural characterization of materials*, volume 69. Springer.

Philipp, H. T., Hromalik, M., Tate, M., Koerner, L., and Gruner, S. M. (2011). Pixel array detector for x-ray free electron laser experiments. *Nuclear Instruments and Methods in Physics Research Section A: Accelerators, Spectrometers, Detectors and Associated Equipment*, 649(1):67–69.

Ping, Y. and Coppari, F. (2016). Laser shock xafs studies at omega facility. *High Pressure Research*, 36(3):303–314.

Ping, Y., Coppari, F., Hicks, D., Yaakobi, B., Fratanduono, D., Hamel, S., Eggert, J., Rygg, J., Smith, R., Swift, D., et al. (2013a). Solid iron compressed up to 560 gpa. *Physical review letters*, 111(6):065501.

Ping, Y., Coppari, F., Hicks, D. G., Yaakobi, B., Fratanduono, D. E., Hamel, S., Eggert, J. H., Rygg, J. R., Smith, R. F., Swift, D. C., Braun, D. G., Boehly, T. R., and Collins, G. W. (2013b). Solid iron compressed up to 560 gpa. *Phys. Rev. Lett.*, 111:065501.

Pozzo, M., Davies, C., Gubbins, D., and Alfe, D. (2012). Thermal and electrical conductivity of iron at earth/'s core conditions. *Nature*, 485(7398):355–358.

Prescher, C. and Prakapenka, V. B. (2015). Dioptas: a program for reduction of two-dimensional x-ray diffraction data and data exploration. *High Pressure Research*, 35(3):223–230.

Qi, T., Millot, M., Kraus, R. G., Root, S., and Hamel, S. (2015). Optical and transport properties of dense liquid silica. *Physics of Plasmas*, 22(6):062706.

Ramis, R., Schmalz, R., and Meyer-ter Vehn, J. (1988). Multi?a computer code for one-dimensional multigroup radiation hydrodynamics. *Computer Physics Communications*, 49(3):475–505.

Recoules, V. and Mazevet, S. (2009). Temperature and density dependence of xanes spectra in warm dense aluminum plasmas. *Physical Review B*, 80(6):064110.

Remus, F., Mathis, S., Zahn, J.-P., and Lainey, V. (2012). Anelastic tidal dissipation in multi-layer planets. *Astronomy & Astrophysics*, 541:A165.

Root, S., Shulenburger, L., Lemke, R. W., Dolan, D. H., Mattsson, T. R., and Desjarlais, M. P. (2015). Shock response and phase transitions of mgo at planetary impact conditions. *Physical review letters*, 115(19):198501.

Root, S., Townsend, J., Shulenburger, L., Davies, E., Kraus, R., Spaulding, D., Stewart, S., Jacobsen, S., and Mattsson, T. (2016). Shock and release data on forsterite (mg2sio4) single crystals. In *AGU Fall Meeting Abstracts*.

Ruprechter, J. (2000). *Entwicklung und Kalibration eines Submikrosekunden-Pyrometers*. na.

Rygg, J. R., Eggert, J., Lazicki, A., Coppari, F., Hawreliak, J., Hicks, D., Smith, R., Sorce, C., Uphaus, T., Yaakobi, B., et al. (2012). Powder diffraction from solids in the terapascal regime. *Review of Scientific Instruments*, 83(11):113904.

Sato, T. and Funamori, N. (2008). Sixfold-coordinated amorphous polymorph of sio 2 under high pressure. *Physical review letters*, 101(25):255502.

Sekine, T., Ozaki, N., Miyanishi, K., Asaumi, Y., Kimura, T., Albertazzi, B., Sato, Y., Sakawa, Y., Sano, T., Sugita, S., et al. (2016). Shock compression response of forsterite above 250 gpa. *Science advances*, 2(8):e1600157.

Shankland, T. (1968). Band gap of forsterite. *Science*, 161(3836):51–53.

Sharma, V., Ram, R., and Sachdev, P. (1987). Uniformly valid analytical solution to the problem of a decaying shock wave. *Journal of Fluid Mechanics*, 185:153–170.

Shen, G. and Lazor, P. (1995). Measurement of melting temperatures of some minerals under lower mantle pressures. *Journal of Geophysical Research: Solid Earth*, 100(B9):17699–17713.

Shim, S.-H. and Catalli, K. (2009). Compositional dependence of structural transition pressures in amorphous phases with mantle-related compositions. *Earth and Planetary Science Letters*, 283(1):174–180.

Smith, R., Eggert, J., Jeanloz, R., Duffy, T., Braun, D., Patterson, J., Rudd, R., Biener, J., Lazicki, A., Hamza, A., et al. (2014). Ramp compression of diamond to five terapascals. *Nature*, 511(7509):330.

Solomatov, V. (2000). Fluid dynamics of a terrestrial magma ocean. *Origin of the Earth and Moon*, pages 323–338.

Spaulding, D., McWilliams, R., Jeanloz, R., Eggert, J., Celliers, P., Hicks, D., Collins, G., and Smith, R. (2012). Evidence for a phase transition in silicate melt at extreme pressure and temperature conditions. *Physical Review Letters*, 108(6):065701.

Spaulding, D. K. (2010). *Laser-driven shock compression studies of planetary compositions*. PhD thesis.

Spitzer, L. and Härm, R. (1953). Transport phenomena in a completely ionized gas. *Phys. Rev.*, 89:977–981.

Stephens, R. E. and Malitson, I. H. (1952). Index of refraction of magnesium oxide. *Journal of Research of the National Bureau of Standards*, 49(4):249–252.

Stevenson, D. J. (2003). Planetary magnetic fields. *Earth and planetary science letters*, 208(1):1–11.

Stixrude, L. (2014). Melting in super-earths. *Philosophical Transactions of the Royal Society of London A: Mathematical, Physical and Engineering Sciences*, 372(2014):20130076.

Stixrude, L. and Karki, B. (2005). Structure and freezing of mgsio3 liquid in earth's lower mantle. *Science*, 310(5746):297–299.

Svendsen, B. and Ahrens, T. J. (1987). Shock-induced temperatures of mgo. *Geophysical journal international*, 91(3):667–691.

Syono, Y., Goto, T., Sato, J.-i., and Takei, H. (1981a). Shock compression measurements of single-crystal forsterite in the pressure range 15–93 gpa. *Journal of Geophysical Research: Solid Earth*, 86(B7):6181–6186.

Syono, Y., Goto, T., Takei, H., Tokonami, M., and Nobugai, K. (1981b). Association reaction in forsterite under shock compression. *Science*, 214(4517):177–179.

Tackley, P. J., Ammann, M., Brodholt, J. P., Dobson, D. P., and Valencia, D. (2013). Mantle dynamics in super-earths: Post-perovskite rheology and self-regulation of viscosity. *Icarus*, 225(1):50–61.

Theobald, W., Miller, J., Boehly, T., Vianello, E., Meyerhofer, D., Sangster, T., Eggert, J., and Celliers, P. (2006). X-ray preheating of window materials in direct-drive shock-wave timing experiments. *Physics of plasmas*, 13(12):122702.

Thomas, C. W. and Asimow, P. D. (2013). Direct shock compression experiments on premolten forsterite and progress toward a consistent high-pressure equation of state for cao-mgo-al2o3-sio2-feo liquids. *Journal of Geophysical Research: Solid Earth*, 118(11):5738–5752.

Torchio, R., Occelli, F., Mathon, O., Sollier, A., Lescoute, E., Videau, L., Vinci, T., Benuzzi-Mounaix, A., Headspith, J., Helsby, W., et al. (2016). Probing local and electronic structure in warm dense matter: single pulse synchrotron x-ray absorption spectroscopy on shocked fe. *Scientific reports*, 6:srep26402.

Townsend, J. (2017). Shock and release of mg_2sio_4 to 1 tpa. In *WDM2017*.

Trainor, R., Shaner, J., Auerbach, J., and Holmes, N. (1979). Ultrahigh-pressure laser-driven shock-wave experiments in aluminum. *Physical Review Letters*, 42(17):1154.

Tsuchiya, T., Tsuchiya, J., Umemoto, K., and Wentzcovitch, R. M. (2004). Phase transition in mgsio 3 perovskite in the earth's lower mantle. *Earth and Planetary Science Letters*, 224(3):241–248.

Umemoto, K., Wentzcovitch, R. M., and Allen, P. B. (2006). Dissociation of mgsio3 in the cores of gas giants and terrestrial exoplanets. *Science*, 311(5763):983–986.

Valencia, D., O'Connell, R. J., and Sasselov, D. (2006). Internal structure of massive terrestrial planets. *Icarus*, 181(2):545–554.

Van den Berg, A., Yuen, D., Beebe, G., and Christiansen, M. (2010). The dynamical impact of electronic thermal conductivity on deep mantle convection of exosolar planets. *Physics of the Earth and Planetary Interiors*, 178(3):136–154.

Wett, J. P. and Ahrens, T. J. (1983). Shock compression of single-crystal forsterite. *Journal of Geophysical Research: Solid Earth*, 88(B11):9500–9512.

Wilding, M., Guthrie, M., Kohara, S., Bull, C. L., Akola, J., and Tucker, M. G. (2012). The structure of mgo–sio2 glasses at elevated pressure. *Journal of Physics: Condensed Matter*, 24(22):225403.

Wilding, M. C., Benmore, C., Tangeman, J., and Sampath, S. (2004a). Coordination changes in magnesium silicate glasses. *EPL (Europhysics Letters)*, 67(2):212.

Wilding, M. C., Benmore, C. J., Tangeman, J. A., and Sampath, S. (2004b). Evidence of different structures in magnesium silicate liquids: coordination changes in forsterite-to enstatite-composition glasses. *Chemical Geology*, 213(1):281–291.

Wilks, S. C. and Kruer, W. L. (1997). Absorption of ultrashort, ultra-intense laser light by solids and overdense plasmas. *IEEE Journal of Quantum Electronics*, 33(11):1954–1968.

Williams, Q. and Jeanloz, R. (1988). Spectroscopic evidence for pressure-induced coordination changes in silicate glasses and melts. *Science*, 239(4842):902–906.

Wu, Z., Wentzcovitch, R. M., Umemoto, K., Li, B., Hirose, K., and Zheng, J.-C. (2008). Pressure-volume-temperature relations in mgo: An ultrahigh pressure-temperature scale for planetary sciences applications. *Journal of Geophysical Research: Solid Earth*, 113(B6).

Yakobi, B., Boehly, T., Meyerhofer, D., Collins, T., Remington, B., Allen, P., Pollaine, S., Lorenzana, H., and Eggert, J. (2005). Exafs measurement of iron bcc-to-hcp phase transformation in nanosecond-laser shocks. *Physical review letters*, 95(7):075501.

Yakobi, B., Boehly, T., Sangster, T., Meyerhofer, D., Remington, B., Allen, P., Pollaine, S., Lorenzana, H., Lorenz, K., and Hawreliak, J. (2008). Extended x-ray absorption fine structure measurements of quasi-isentropically compressed vanadium targets on the omega laser. *Physics of Plasmas*, 15(6):062703.

Yoshimura, T., Tamenori, Y., Iwasaki, N., Hasegawa, H., Suzuki, A., and Kawahata, H. (2013). Magnesium k-edge xanes spectroscopy of geological standards. *Journal of synchrotron radiation*, 20(5):734–740.

Zeldovich, Y. B. and Raizer, Y. P. (1965). Physics of shock waves and high-temperature hydrodynamic phenomena. Technical report, FOREIGN TECHNOLOGY DIV WRIGHT-PATTERSON AFB OH.

Zerr, A., Diegeler, A., and Boehler, R. (1998). Solidus of earth's deep mantle. *Science*, 281(5374):243–246.

Zhao, S., Kad, B., Remington, B. A., LaSalvia, J. C., Wehrenberg, C. E., Behler, K. D., and Meyers, M. A. (2016). Directional amorphization of boron carbide subjected to laser shock compression. *Proceedings of the National Academy of Sciences*, 113(43):12088–12093.

Ziegler, L. and Stegman, D. (2013). Implications of a long-lived basal magma ocean in generating earth's ancient magnetic field. *Geochemistry, Geophysics, Geosystems*, 14(11):4735–4742.

Résumé en langue française

La découverte récente d'un grand nombre d'exoplanètes et en particulier des planètes potentiellement habitables suscite une grande fascination. Pour modéliser les intérieurs de ces planètes, il est crucial de connaître avec précision les diagrammes de phases, les propriétés physiques et chimiques et les équations d'état des matériaux constituant les intérieurs planétaires: l'existence d'un champ magnétique est liée la conductivité électrique et aux propriétés rhéologiques des composants planétaires; les transitions de phase ont des répercussions considérables sur la structure interne et peuvent être l'origine de discontinuités sismiques.
Dans les intérieurs planétaires, la matière est soumise des conditions de pression et de température extrêmes ce qui rend difficile sa description théorique. Dans ce régime thermodynamique de la Matière Dense et Tiède (WDM, Warm Dense Matter), les approximations usuelles utilisées en physique des solides et en physique des plasmas ne sont plus valides.
Numériquement, les propriétés physiques de la WDM peuvent être obtenues par des simulations atomistiques (dynamiques moléculaires couplées des calculs de structures électroniques basés sur la théorie de la fonctionnelle de la densité, DFT-MD). Cependant, des mesures expérimentales sont nécessaires pour valider les résultats de ces simulations.
Ce projet de thèse s'inscrit dans ce contexte. En particulier, il a été conçu pour étudier expérimentalement les propriétés physiques et les diagrammes de phases de MgO, $MgSiO_3$ et Mg_2SiO_4 des conditions des pressions et températures représentatives des intérieurs planétaires. Ces trois matériaux ont un intérêt géophysique majeur: ce sont les pôles purs magnésiens du (Fe, Mg)SiO_3 et (Fe, Mg)$_2SiO_4$ qui sont parmi les composantes plus abondantes du manteau terrestre et très probablement des manteaux des Super-Terres et des noyaux des planètes géantes.
Pour atteindre ces conditions thermodynamiques extrêmes nous avons utilisé des compressions dynamiques par chocs laser lors de campagnes expérimentales menées sur de grandes installations: LULI2000 (Ecole Polytechnique, France), GEKKOXII (Osaka University, Japan), MEC at LCLS (SLAC, USA). Afin d'obtenir une caractérisation la plus riche possible des propriétés physiques de la matière comprimée, nous avons

réalisé trois types d'expériences en utilisant différents diagnostiques expérimentaux. LULI2000 et GEKKOXII,nous avons réalisé une expérience de chocs décroissants couplée avec des diagnostiques optiques (interférométrie Doppler et pyrométrie). Ainsi nous avons pu caractériser les propriétés de MgO, $MgSiO_3$ et Mg_2SiO_4 l'état liquide et contraindre leurs courbes de fusion. Ces mesures ont permis de déterminer le point de fusion de MgO sur l'Hugoniot principal 0.47±0.04 TPa et 9860±810 K et des limites supérieures pour le courbes de fusion du $MgSiO_3$ et Mg_2SiO_4. Nos résultats impliquent une révision des diagrammes de phase de ces trois matériaux, préalablement basés sur un faible nombre de données existantes. Nos mesures mettent en évidence qu'aucune transition de phase a lieu le long de l'Hugoniot de la forstérite (Mg_2SiO_4 cristal) et du verre du $MgSiO_3$ pour des pressions supérieures 200 GPa. Ces résultats ont d'importantes implications géophysiques. Par exemple la détermination des courbes de fusion des composants planétaires est fondamentale pour calculer les profils de températures planétaires. En plus, la stabilité des phases liquides de $MgSiO_3$ et Mg_2SiO_4 dans les conditions explorées ont des implications qui concernent la différentiation géochimique des planètes.
Nous avons étudié les propriétés structurelles et électroniques du MgO par spectroscopie d'absorption X près du flanc (XANES) dans une large gamme de densité et température. Cette expérience a été conduite au LULI2000 o nous avons utilisé un faisceau laser impulsions d'une durée de 300 pico-secondes (ps) pour comprimer et chauffer la matière et un second laser impulsions d'une durée de 3 ps pour générer un faisceau de rayons X. Les mesures, les premières de ce type, ont été interprétées en utilisant des simulations DFT-MD. Cette étude a permis de comprendre le mécanisme de fermeture du gap électronique lors de l'augmentation de température. Elle apporte également une description de la structure locale des ions dans le liquide de MgO et de ses variations en fonction des conditions de pression et de température.
La dernière expérience concerne l'étude par diffraction des rayons X des changements structurels du $MgSiO_3$ et Mg_2SiO_4 sous choc pour des pressions comprises entre 30 GPa et 150 GPa. Elle a été conduite la station Matter at Extreme Conditions (MEC) du Linac Coherent Light Source (LCLS). Un laser de haute puissance, utilisé pour générer le choc, est couplé avec le rayonnement X extrêmement intense de l'X-Fel, particulièrement bien adapté pour la diffraction des rayons X. Cette étude apporte la première preuve que la fostérite se vitrifie sous compression par choc environ 40-50 GPa. Nous caractérisons également des changements structurels du verre de $MgSiO_3$ dans une gamme de pression jamais explorée auparavant en utilisant la diffraction rayons X. Ces résultats ont des répercussions directes sur la connaissance des phénomènes liés aux impacts des météorites. En fait la compréhension des changements structurels des composants planétaires sous compression dynamique est fondamentale pour interpréter l'histoire géologique des cratères qui se sont formés lors d'impacts météoritiques.

L'ensemble de ces travaux constitue une avancée dans la compréhension des diagrammes de phases de MgO, $MgSiO_3$ et Mg_2SiO_4 dans un domaine de pressions ayant un intérêt en planétologie. En particulier les diagrammes de phases de $MgSiO_3$ et Mg_2SiO_4 ont été étudiés dans les phases solide et liquides le long des courbes Hugoniot. Enfin, nous avons obtenu une caractérisation assez riche de MgO en mesurant les propriétés optiques, un point de la courbe de fusion et les propriétés structurelles et électroniques.

Ackowledgements

First of all I acknowledge the supports of the PlanetLab program of the Agence Nationale de la Recherche (ANR) grant ANR-12-BS04-0015-04, of the GDRI N 118 MECMA TPLA and of the COST Action MP1208 "developing the physics and the scientific community for inertial fusion".

Je tiens à remercier chaleureusement A. Benuzzi-Mounaix qui a dirigé ce projet de thèse. Son attention et sa disponibilité ont été essentielles et ont permis de concrétiser ce projet ambitieux. Je la remercie aussi pour ses qualités humaines car elle a su construire avec moi un rapport de confiance et d'amitié qui m'a permis d'apprécier encore plus ces trois années.

Un grand merci à A. Ravasio, qui m'a offert la possibilité de participer à la campagne de diffraction à LCLS. Merci pour m'avoir guidé dans une analyse difficile, pour m'avoir appris à avoir un esprit critique et combattif, et pour sa disponibilité pendant la correction du manuscrit. Je tiens particulièrement à remercier Tommaso Vinci. Il m'a soutenu dans beaucoup d'aspects techniques (alignement des optiques, simulations numériques) et sa présence pendant mes premiers mois de thèse a été décisive pour bien m'intégrer au LULI.

Je tiens à remercier les directeurs du laboratoire LULI, François Amiranoff et Patrick Audebert, pour m'avoir accueilli et mis dans de conditions de travail excellentes. Je suis très reconnaissant envers les membres de mon jury qui m'ont fait l'honneur d'évaluer ma thèse: Dr. Thomas Boehly et Dr. Laurent Berthe pour leur travail de rapporteurs, Dr. Patrick Renaudin pour avoir présider le jury et Dr. Patrick Audebert, Dr. Thibaut de Resseguier et Dr. Guillaume Fiquet pour leur travail d'examinateurs.

Un grand merci à E. Brambrink pour tout le temps qu'il m'a dédié. Sa contribution a été décisive dans plusieurs domaines (alignement optiques, calibration diagnostiques, interprétation des données ...). J'adresse un remerciement chaleureux à Marco Guarguaglini avec lequel j'ai partagé le bureau et beaucoup d'aventures. Ensemble on a vécu des succès, des moments difficiles et des aventures inoubliables (en particulier une épique course en taxi à Osaka). Un grand merci à Jean-Alexis Hernandez, pour le ski à Montgenèvre, le burrito à San Francisco et ses conseils

géophysiques très précieux. Je remercie également A. Denoued pour m'avoir introduit à l'alignement VISAR et aux simulations MULTI et pour le temps qu'il m'a dédié pendant ses derniers mois de thèse. Je remercie aussi M. Koenig qui, avec sa discrétion ;) , nous témoigne un esprit critique et combattif.

Je tiens particulièrement à remercier G. Morard avec lequel j'ai partagé des mois de polissage e de préparation des cibles. Merci pour toutes les fois que tu m'as accueilli dans ton bureau et pour avoir partagé avec moi tes passions sportives. J'adresse un grand merci aussi a F. Guyot. Discuter de science avec toi a été un plaisir et un privilège. Ta passion pour la science est un exemple que je ne oubliera pas. Un grand merci aussi à M. Harmand pour sa sympathie et sa disponibilité. Je tiens aussi à remercier V. Recoules, disponible et professionnelle, pour sa contribution indispensable pour interpréter les résultats de la campagne XANES. Les discussions avec elle ont été toujours très instructives. Je remercie également F. Dorchies et N. Jourdain pour l'aide précieuse qu'ils nous ont donné pendant la campagne XANES. Travailler avec eux a été très agréable.Je remercie aussi R. Musella et F. Remus pour leur contribution précieuse pour interpréter le résultats concernant les chocs decroissants.

Many thanks to N. Ozaki for allowing me to participate to a campaign at GEKKO and for the precious discussions to interpret decaying shock data. I want to thank also K. Miyanishi for all the help during my stay in Osaka. Many thanks to R. Alonso Mori - I consider myself fortunate to have had the opportunity to work with him on his experiment at LCLS.

Un grand merci à tous le joueurs de foot de polytechnique et en particulier à S. Savalle. Avec vous j'ai passé de moments de détente agréables et décisifs pour mon équilibre psychophysique.ù Je tiens à remercier aussi tous les doctorants, les chercheurs et postdocs du LULI avec lequel j'ai partagé ce parcours d'études et beaucoup de café: Thibaut, Guilhem, Gabriel, Paul, Ambra, Anna, Alexandre, Simon, Claire, Roman, Frederic. Une dédicace particulière à Bruno, notre petit Mozart de .. (de quoi en fait?), avec lequel j'ai eu la chance de partager le bureau et dont j'ai pu connaitre l'esprit délicat et fin.

Je tiens à remercier aussi les équipes techniques et administratives: les secrétaires qui ont étés indispensables pour maintenir la calme face à la bureaucratie français, les laseristes pour leur travail décisif, Emilie, Mathieu et Fabien, pour leur patience, leur calme et leur disponibilité face à nos exigences (de fois bizarres), Frédéric et Melanie pour leur travail indispensable.

Infine ringrazio tutti gli amici. In questi anni ci siamo visti di meno, ma il mio affetto per voi non é diminuito. In particolare ringrazio Zanna e Laura per la vostra amicizia fedele.

L'ultimo pensiero alla mia famiglia (tutta) a cui questa tesi é dedicata. Innanzi-

tutto ringrazio mia moglie Marta, compagna di questa avventura, e mio figlio Pietro che ci ha raggiunto a metà dottorato. Siete segno dolcissimo di un amore immeritato. Ringrazio i miei genitori Mirella e Antonello, i miei fratelli Alessandro e Matteo e le mie belles-soeurs (in francese é più bello) Lucrezia e Alissa; la lontananza é stato un sacrificio grande che sicuramente non ha diminuito il mio affetto per voi. Il vostro affetto e sostegno sono un regalo grande. Ringrazio i miei nonni Ermelina e Albino e mio zio Santo. Non sapete il dolore che provo per non potervi venire a trovare più spesso. Vi penso sempre. Una dedica speciale anche a mio nonno Marino, salito al cielo mentre ero lontano da casa, e mia a nonna Melania che sicuramente non ha mai smesso di guardarmi. Ci tengo anche a ringraziare i miei beaux-parents, Laura e Roberto, e Anna e Chiara per il sostegno datoci in questi tre anni, la disponibilità e l'ospitalità con cui mi fate sempre sentire a casa.

université PARIS-SACLAY | ÉCOLE DOCTORALE Ondes et Matière (EDOM)

Titre : Etude des diagrammes de phase des systèmes MgO-SiO2 à hautes pressions générées par chocs laser

Mots clés : Planetologie,laser choc,matière tiede et dense.

Résumé : La découverte récente d'un grand nombre d'exoplanètes et en particulier des planètes potentiellement habitables suscite une grande fascination. Pour modéliser les intérieurs de ces planètes, il est crucial de connaître avec précision les propriétés physiques et les équations d'état des composants planétaires. Ces matériaux se trouvent à des conditions de pressions et températures extrêmes (1-100 Mbar, 10^3-10^4 K), correspondantes à celles de la matière dense et tiède ou Warm Dense Matter (WDM). La description théorique de cette matière a progressé grâce aux calculs ab initio, mais reste complexe. Les données expérimentales sont fondamentales dans ce contexte. Ce projet de thèse porte sur l'étude expérimentale de trois matériaux importants pour la géophysique, le MgO, $MgSiO_3$ et Mg_2SiO_4 dans le domaine ~0.5-10 Mbar. Ces trois matériaux en fait sont les pôles purs magnésiens du (Fe, Mg)SiO_3 and (Fe, Mg)$_2SiO_4$ qui sont parmi les composantes plus abondantes du manteau terrestre et très probablement des manteaux du Super-Terres et des noyaux des planètes géantes. Pour amener ces matériaux aux conditions typiques des intérieurs planétaires on a utilisé la technique de chocs laser. En particulier, nous avons réalisé trois campagnes expérimentales sur des grandes installations: LULI2000 (Ecole Polytechnique, France), GEKKOXII (Osaka University, Japan), MEC à LCLS (SLAC, USA). Pour chaque campagne, on a utilisé une technique différente. Sur LULI2000 et GEKKOXII nous avons étudié les propriétés de MgO, $MgSiO_3$ et Mg_2SiO_4 liquide et la fusion avec des chocs décroissants couplés avec des diagnostiques optiques. Sur LULI2000 on a étudié les propriétés électroniques et structurelles du MgO liquide avec la spectroscopie XANES. Sur MEC, on a conduit une expérience de diffraction X pour déterminer les changements structuraux induits par des chocs stationnaires dans le régime solide sur le $MgSiO_3$ et le Mg_2SiO_4. Dans leur ensemble, les résultats de ces expériences impliquent une révision des diagrammes de phase des matériaux étudiés. En particulier, on a déterminé un nouveau point de fusion pour le MgO (à 470±40 GPa et 9860±810 K), on a résolu une controverse sur la présence d'une transformation liquide-liquide dans le diagramme de phase du $MgSiO_3$ (qui concernait une région autour de ~400 GPa sur la Hugoniot) et on a obtenu pour la première fois des évidences de la amorphisation de la Forsterite (Mg_2SiO_4 cristal) sous choc (à ~50 GPa sur la Hugoniot). En plus on a obtenu des informations sur la réflectivité (liée à la conductivité) pour le trois matériaux, et les données de spectroscopie XANES ont permis de comprendre le mécanisme de fermeture du gap (métallisation) du MgO sous effet de la température.

Title : Laser shock compression studies of MgO-SiO_2 systems at high pressures

Keywords : planetology,laser shock,warm dense matter

Abstract : Two decades of exoplanet discoveries brought the physics of planetary interiors among the topics of broad and current interests. To advance in this field, one of the key ingredient is the knowledge of the equation of states and physical properties of planetary constituents. At the extreme conditions of planetary interiors (1-100 Mbar, 10^3-10^4 K), matter lies in the Warm Dense Matter (WDM) regime and theoretical descriptions are not trivial. Important progress have been done with ab-initio calculations based on differential functional theories, but such calculations need to be validated by experiments. In this thesis, we experimentally characterized phase diagrams and physical properties of MgO, $MgSiO_3$ and Mg_2SiO_4 at conditions relevant for planetary science (0.5-10 Mbar). The studied compounds are the Mg end members of (Fe, Mg)SiO_3 and (Fe, Mg)$_2SiO_4$ that are among the most abundant components of Earth's mantle and are also thought to be abundant in Super-Earth's mantle and giant planet cores. To bring these materials to planetary interior conditions we performed laser shock compression experiments at three high power laser facilities: LULI2000 (France), GEKKOXII (Japan), MEC at LCLS(USA). At LULI2000 and GEKKOXII we investigated the liquid properties and melting of MgO, $MgSiO_3$ and Mg_2SiO_4 using decaying shocks coupled to visible diagnostics. At LULI2000 we studied with XANES spectroscopy MgO in the WDM regime highlighting its metallisation mechanism and structural properties in the liquid phase. Finally, at the MEC end station of LCLS, we used X-ray diffraction to measure shock induced structural changes on $MgSiO_3$ and Mg_2SiO_4 in the solid region of their phase diagrams. Altogether these works, obtained with different diagnostics, imply a revision of the phase diagrams of the studied compounds. In particular we determined a new experimental melting point for MgO (at 470 ± 40 GPa and 9860 ± 810 K), we ruled out the occurrence of an $MgSiO_3$ liquid-liquid transition (supposed to occur at ~400 GPa along the Hugoniot) and we evidenced for the first time the occurrence of an amorphous phase along the Forsterite (Mg_2SiO_4 crystal) Hugoniot (at ~50 GPa).